Spring 2015

Unveiling the mechanical behavior of the rod-like microstructure in the radular teeth of cryptochiton stelleri

Enrique Escobar de Obaldia
Purdue -University, United States

Graduate School Form 30
Updated 1/15/2015

PURDUE UNIVERSITY
GRADUATE SCHOOL
Thesis/Dissertation Acceptance

This is to certify that the thesis/dissertation prepared

By Enrique Raul Escobar de Obaldia

Entitled

UNVEILING THE MECHANICAL BEHAVIOR OF THE ROD-LIKE MICROSTRUCTURE IN THE RADULAR TEETH OF CRYPTOCHITON STELLERI

For the degree of Doctor of Philosophy

Is approved by the final examining committee:

Dr. Pablo Zavattieri

Dr. Arun Prakash

Dr. Jason Weiss

Dr. David Kisailus

To the best of my knowledge and as understood by the student in the Thesis/Dissertation Agreement, Publication Delay, and Certification Disclaimer (Graduate School Form 32), this thesis/dissertation adheres to the provisions of Purdue University's "Policy of Integrity in Research" and the use of copyright material.

Approved by Major Professor(s): Dr. Pablo Zavattieri

Approved by: Dr. Dulcy Abraham 4/20/2015

Head of the Departmental Graduate Program Date

UNVEILING THE MECHANICAL BEHAVIOR OF THE ROD-LIKE MICROSTRUCTURE IN THE RADULAR TEETH OF CRYPTOCHITON STELLERI

A Dissertation

Submitted to the Faculty

of

Purdue University

by

Enrique Raul Escobar de Obaldia

In Partial Fulfillment of the

Requirements for the Degree

of

Doctor of Philosophy

May 2015

Purdue University

West Lafayette, Indiana

To my beautiful wife Katharina

and

my son Alejandro Enrique

ACKNOWLEDGEMENTS

I would like to give my sincere gratitude to all of those who helped make this PhD thesis possible. I would like giving my sincere gratitude to Professor Pablo Zavattieri, for his guidance and patience that was necessary in these years. The hours spent discussing the theoretical and technical background presented in this document will be always remembered.

I also would express my gratitude to Professor David Kisailus, for his personal and scientific knowledge that contributed so much in this project. The success of this research was not going to be possible without his participation. Also, I would like to give the thanks to Professor Jason Weiss and Professor Arun Prakash for their suggestions and support.

The analysis of the experimental data was not going to be possible without the help of Dr. Qianqian Wang, Dr. Lessa Grunenfelder, Christopher Salinas and Steven Herrera. I am grateful for the patience and time answering my questions and following my suggestions. My special gratitude to Chanhue Jeong, for his help in the mechanical testing and fabrication, to Rick Womack of the Prototype Lab, to the team of the Artisan and Fabrication Lab and the Microstructure Testing and Analysis Lab at Purdue University.

In addition, I would like to thank my friends and colleagues at Purdue University. Especially to Fernando Cordisco, Fernando Dri, Ferderico Antico, David Restrepo, Nicolas

Guarin, Nobphadon Suksangpanya and all the members of the CMMLAB that helped me in personal and professional discussions.

Finally, my deepest gratitude to my beloved wife Katharina that was always there in the most difficult times, to my beautiful son Alejandro that joined us in the finalization of this project, and to our family that always supported our decisions and helped so much in the last years. This research was supported by the Airforce Office of Scientific Research through award No. FA 9550–12–1–0249.

TABLE OF CONTENTS

Page

LIST OF FIGURES ix
CHAPTER 1. INTRODUCTION 1
1.1 Research objectives 5
1.2 Thesis organization 6
CHAPTER 2. BACKGROUND 9
2.1 Biomineralized microstructures 9
2.2 Indentation tests 12
2.3 Concepts of linear elastic fracture mechanics 14
2.4 Fracture toughness estimations by LEM model 18
2.5 Critical load for yielding 21
CHAPTER 3. MODELING THE RADIAL CRACK PROPAGATION OF AN ISOTROPIC MATERIAL 24
3.1 Introduction 24
3.2 Interface element 25
3.3 Indentation of an isotropic material 29
3.4 Conclusion 37
CHAPTER 4. ON THE WEAR RESISTANT MECHANICS OF NATURALLY-OCCURRING ROD-LIKE MICROSTRUCTURES 38
4.1 Introduction 38
4.2 Experimental analysis 42
4.2.1 Material characterization of magnetite 43

Page

4.2.2 Comparison of the resistant to penetration of the tooth and the magnetite ... 45
4.3 Micromechanical model ... 48
4.3.1 Computational domain ... 49
4.3.2 Interfacial behavior of the organic layer ... 51
4.3.3 Deformation modes ... 54
4.4 Results ... 55
4.4.1 Loading displacement curves ... 55
4.4.2 Energy dissipation ... 57
4.4.3 Failure of the rods ... 62
4.4.4 Determination of the strength of the magnetite ... 63
4.4.5 Maximum principal stresses ... 67
4.4.6 Competing mechanisms ... 70
4.5 Conclusions ... 73
CHAPTER 5. STRESS AND DAMAGE MITIGATION FROM ORIENTED NANOSTRUCTURES WITHIN THE RADULAR TEETH ... 74
5.1 Core-shell architecture and rod-like microstructure ... 74
5.2 Micromechanical analysis ... 76
5.3 Surface analysis ... 79
5.4 Modeling ... 81
5.5 Summary ... 86
5.6 Conclusions ... 90
CHAPTER 6. UNVEILING WITH BIOMIMETIC DESIGNS THE RESISTANCE TO PENETRATION OF THE RADULAR TEETH OF THE CRYPTOCHITON STELLERI ... 91
6.1 Introduction ... 91
6.2 Biomimetic composites ... 93
6.3 Experimental setup and procedure ... 96
6.4 Experimental results ... 98
6.4.1 Building blocks ... 98

Page

6.4.2 Effect of spatial orientation 100
6.4.3 Property maps 103
6.4.4 Abrasion resistance and fracture toughness 105
6.5 Computational models 109
6.6 Discussion 119
6.7 Conclusions 124
CHAPTER 7. ROLE OF THE ROD-LIKE MICROSTRUCTURE UNDER TENSILE LOADING 125
7.1 Introduction 125
7.2 Theoretical background 128
7.3 Parametrization 132
7.4 Biomimetic composites 135
7.5 Results 138
7.5.1 Strain contours 140
7.5.1.1 Plate-like composites 140
7.5.1.2 Rod-like composites 144
7.5.2 Stiffness calculation 148
7.6 Discussion 149
7.7 Conclusions 151
CHAPTER 8. INVESTIGATING THE TOUGHENING MECHANISMS OF THE STROMBUS GIGAS 153
8.1 Introduction 153
8.2 Influence of the building block orientation in the surface damage 156
8.3 Application of the micromechanical model 157
8.4 Biomimetic approach 162
8.5 Summary 164
CHAPTER 9. CONCLUSIONS 166
LIST OF REFERENCES 171
VITA 188

LIST OF TABLES

Table Page

Table 4-1 Summary of the experimental values obtained from the cube corner indentation tests in the mineral and chiton teeth at h_{max} = 200 nm. The curves from the *LE* and *TE* have been taken with permission of Grunenfelder et al. [67]. 47

Table 6-1 Experimental data obtained in indentation tests at a maximum depth of 6mm displaying volume fraction of interface material (Vf_s), orientation (*OR*), maximum load (P_{max}), reduced Young's modulus (E_r) and hardness (H)..... 97

Table 6-2 Mechanical properties of the building blocks measured by independent set of tests. 98

Table 6-3 Effect in σ_{yield} of the interface material in the site specific properties measured after indentation in $L/2W$ = 10 111

Table 7-1 Geometrical parameters of the chiton shell and Nacre microstructure [1], [2], [9], [10]..... 130

Table 7-2 Values of V_f (%) and A/V (1/nm) calculated in this study. 134

Table 7-3 Parameters of the rod-like composites 136

Table 7-4 Parameters of the plate-like composites 136

LIST OF FIGURES

Figure Page

Figure 1-1 Comparison of the chiton tooth and the magnetite (building block) with respect to metals and ceramics. The tooth possesses the greatest resistance to plastic deformation observed in biomineralized composites. Biological materials (green), ceramics (yellow) and metals (blue) are compared with respect their Young's Modulus. Data collected from the references [9], [10]. 2

Figure 1-2 (A) The tendency to decrease the onset of plastic behavior of the *P. Senegalus* and cortical bone as (B) compared with the chiton tooth, where the stress required for plastic yielding is greater for the chiton as compared to the magnetite[5], [13], [14],[15],[16], [17]. The values of yield stress have been approximated as $\sigma_y=3H$ [11][18]. 3

Figure 2-1 (A) Rod microstructure observed in the hardest layer of the *P. Senegalus* and (B) crack patterns observed by compression tests made with a flat nano-indenter, adapted from Han et al.[22]. 10

Figure 2-2 (A) Different orders observed in the shell of the Strombus Gigas, (B) rod alignment showing the different layers at the shell, (C) 3rd order planks observed in 1st and 2nd order lamellae and (D) aragonite building blocks of the shell. Images adapted from Kamat et al. [25]. 11

Figure 2-3 (A) Indentation data and (B) indenter tips commonly used. 12

Figure 2-4 (A) LEFM applied in K-dominance zone and (B) definition of the coordinate system at the crack tip. 16

Figure 2-5 Border effects in a notched sample. At $H/a=2$, the value is almost constant indicating that singular stresses are dominant as compared with the other two cases [5]. 17

Figure Page

Figure 2-6 3D view of physical variables considered in the LEM model. Contour obtained from the elasto-plastic model developed in this thesis (chapter 3) with fracture planes at the edges of the indenter. Red contour displaying the plastic region of the solid ($\sigma_{VM} > \sigma_{yield}$) and blue lines are cracks at the edges of the Vickers tip (4 sided indenter)[30]..... 19

Figure 2-7 (A) constant resistance to plastic deformation (H^3/E^2 = 0.5GPa) and (B) linear relationship between H and E_r. Images adapted from Musil et al. [48]..... 23

Figure 3-1 Bilinear law of the cohesive zone model. Isoparametric curves with the correspondent (A) normal and (C) transversal components. 2D views with respect to the (B) normal and (D) transversal displacement. The (B) normal traction as compared with the transversal law has a steep slope when $u_n/\delta_n < 0$, region that is not included in the plot..... 27

Figure 3-2 (A) Middle plane of a zero thickness interface element, (B) DCB model with a section with and without interface elements and a (C) validation comparing the analytical solution [33] with different mesh refinements. 29

Figure 3-3 (A) dimensions of the homogenous solid modeled in μm, (B) interface elements embedded in the walls of the solid that coincide with (C) indenter edges and (D) indentation marks over Al_2O_3 showing radial cracks coinciding with indenter edges[44]..... 30

Figure 3-4 Loading displacement curve of an isotropic material with/without cohesive elements. 31

Figure 3-5 (A) Reduced Young's modulus and (B) hardness measured with the standard experimental procedure. Green dotted line represents the average value while blue line the input value of the FEM. 32

Figure 3-6 Variation of the plastic von Mises stresses (GPa) for the different h_{max}..... 33

Figure 3-7 Variation of the radial cracks for the different h_{max}. The red color refers to elements with values of $\lambda = \lambda_{max}$. The countours are displayed at the maximum load and after removing the indenter (equilibrium)..... 34

Figure Page

Figure 3-8 Comparison of fracture toughness estimation by LEM model with crack length of equilibrium and maximum depth. Also the input Kc value of the FEM is plotted as a constant (K_c = 0.75 MPa $m^{0.5}$)..... 36

Figure 4-1 *Cryptochiton stelleri* [74] in the marine habitat, (b) SEM image showing the alignment of the teeth in the radulae and (c) an overview of a post-indented sample (obtained with permission from Grunenfelder et al.[67]). The lines in (b) coincide with the alignment of the mineralized rods [67]. The indentation mark in (c) is with a rod-like microstructure aligned perpendicular to the surface in (b)..... 40

Figure 4-2 Constitutive model of the single crystal magnetite considered in this study (a). Different values of H_{iso} and a constant σ_y = 3.5 GPa are considered in the numerical model (b), where H_{iso} = 40 GPa shows good agreement with respect the Vickers indentation data of Chicot et al. [78]. The value of σ_y = 3.5 GPa was obtained with the contact formulation [82]. The experimental and numerical results of a cube corner indentation test in (c). 44

Figure 4-3 (a) Cube corner indentation data of the magnetite obtained with a cube corner indenter in this study, and loading curves of the leading and trailing edge from the literature [67]. A comparison of the indentation modulus obtained with the cube corner indenter is shown in (b) with respect to the slope of the indentation data (c_1). An R^2 = 0.98 is the correlation coefficient of c_1 for the magnetite and chiton tooth. The error bars of this figure are one standard deviation..... 46

Figure 4-4 Summary of the computational domain considered. Homogenous rods surrounded by cohesive interfaces are shown in (a) and (b)..... 49

Figure 4-5 Details of the numerical model of the cube corner indentation test. Cube corner indenter placed above the idealized rod-like microstructure in (a) and a 1/6th domain and cube corner indentation model in (b). The rods are oriented perpendicular to the surface..... 50

Figure Page

Figure 4-6 (a) TEM image of the rods (adopted with permission from Grunenfelder et al. [67]) where the arrows indicate the mineral bridges observed. Diagram of the micromechanical analysis of the crystal bridges and organic layer (b). Traction separation laws that mimic the fracture of the organic material and crystal bridges in mode I (c) and mode II (d). 53

Figure 4-7 Indentation mark observed in a computational model at h_{max} = 700 nm. Radial cracks coinciding with the indenter tips are observed in the interface layer. . 54

Figure 4-8 Comparison of the influence of T_{max} and G_c in the loading data. Traction separation laws with G_c = 70 J/m^2 in (a) and T_{max} = 0.5 GPa in (c). The loading data in (b) corresponding to the traction laws in (a), and in (d) to the traction laws in (c)..... 57

Figure 4-9 Influence in the variation of U_p (b) and U_{dis} (c) with respect to T_{max} (a). The values were calculated with a G_c = 70 J/m^2 and have been augmented for displaying purposes in (a). The dashed lines in (b) represent the solid materials. 59

Figure 4-10 Visualization of the variation of G_{dis} (nJ/μm^2) against T_{max} and h_{max}. The value of G_c = 70 J/m^2. The contours are only plotted for values of $G_{dis} > 0$. 61

Figure 4-11 Map of the variation of the maximum principal stresses against T_{max} and h_{max}. 63

Figure 4-12 Standard deviation data of cube corner indentation tests in the monolithic material (a). SEM analysis at different penetrations suggest that the onset of fracture is around h_{max}=80nm (B) value that coincides with the pop-in event observed in (a). Greater surface damage is observed at h_{max}=150 nm (b) and h_{max} = 200 nm (c). The onset in (a) corresponds to the mean and standard deviation obtained with h_{max} = 200 nm. 66

Figure Page

Figure 4-13 Comparison of the volume associated to the principal stresses at different h_{max}. The curves are compared in the solid (a), where equation 4.9 is plotted. The comparison also includes the rod-like microstructures at h_{max} = 50 nm (b), h_{max} = 100 nm (c) and h_{max} = 150 nm (d). Different values from T_{max} = 0.4 Gpa to 16GPa were considered. The inset in (a) shows the fracture of rods of different diameters and in (b) the fracture of rod-like microstructures of unique diameter and different volume. The error bars show the standard deviation of 19% computed from different meshes. 69

Figure 4-14 A competing mechanism between the failure of the rods and resistance to penetration of the indenter is visualized in (a). The optimum values of T_{max} are displayed in (b). The intersection between the data points shown in (a) determine the optimum values in (b). 72

Figure 5-1 Core-shell architecture and local microstructural features of mineralized teeth. (A) BSE overview of a longitudinal fracture, highlighting a heavily mineralized outer shell and organic rich core; (B) Aligned and staggered nanorods in the leading edge of the shell; (C) Amorphous core region; (D) Apex of longitudinal fracture, revealing nanorod orientation and continuity around the shell of the tooth; (E) Latitudinal fracture near the tip of the tooth; (F) Center of the latitudinal fracture, demonstrating curvature of nanorods following the contour of the tooth; (G) Latitudinal fracture within the shell region, highlighting highly oriented nature of nanorods; (H) Micrograph of partially mineralized tooth showing mineral formation along alpha-chitin fibrils. 76

Figure Page

Figure 5-2 Nanomechanics of core and shell regions of a fully mineralized tooth in latitudinal and longitudinal sections. (A) BSE micrograph of a latitudinal polished section showing the core-shell structure of the tooth; (B) Modulus and (C) Hardness maps from nanoindentation of a latitudinal section; (D) BSE micrograph of a longitudinal polished section of the entire tooth, highlighting the thickness of leading and trailing edges as well as extent of core region throughout tooth; (E) Modulus and (F) Hardness maps from nanoindentation of the longitudinal section, demonstrating a clear interface between core and shell as well as a gradient from leading edge to trailing edge of the tooth; (G) SEM micrograph of the leading edge of the longitudinal section after indentation, highlighting a crack running parallel to the edge of the sample; (H) BSE micrograph revealing cracking at the core-shell interface of the tooth. 78

Figure 5-3 Surface analysis of the leading and trailing edges of the fully mineralized tooth. Longitudinal fracture surface of (A) the leading edge, highlighting a 2 μm thick dense nanoparticulate layer, transitioning to nanorods (observed perpendicular to the field of view), which rotate 90° over a region of ≈ 1 μm to orient parallel to the tooth surface; Longitudinal fracture surface of (B) the trailing edge, revealing a 1 μm thick dense nanoparticulate layer that abruptly transitions to nanorods oriented parallel to the tooth surface (no rod rotation observed); (C) Histogram of rod diameters on the leading edge; (D) Histogram of rod diameters on the trailing edge. 80

Figure 5-4 Finite element models of a fully mineralized tooth. (A) Digitization of tooth geometry; (B) The four individual components used to create the model and the association of each part into the full model; (C) Mesh and boundary conditions; (D) Direction of tensile (red) and compressive (blue) stresses in a worn (left) and fresh (right) tooth; (E) Rotation in the direction of stresses at the transition zone between the leading and trailing edges above the core. 83

Figure Page

Figure 5-5 Displacement magnitude in micrometers showing initial and deformed position of the tooth at a load of 0.1N (A); contour of von Mises stress distribution in Pa (B); maximum and minimum principal strains showing regions with tensile deformations in the leading edge (C) and compressive strains in the trailing edge (D). 83

Figure 5-6 Pile up of staggered hexagonal rods idealized for illustration purposes to show the ultrastructure of the tooth; (B) Rod cross sections assumed in the FEM for the trailing edge (250 nm) and leading edge (150 nm); (C) Indentation data of experimental curves at the leading and trailing edge compared with the elastic-plastic FEM; (D) Indentation mark at the leading edge of the tooth with rods aligned orthogonal to the surface; (E) Comparison of stress contours in the same direction of indentation for an elastic model at maximum penetration (≈ 700 nm) showing material removal and crack propagation; (F) Cube corner indenter placed above the model showing material removal and small radial cracks. . 85

Figure 6-1 Experimental values of reduced modulus E_r and hardness, H, as a function of rod diameter (ϕ) measured from the leading and trailing edge of the mature tooth of the *Cryptochiton stelleri* [67]. 93

Figure 6-2 (A) Structural details of the idealized rod-like microstructure of the radular teeth. (B) Top and (C) side view with hexagonal cross sections and rods alignment. (D) Schematics and details of the design of the hexagonal rods with side length W = 0.5mm and interfacial material of thickness t = 0.1mm (E) side view showing staggered rods of variable length L. (E) Cube corner indenter placed above an intact sample (F). 94

Figure Page

Figure 6-3 Double cantilever beams (DCB) manufactured to test the use of rapid prototypes in fracture mechanics problems, test were performed in an MTS machine of 0.1 kN-load cell. The total length of the beams was 80 mm, with a pre-crack of 30mm and an interface of 0.1 mm (same interface thickness used in our indentation studies). (A) Shows the DCB test in opening mode and (B) experimental and fitting curves under *LEFM* premises. Banded region in (B) is obtained from 6 for values of 2-3.5 J/m^2 of fracture energy..... 100

Figure 6-4 Load versus displacement curves for the parallel (A) and perpendicular (B) configurations, and different *L/2W* with error bars of one standard deviation. Inset in A indicating the value of P_{max} and h_{max} in an indentation test. Indentation marks with damage areas after indentation of rods (∥) parallel (C) and (⊥) perpendicular (D) to the indenter. 101

Figure 6-5 3D printed specimen used to quantify the shear strength in the interface material. The dimensions of the samples are shown in (A) and the loading curves obtained after the tests in (B). 102

Figure 6-6 Effect of rod alignment in the site-specific properties (A). Despite having the same material composition, the staggered rods exhibit higher values of E_r and H than the randomly oriented composite. CAD of randomly distributed composite created with GeoDict [154] (B). (C) E_r vs. *L/2W* and (D) H vs. *L/2W*. Errors bars indicate one standard deviation. 104

Figure 6-7 Higher magnification of the edge of an indentation mark exhibiting crack patterns in the interface material that surrounds the rods of parallel configuration (A). Values of K_c estimated with Equation 6.3 (B) as a function of *L/2W*. Parameters (c and a) from the *LEM* expression are shown in B. Inelastic deformation and damage at the center of the mark (C) and values of abrasion resistance (D) as a function of *L/2W*. 107

Figure 6-8 Load versus displacement curves at different maximum penetrations (A) and a comparison of the values of K_c obtained from $Kc \approx \alpha 3/4 \chi (HEr2Pc) 1/4$ [27], [43], [155], [156] with respect to h_{max} (B). 108

Figure Page

Figure 6-9 Cube corner indenter placed above a uniform rod-like microstructure of the same dimensions (*W,t*) that the 3D printing designs (A, B). FEM of indentation tests in an elastic microstructure (*L/2W* = 10), rod and support materials (C). Comparison between the elastic-plastic model of *L/2W* = 10, the experimental data and different values of *L/2W* (D). Effect of aspect ratio on P_y in the load displacement curve (E) P_y as a function of *L/2W* (F). Error bars in F account for the effect of mesh refinement in the load versus displacement curves (10%). 112

Figure 6-10 Values of effective strain in the interface material at different h_{max} = 0.15mm (A, B and C) and h_{max} = 0.6mm (D, E and F) for *L/2W* = 10, 15 and 25 obtained from our FEM simulations. 113

Figure 6-11 Comparison of the analytical model proposed by Tsai et al. [162] of rods surrounded by weak interfaces in shear mode. Configuration of rods exposed to a load per unit length (*T = 1N/m*), where the shear strain (γ) in the interface material is expressed as a function of the shear modulus (G_i = 1.5 MPa and G_r = 0.961 GPa) and geometrical parameters of the rod-like microstructure (A). The overlap dimension considered is $L-\Delta x$, where $\Delta x = 1mm$. Shear strains in the interface layer show higher values for the smaller *L/2W* = 10 as compared with *L/2W* = 25 (B), results that are in agreement with the FEM (Fig 6.10). 114

Figure 6-12 Sectioned samples of h_{max} = 6mm. (A) Parallel configuration: crack patterns propagate through the interface material (a arrow) but for the perpendicular configuration (B) Perpendicular configuration: the energy dissipates not only through the interface material (c and d arrows) but also though the rods (b arrow). 116

Figure Page

Figure 6-13 Comparison between the displacement magnitude in the direction of penetration (uz), the magnified deformation and radial displacement (ur) for $L/2W$ = 10 (A, B and C), $L/2W$ = 15 (D, E and F) and $L/2W$ = 25 (G, H and I) respectively at 0.6mm of penetration. For displaying purposes, the deformation of the rods is magnified by 100 times in the X axis (B, E and H) and ur by 10 times in the vertical direction..... 118

Figure 6-14 Comparison between a (A) post-sonication indentation mark at the leading edge of the tooth with rods oriented parallel to the indenter at maximum penetration of 2000nm[67] and (B) damage area surrounding biomimetic composites at maximum penetration of 6mm. Arrows in (A) and (B) pointing to regions with radial and circumferential cracks. Effect of $L/2W$ in the P_{max} measured during the indentation tests (C), and comparison of critical loads P_b calculated with equations 6.6 and 6.7 with respect $L/2W$ (D). The insets in (C) indicate rigid body rotation ($L/2W < 15$) and lateral bending ($L/2W > 15$). The insets in (D) show the rigid deformation of a rod (green) and bending (red) surrounded by an elastic matrix. 123

Figure 7-1 Overall comparison of the microstructure of the mother-of-pearl with respect to the chiton tooth. Inside view of the microstructure and strain-strain curves from Barthelat et al. [64] (A and B). Bottom view of the *Criptochiton stelleri* compared with a measuring stick of 15 cm of length (C) and rows of teeth located in the ribbon (D). Sheet arraignment of a plate-like microstructure displaying bi-axial forces (E) and close up of the plate-like microstructure (F)[64]. Rod-like microstructure working in tension in the leading edge and in compression in the trailing edge of the tooth (G)[67]..... 128

Figure 7-2 Tension shear model (A) adapted by Ji and Gao [4], [5]. Overview of the geometrical parameters of the microstructures (B). Predictions made by equation 7.1 of E for the nacre and chiton in tension, with constant V_{fm} (C) and $\rho = 20$ (D)..... 131

Figure Page

Figure 7-3 Representative volume element of the microstructures. RVE of a plate-like microstructure (A and B). Description of the RVE's in terms of *W, t* and *L* (C and D)..... 132

Figure 7-4 Isoparametric surfaces comparing the V_{fm} (A) and A_{ol}/V_{mb} (B) for the nacre and chiton tooth. Despite having the same order of V_{fm}, the rod-like microstructure of the chiton reveals a higher value of A_{ol}/V_{mb} as compared to the plate-like microstructure. The surfaces were generated with equations 7.2 and 7.3, with t = 25nm..... 134

Figure 7-5 Experimental setup and biomimetic composites manufactured. Sketch of rapid prototypes used to test the effect of V_f and A/V (A). To avoid defects in the manufacturing process, the biomimetic designs were created with a layer of support material at the top and the bottom of the sample that was removed before the tests (B). Set of two cameras (C) and painted sample with a random distribution of speckles (D). C and D were required for the analysis made with the DIC..... 137

Figure 7-6 Load versus displacement curves obtained in the test at t = 0.1 mm (A), t = 0.3 mm (B) and t = 0.4 mm (C). SEM images displaying the rods of 1mm of cross section and t = 0.1 mm (D), where in the top of the rods surface irregularities are observed in (E) (SEM image courtesy of UC Riverside). Sketch magnifying the thickness of the binder, displaying the possible presence of defects at t = 0.1 mm of separation (F)..... 139

Figure 7-7 Analysis of strain contours in the plate-like microstructure at different penetrations. Experimental output obtained in A at t = 0.1 mm. Axial (ε_{yy}[]) and shear (ε_{xy}[]) strains at 0.05 mm (B,G), 0.6 mm (C,H), 2.1 mm (D,I) and 2.45 mm (E,J). The plate-like microstructure in F is shown at the same scale for comparison..... 141

Figure Page

Figure 7-8 Analysis of strain contours in the plate-like microstructure at different penetrations. Experimental output obtained in A at t = 0.3 mm. Axial (ε_{yy}[]) and shear (ε_{xy}[]) strains at 0.09 mm (B,G), 0.42 mm (C,H), 0.76 mm (D,I) and 0.9 mm (E,J). The plate-like microstructure in F is shown at the same scale for comparison. 142

Figure 7-9 Analysis of strain contours in the plate-like microstructure at different penetrations. Experimental output obtained in A at t = 0.4 mm. Axial (ε_{yy}[]) and shear (ε_{xy}[]) strains at 0.17 mm (B,G), 0.38 mm (C,H), 0.47 mm (D,I) and 0.59 mm (E,J). The plate-like microstructure in F is shown at the same scale for comparison. 144

Figure 7-10 Analysis of strain contours in the rod-like microstructure at different penetrations. Experimental output obtained in A at t = 0.1 mm. Axial (ε_{yy}[]) and shear (ε_{xy}[]) strains at 0.21 mm (B,G), 0.19 mm (C,H), 4 mm (D,I) and 7.91 mm (E,J). The rod-like microstructure in F is shown at the same scale for comparison. 145

Figure 7-11 Analysis of strain contours in the rod-like microstructure at different penetrations. Experimental output obtained in A at t = 0.3 mm. Axial (ε_{yy}[]) and shear (ε_{xy}[]) strains at 0.18 mm (B,G), 0.6 mm (C,H), 1.25 mm (D,I) and 1.5 mm (E,J). The rod-like microstructure in F is shown at the same scale for comparison. 146

Figure 7-12 Analysis of strain contours in the rod-like microstructure at different penetrations. Experimental output obtained in A at t = 0.4 mm. Axial (ε_{yy}[]) and shear (ε_{xy}[]) strains at 0.15 mm (B,G), 0.5 mm (C,H), 0.99 mm (D,I) and 1.25 mm (E,J). The rod-like microstructure in F is shown at the same scale for comparison. 147

Figure 7-13 Summary of Young's modulus obtained in the tensile tests. Young's modulus versus the Vf() in (A) and versus A/V(1/mm) in (B)..... 149

Figure Page

Figure 7-14 Failure modes observed in the rod-like and plate-like microstructures. While localized damage is observed at t = 0.1 mm (A), spread of damage and rod debonding is observed for t = 0.3 mm (B) and t = 0.4 mm(C). In contrast to the rod-like composites, the plate-like layout shows a row of plates with crack patterns (D). The contours below reveal the out of plane deformation of the samples..... 151

Figure 8-1 The Strombus Gigas in (A), a gastropod that can be found in the Caribbean region[185]. Its aragonite shell (B) is composed of different layers (Inner, Middle and Outer) with the dip directions aligned ± 45° from N (radial direction). An illustration of the fracture shell showing the different layers with alternating 1st order lamellae. Representation of the geometry of the 0th through 3rd order features of the cross lamellar structure, where the SEM images are shown at the bottom of (C). In (C), *T* is referred to the thickness and *W* to width of the blocks. Images on (C) are courtesy of UC Riverside. 155

Figure 8-2 Indentation data obtained at ±45° of plank orientation (A and B). SEM images of the damage observed in the surface of the microstructure at -45° (C) and +45° (D) orientation..... 157

Figure Page

Figure 8-3 Diagram displaying the cube corner indenter alignment with respect a 2nd order lamellae (4 μm x 4 μm x 2 μm) embedded in a semi-infinite solid that for simplification is not shown above. Around 840 building blocks included in the model are exposed to the cube corner indenter with microstructural architecture of -45°, 45° and 90° with respect the Z-Y plane (A, B and D) and offset configuration of 45° with respect the X-Y plane (E). Comparison of an average experimental data shows that the continuum model predicts an increase in the loading response of -45° with respect the Z-Y plane, as T_{max} and G_c increase (C); an illustration plot of the different traction-separation laws is shown in C for I (T_{max}=12.5 MPa,G_c=0.625 J/m^2), II (T_{max}=25 MPa,G_c=1.25 J/m^2) ,III(T_{max}=200 MPa,G_c=10 J/m^2) and IV(T_{max}=800 MPa,G_c=40 J/m^2); FEM shows that microstructural alignment is not largely affecting the response of the material with a traction-separation law (I) (F). Values were fitted with the power function, $P=Ch^{\alpha}$, where C is a constant and α=1.5 for a cube corner indenter; data points are shown in F. 160

Figure 8-4 Sliced views of von Mises stress contours indicating regions with inelastic deformation in GPA at 400nm of penetration depth, the sliced views coincide with a symmetry plane of the indenter; despite obtaining similar loading indentation curves, cracks patterns and localized damage differ in the different configurations. While the orientation of 135° (A) and offset (E) alignments show similar crack patterns and deformation mechanisms to those analyzed by SEM (F), the 45° orientation shows an area with more localized damage (B) comparable with experimental observations made at a maximum displacement of 500nm of penetration (C); FEM of the 90° shows the disadvantage of 2nd order bricks perpendicular to the surface of the conch, where inelastic deformation is more evenly distributed affecting a larger number of aragonite blocks. Arrows indicate areas with pile up and crack patterns. 162

Figure Page

Figure 8-5 Overview of the indentation data and marks obtained in the biomimetic designs. (A) Indentation data obtained (E_r and H) versus P_{cri}, post intended marks showing energy dissipation at +45° (B) and 90° (C). Indentation marks in B were performed at h_{max}=6mm and in C at h_{max}=3mm. 164

ABSTRACT

Escobar de Obaldia Enrique R. Ph.D., Purdue University, May 2015. Unveiling the Mechanical Behavior of the Rod-like Microstructure in the Radular Teeth of *Cryptochiton stelleri*. Major Professor: Pablo Zavattieri

Natural ceramics provided with high volume fractions of mineralized materials that are surrounded by a weak organic interface combine the stiff mechanical behavior of building blocks, like hydroxyapatite or aragonite, and the compliance of the organic surroundings. Unique mechanical properties (e.g. light density and toughness) distinguish bio-composites from common engineering materials. A key example is the highly mineralized shell of the radular teeth of the *Crypochiton stelleri*. Nature has provided the radular teeth with a highly oriented rod-like microstructure of nano-scale dimensions embedded in a matrix of chitin sheaths. Compared to other biological materials, the external iron oxide layer of the mature teeth is characterized with an outstanding abrasion resistance. Studies of the functionality of the tooth have been performed so far with site-specific estimations made by nanoindentation tests and advanced microscopic imaging techniques.

The aim of this work is to analyze the mechanical behavior of the rod-like microstructure of the teeth with biomimetic composites and computational models. A three-dimensional computational model is implemented to unveil the role of the nanoscale features in the response of the microstructure to the penetration of a cube corner indenter. The computational model considers isotropic rods surrounded by cohesive interfaces. The analysis of the damage model indicates competing mechanisms between energy dissipation at the interfaces and rod material. While the localization of damage leads to a higher resistance to penetration, it enhances the probability of failure in the rods.

An experimental approach was developed with additive manufacturing, mimicking the mineral/organic composites with strong materials surrounded by weak interfaces. To assess the role of the geometrical features, a detailed set of experiments was used to quantify the effect of rod orientation and aspect ratio in the site-specific properties measured. Both the experimental and computational frameworks indicate that during indentation the aspect ratio of the rods influences the abrasion resistance and toughness, where the rod deformation plays a critical role in the dynamic response of the microstructure. Finally, to demonstrate the possible applications of the computational and biomimetic approaches presented in this work, the abrasion resistance of another gastropod has been studied. The findings of this research are applicable to other biomineralized materials, and to gain insights into the development of wear resistant composites.

CHAPTER 1. INTRODUCTION

The unique mechanical properties observed in biological composites (e.g. light density and impact resistance) distinguish themselves from common engineering materials [1]. Natural ceramics are composed by organic (e.g. keratin, collagen, chitin) and mineral phases (e.g. hydroxyapatite, magnetite or silicon carbide) with a common feature in their hierarchical structure, a microstructure characterized by building blocks of prismatic shape (e.g. cubic, hexagonal, pentagonal). Multifunctional features adapted from biomaterials inspired multiple designs and applications that are used today. A good example is Velcro, bio-inspired by the seeds of burdocks [2], [3]. The combination of weak organic interfaces with strong mineralized materials can lead to outstanding mechanical properties. An example is the bone tissues, that can withstand large tensile, shear and compressive loads [4]–[6]. Biological materials tend to invert the tendency of toughness versus Young's modulus observed in engineering materials [7], where for instance the combination of collagen and hydroxyapatite in bones show the best compromise between these two properties [8].

Compared to other biological materials, the external iron oxide layer of the chiton radular teeth has been characterized with the highest resistance to inelastic deformation (P_y) known today (Figure 1-1) [9], [10]. The resistance to inelastic deformation observed in the chiton tooth is the inverse of most engineering and biological materials

(e.g. like bones and fish scales) [9], [10]. In most biological composites, the onset of plasticity is lower for the composites as compared with the stiff mineral (Figure 1.2A). In the chiton tooth, the critical load for plastic deformation is higher than the stiff magnetite (Figure 1-2-B), values estimated by nanoindentation tests as $P_y \propto R^2H^3/E^2$ and $\sigma_y = 3H$ [9], [11], [12].

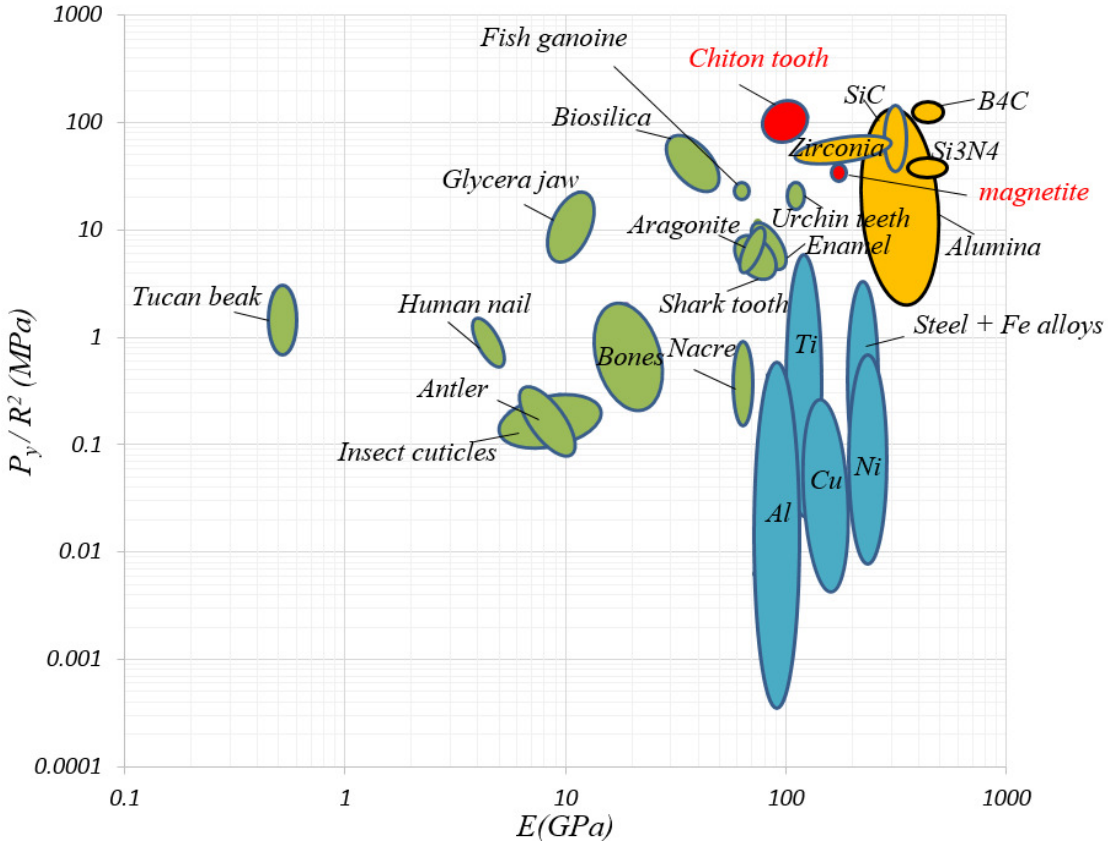

Figure 1-1 Comparison of the chiton tooth and the magnetite (building block) with respect to metals and ceramics. The tooth possesses the greatest resistance to plastic deformation observed in biomineralized composites. Biological materials (green), ceramics (yellow) and metals (blue) are compared with respect their Young's Modulus. Data collected from the references [9], [10].

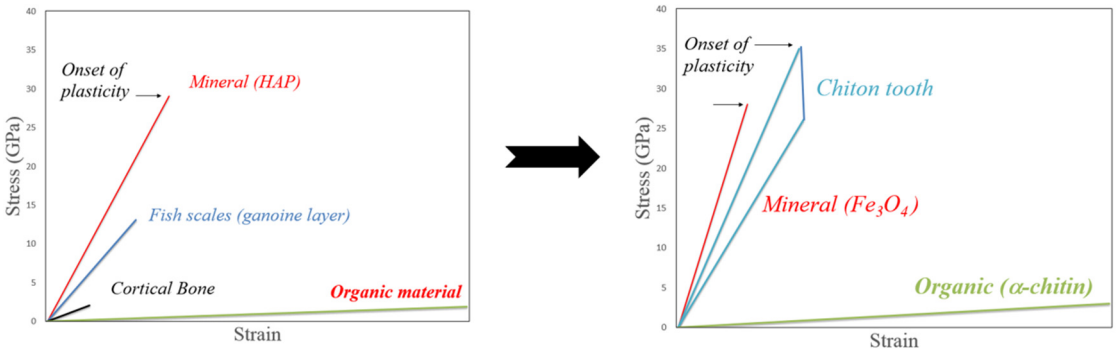

(A) (B)

Figure 1-2 (A) The tendency to decrease the onset of plastic behavior of the *P. Senegalus* and cortical bone as (B) compared with the chiton tooth, where the stress required for plastic yielding is greater for the chiton as compared to the magnetite[5], [13], [14],[15],[16], [17]. The values of yield stress have been approximated as $\sigma_y=3H$ [11][18].

Despite the outstanding abrasion resistance observed in the chiton tooth, many questions regarding the local and global mechanisms used by the tooth to resist penetration and avoid catastrophic failure still remain unanswered. Studies of the functionality of the tooth have been performed with site-specific estimations made by nanoindentation tests and advanced microscopic imaging techniques. These studies have focused in punctually characterizing the reduced Young's modulus and hardness, without trying to systematically identify the deformation mechanisms in the global and local perspective. The aim of this research is to analyze the effect of the rod-like microstructure on the abrasion resistance and fracture toughness, nano-scale features (e.g. crystal bridges and nano-asperities), and to combine a set of numerical models with experimental tests that can help to elucidate the mechanical behavior of the chiton tooth. Therefore, the objective is to understand the

synergetic interaction between the strong mineral and weak interfaces in the mechanical properties of the tooth.

It is then proposed that the tooth has a global and local mechanism to arrest fracture and plastic deformation. This hypothesis is supported by finite element models of the entire chiton tooth in which the directions of the principal stresses observed in the tooth coincide with the rod alignment and the high tensile and compressive stresses observed in the sides of the tooth. In the experimental observations, in the leading and trailing edge of the tooth, a correlation between the properties measured by indentation and the size of the rods has been observed. A notable decrease in hardness and reduced Young's modulus coincides with an increase of the rod diameter from approximately 160 nm in the leading edge to 190 nm in the trailing edge [19]. The local mechanism is observed in the worn tooth during feeding when the rod-like-microstructure is in direct contact with erosive particles and external agents in the rocky substrate. The ultra-structure is configured in such a way that it can resist large compressive punctual stresses without sacrificing the structural resistance of the tooth. The global deformation is concentrated at the leading and trailing edges, where large tensile and compressive stresses affect the strength of the tooth.

1.1 Research objectives

In this research, local and global mechanisms are addressed with a set of 3D printed composites together with micromechanical and analytical models. In order to understand the energy dissipation mechanisms observed during the indentation tests, a 3D micromechanical model of a sharp indenter being in contact with the rods is developed. Indentation tests have been chosen due to the similarity of having a sharp particle in contact with the worn microstructure and also to understand the trend lines of the load displacement curves observed in the nanoindentation tests. The continuum fracture model applied in this research takes into account the normal and transverse traction behavior, where the interface elements have been implemented in an explicit and non-linear approach. The cohesive zone model is used to quantify the mechanical properties (e.g. K_c) and to understand the energy dissipation and abrasion resistance in the indentation tests. The computational framework has been developed as user subroutines in FEAP [20].

To address the influence of the rod-like microstructure in the global mechanism of the tooth, a set of biomimetic 3D printed composites were tested under uniaxial tension. The 3D printing technology is a relatively new technique with advantages and limitations that are not yet well known. Therefore, this research also requires an analysis of the influence of production variables (e.g. deteriorative time effects and layout of the sample) on the mechanical properties. These mechanical tests and computational models have been developed during the last years of this study, and as far as the author knows, are an original application that not only helps to understand the microstructural mechanisms of the chiton, but also can be applied to study other biomineralized and engineering materials.

The objectives of this Ph.D. thesis are:

i) Analyze the failure mitigation mechanisms in the organic/mineral interaction of the mature chiton tooth.

ii) Quantify the influence of geometrical and nano-scale features in the mechanical behavior of the rod-like microstructures.

iii) Develop numerical models combined with experimental setups, which can set a methodology to characterize the material behavior of the rod-mineralized microstructure of the tooth.

1.2 Thesis organization

This dissertation consists of nine chapters, in which chapter 2 includes the theoretical background necessary to understand the building blocks associated with some biomineralized materials, also important concepts of site-specific modulus obtained during indentation tests and fracture mechanics. A review of estimations of K_c and H^3/E_r^2 measured during the indentation tests is included in this chapter.

A comprehensive analysis of the use of the continuum damage model of crack propagation during indentation of an isotropic material is examined in chapter 3. The formulation of the three dimensional cohesive zone model is also included in this chapter. As this is a novel application to indentation tests, this chapter was necessary in order to assess the validity of the model.

In chapter 4, a micromechanical model of a rod-like microstructure is presented. The study considers magnetite rods that are surrounded by interface elements that mimic

the behavior of the chitin. To understand the influence of the material parameters, the computational models are compared with respect the slope of the indentation data. The study includes a dimensional analysis to address the influence of material and interface parameters in the slope. The analysis also shows the competing mechanisms of energy dissipation by inelastic deformation of the rods and by crack propagation of the interfaces.

An experimental and numerical analysis of the microstructure of the mineralized radulae teeth is discussed in chapter 5. The study includes an analysis of the material properties of the core and exterior shell, a surface analysis of the rod diameter and mineral content, and a three dimensional model of the tooth deformation during an abrasive contact. A micromechanical model is also addressed in this chapter to quantify the effect of rod diameter in the indentation data of the chiton.

A novel application of 3D printed biomimetic composites is discussed in chapter 6, where strong hexagonal rods are surrounded by weak interfaces. The study presented in this chapter includes a quantification of the mechanical properties measured during indentation of the alignment and aspect ratio of the rods. To explain the experimental results obtained in this chapter, analytical (e.g. K_c estimations, Euler loads) and computational models are taken into account. A comprehensive review of the use of biomimetic composites to study fracture problems is also given.

To assess the role of the rod-like microstructure during tension, chapter 7 presents the analysis with DIC of biomimetic composites exposed to tensile loads. The rod-like microstructure is compared to a plate-like that resembles the tablets of nacre, material with an outstanding toughness that has been well studied. To explain the hardening observed in the microstructures, the experimental results are compared at different stages of the

mechanical tests. The purpose of this chapter is to stablish design guidelines that can be used to test the mechanical properties in the chiton tooth.

An application to study the abrasion resistance of a gastropod is discussed in chapter 8. The analysis of the indentation marks suggest, that the orientation of the building blocks are optimized to withstand damage. The results presented in chapter also indicate the applicability of this framework to study other biological material. Finally, the summary of the findings from the experimental, analytical and numerical models developed in this Ph.D. thesis are summarized in chapter 9.

CHAPTER 2. BACKGROUND

2.1 Biomineralized microstructures

In many biomineralized species, the complex nano-scale microstructure is dominated by a natural abrasion resistance to external forces, like the hierarchical multilayered structure of the dental armour of the *Polypterus senegalus* fish. The thin ganoine outside layer of the armour (thickness ≈10 μm) is composed of a rod-like microstructure of apatite crystallites of diameter ≈ 40 nm and length ≈ 220 nm (aspect ratio ≈ 5) [21][15][22]. In the dental armour, the HAP nano-crystals are aligned orthogonal to the exterior of the fish, and the microstructure is characterized by a low content of organic matrix (≈ 5%) (Figure 2-1A). In-situ mechanical compression test were performed to address the influence of the building block orientation in the mechanical properties [22]. Experimental observations of the fish scales, revealed that the geometrical anisotropy influenced the mechanical properties and crack patterns observed, where the orientation parallel to the load ($\theta = 0°$) is characterized with a higher yield stress and elastic modulus. Examinations of the damaged fish scales, suggested that the crack propagation followed the weak interfaces of rod oriented at $\theta = 0°$and $\theta = 90°$, and deviated at $\theta = 45°$ (Figure 2-1B). These results confirm the advantageous anisotropy orientation of the building

blocksthat characterize biological composites [21][15][22].

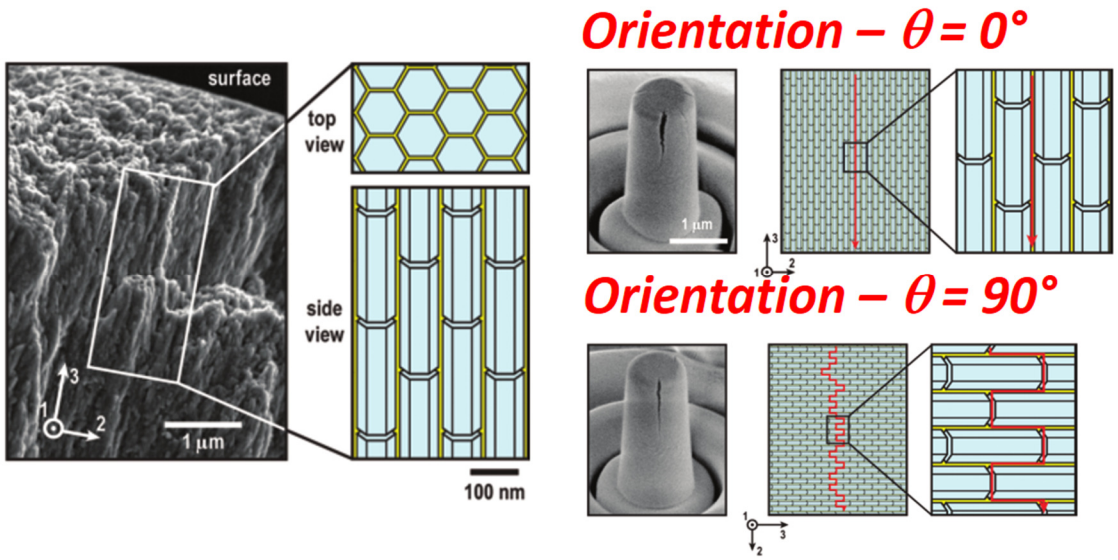

(A) (B)

Figure 2-1 (A) Rod microstructure observed in the hardest layer of the *P. Senegalus* and (B) crack patterns observed by compression tests made with a flat nano-indenter, adapted from Han et al.[22].

Not only the scales of the *P. senegalus* are characterized by a mineralized structure that enhances the functionality of the dermal armor, also the arrangement of helicoidally collagen fibrils of the *Arapaima* scale revealed an arrangement of HAP fibers optimized to withstand large tensile and compressive stresses[23], [24]. Another biological example of a rod-like microstructure is the crossed lamellar shell of the *Strombus gigas*, constituted by mineralized building blocks surrounded by an organic interface [25]. The hierarchical structure of this shell is commonly observed in gastropods [26] and is conformed of different orders from macro- to nano-scales, in which the smaller order is composed of aragonite planks (≈ 100 nm of thickness by micrometers of elongation) (Figure 2-2). Mechanisms to mitigate crack propagation and therefore catastrophic failure have been observed in the shell, in which the energy dissipates as cracks from the inner layers heading

into a middle layer that naturally arrests cracks to propagate even further into the outer layer. The difference in cracks patterns observed by three point bending tests[25], have been explained by an enhancement in the fracture toughness of the middle layer.

Similar to hard biological materials (e.g. bone, shell and teeth) the flexible *Sponge biosilica* displays an asymmetric laminate architecture with an alternate structure of mineral (≈ 99% monolithic hydrated silica) and organic phase [27][3]. The sponge consists of a monolithic mineral surrounded by alternating layers (thickness ≈ 2-10 μm) of soft proteinaceous material, a microstructure that enhances the toughness of the long spicules by a factor of ≈ 2.5 with respect to the monolithic material, adapting thus to tensile and compressive loads.

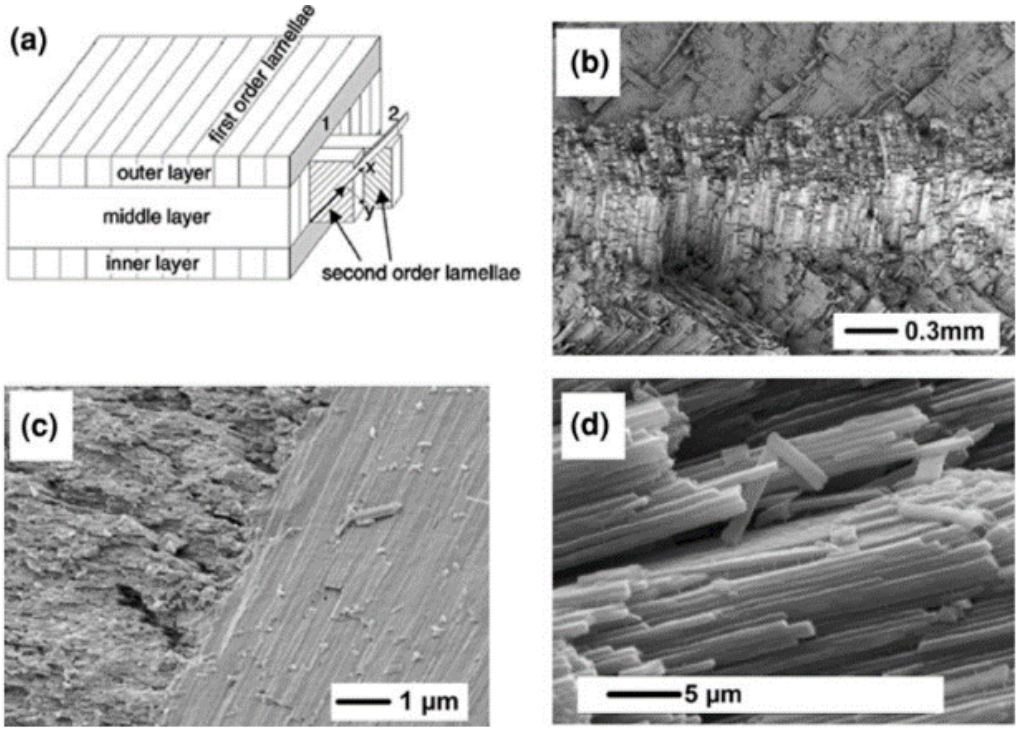

Figure 2-2 (A) Different orders observed in the shell of the Strombus Gigas, (B) rod alignment showing the different layers at the shell, (C) 3rd order planks observed in 1st and 2nd order lamellae and (D) aragonite building blocks of the shell. Images adapted from Kamat et al. [25].

2.2 Indentation tests

In an indentation test, a material is exposed to the contact of a rigid indenter and the loading displacement is acquired during this process (Figure 2-3). Since the first applications of indentation tests in the 19th century, the procedure has been widely validated and successfully used to characterize the mechanical properties of a large group of materials (e.g. metals, ceramics, and polymers) with a variety of tips (Figure 2-3). The main advantages with respect to standard mechanical tests (e.g. tensile test, double cantilever beams, torsion test) is the small specimen size that is required and the relatively easy experimental procedure that follows. Therefore, indentation tests are preferred to characterize nano-scale films and micro-scale biological materials.

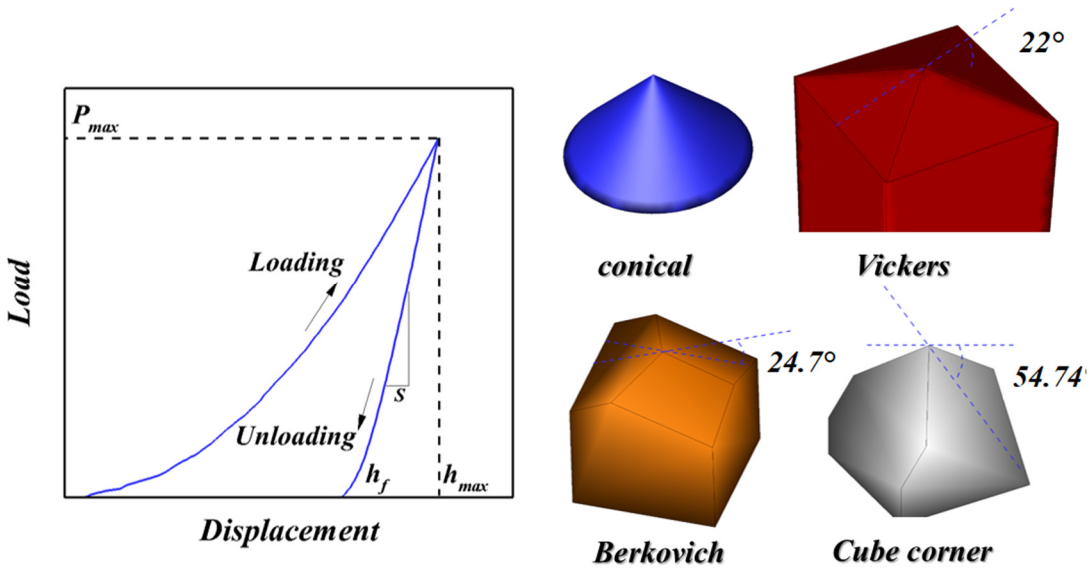

(A) (B)

Figure 2-3 (A) Indentation data and (B) indenter tips commonly used.

Hardness (*H*) is an indentation pressure and is defined by the ratio of the maximum load (P_{max}) to the contact area at maximum penetration (*A*) given by $H = P_{max}/A$. As the dimension of the samples get closer to the nanometer scale, the contact area is more difficult to measure. Oliver and Pharr formulated the contact area (*A*) as a function of the maximum *contact depth* (h_c) (Equation 2.1) [28].

$$A(h_c) = C_0 h_c^{\,2} \tag{2.1}$$

The previous estimation of (*A*) is frequently used by industrial nano-mechanical testing instruments [29]. It avoids the tedious measurement of contact areas by optical microscopy, where $C_0 \approx 24.5$ for a Berkovich tip and $C_0 \approx 2.598$ for a cube corner indenter. If optical microscopy is used to estimate *A*, the side length of the indentation mark (*a*) is measured and it becomes possible to calculate the area by basic trigonometry (Equation 2.2), where α is a function of the geometry of the indenter [30].

$$A(a) \approx \alpha a^2 \tag{2.2}$$

Based on Sneddon's [31] power load expression of load and displacement of a rigid indenter in contact with a surface, the reduced modulus is calculated from the unloading part of the indentation data defined in Equation 2.3, where *S* is the slope of the unloading section of the curve (Figure 2-3A).

$$E_r = 0.5S\sqrt{\pi/A} \tag{2.3}$$

If the unloading section of the indentation test is defined by a power law (Equation 2.4), then the slope is given by Equation 2.5, where *a* and *m* are constants obtained by fitting the unloading of the indentation data

$$P(h) = a(h - h_f)^m \tag{2.4}$$

$$S_{max} = \frac{dP(h_{max})}{dh} = ma(h_{max} - h_f)^{m-1} \tag{2.5}$$

. Commercial nano-indenters use a material of known E_r to calibrate the area coefficients ($C_0, C_1, C_2 \ldots C_8$), where the contact area is approximated by $A(h_c) = C_0 h_c^2$.

2.3 Concepts of linear elastic fracture mechanics

The theoretical strength of a material can be estimated either by atomistic models or by classical fracture mechanics [32]. As the exclusion of material flaws and grain boundaries in the delamination of atomistic models can lead to values of three of four orders of magnitude above the theoretical cohesive strength of materials. The fracture theory proposed by Griffith, Irwin and others takes into account size, shape and mode effects in the strength analysis[33]. Griffith [33] postulated, that cracks exist in brittle materials acting as stress concentrators and proposed an energy balance, in which cracks can grow when the potential energy is greater or equal to the surface energy ($d\Pi \geq dW_s$). Griffith [33] estimated the critical stress required for a crack to propagate in a infinitively

brittle wide plate subjected to tensile stresses as a function of the size of the elliptic crack (a), Young's modulus (E) and surface energy (γ), given by:

$$\sigma_{cr} = \sqrt{2E\gamma/\pi a} \tag{2.6}$$

In a solid body, a crack can be idealized as a disjunction between two surfaces and three basic fracture modes (opening, in-plane shearing and out-of-plane shearing) describe the cracks as a combination of those. In Linear Elastic Fracture Mechanics (LEFM), the non-linearity (e.g. plasticity and damage) is constrained near the crack tip in a small region, which is smaller than the dimensions of the body (Figure 2-4A) and that is not affected by the elastic stress fields in the rest of the solid. Later on, Irwin introduced the *energy release rate* (G) as the increment of the potential energy with respect to the crack area ($G = -d\Pi/dA$) [34]. It is possible to demonstrate by analyzing the stress ahead of the crack tip for each mode, that the stress fields are proportional to the stress intensity factor (K_I, K_{II} and K_{III}), a dimensionless function of θ and $1/r^{0.5}$ (Figure 2-4B).

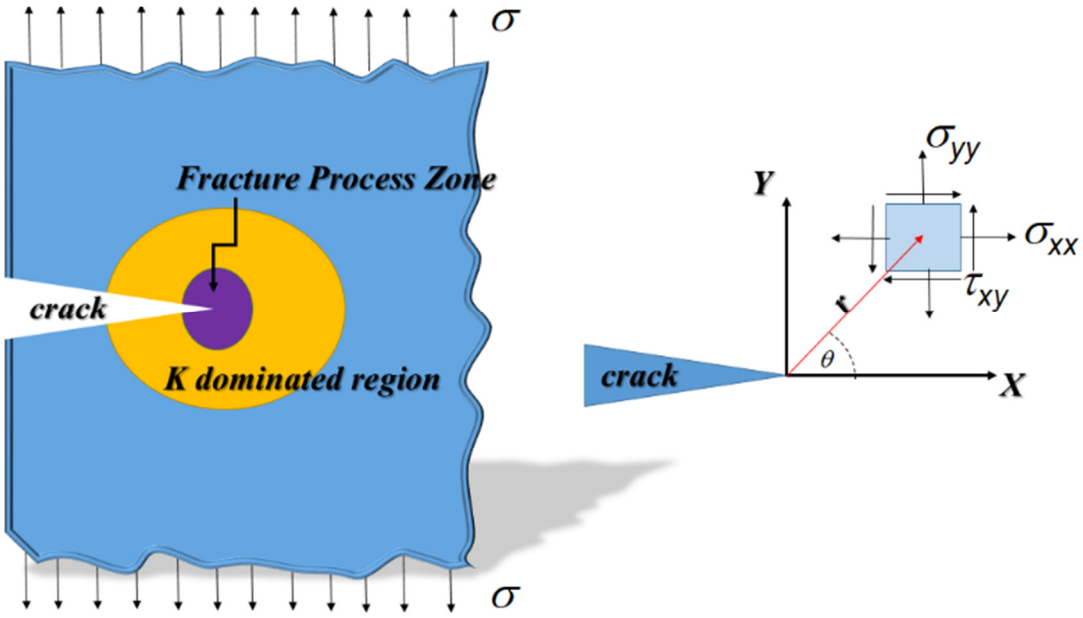

(A) (B)

Figure 2-4 (A) LEFM applied in K-dominance zone and (B) definition of the coordinate system at the crack tip.

Considering the opening mode only (mode I), the stress fields can be expressed by $\sigma_{yy} = {K_I}/{\sqrt{2\pi r}}$, where K_I is the stress intensity factor. An important consideration of the LEFM is that the size of the fracture process zone must be much smaller than the size of the body. Solutions to the finite problems assuming collinear cracks in infinite planes and dimensionless groups have been referenced in the literature [32], [33]. In the handbook of Tada et al. [35], stress intensity factors for mode I (e.g. 3 point bending specimens) are generally approached by $K_I \propto {P}/{B\sqrt{w}}$, where the applied load (P) and dimensions (thickness (B), width (w)) of the samples are taken into account. The applicability of the fracture criterion for different K-dominance zones have been studied with FEM, showing

that for larger specimens (length/crack size = 2) the K_I criteria estimates the stress fields with more accuracy near the singularity (Figure 2-5) [32].

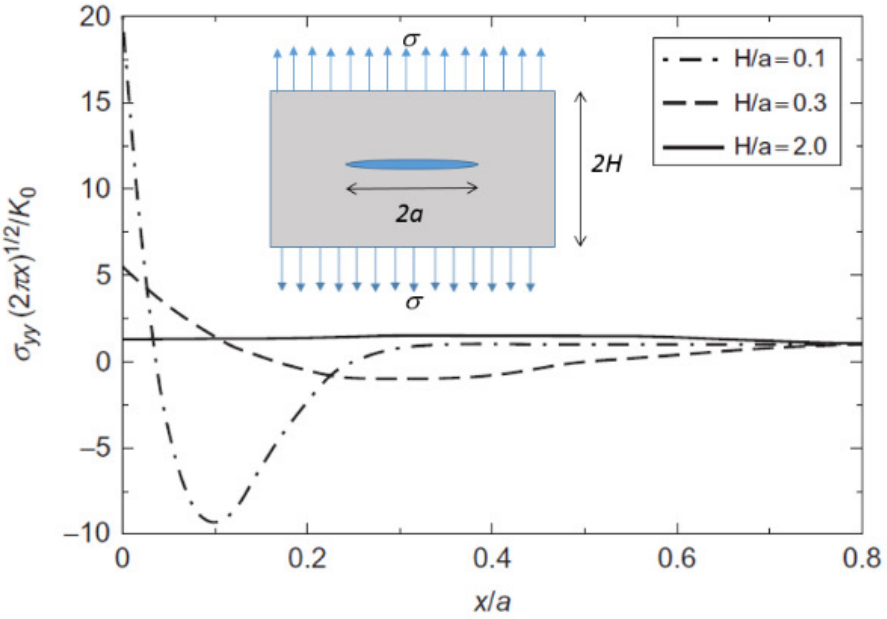

Figure 2-5 Border effects in a notched sample. At *H/a=2*, the value is almost constant indicating that singular stresses are dominant as compared with the other two cases [5].

Under mode I conditions, Irwin proposed that the fracture process zone initiates when the stress intensity factor is equal to the *fracture toughness* (K_c), where the resistance to fracture is an intrinsic material property. The Irwin-Griffith relation between K_c and G_c for mode I is defined by $G_c = {K_c}^2/E'$, where *E'* has a different value for plane stress (*E'* = *E*) and strain ($E' = E/(1-\nu^2)$) conditions. To conclude this section, the theoretical length of the fracture process zone (L_{fpz}) is proportional to the limiting separation (δ_{max}), the strength (σ_o) and the Young's modulus (Equation 2.7) [36].

$$L_{fpz} \propto {E'\delta_{max}}/{\sigma_o} \tag{2.7}$$

2.4 Fracture toughness estimations by LEM model

Since the early approaches of Palmqvist [37] to relate the length of radial cracks with K_c of metal carbides, numerous studies explore the advantages of indentation tests [38]. In comparison with blunt indenters, the effective exposure angle of sharper tips offer more material removal at a lower penetration of the indenter. This is the case of the cube corner indenter, an ideal abrasive geometry for crack studies [39] which is going to be considered in the computational and experimental setups performed in this dissertation. Fracture models in indentation tests can be classified by the type of fracture morphology (e.g. radial-median, lateral, radial) and the geometry of indenter tip considered (e.g. Vickers, cube-corner). Although there are more than 30 different estimations of K_c derived on experimental observations [40], Lawn et. al (LEM) developed an analytical solution of K_c with a half-penny shape configuration of radial/median orientation created with a Vickers indenter [30], [41],[42]. Due to the large number of references of the LEM method in the estimation of K_c in many materials [40][43][27] (e.g. ceramics and biological), this physical model is reviewed in this chapter. A representation of this model, where the crack length (*c*), indentation mark *(a)*, size of plastic zone (*b*) and maximum penetration of the indenter (*d*) is shown in Figure 2-6.

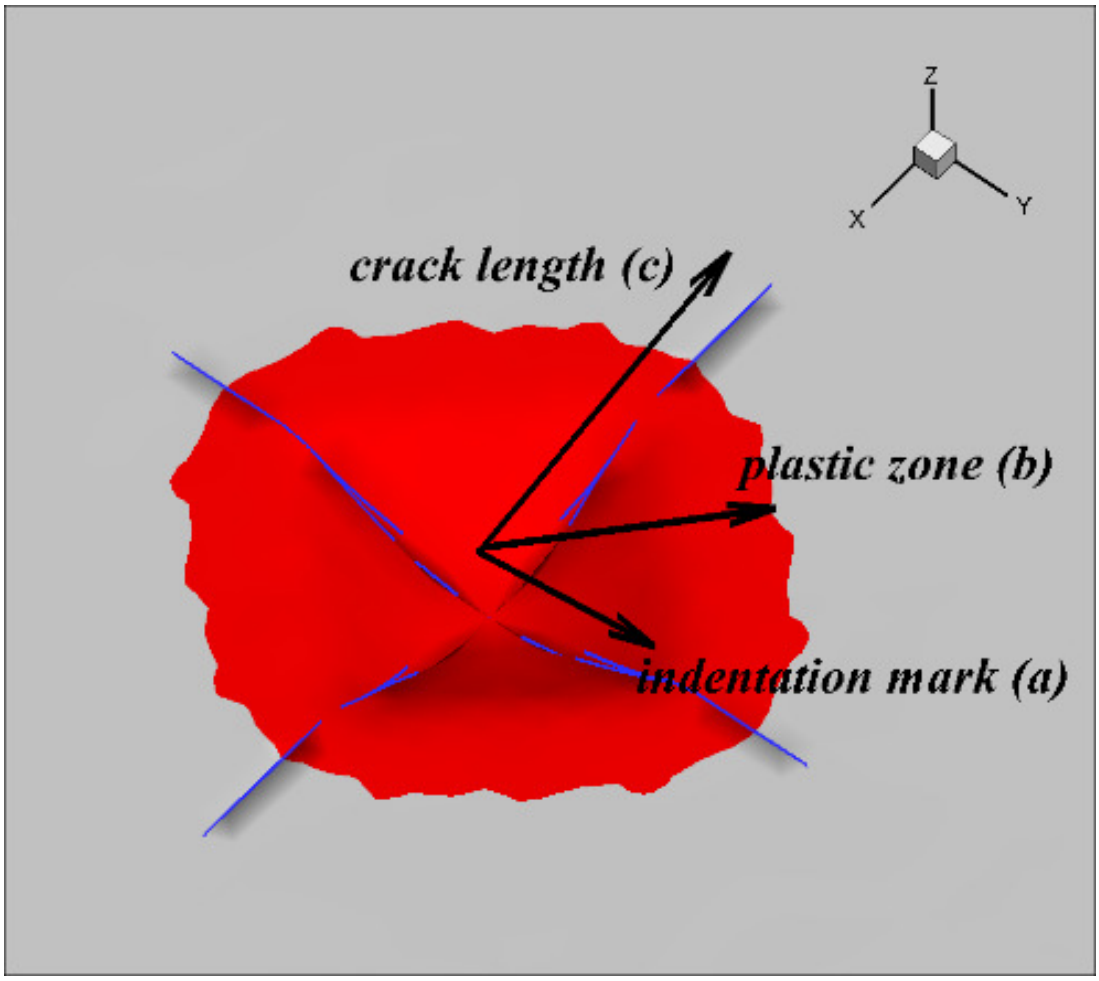

Figure 2-6 3D view of physical variables considered in the LEM model. Contour obtained from the elasto-plastic model developed in this thesis (chapter 3) with fracture planes at the edges of the indenter. Red contour displaying the plastic region of the solid ($\sigma_{VM} > \sigma_{yield}$) and blue lines are cracks at the edges of the Vickers tip (4 sided indenter)[30].

Based on experimental observations, Lawn et al. [41] predicted that tensile stresses in brittle materials (e.g. soda lime glass) are the driving force for median and radial cracks. An indentation test is then simplified by Lawn et al. [41] in two stages: at loading where elastic and residual forces are generated and, at complete unloading (e.g. Load = 0) where only residual forces are present. Idealizing radial cracks as a half-penny geometry, the

stress intensity factor for the elastic and residual components are estimated by the LEFM expression $K_I^{e,r}=\chi_{e,r} P/c_t^{1.5}$, where $\chi_{e,r}$ is a term that depends of material parameters (E_r, H) obtained from the loading displacement curves and the indenter geometry. After applying the principle of superposition, the fracture toughness $K_c = K_r + K_e$. By separating the contribution of the indentation stages, the fracture toughness at full loading is given by Equation 2.8 and during unloading by Equation 2.9.

$$K_c = \chi_e \, P/{c_t}^{3/2} + \chi_r \, P/{c_t}^{3/2} \tag{2.8}$$

$$K_c = \chi_e \, P/{c_t}^{3/2} + \chi_r \, P_{max}/{c_t}^{3/2} \tag{2.9}$$

Finally, the well-known fracture toughness expression is obtained as a function of the equilibrium crack length after fully unloading the sample (e.g. $P = 0$) (Equation 2.10):

$$K_c = \chi_r \, P_{max}/{c^{3/2}} = \chi\sqrt{E_r/H} \, P_{max}/{c^{3/2}} \tag{2.10}$$

It is important to clarify that the parameter χ is an experimentally calibrated constant ($\chi = 0.016 \pm 0.004$ for Vickers[44] and $\chi = 0.04$ for a cube corner indenter[39]), c_t is the crack length in non-equilibrium and c the crack length after unloading. As compared with macroscopic experimental techniques (e.g. double cantilever beams and three point bending), the fracture toughness measured with the LEM model can show up to a 50% of discrepancy [40]. However, multiple factors affect the K_c values measured from the experiments; (i) miscalculations while optically measuring radial cracks (c) due to surface stresses that may have been inflicted before the tests (e.g. thermal tempering or

surface grinding), material removal around the indentation mark (chipping) or crack closures [40]. The empirically use of the parameter (ii) χ which is a variable in equation 2.10 also influences the calculations. Other physical uncertainties include: (iii) the miscalculations in the length of deflected cracks and (iv) the application of this model with crack lengths where LEFM conditions are not always satisfied [40]. Nanoindentation tests in single crystals (Si and Ge) [43] demonstrated that even with short crack lengths, the K_c values are practically constant and estimated from equation 2.10, with the load for crack initiation ($P_c = P_{max}$) and $c \approx a$ (Equation 2.11)

$$P_c \approx {0.46K_c^4}/{\chi^4 H E^2} \tag{2.11}$$

2.5 Critical load for yielding

An analytical solution of the load required to initiate plastic yield between two bodies in contact was derived by Johnson [45]. The elastic Hertzian theory formulated under the premises of small strains, frictionless solids and contact areas much smaller than the size of the bodies is used to estimate the compressing load (P) between two solids of revolution as a function of the maximum pressure (P_0) and the size of the cylindrical contact (a) (equation 2.12).

$$P \approx 0.7 P_0 \pi a^2 \tag{2.12}$$

Combining the von Misses shear-strain energy criterion ($J_2 = \sigma_{yield}^2/3$) together with a solution of axi-symmetrical pressure distribution at the maximum shear stress, the

maximum contact pressure is given by $P_0 = 1.6\sigma_{yield}$. It is then possible to derive a critical load to initiate yielding with the elastic solution, the maximum contact pressure distribution and Tabor's [11] relationship between the hardness and yield strength ($\sigma_{yield} \approx 3H$). The critical load to initiate plastic deformation (P_y) is given by equation 2.13, where R is the radius of an sphere in contact with the surface[45].

$$P_y \propto {R^2H^3}/{E^2} \tag{2.13}$$

This formulation has been applied to study fracture processes in T_iN coatings with spherical indenters [46], carbon coatings tested with Berkovich indenters [47] and hard nano-composite coatings using a Vickers indenter [48]. At this point, it is important to consider the differences between the threshold load for crack initiation (P_c) and the load for plastic yield deformation (P_y). The first criteria follows the principles of LEFM and is proportional to K_c/HE^2, suggesting that higher values of P_c are required for crack initiation in tougher materials. As the general tendency is to keep the ratio H/E constant (Figure 2-7A) the last criterion (P_y) suggests that materials with higher values of H are desired to raise the initial load for plastic deformation. To sum up, the values of P_c mostly depends on intrinsic material properties (E and K_c) and P_y in the hardness or in the loading part of the indentation data. Materials can be characterized with the same values of P_y with a combination of different mechanical properties. An example of this was observed in coatings of metallic alloys, Figure 2-7A compares the indentation response for two alloys with the same P_y but different film hardness and Young's modulus and Figure 2-7B showing the general tendency of materials to linearly increase H as E is increased [48].

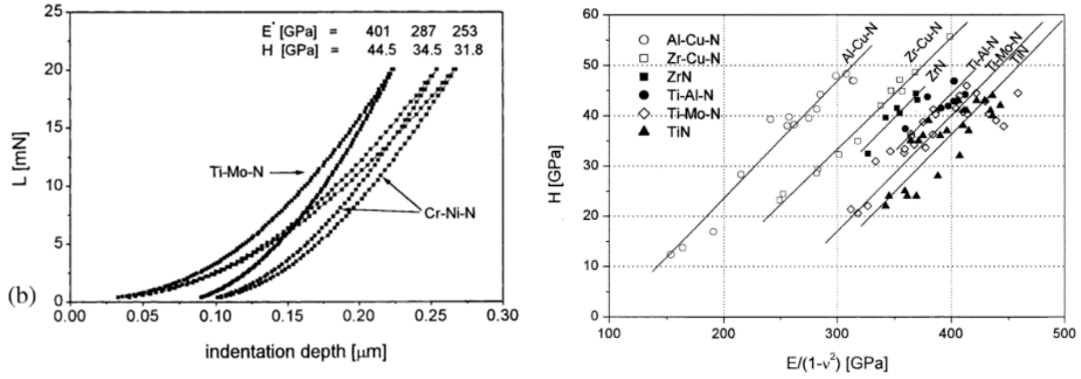

(A) (B)

Figure 2-7 (A) constant resistance to plastic deformation ($H^3/E^2 = 0.5$GPa) and (B) linear relationship between H and E_r. Images adapted from Musil et al. [48].

CHAPTER 3. MODELING THE RADIAL CRACK PROPAGATION OF AN ISOTROPIC MATERIAL

3.1 Introduction

A literature review of computational models of indentation tests suggest that while most of the FEM study plastic deformation in three dimensional geometries, only a scarce number of analyses take the energy dissipation with interface elements in a three dimensional domain [49]–[52] into account. In the interim of this research, fracture models of indentation tests were published in 2012 by Lee et al.[50] and later by other authors [51], [52]. These studies [50]–[52] consider the probability of crack propagation in planes aligned parallel to the indenter edges, carrying a sensitivity analysis of the cohesive zone model in the crack morphology and in the assumptions made by the LEM model [30], [41]. To further analyze some of the concepts mentioned in these studies and to identify the validity of my implementations carried out in the open source code FEAP[20], an analysis of the crack evolution in an isotropic material is presented in this chapter. The continuum damage model is developed with interface elements of 6 nodes preembedded in the solid [53], [54]. The study presented in this chapter considers the influence of having cohesive elements in the site specific modulus measured after indentation [28] and the loadingdisplacement curves. Also, an analysis of the size of the plastic zone, the crack lengths during indentation and the K_c values measured with the LEM model [30], [41] are

discussed. This chapter is divided in three sections: The first section includes the formulation of the damage model whereas the second section provides an analysis of the crack propagation in an isotropic material. Finally, the conclusions of the chapter are presented in the third section.

3.2 Interface element

The cohesive zone model (CZM), largely used as a damage criterion in fracture studies of brittle and ductile materials[55][56], takes into account the surface degradation leading to crack growth when the normal or transversal displacements reach a limit value. While different shapes of cohesive laws can be used, Figure 3-1 shows the bilinear cohesive law adapted in this study [56]. The non-dimensional displacement jump (λ) takes into account the normal and traction separation jumps (equation 3.1).

$$\lambda = \sqrt{\left(\frac{u_n}{\delta_n}\right)^2 + \left(\frac{u_{t1}}{\delta_{t1}}\right)^2 + \left(\frac{u_{t2}}{\delta_{t2}}\right)^2} \tag{3.1}$$

The non-dimensional parameter defines the interface degradation by tracking (equation 3.2) the normal and transversal displacements at the interface (u_n, u_{t1}, u_{t2}), a parameter that depends on the maximum displacement values to reach failure (δ_n, δ_{t1}, δ_{t2}). The value of G_c in each mode is defined under the curve of the bilinear law (equation 3.3)[53] .

$$\lambda = \max(\lambda_{max}, \lambda) \tag{3.2}$$

It is possible to identify the degradation of the material in the bilinear law (Figure 3-1); initially when λ is less than $\lambda*$ (critical value) the element is considered intact. After reaching a maximum stress (T_{max}) degradation occurs, and irreversible unloading between $\lambda*<\lambda<1$. At $\lambda=1$, the interface element is considered broken and cracks evolve.

$$\mathrm{G}_c = \int_0^{\lambda} \sigma(\lambda')d\lambda' \tag{3.3}$$

A cohesive energy (ϕ) determines the normal and transversal tractions (3), in which the potential form (Equation 3.4) and traction separation laws (Equation 3.5) were adopted from Espinosa et al. [53].

$$\emptyset = (2-\lambda^2)\,{}^{\delta_n T_{max}}/_{2(1-\lambda^*)} \tag{3.4}$$

$$T_n = \frac{d\phi}{du_n} \qquad T_{t1} = \frac{d\phi}{du_{t1}} \qquad T_{t2} = \frac{d\phi}{du_{t2}} \tag{3.5}$$

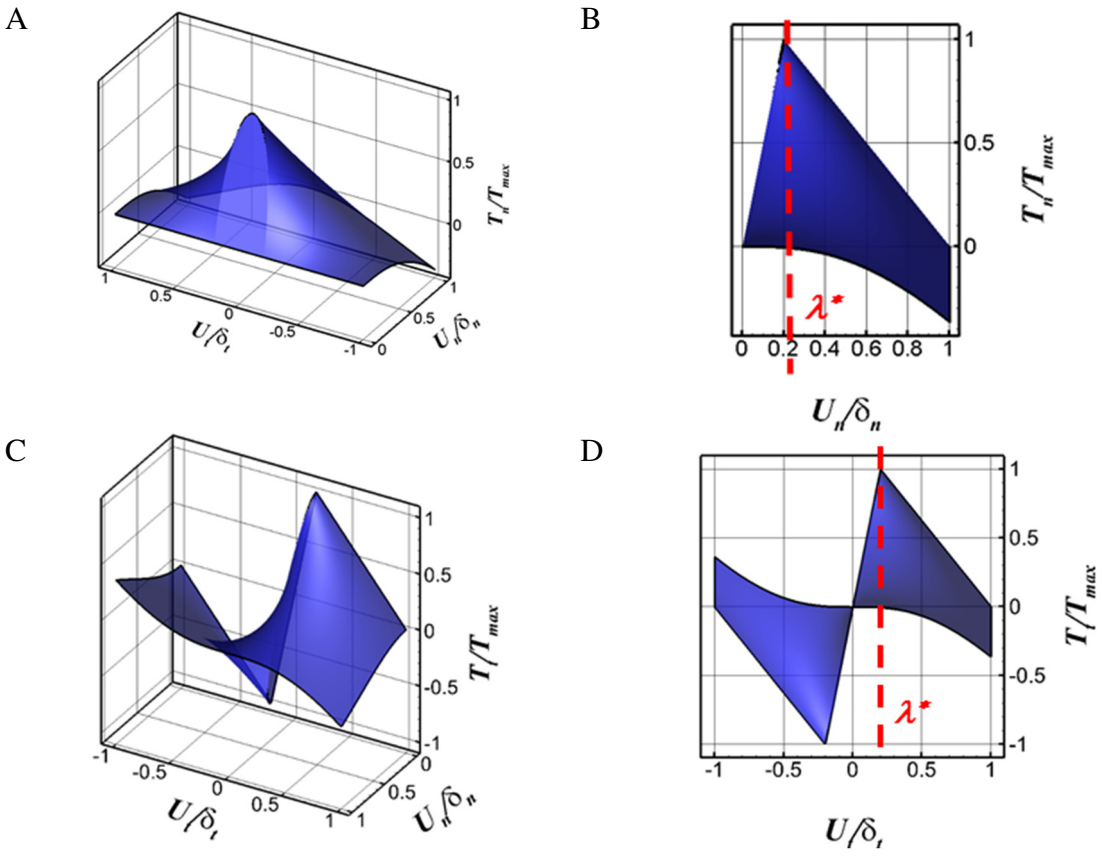

Figure 3-1 Bilinear law of the cohesive zone model. Isoparametric curves with the correspondent (A) normal and (C) transversal components. 2D views with respect to the (B) normal and (D) transversal displacement. The (B) normal traction as compared with the transversal law has a steep slope when $u_n/\delta_n<0$, region that is not included in the plot.

Due to the nature of the indentation test, the compressive behavior of the cohesive law is taken into account by a penalty value and is excluded of the non-displacement jump (Equation 3.1). Otherwise, the interface elements will fail at high compressive stresses in the area in contact with the indenter. The cohesive law parameters (T_{max}, λ^*, G_c), with their origins in separation mechanics at atomistic levels, can be obtained from experiments. The

CZM has the advantage that it can be easily implemented into the finite element code. In the principle of virtual work, the surface tractions are a source term (equation 3.6):

$$\int \delta\varepsilon^T \sigma d\mathrm{V} = \int \delta\Delta^T F d\mathrm{V} + \int \delta\Delta^T t d\Gamma \tag{3.6}$$

The left term considers the vector of strains ($\delta\varepsilon$) and the array of stresses (σ), the middle term the body forces (F) and virtual displacements ($\delta\Delta$), and the right term the surface tractions (t) over an area. The CZM is implemented as a traction component (t) in Equation 3.6 and the values are calculated at the interface of a middle plane in a zero thickness element (Figure 3-2A). The implementation has been done as a user subroutine in the finite element code, FEAP [20]. An non-linear method is used to calculate the nodal internal forces that computes the tangent stiffness matrix in a linear hexahedral (cohesive interface of 8 nodes) and tetrahedral element (cohesive interface of 6 nodes). The validations included normal and mixed modes and the comparison of a DCB with an analytical solution (Figures 3.2B and C). A penalty contact element was also implemented with a non-linear algorithm, and validated with analytical solutions [28], [31], [57] and commercial FEM codes (ABAQUS and ANSYS).

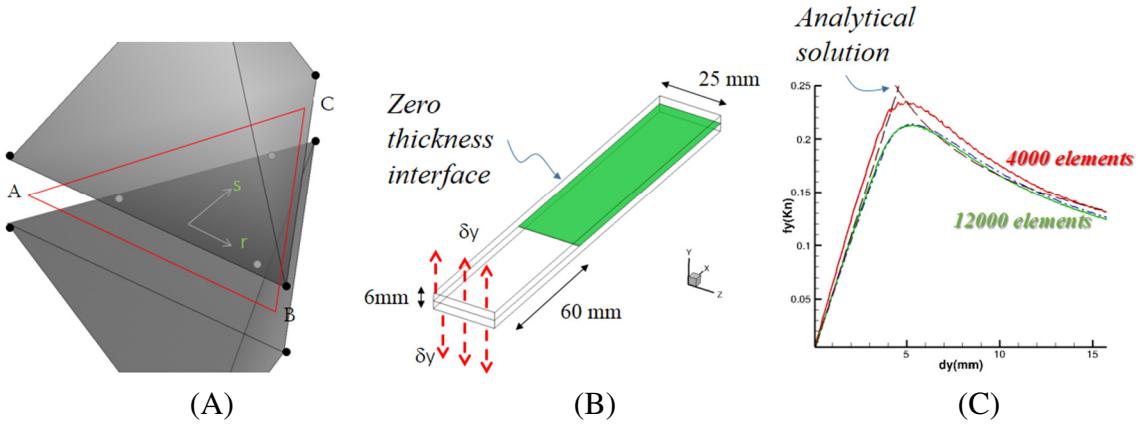

(A) (B) (C)

Figure 3-2 (A) Middle plane of a zero thickness interface element, (B) DCB model with a section with and without interface elements and a (C) validation comparing the analytical solution [33] with different mesh refinements.

3.3 Indentation of an isotropic material

Following the study published in 2012 by Lee et al. [50], an indentation test of an homogenous material with interface elements aligned parallel to the indenter edges has been modeled (Figure 3-3A). The dimensions of the sample are in micrometers with interface elements in the side walls that coincide with the edges of a 4-sided Vickers indenter (Figure 3-3B and C). Because the models takes into account a $1/4^{th}$ domain, the interface elements must be pre-inserted at the walls. A "half-interface" element was implemented in FEAP that follows the same principles discussed in the previous section except for the fact that instead of requiring 6 nodes to define the middle plane, it only requires 3 nodes to conform the plane (Figure 3-3B). Pre-processing tools were developed to rearrange the new half interface counter-clockwise element connectivity. The idea

behind this application [50], is to model the radial cracks that are commonly observed aligned parallel with the edges of 4 sided indenters (Figure 3-3D).

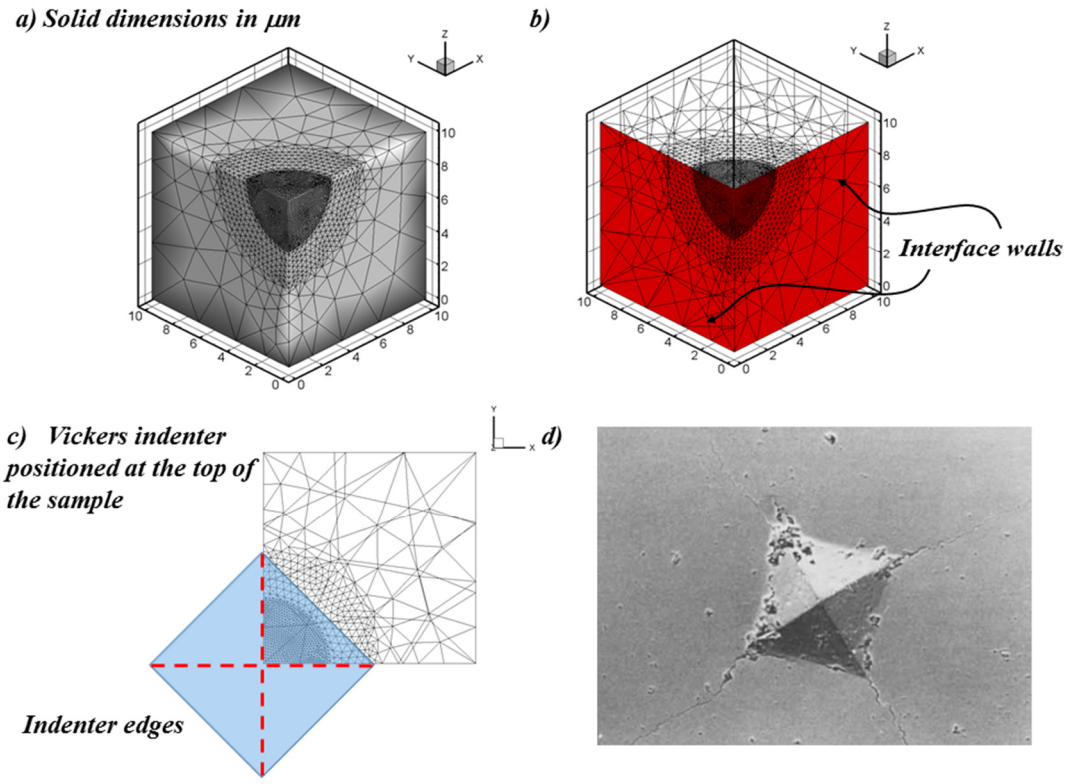

Figure 3-3 (A) dimensions of the homogenous solid modeled in μm, (B) interface elements embedded in the walls of the solid that coincide with (C) indenter edges and (D) indentation marks over Al_2O_3 showing radial cracks coinciding with indenter edges[44].

For the homogenous material (*Young's modulus* = 200GPa and poisson's ratio $\nu = 0.35$) is considered a work hardening law with a yield stress of 4 GPa and isotropic hardening of 10 GPa. The interface properties ($T_{max} = 0.5$ GPa, $\delta_{max} = 0.01$ μm) are defined in such a way that the fracture process zone (where $l_{fpz} \approx 1$ μm was calculated with equation

2.7) is lower than the size of the geometry (10 μm). The first set of results show a comparison of the indentation models at different maximum penetrations with and without interface elements (Figure 3-4). The results indicate that the artificial stiffness added into the system is not affecting the mechanical response of the model. Also, the loading response seems to coincide for all the models.

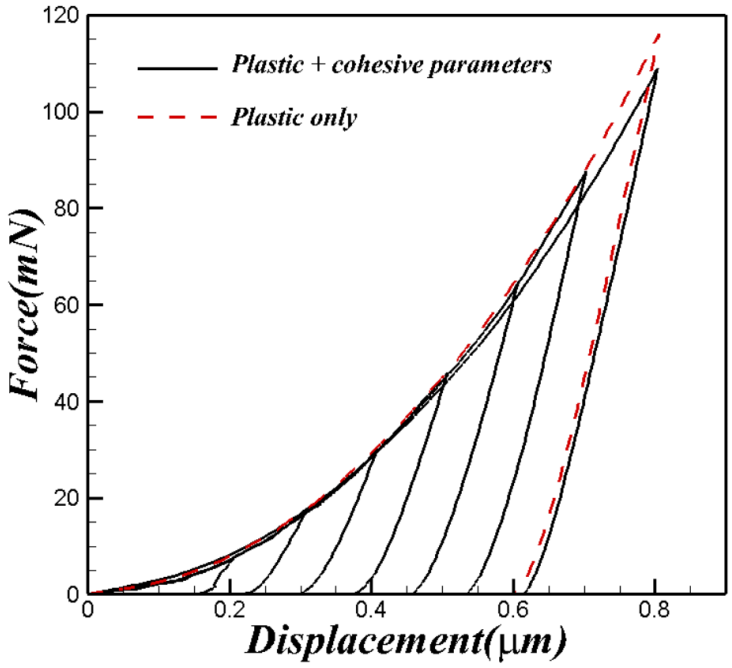

Figure 3-4 Loading displacement curve of an isotropic material with/without cohesive elements.

From the indentation data, the *reduced stiffness* (E_r) and *hardness* (H) can be directly obtained by applying the Oliver-Pharr method [28]. The computational models indicate that, despite the difference in the maximum loads obtained, the hardness and stiffness remains almost constant at the different penetration depths (h_{max}) (Figure 3-5-a).

Even more, the average measured reduced Young's modulus (195.29 ± 15.76 GPa) shows a discrepancy of 3% with respect to the input value of 200 GPa. Also, Tabor's relation between hardness and yield stress is maintained $\sigma_{yield} \approx 3H$ [58].

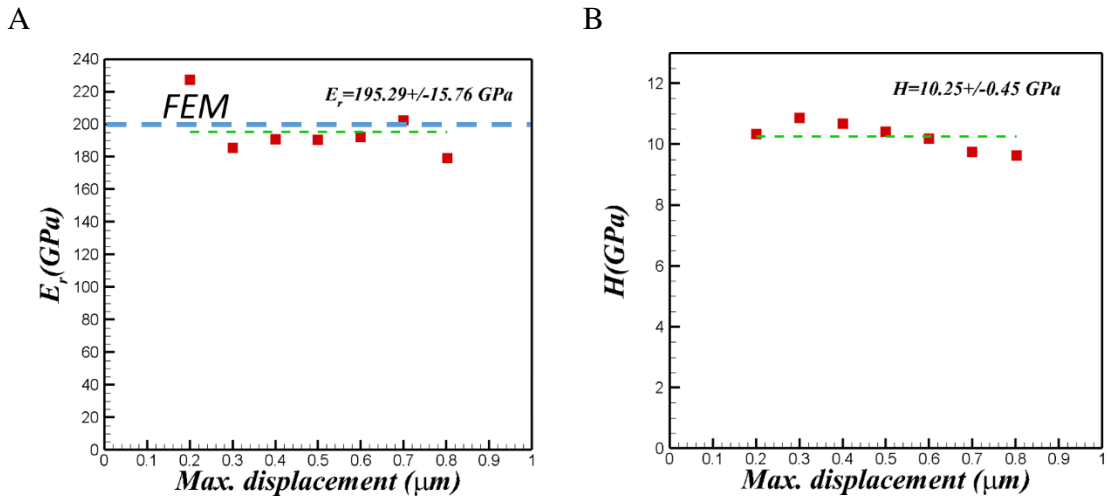

Figure 3-5 (A) Reduced Young's modulus and (B) hardness measured with the standard experimental procedure. Green dotted line represents the average value while blue line the input value of the FEM.

The plastic stresses are plotted together with the fracture regions (when $\lambda = \lambda_{max}$) at different maximum penetrations (h_{max} = 0.2 μm, 0.4 μm, 0.6 μm and 0.8 μm). The red contour reveals the plastic region below the tip of the indenter; results are displayed at the maximum loads in each of the models. As the indentation depth increases, from top to bottom in Figure 3-6, the radial crack also increases. At low penetration depths (e.g. 0.2 μm and 0.4 μm), the plastic zone is larger than the radial crack extension. At indentation depths

greater than 0.8 μm, the crack propagates in the coarse mesh region and the simulations become unstable leading to catastrophic failure.

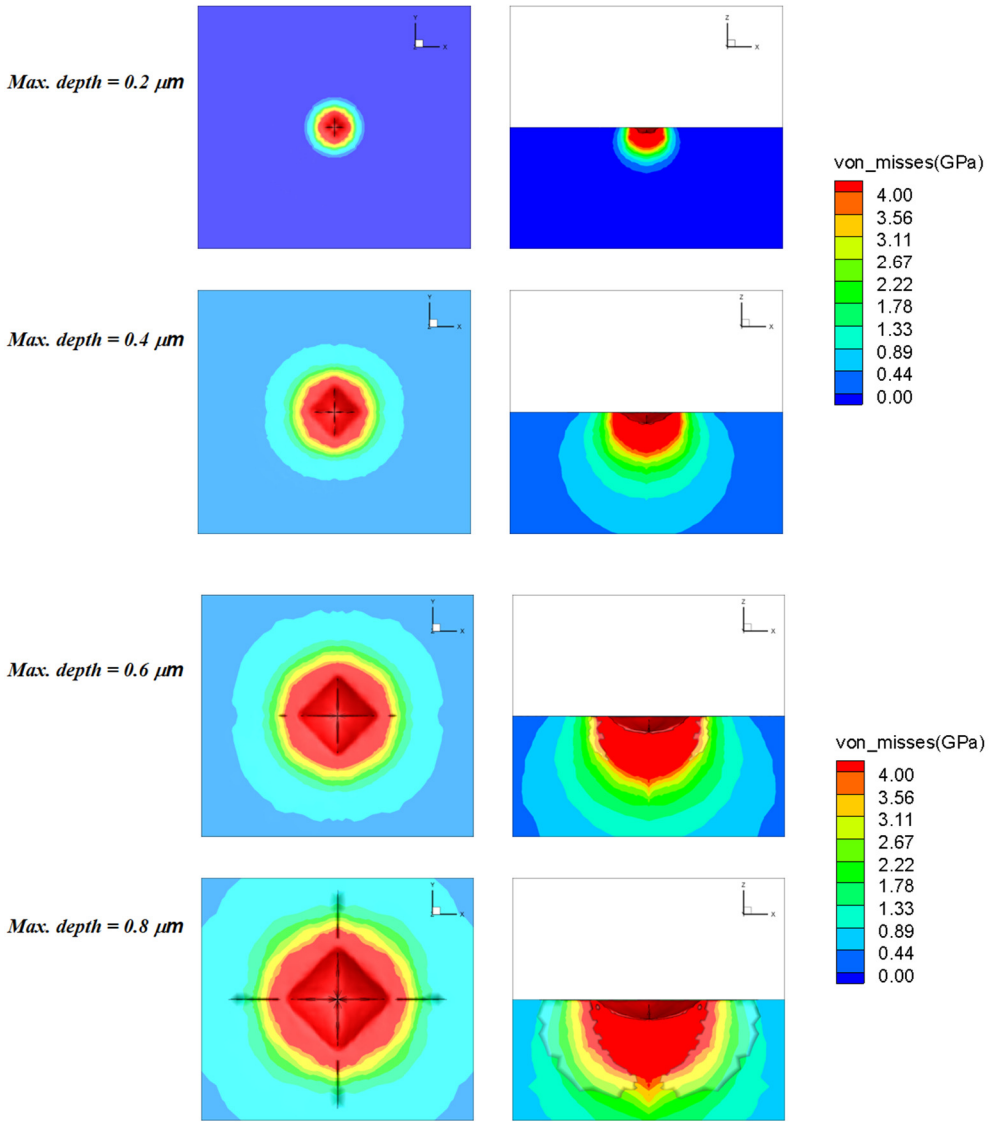

Figure 3-6 Variation of the plastic von Mises stresses (GPa) for the different h_{max}.

The evolution of the radial cracks is displayed in Figure 3-7 at h_{max} = 0.4 µm, 0.6 µm and 0.8 µm. Because, the radial cracks were not observed for values of h_{max} < 0.4 µm, the contours are not displayed in the figure. As the maximum penetration of the indenter is incremented in the tests, the radial cracks start to evolve as half penny shape configurations [59]. Figure 3-7 also shows a comparison of the cracks at the maximum load and after removing the indenter, where the length of the cracks reveal an expansion at equilibrium of 16% at h_{max} = 0.6 µm and 8% at h_{max} = 0.8 µm.

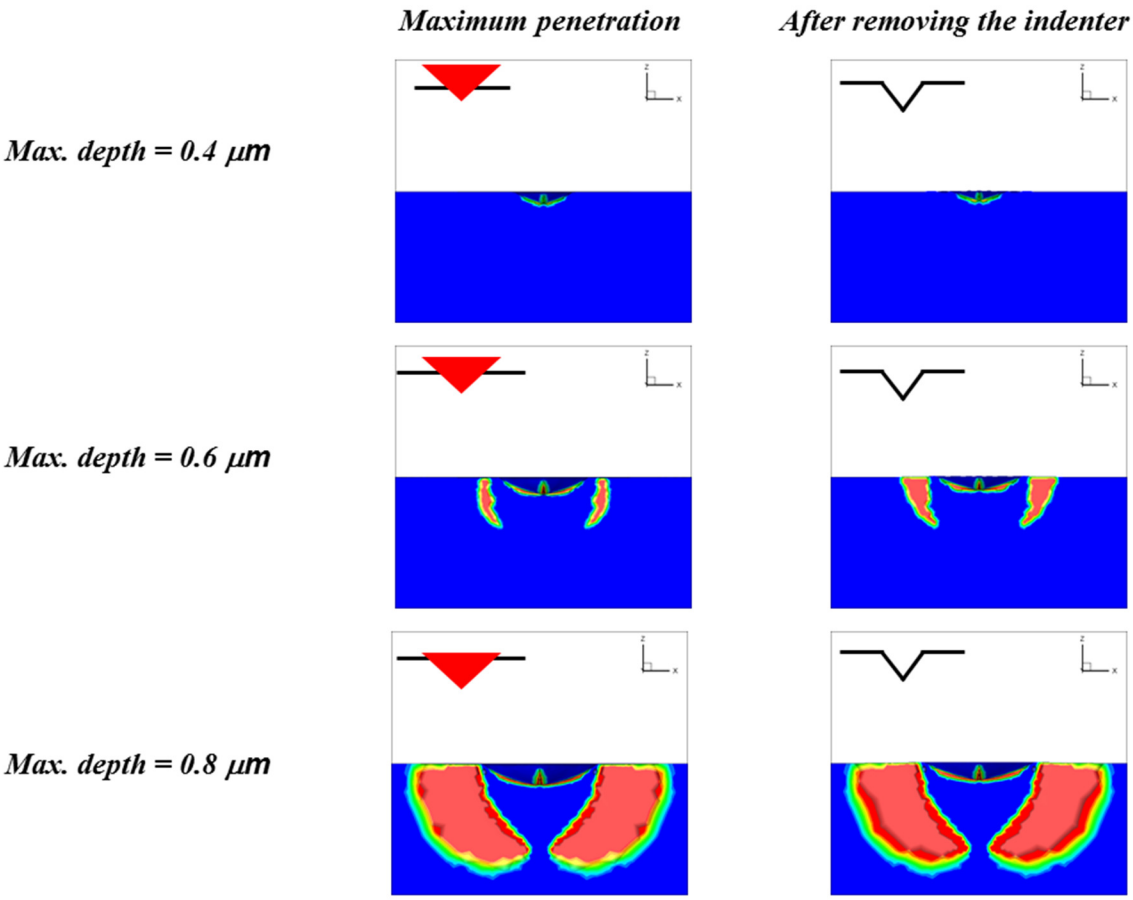

Figure 3-7 Variation of the radial cracks for the different h_{max}. The red color refers to elements with values of $\lambda = \lambda_{max}$. The countours are displayed at the maximum load and after removing the indenter (equilibrium)

The effect of the radial crack lengths at the different h_{max} and at equilibrium in the fracture toughness estimation by the FEM is revealed in Figure 3-8. In order to reproduce the experimental observations of valid crack lengths made in ceramics, the results are plotted against the ratio of *crack length* (*c*) and *indentation mark* (*a*). Experimental observations predicted that the LEM model [30], [41] is valid when $c \geq 2.5a$ [40]. The computational model reveals a trend line to decrease K_c as the ratio of *c/a* increases. The results are compared with respect to the input fracture toughness of the interface element ($K_c = 0.75$ MPa $m^{0.5}$). These results confirm the assumptions made by the LEM model [30], [41] of crack lengths (*c*) greater than the plastic zone (*b*), where $c \approx 1.5b$ at $h_{max} = 0.8$ μm. The comparison also shows that the equilibrium crack length (*c*) is different to the crack length measured at maximum penetration (c_t). The LEM estimation (equations 2.9-2.11) shows a difference of 20% with respect to the input value by measuring K_c at $h_{max} = 0.8$ μm as compared with a difference of 10% after removing the indenter (Figure 3-8), where equilibrium refers to the crack length after removing the indenter. Despite this difference in the crack lengths, the trend line to decrease the value of K_c while $c/a \leq 2.2$ remains valid.

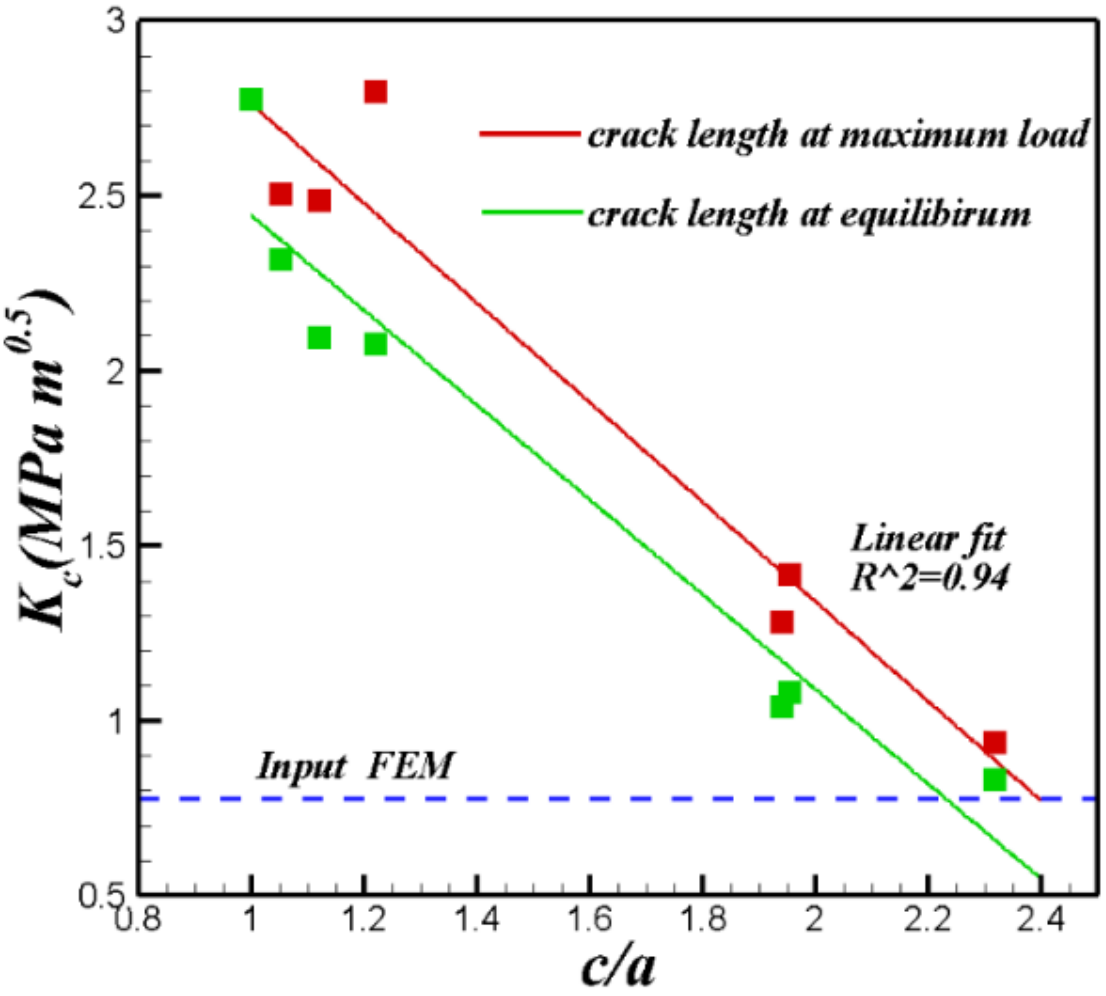

Figure 3-8 Comparison of fracture toughness estimation by LEM model with crack length of equilibrium and maximum depth. Also the input Kc value of the FEM is plotted as a constant (K_c = 0.75 MPa m$^{0.5}$).

3.4 Conclusion

A three dimensional continuum damage model based on zero thickness interface elements has been presented. The model takes into account the material degradation in shear and opening modes. The implementation has been done as an non-linear algorithm with interface elements of 6 nodes, where the displacement and traction values are calculated in the middle surface of the elements. The damage model has been applied to study the crack propagation during an indentation test of an isotropic material for a range of h_{max} between 0.2 μm and 0.8 μm. The loading displacement curves indicate that the presence of the interface elements are not influencing the natural response of the material. The values of E_r estimated from the indentation data display a discrepancy of less than 3% with respect the input value, where the values of E_r and H remain relatively constant for the different h_{max}. The evolution of the crack length (c) indicates that at low penetrations ($h_{max} \leq 0.4\mu m$), the length of the plastic zone is greater than the size of the radial cracks. A half penny shape configuration is revealed in the plots, where the length of the cracks reveal an expansion at equilibrium of 16% at $h_{max} = 0.6$ μm and 8% at $h_{max} = 0.8\mu m$.The simulation results indicate that for crack lengths greater than the size of the indentation marks ($c/a \geq$ 2.2), the values estimated with the LEM model predict a 10% of difference with respect to the input value. Also, the results indicate the advantages of the computational model in the visualization of the crack patterns.

CHAPTER 4. ON THE WEAR RESISTANT MECHANICS OF NATURALLY-OCCURRING ROD-LIKE MICROSTRUCTURES

4.1 Introduction

Inspired by remarkable mechanical properties, material designs seek for guidelines in the evolutionary features observed in nature. Sustainable building cooling systems based on termite mounds [60], protective coating designs inspired by crocodile's skin [61] and turbine blades mimicking the flippers on humpback whales [62] are some recent applications inspired by nature. In natural material, extraordinary mechanical properties have been attributed to their microstructural design, which consists of an arrangement of crystalline bundles surrounded by a thin organic layer [3], [63], [64]. Natural ceramics, microstructures composed by mineralized prismatic shapes surrounded by weak interfaces (i.e. polypeptides), are conformed by a complex hierarchical structure with features that range from atomistic to macroscopic scales [13], [65].

One mechanical property of interest in natural materials is abrasion resistance. An innovative abrasion resistant composite has been found in the radulae teeth of the marine mollusk *Criptochiton stelleri* (Figure 4-1a). This species of the phylum *Mollusca* [66] is provided with a highly mineralized radulae, which contains 70 rows of aligned teeth [9], [67]. As compared to the shape of the human enamel, the head of the tooth resembles a "garden hoe" that is oriented 90° with respect its base (Figure 4-1b). Living at the bottom

of the ocean, the chitons seek for algae in the surface of hard rocky substrates [9], [68]. Optical examination has shown that even when teeth are worn over time by abrasive surfaces, structural integrity is preserved through their life-time [69]. The tricuspid of the tooth is composed of a compliant amorphous core surrounded by a hard mineralized shell, which is characterized by a rod-like microstructure with a high concentration of magnetite (around a volume fractio of 90% of Fe_3O_4) surrounded by layers of organic α-chitin [63], [67]. Scanning electron microscopy (SEM) images have revealed a composite formed by rods of 150 nm of diameter and interfaces of 20 nm of thickness [67]. Although the rod-like microstructure is a common feature observed in mineralized composites [3], [24], [25], [64], [70]–[73], the rods are aligned parallel to the exterior surface of the tooth in the radular teeth (lines in Figure 4-1b) [9]. Numerical studies of the structural behavior of the radulae have revealed that the rod alignment coincides with the direction of principal stresses[67], [69], suggesting that the architecture of the tooth is optimized to withstand abrasive loading conditions. Compared to other mineralized materials, it has been suggested that the chiton tooth is the most abrasion resistant material known in nature[9], [10].

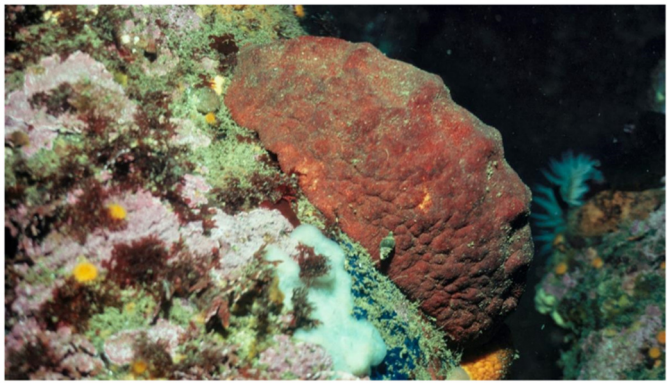

(a)

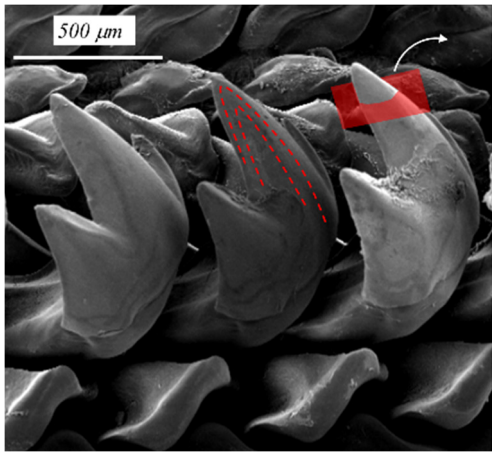

(b)

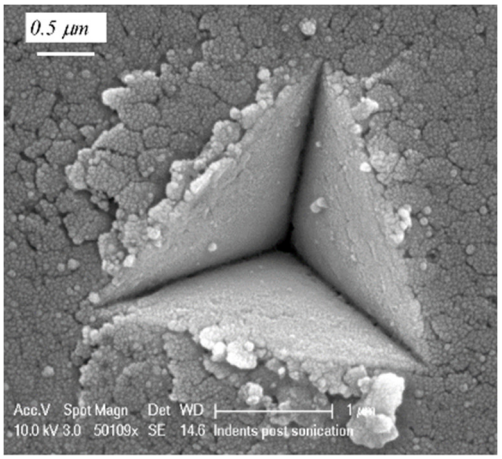

(c)

Figure 4-1 *Cryptochiton stelleri* [74] in the marine habitat, (b) SEM image showing the alignment of the teeth in the radulae and (c) an overview of a post-indented sample (obtained with permission from Grunenfelder et al.[67]). The lines in (b) coincide with the alignment of the mineralized rods [67]. The indentation mark in (c) is with a rod-like microstructure aligned perpendicular to the surface in (b).

Nano indentation tests of the exterior shell of the tooth [67] have revealed higher site-specific modulus in the region in direct contact with the abraded solid (*leading edge*) as compared with the posterior region of the tooth (*trailing edge*). These observations coincide with a larger rod diameter in the trailing edge (*TE*) as compared with the leading edge (*LE*) of the tooth [67]. A micromechanical analysis performed by Grunenfelder et al.[67] indicates that, while the rod diameter has an influence on the loading response, other

nano-scale features (i.e. asperities, mineral bridges) could also be responsible for the outstanding abrasion resistance of the tooth. A detailed analysis of a cube corner indentation marks of rods oriented perpendicular to the surface (Figure 4-1c) reveals the lack of material removal and fracture propagation through the rods[67]. The outstanding damage mitigation and abrasion resistance of the chiton tooth is desired for cases where materials undergo large contact pressure [69]. While considering the contact between two solids, deteriorative effects from wear and friction are very common. Rolling, sliding and adhesion are some of the mechanical actions that influence the lifetime of industrial cogs and tunnel boring machines[75]. For industrial processes, wear resistant materials are necessary for tools (i.e. drills) that are engaged in cyclic loading and under high compressive stresses. Endurance materials which are able to withstand wear are preferred for these applications.

From many decades, analytical models have been addressed to study the crack propagation during indentation tests by the researchers [50]–[52]. As many of these models relate the crack morphology [30], [41], [42] with the fracture toughness (K_c), experimental errors have been shown to influence by 50% the estimations [40]. Instead, computational models allow a better determination of the crack tortuosity and spread of damage[50], [51]. Studies carried out by Lee et al.[50], [51] to understand the limitations of the LEM analytical model [41] considered the crack propagation thru walls aligned parallel to the indenter edges. Other numerical advantages also include the prediction of the mechanical response of material layers in fish scales to resist the penetration of the indenter tip [76]. In this study, we propose a combined experimental/computational model to analyze the cube corner indentation test of the mineralized shell of the chiton tooth. The computational

model allows for crack propagation through the rod-like microstructure, and inelastic deformation and damage in the rods. The fracture model allows the crack propagation through the interfaces, where a traction separation law mimics the debonding of the organic material and mineral bridges between rods[67]. The failure of the rods considers a Weibull distribution [77], which has been obtained from the material characterization of the monolithic magnetite. The hypothesis is that the competition between interfacial properties of the organic layer, and strength of the rods, governs the wear resistance of the rod-like microstructure of the chiton tooth. The purpose of this work is to examine the influence on the abrasion resistance of the failure of the rods and interfaces of the rod-like microstructure.

4.2 Experimental analysis

Nano indentation tests were used to obtain the constitutive model of the solid material. The values obtained with a cube corner indenter were compared with respect to a Vickers pyramidal [78]. Because of the disadvantage of chipping in abrasion resistant materials, the indention damage was studied. The experimental analysis also addressed the resistance to penetration (c_1) of the magnetite and the rod-like microstructure of the tooth. The values of c_1 obtained from the experimental data are used later to compare the numerical results.

4.2.1 Material characterization of magnetite

A non-linear isotropic hardening law [79] (Equation 4.1) considered in geological materials [80] is taken into account to model the constitutive law of the magnetite shown in Figure 4-2a. The plastic yield stress (σ_p) is given by a material constant (H_{iso}), the initial yield stress (σ_y) and the plastic strain (ε^p) [20].

$$\sigma_p = \sigma_y + H_{iso}\varepsilon^p \tag{4.1}$$

To determine the initial yield stress we followed the analysis of the cavity model [18]. Considering the indentation modulus and indenter geometry of a Vickers indentation test [78], the value of σ_y = 3.5 ± 0.1 GPa. On the other hand, the value of H_{iso} was obtained by fitting a 3D FEM model of a homogenous isotropic solid material with the experimental data provided by Chicot et al. [78] using a Vickers tip. Figure 4-2b shows the influence of varying H_{iso} in the loading data (with σ_y = 3.5 GPa). These results indicate that a H_{iso} =40 ± 4 GPa best matches the experimental curve. Compared to other materials observed in natural ceramics [18], [81], the literature indicates that the iron oxide magnetite shows loading behavior that is independent of the crystallographic orientation [78]. Because the loading portion of the indentation tests is correlated with the plastic behavior of the material, the monolithic material is treated as isotropic and homogenous.

To validate the material characterization obtained from the Vickers indentation with cube corner indenters, displacement control nanoindentation tests were carried out at

maximum penetrations (h_{max}) from 50 nm up to 1 μm. The tests were performed on a polished polycrystalline geological magnetite sample, using a nanomechanical testing system (TI 950 Triboindenter, Hysitron, USA) at a loading rate of 10 nm/sec. To avoid inconsistencies in the unloading section of the curves, a 10 sec hold was applied after reaching h_{max} in each test. The nanoindentation tests used a diamond cube corner indenter tip. The average indentation data obtained with the cube corner indentation (σ_y = 3.5 GPa and H_{iso} = 40 GPa) reveals an error of ~9% in the maximum load with respect the constitutive model obtained from a Vickers indenter [78] (Figure 4-1c).

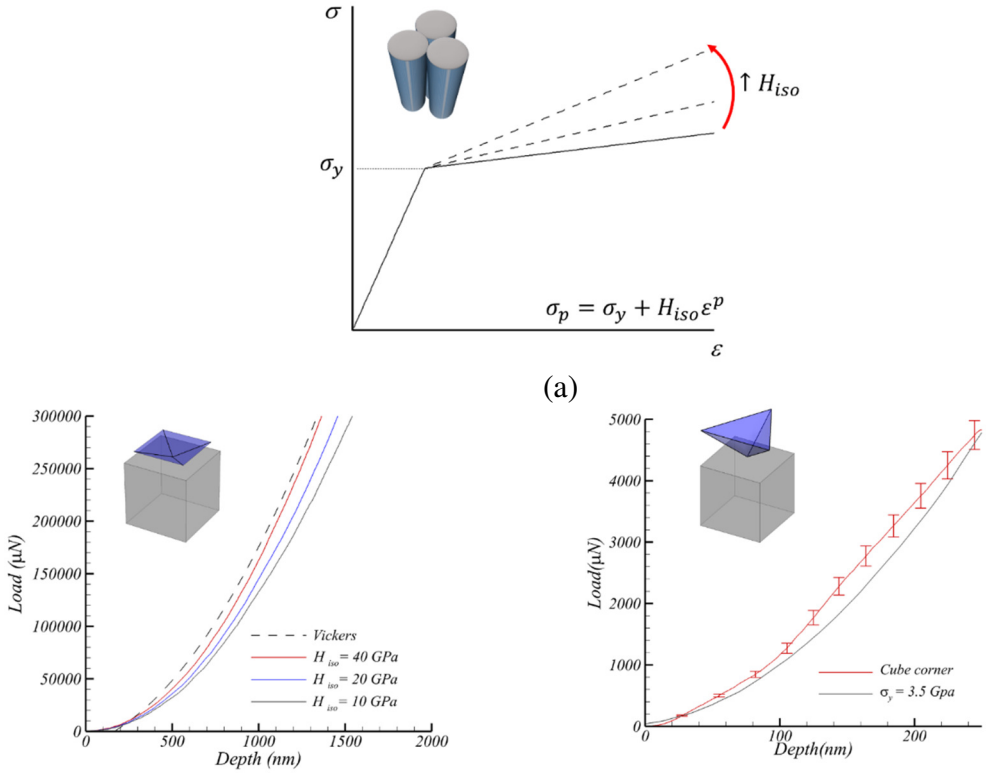

Figure 4-2 Constitutive model of the single crystal magnetite considered in this study (a). Different values of H_{iso} and a constant σ_y = 3.5 GPa are considered in the numerical model (b), where H_{iso} = 40 GPa shows good agreement with respect the Vickers indentation data of Chicot et al. [78]. The value of σ_y = 3.5 GPa was obtained with the contact formulation [82]. The experimental and numerical results of a cube corner indentation test in (c).

4.2.2 Comparison of the resistant to penetration of the tooth and the magnetite

While considering an elastic homogenous isotropic material, Sneddon [31] proposed that the load (P) obtained from the contact of an indenter approximated as a paraboloid of revolution is proportional to a variable (c_1), the penetration depth of the indenter (h) and a constant m which depends of the indenter shape (m = 1.5 [83] for a cube corner indenter) (Equation 4.2). As proposed by Giannakopoulos et al.[84], the coefficient c_1 can be seen as a resistance to penetration of the material. This expression has been widely used to study different materials [57], [83], [85], [86].

$$P = c_1 h^m \tag{4.2}$$

The values of c_1 were computed with a cube corner tip in the magnetite sample and in the chiton tooth mineralized shell. While the magnetite has a value of c_1 = 1.27 ± 0.06 μN/nm$^{1.5}$, the microstructure shows lower values. The comparison of c_1 computed from the loading displacement curves in the different sections of the tooth presented by Grunenfelder et al. [67], reveals an R^2 = 0.98 of correlation with the loading displacement data obtained during indentation (Figure 4-3a). This analysis reveals a value of c_1 = 0.68 ± 0.04 μN/nm$^{1.5}$ for the leading edge and c_1 = 0.47 ± 0.05 μN/nm$^{1.5}$ for the trailing edge of the tooth. . The reduced Young modulus (E_r) and hardness (H) obtained from the cube corner indentation followed the experimental procedure proposed by Oliver and Pharr [86]. The values of E_r and H of the mineral and chiton tooth are compared with respect to c_1 in Figure 4-3b. It is depicted in Figure 4-3b that by increasing c_1, the reduced Young's

modulus (E_r) and the hardness (H) increase. As it is shown in Figure 4-3, c_1 correlates the response of the material to the penetration, E_r and H. Therefore, the results of the numerical models are compared with respect to the values of c_1.

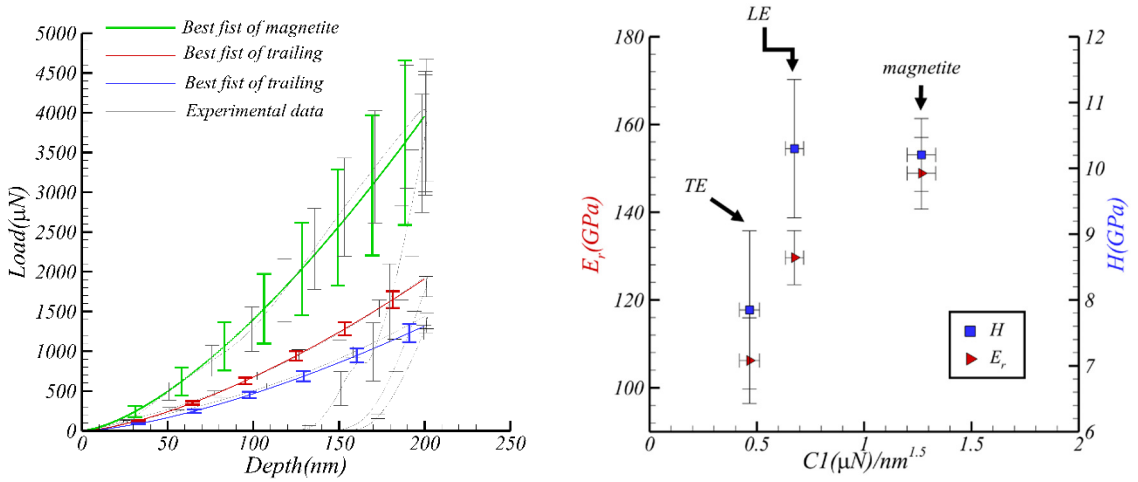

(a) (b)

Figure 4-3 (a) Cube corner indentation data of the magnetite obtained with a cube corner indenter in this study, and loading curves of the leading and trailing edge from the literature [67]. A comparison of the indentation modulus obtained with the cube corner indenter is shown in (b) with respect to the slope of the indentation data (c_1). An R^2 = 0.98 is the correlation coefficient of c_1 for the magnetite and chiton tooth. The error bars of this figure are one standard deviation.

The curves of Figure 4-3a display that the loading displacement curves of the magnetite are in general greater than the chiton tooth. In the study of the fracture mechanics, the fracture energy (G_c) provides insights of the coalescence and growth of voids. Although not much is known about the resistance to fracture of the pure magnetite, an atomistic model [87] estimates a value of G_c = 12 J/m^2. The indentation moduli obtained with the cube corner indenter are summarized in Table 4-1. The indentation pressure (H) is measured as the ratio between P_{max} and the contact area of the indenter (A) which is deduced with an standard procedure from the literature [83]. In the quantification of H,

Tabor [11] proposed that the value was directly correlated with the plasticity of the material ($H \approx 3\sigma_y$). The estimation *of* $H = 10.2 \pm 0.6$ *GPa* in the magnetite is also in agreement with the results reported by Tabor [11] .

Figure 3b shows a comparison of H with respect to c_1, where the hardness shows a close value in the *LE* (H = 10.3 ± 1.1 GPa) as compared to the pure magnetite (H = 10.2 ± 0.6 GPa). An analysis of obtained from the analytical model [28] shows a reduction of the contact area of one order of magnitude in the *LE* of the tooth (A = 0.185 ± 0.031 μm^2) as compared to the mineral (A = 0.351 ± 0.038 μm^2). A plausible explanation of the reduction in the contact area could be correlated with the energy dissipation of the material, as more energy is dissipated through the weak organic layers of the rod-like microstructure, leading to material relaxation and reducing the area in contact with the indenter. Like the hardness, the value of E_r increases with respect to c_1 (Figure 4-3b). We surmise that the excess of plastic deformation accumulated leads to less material recovery in the magnetite (E_r =148.8 ± 8.2 GPa) as compared with the more compliant leading edge (E_r =129 ± 6.2 GPa). The values from E_r of the chiton tooth obtained in this study are of the same order as those found in the literature [9], [88].

Table 4-1 Summary of the experimental values obtained from the cube corner indentation tests in the mineral and chiton teeth at h_{max} = 200 nm. The curves from the *LE* and *TE* have been taken with permission of Grunenfelder et al. [67].

	$c_1(\mu N/nm^{1.5})$	$P_{max}(\mu N)$	$A(\mu m^2)$	$E_r(GPa)$	$H(Gpa)$
Magnetite	1.27 ± 0.06	3583.61 ± 191.1	0.351 ± 0.038	148.8 ± 8.2	10.2 ± 0.6
LE	0.68 ± 0.04	1909.18 ± 121.3	0.185 ± 0.031	129 ± 6.2	10.3 ± 1.1
TE	0.47 ± 0.05	1317.8 ± 122.2	0.167 ± 0.041	106.2 ± 9.8	7.85 ± 1.2

Many of the considerations mentioned above are based on hypothesis from the authors. In complex microstructures as the one observed in biocomposite materials, three dimensional continuum models are used to quantify the fracture energy dissipation during crack propagation [15], [21], [89]. As many of the analytical solutions to study crack propagation in indentation tests consider superficial cracks observed in post indented marks[30], [41], [90], a computational model must be addressed.

4.3 Micromechanical model

Compared to two dimensional fracture models [51], [91], estimations made with three dimensional simulations in indentation tests can lead to better predictions of complex crack morphologies [49]–[51], [92]. The FEM model considered in this study accounts for magnetite rods of hexagonal cross section. TEM analyses of the magnetite rods suggested the hexagonal shape profile[67], which has been considered is the study of other rod-like microstructures of natural abrasion resistance materials [2], [15], [63]. A unique cross section of 0.15 μm is considered. Computational models of the chiton tooth [67] revealed that the variation in the rod diameter between the leading and trailing edge is not largely influencing the indentation data observed in Figure 4-3a. As previous analyses has been addressed by references [63], [72], [93] to understand the influence of the length of the rods in the mechanical properties of biomineralized materials, a constant length of 30 μm has been taken into account. The micromechanical analysis considers a set of rods surrounded by pre-embedded cohesive elements, where the rods are homogenous and isotropic (Figure 4-4a). To model the plastic deformation of the rods, the constitutive model

(Figure 4-2a) obtained in the magnetite is considered. The debonding between the rods is modelled with cohesive interface elements pre embedded in the solid (Figure 4-4b). The organic layer between the rods followed a cohesive traction separation law [64].

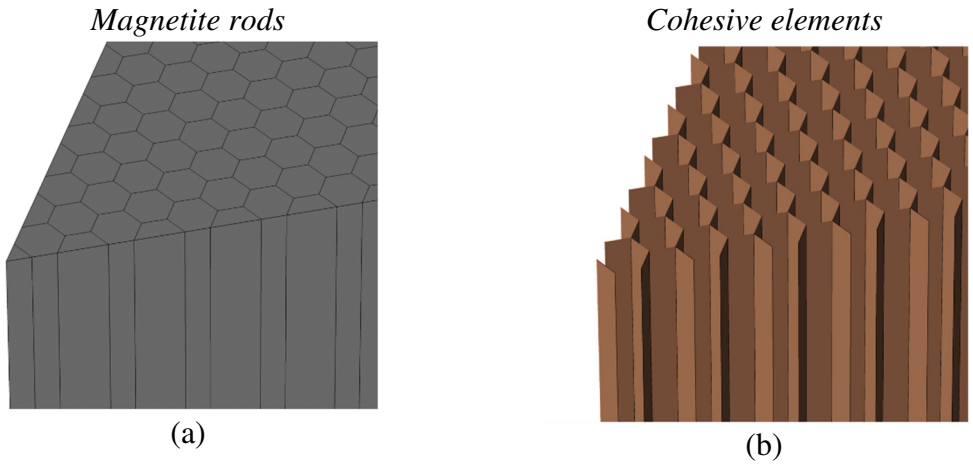

Figure 4-4 Summary of the computational domain considered. Homogenous rods surrounded by cohesive interfaces are shown in (a) and (b).

4.3.1 Computational domain

The 1/6th fraction of the domain satisfies the symmetry planes of the pyramidal indenter (Figure 4-5). Cube corner tips have the advantage of removing more material as compared with the Berkovich and Vickers indenters [43], [94]. A frictionless contact was considered in the indentation tests [57], [95]. At edges of the 1/6th domain, symmetry planes are considered between partly rods and interface elements for fully rods. As it is depicted in Figure 4-5b, the computational domain considers a region of more than 1000 rods in direct contact with the indenter and a bulk of solid material surrounding the

microstructure. The bulk of solid material is also modeled with the isotropic and homogenous constitutive model of magnetite. To fulfill the infinite half-space boundary conditions, a large cylindrical base has been modelled surrounding the rod-like microstructure with a domain of 22.5 μm of radius. The 1/6th domain takes into account 47810 nodes and 213816 tetrahedral elements, in which the mesh refinement in the region in contact with the indenter adds up to a 10% of uncertainty in the simulations. The uncertainty is measured by comparing the values of P_{max} from the different meshes at the same penetration. The mesh refinement was deemed to ensure convergence.

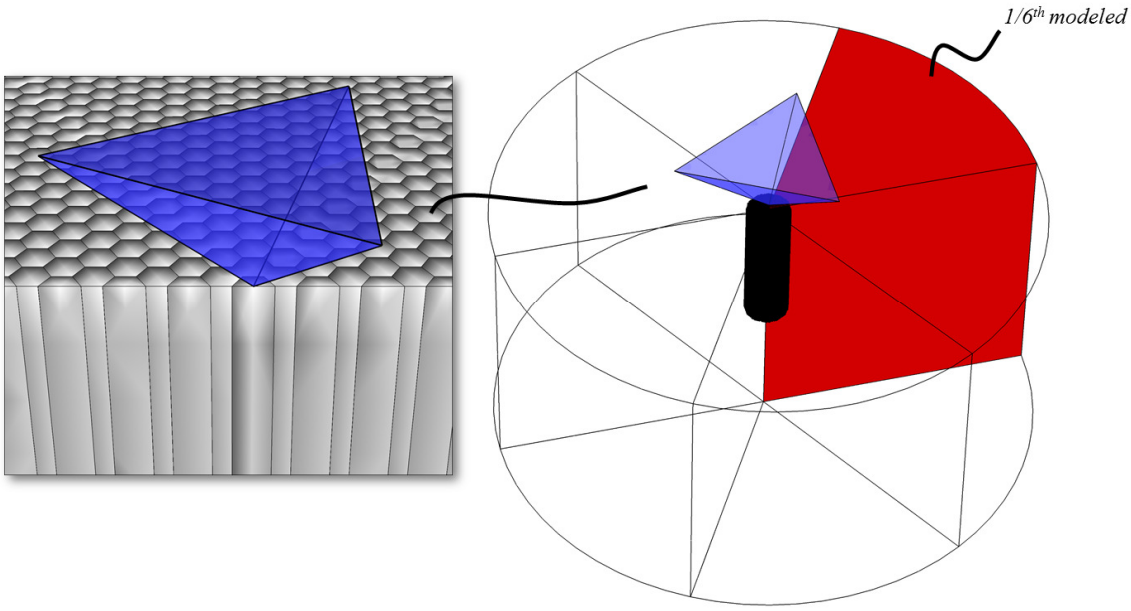

Figure 4-5 Details of the numerical model of the cube corner indentation test. Cube corner indenter placed above the idealized rod-like microstructure in (a) and a 1/6th domain and cube corner indentation model in (b). The rods are oriented perpendicular to the surface.

4.3.2 Interfacial behavior of the organic layer

Similar to other bio-mineralized materials, the exterior shell of the microstructure is characterized with an organic material, and structural features such as mineral bridges and surface asperities [96], [97]. Mineral bridges as shown in Figure 4-6a have been identified between rods of the leading and trailing edge [67]. Mimicking the thin α-chitin layer and crystal bridges surrounding the rods, are interface elements are pre-embedded in the solid (Figure 4-6b). To model the fracture behavior, a bi-linear traction-separation law used for brittle materials [56] was considered and implemented in other indentation models [49]–[51], [92]. The shape of the cohesive law taken into account has been used before to model organic debonding in other biological materials [89], [98]. A non-linear formulation of the cohesive zone model was implemented in the finite element code FEAP [20]. The non-dimensional displacement jump (λ) describes the interface degradation by tracking the normal and transversal displacements (u_n, u_{t1}, u_{t2}), where the non-dimensional effective displacement jump (λ) is a function of the maximum displacement values to reach failure ($\delta_n, \delta_{t1}, \delta_{t2}$) [54], [99], [100] :

$$\lambda = \sqrt{\left(\frac{u_n}{\delta_n}\right)^2 + \left(\frac{u_{t1}}{\delta_{t1}}\right)^2 + \left(\frac{u_{t2}}{\delta_{t2}}\right)^2} \tag{4.3}$$

The mechanical behavior of the interface between rods is mainly influenced by different fracture mechanisms. The interfaces between two rods is composed by the bio-glue and mineral bridges. The mineral bridges contribute with the initial stiffness and

strength of the interface, the glue contributes to the toughness and cohesive energy between rods. A sketch of a traction separation law in opening and shear mode is shown in Figure 4-6c and d respectively. The resistance to separate between two rods is given by a traction in normal (T_n) and shear direction (T_{t1} and T_{t2}) [56], [100]. The values of normal and shear traction are related to the displacements by [56], [100]:

$$T_n = \frac{1-\lambda^*}{\lambda^*}\left(\frac{u_n}{\delta_n}\right)\frac{T_{max}}{(1-\lambda_{cri})} \tag{4.4}$$

$$T_{t1} = \frac{1-\lambda^*}{\lambda^*}\left(\frac{u_{t1}}{\delta_t}\right)\frac{T_{max}}{(1-\lambda_{cri})} \tag{4.5}$$

$$T_{t2} = \frac{1-\lambda^*}{\lambda^*}\left(\frac{u_{t2}}{\delta_t}\right)\frac{T_{max}}{(1-\lambda_{cri})} \tag{4.6}$$

The value of λ^* is monotonically increasing and given by $\lambda^* = \max(\lambda_{max}, \lambda)$ [56], [100], where is $\lambda_{max} = 1$. When $\lambda=\lambda_{cri}$ the normal and shear tractions reach their maximum values [56], [100]. In this chapter, the values of strength and maximum opening are referred to T_{max} and δ_{max}. The area under the traction-separation law defines the cohesive energy ($G_c = 0.5\ T_{max}\ \delta_{max}$) required to create new surfaces per unit area, which is correlated by the Irwin-Griffith [33] relationship to the fracture toughness ($K_c^2 = EG_c$). When the interface elements remain intact, the initial slope ($S = T_{max}/(\lambda_{cri}\ \delta_{max})$ can be compared to the stiffness of the interface[56]. In this analysis a constant value of $S = \zeta E_{mag}/d$ is considered, where d is the separation between rods (≈ 20nm [67]) and $\zeta = 1$. In the calculation of the tractions and displacements, we followed the formulation proposed in the references [54], [99], [100], in which the values are computed in the middle plane and interpolated to the nodes. In fracture mechanics, the values of G_c and T_{max} can be

characterized with double cantilever beams (mode I) and lap shear tests (mode II) [63], [101]. However, to avoid time consuming experimental setups in the intricate microstructure, a range of values of G_c and T_{max} are considered. The values of G_c (from 20 J/m^2 to 150 J/m^2) and T_{max} (0.3 GPa to 28 GPa) taken into account are between those measured in high mineralized materials [10], [102].

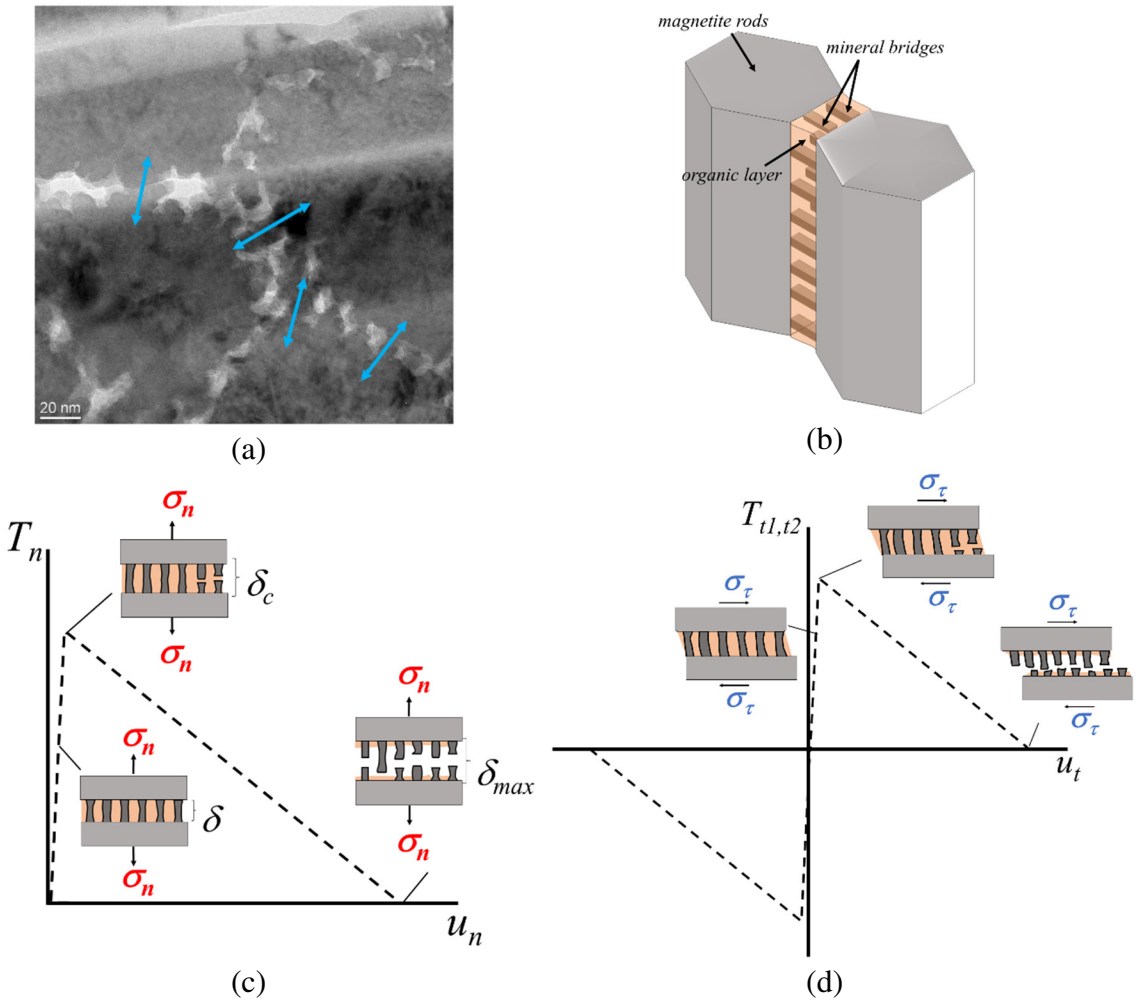

Figure 4-6 (a) TEM image of the rods (adopted with permission from Grunenfelder et al. [67]) where the arrows indicate the mineral bridges observed. Diagram of the micromechanical analysis of the crystal bridges and organic layer (b). Traction separation laws that mimic the fracture of the organic material and crystal bridges in mode I (c) and mode II (d).

4.3.3 Deformation modes

Different energy dissipation mechanisms are associated to indentation tests. Radial and median crack propagation [30], [41], and plastic deformation [103] are some of the mechanisms identified in brittle and ductile materials. To model the damage associated in the microstructure of the tooth (Figure 4-1c), the constitutive model of magnetite has been considered in the rods and crack propagation through the interfaces. An advantage of the numerical model is the visualization of radial cracks during penetration. The FEM shown in Figure 4-7 indicates the lack of radial cracks through the interface and the localization of damage around the indenter.

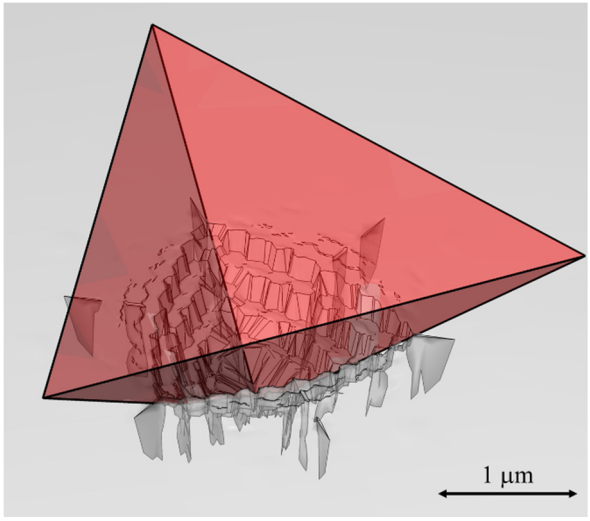

Figure 4-7 Indentation mark observed in a computational model at h_{max} = 700 nm. Radial cracks coinciding with the indenter tips are observed in the interface layer.

4.4 Results

To validate the hypotheses considered in the experimental analysis, the continuum framwork is used to quantify the energy dissipation mechanisms during indentation. The simulations considered the influence of T_{max} and G_c on the loading response of the material. An advantage of the abrasion resistant microstructure of the tooth with respect to the monolithic magnetite is the lack of material removal around the indentation mark[67]. To account for the damage of the rods in the subsurface of the sample, a Weibull distribution [77] of the failure of rods is taken into account. The probability of failure of the rods has been obtained from indentation tests performed at different penetrations in the monolithic magnetite.

4.4.1 Loading displacement curves

Similar to the analysis performed in the experimental section, the loading response obtained from the simulations is first fitted with equation 4.2. The solution of the response of an elastic material formulated in equation 4.2 [31] postulates that the constant (is proportional to material properties (E and ν) and the shape of the solid of revolution (k) as follows: $c_1 \approx 1.9Ek/(1-\nu^2)$. Indentation analyses carried out by Cheng et al. [85], [104] suggest that the length scales in the material could be responsible for discrepancies between the elastic formulation [31] and the loading data. Because the value of c_1 proposed by the references have been calculated in elastic materials, under plastic deformation c_1 is no longer a material constant but a function of material and interface parameters. This is

confirmed by comparing the values of c_1 obtained from the material characterization of the magnetite, where the cube corner indentation shows a value of $c_1 = 1.27 \pm 0.06$ μN/nm$^{1.5}$ as compared to the Vickers tip, where $c_1 = 2.1 \pm 0.1$ μN/nm$^{1.5}$. The traction separation law shown in Figure 4-8a is used to compare the influence of T_{max}. By increasing the value of T_{max} from 0.5 GPa to 1 GPa the P_{max} achieved at h_{max} = 200 nm has a deviation of 23%. This value is greater than the 10% of difference at maximum penetration observed by varying almost by a factor of 2.8 the value of G_c from 25 J/m^2 to 70 J/m^2 (Figure 4-8c)[105]. In the loading response shown in Figure 4-8b, the arrows coincide with a new set of rods being in contact with the indenter. The instabilities indicated with the arrows in Figures 4.8b and c are correlated with the onset of plasticity as a new set of rods are in direct contact with the indenter; a response that is in agreement with experimental observations of pop-in events in coating systems [106], [107]. In hard substrates, dislocation nucleation have been correlated with the sudden shift of the loading displacement curves [106].

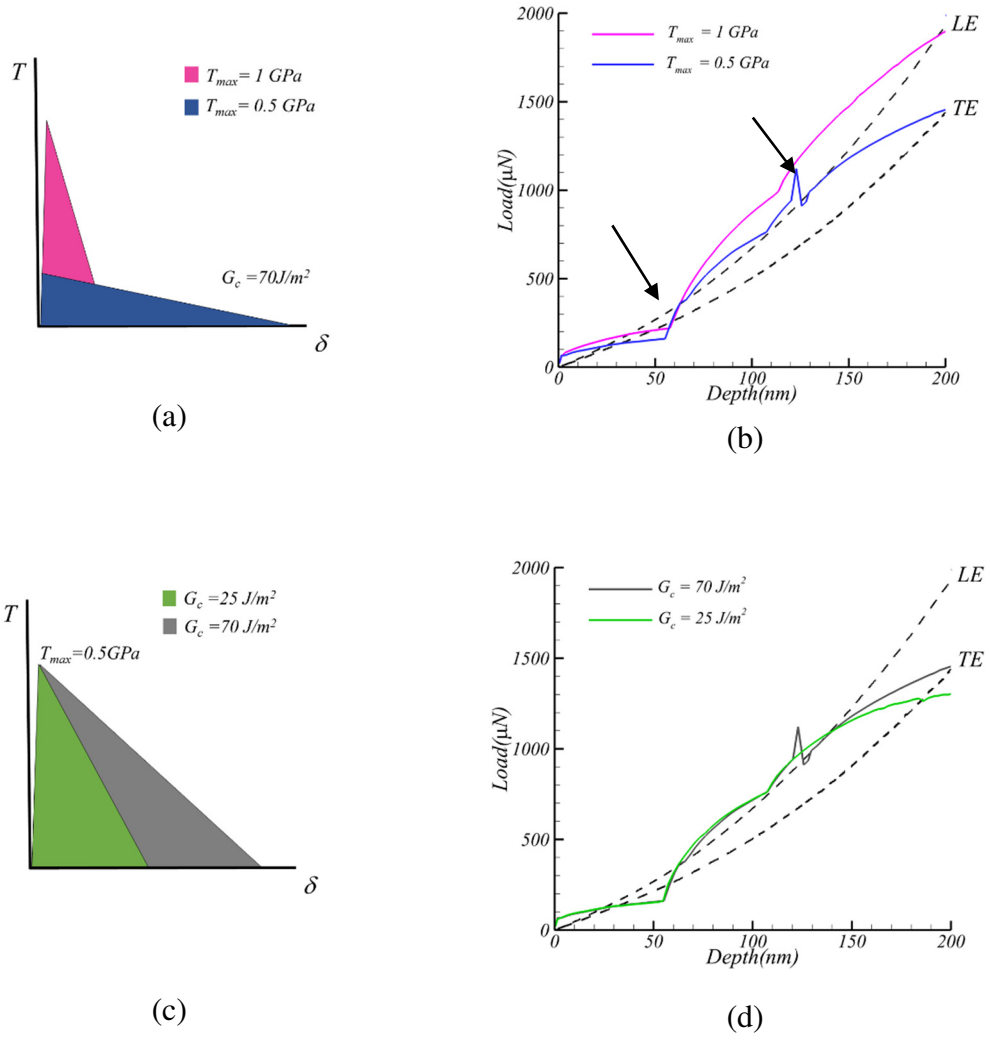

Figure 4-8 Comparison of the influence of T_{max} and G_c in the loading data. Traction separation laws with G_c = 70 J/m^2 in (a) and T_{max} = 0.5 GPa in (c). The loading data in (b) corresponding to the traction laws in (a), and in (d) to the traction laws in (c).

4.4.2 Energy dissipation

In this section, the energy dissipation in the rods through inelastic deformation and the interfaces is calculated with a reference value of G_c = 70 J/m^2. The variation of T_{max} also accounts for the density of mineral bridges that could enhance the response of the

material [108]. An sketch of the traction separation laws considered is shown in Figure 4-9a. The quantification of the plastic energy dissipated in the rods is given by $U_p = \int U_o dV$ [109], where U_o is the supplied plastic energy per unit volume (V). The analysis of the plastic energy in Figure 4-9b indicates that by enhancing the strength of the interfaces (T_{max}) the rod-like microstructures resemble a solid material (dashed lines in Figure 4-9b). At low penetrations (h_{max} = 80nm), the numerical results suggests a relatively constant value of U_p. By increasing the maximum penetration to h_{max} = 100nm, the weak interfaces (T_{max} = 0.4 GPa) reveal 100% of difference in the value of U_p with respect to T_{max} = 28 GPa. In contrast with the behavior of U_p, the trend line of energy dissipation through fracture of the interfaces is enhanced with low values of T_{max}. The value of fracture of energy dissipated per unit area is: $G_{dis} = {}^{1}/_{2}\, \delta_n T_{max} \left({}^{(\lambda_{max} - \lambda_{cri})}/_{(1 - \lambda_{cri})} \right)$ [56]. The dissipation of energy through crack propagation in the interfaces is given by equation 4.7, where A are the areas of the middle planes of the cohesive elements with $G_{dis} \neq 0$.

$$U_{dis} = \int G_{dis}\, dA \tag{4.7}$$

To understand this expression, we must refer to the initial debonding of one element where the value of U_{dis} = 0, or when the interfaces fracture ($\delta = \delta_c$ in Figure 4-6c) the value of U_{dis} is the maximum value (= $G_c A$) where A is area of the interface element. Compared to G_{dis}, which is the value of energy dissipated per area in each element, U_{dis} is the summation of the energy dissipated in all the cohesive elements. Figure 4-9c shows higher values of U_{dis} by increasing the penetration of the indenter into the microstructures.

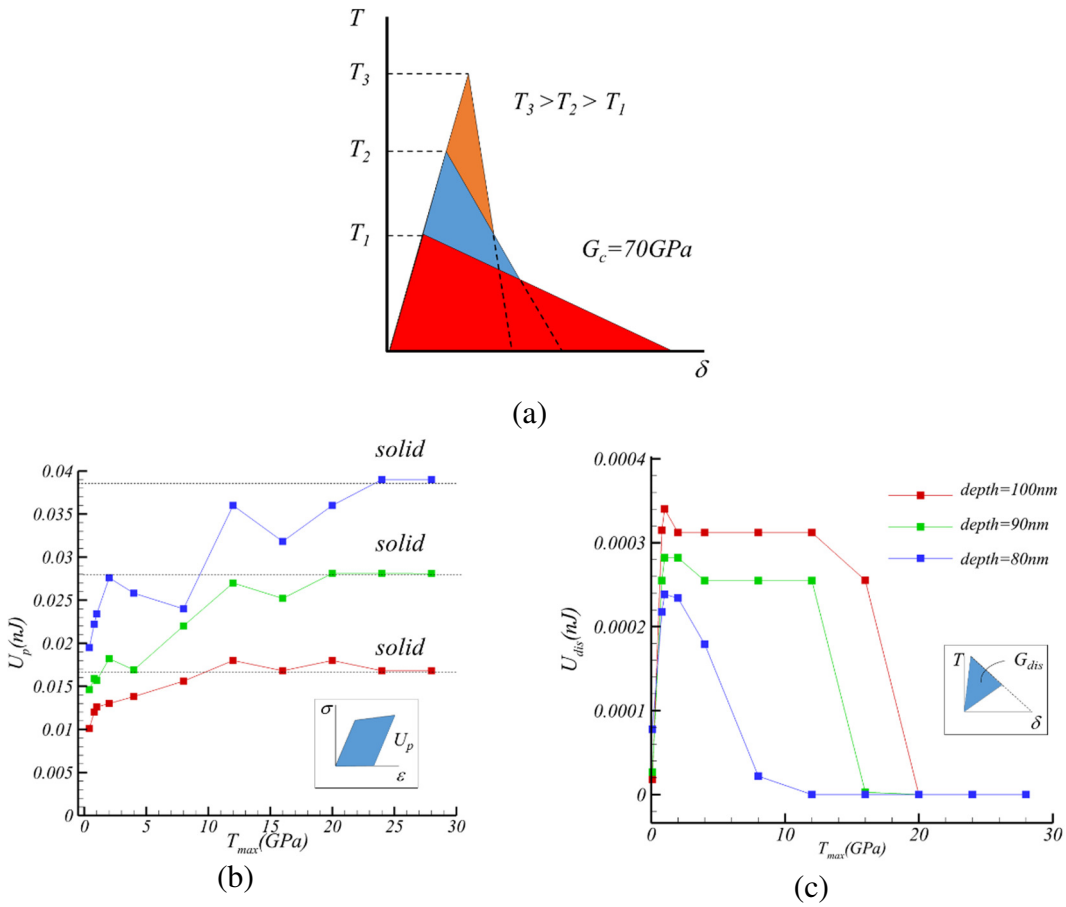

Figure 4-9 Influence in the variation of U_p (b) and U_{dis} (c) with respect to T_{max} (a). The values were calculated with a $G_c = 70$ J/m^2 and have been augmented for displaying purposes in (a). The dashed lines in (b) represent the solid materials.

The plot of G_{dis} is shown in Figure 4-10. The visualization is obtained by extrapolating the values of G_{dis} from the integration points into the element nodes. As many elements could share a common node, the mean value of G_{dis} is plotted in the element nodes. In the vertical axis of Figure 4-10 the fracture energy dissipation contour of G_{dis} is plotted with respect to h_{max} and in the horizontal direction with respect to T_{max}. All the values of G_{dis} greater than 0 are shown in the energy map. The trend line observed in Figure 4-9c to increase the energy dissipated in the weak interfaces is corroborated in Figure 4-10. At a

T_{max} = 0.6 GPa, a greater volume of rods surrounded by interface elements that are dissipating energy are observed for all the h_{max}. At low penetrations (h_{max} = 50 nm) and a higher strength (T_{max} = 8 GPa), the microstructure remains intact and therefore behaves like a solid material. As compared to the weaker material of T_{max} = 0.6 GPa, more localization of damage is observed in the stronger interfaces at T_{max} = 8 GPa. These results could also be used to understand the influence of the distance left between indentation marks. In the study of biomineralized microstructures, it is a common practice to perform indentation tests in aligned rows. However, if two indentation marks are not separated enough, the spread of damage in the subsurface of the first indentation mark could influence the values of E_r, H and loading response obtained in the consecutive indentation mark[40].

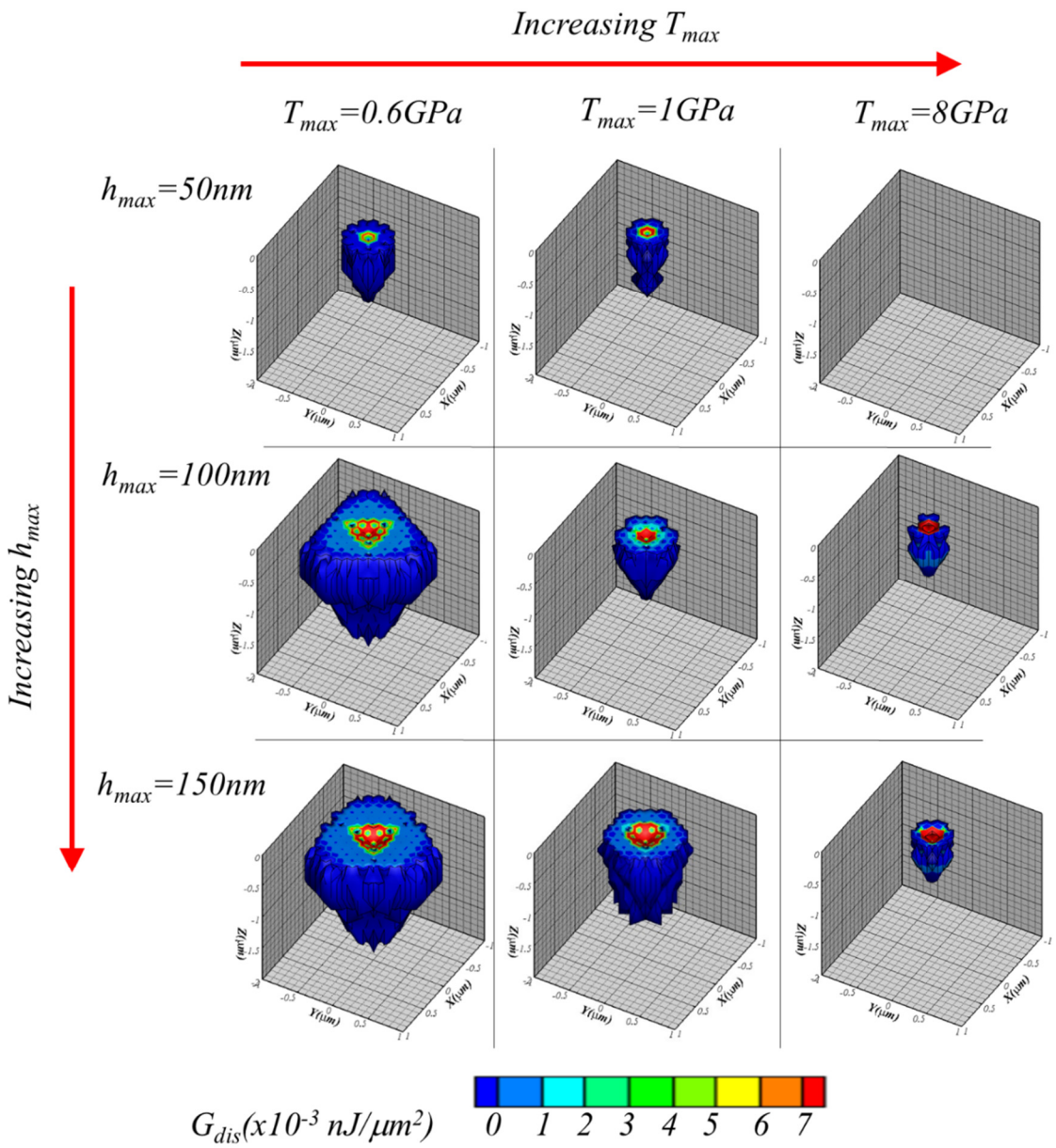

Figure 4-10 Visualization of the variation of G_{dis} (nJ/μm^2) against T_{max} and h_{max}. The value of G_c = 70 J/m^2. The contours are only plotted for values of G_{dis} > 0.

4.4.3 Failure of the rods

To account for the failure of the magnetite, a comparison of the maximum principal stresses at different h_{max} is addressed in Figure 10. The stress contour represents a sample of the different values of T_{max} considered in this study. Because the map of maximum principal stresses (σ_1) surrounding the indenter, Figure 4-11 suggests that an increase in the strength of the interfaces leads to the localization of damage. An advantage of the rod-like microstructures observed in biocomposites, such as HAP crystals nano rods in fish scales of the P. Senegalus [15], [89] and millimeter scale 3D printed biomimetic composites [63] is to localize the damage around the indentation region by dissipating energy in the form of lateral cracks. At low penetration (h_{max} = 50 nm) and weak interfaces (T_{max} = 0.6 GPa), high values of tensile stresses are observed in the top surface of the microstructure. At h_{max} = 150 nm increasing the strength of the interfaces to T_{max} = 8 GPa leads an increase of 60% in the values of σ_1 below the indentation mark, which are associated in solids with crack propagation in the median direction [49], [110]. However, not only the values of σ_1 need to be considered, but also the volume of the material associated with those stresses. To analyze the failure of the volume corresponding to the high values of σ_1, a statistical Weibull distribution has been carried out.

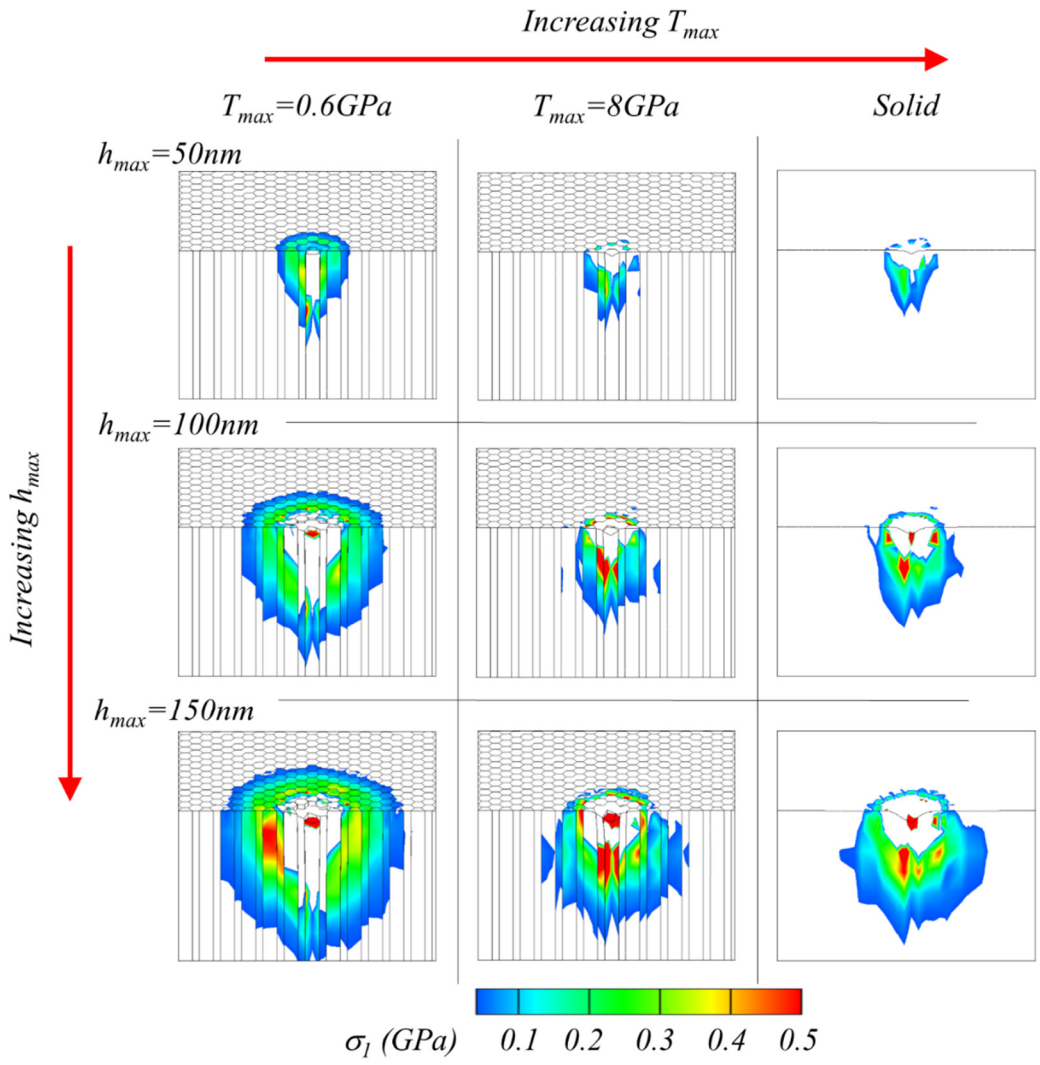

Figure 4-11 Map of the variation of the maximum principal stresses against T_{max} and h_{max}.

4.4.4 Determination of the strength of the magnetite

The analysis presented in this section accounts for the damage mitigation mechanisms of the magnetite rods. To calculate the strength of the monolithic material that compose the rods and to understand the limitations of our model, a probability of failure

of the solid based in a Weibull [77] distribution is employed. While there is a plethora of work associated with the magnetite in the literature [111]–[113], knowledge of the tensile strength of the magnetite is limited. Taking into account the failure of an element in a solid of a given volume (V), Weibull [77] proposed an analysis (equation 4.8) of the probability of failure (P_f). Even though the FEM considers the plastic deformation typical of ductile materials, the calculation of P_f takes into account the worst scenario in which the material shows a distribution of defects typical of brittle materials [114], [115]. In the approach considered in this study, the possibility of plastic deformation observed in nanoscale rods is not considered, like necking observed in the aragonitic tablets of the conch shell [116] and metals [117].

$$P_f = 1 - \exp[-V/V_o(\sigma/\sigma_o)^m] \tag{4.8}$$

In the statistical analysis, the exponential function of P_f is a function of the stress (σ), an scale parameter (σ_o), the shape of the distribution (m) and a reference volume (V_o) [115]. We first carry out indentation tests at different values of h_{max} to understand the probability of failure of the monolithic magnetite. Figure 4-12a shows the mean of the load displacement curves carried out at values of h_{max} from 50nm to 300nm, where 9 indentation curves where obtained at each h_{max}. The inset on Figure 4-12a shows the experimental and the mean values, where the error bars correspond to the standard deviation at h_{max} = 200nm.

Detailed examination of the SEM images of indentation marks revealed that the onset of material removal coincides with a change of the slope in the loading data at approximately h_{max} = 100 nm (Figure 4-12a). This is in agreement with previous

indentation work done on single crystals, where the change in slope of the indentation load vs displacement curve has been correlated with an increase of the material in contact with the indenter due to chipping and material removal [43]. The analyses of the images indicate that the material does not exhibit cracks for $h_{max} \leq 50$ nm in any of the samples that were tested. As such the probability of failure is zero (which yields a value of $P_f = 0.0$). However, for larger values of h_{max} the material begins to show cracking in some samples. For instance, at a $h_{max} = 100$ nm, there were 4 out of 9 samples revealing material removal (which yields a value of $P_f = 0.44$). Finally, 100% of the samples tested at $h_{max} = 150$ nm displayed chipping indicating that the probability of failure is 1 ($P_f = 1$).

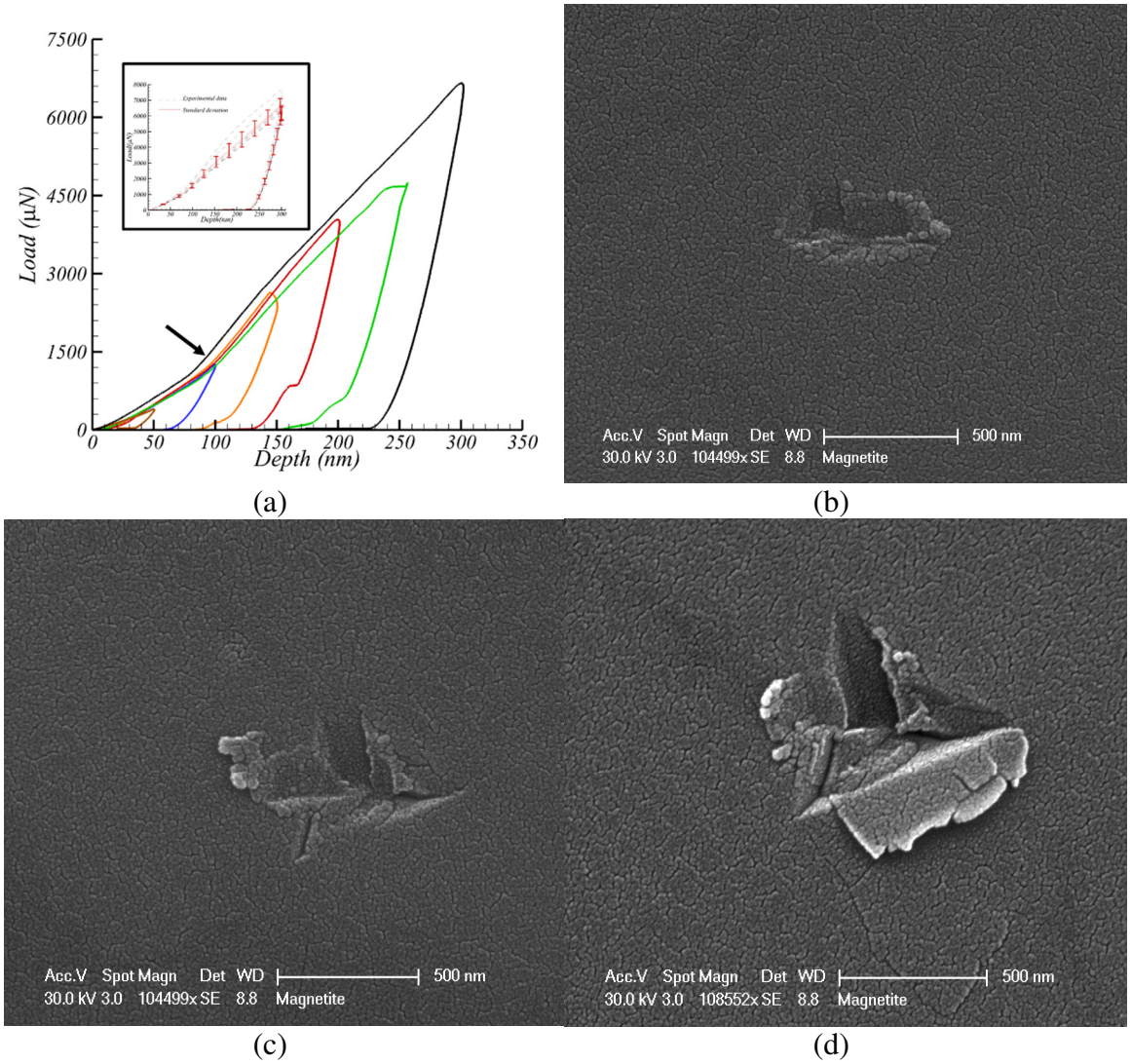

Figure 4-12 Standard deviation data of cube corner indentation tests in the monolithic material (a). SEM analysis at different penetrations suggest that the onset of fracture is around h_{max}=80nm (B) value that coincides with the pop-in event observed in (a). Greater surface damage is observed at h_{max}=150 nm (b) and h_{max} = 200 nm (c). The onset in (a) corresponds to the mean and standard deviation obtained with h_{max} = 200 nm.

4.4.5 Maximum principal stresses

To quantify the probability of failure of the rods in the simulations, the distribution of volumes versus σ_1 has been plotted for different values of T_{max} in Figure 4-13. Multi-axial heterogeneous stresses (tensile and compressive) are produced under the contact of the indenter in the material[41]. However, in brittle materials tensile stresses can cause the onset of lateral cracks which can evolve in chipping around the indenter [59], [110]. Under these considerations, we hypothesize that during indentation the tensile stresses are correlated to the fracture of the rods and later to the material removal around the cube corner indenter.

In the solid material, rods of different volumes and diameters are fracturing in mode I (see inset in Figure 4-13a). The values are plotted for the all the volumes associated with maximum principal stresses (σ_1) greater than 0.08 GPa. The volumes associated with values of σ_1 less than 0.08 GPa represent a 97% of the domain and are considered part of the bulk material. In fact the volume associated with values less than 0.08 GPa are blanked in Figure 4-11. To measure the error bars, simulations were performed with two different meshes. The analysis indicates that the volume associated with the principal stress distribution have a 19% of difference within the two meshes. The value of P_f was obtained from the indentation experiments and the value of σ_o is obtained by comparing the volume (V) of the elements with a $\sigma_1 > 0.08$ GPa with the numerical models:

$$V = -V_o \left(\frac{\sigma_o}{\sigma}\right)^m \ln\left(1 - P_f\right) \tag{4.9}$$

The Weibull modulus (m), defines the distribution around σ_o [118] and in brittle materials has a value between m = 3 and 10 [114]. A sensitivity analyses carried out in this study indicated that the value of m chosen (= 3 or 10) showed a 10% of difference in the estimation of σ_o. Therefore, in this study we considered a reference Weibull modulus for brittle materials of m = 5 [114]. The representative volume of a continuous domain (V_o = 0.005 μm^3) was determined at an h_{max} = 100 nm where the stresses are larger than $\sigma_1 \approx 0.1\sigma_y$. In indentation tests in solid materials, Lee et al. [50] found that when $\sigma_1 \approx 0.1\sigma_y$ the cracks propagate under LEFM conditions. In Figure 4-13a, the values indicated with the arrow in the shaded region correspond to those with V_o and a P_f = 0.44. The strength of the magnetite (σ_o) of 0.375 GPa is computed by comparing the volume of the Weibull distribution (Equation 4.9) with the FEM at an h_{max} = 100 nm, the P_f = 0.44 computed from the indentation tests in the magnetite and V_o. To understand the plot 12a, we can refer to an extreme case: In large volumes where the values of σ_1 are less than 0.08 GPa, the P_f have values lower than 0.1 %.

Compared to the solid material where rods of different diameter are taken into account, in the microstructure we considered set of rods of unique diameter with different volumes (see inset in Figure 4-13b). The comparison in Figure 4-13b, c and d includes the distribution of stresses in the rod-like microstructure. The simulations are compared with the volume associated at different values of P_f (0.1, 0.44, and 0.9). At low penetrations (h_{max}= 50 nm), the distribution of stresses associated with the different microstructures show values below the curve of P_f = 0.1 (Figure 4-13b). As the value of h_{max} increases to 100 nm and 150 nm, the stress distribution in the microstructures resemble the curve of P_f

= 0.9 (Figure 4-13c and d respectively). This coincides with the experimental observations that at h_{max}= 150 nm all the samples revealed material removal around the indentation marks. The simulations indicate that by increasing the strength of the interfaces the stress distribution resembles the solid material.

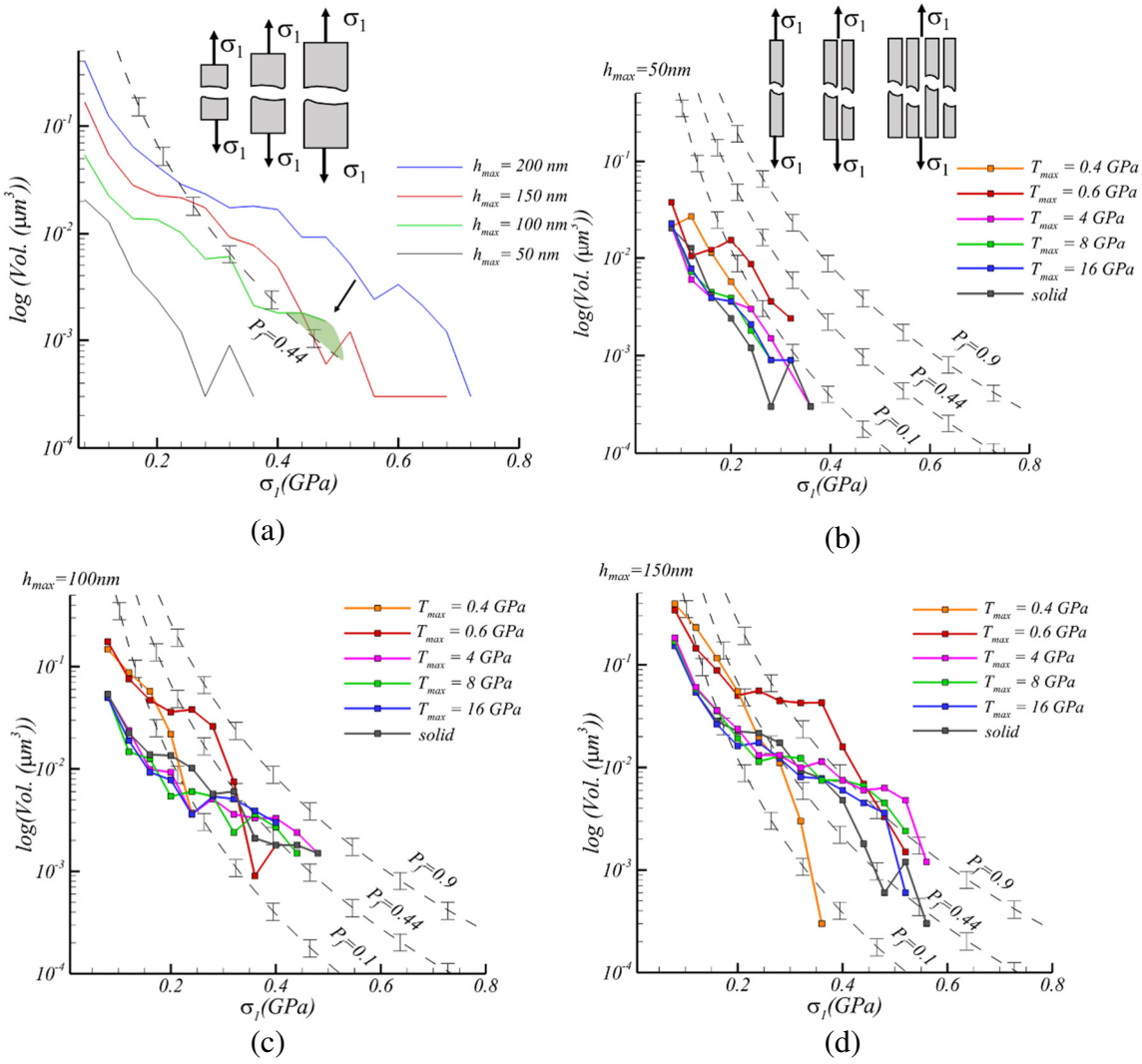

Figure 4-13 Comparison of the volume associated to the principal stresses at different h_{max}. The curves are compared in the solid (a), where equation 4.9 is plotted. The comparison also includes the rod-like microstructures at h_{max} = 50 nm (b), h_{max} = 100 nm (c) and h_{max} = 150 nm (d). Different values from T_{max} = 0.4 Gpa to 16 GPa were considered. The inset in (a) shows the fracture of rods of different diameters and in (b) the fracture of rod-like microstructures of unique diameter and different volume. The error bars show the standard deviation of 19% computed from different meshes.

4.4.6 Competing mechanisms

In this study the abrasion resistance of rod-like microstructure of the chiton is analyzed in terms of the competition between the energy dissipation through the interfaces and the inelastic deformation of the rods. In abrasive events with rough surfaces, particles in direct contact with the rod-like microstructure could lead to rod debonding and eventually to crack propagation in the entire microstructure [119]. In the models of indentation tests presented in this work it has been observed that an increase in the energy dissipation through the weak interfaces (Figure 4-9c) decreases the plastic energy dissipated in the rods (Figure 4-9b). This mechanism can be correlated to the outstanding abrasion resistance observed in the tooth[9], [10] as the energy dissipated through the interfaces decreases the slope of the loading data (see Table 4-1). The quantification of the abrasion resistance by indentation tests is widely used [10], [47], [48], [63]. The analytical solution of Johnson [45] estimates the critical load of inelastic deformation ($P_y \approx R^2H^3/E_r^2$) as a function of the radius of the indenter (R) and indentation modulus. A direct correlation between the separation of the loading data (P_y) of the biocomposite and the idealized elastic response [10], where P_y is load that indicates the onset of plastic deformation has been suggested by Johnson ($\alpha\ H^3/E_r^2$ [45]). As the confidence of this expression could affected by the crack propagation in the microstructure, a computational model must be considered. To understand the correlation between the competition between energy dissipation in the interfaces, in the rods and c_1 we analyze the probability of survival of the magnetite rods (equation 4.10).

$$P_s = 1 - \max(P_f) \tag{4.10}$$

The values of P_s are interpreted as the probability of the rods to avoid fracture that could later degenerate in chipping, where P_s = 1 represents a solid material that remains intact from catastrophic failure and P_s = 0 denotes that there is a high probability that rod failure may lead to catastrophic failure and subsequently material removal. A plot of c_1 and P_s with respect to T_{max} and G_c is presented in Figure 4-14a. The values of c_1 obtained from the numerical models have been best fitted with the loading data and have a correlation coefficient of R^2 = 0.62. The comparison of Figure 4-14a includes the values of c_1 from the *LE*, *TE* and the monolithic magnetite at h_{max} = 100 nm (see Table 4-1). While a logarithmic growth from c_1 in Figure 4-14a and exponential decay characterizes the P_s for different T_{max}. It is observed in Figure 4-14a that T_{max}, which we hypothesize represents the number of crystal bridges between rods, controls c_1 and P_s. In weak interfaces (T_{max} = 0.6 GPa), the values of P_s show a value of 0.4 that coincides with more spread of damage (Figure 4-10). However, with higher values of P_s, the resistance to penetration to the indenter is much lower as those of the mineralized material. This is not an ideal case, as c_1 is correlated with the hardness and stiffness of the microstructures (see Table 4-1) and low values of c_1 would lead to more compliant and soft materials. At stronger interfaces, higher values of c_1 are observed to the extent of more fracture of the rods (lower values of P_s) which is evaded in wear resistant materials.

A tradeoff between c_1 of the indenter and P_s is observed in *LE* and *TE*. Although the monolithic material reveals a higher c_1 than the leading edge, the excess of material

removal leads to a poor abrasive resistant material. The comparison of Figure 4-14a includes range of values of G_c that are between those measured in nacre (25, 70 and 150 J/m^2)[105]. The cohesive energy can interpreted as the elastic energy in the rods and organic material. The results indicate that G_c as compared to T_{max} has a lower influence in c_1 and P_s. The *critical* values of T_{max} observed in Figure 13a from the intersection of the values of c_1 and P_s are plotted in Figure 4-14b. These results suggest that for the different values G_c, the critical $T_{max\_cv} = 0.5 \pm 0.08$ GPa is characterized with a $P_{s\_cv} = 0.35 \pm 0.01$. As such, the critical values plotted in Figure 4-14b are between those observed in *LE* and *TE* (Figure 4-14a), results that suggest that the microstructure of the chiton tooth is optimized to improve the probability of chipping without sacrificing the stiffness of the material.

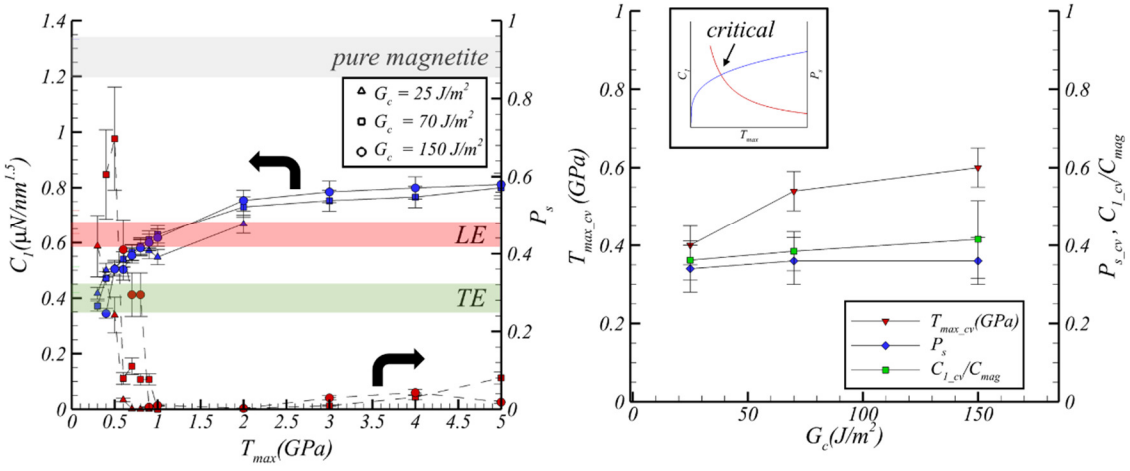

Figure 4-14 A competing mechanism between the failure of the rods and resistance to penetration of the indenter is visualized in (a). The optimum values of T_{max} are displayed in (b). The intersection between the data points shown in (a) determine the optimum values in (b).

4.5 Conclusions

The wear resistance associated with the rod-like microstructure of the chiton tooth and the monolithic material have been studied. To understand the energy dissipation of the microstructure in contact with a cube corner indenter, a comprehensive analysis of an indentation test has been carried out. The continuum framework considers energy dissipation through the rods and interfaces, where the onset of fracture in the mineral has been determined with a probability function. Three dimensional maps indicate the variability of damage and localization associated with the strength of the interfaces. Comparing the values of the loading stiffness at the leading and trailing edge of the tooth, the results indicate that a competing mechanism between energy dissipation in the rods and interface material is responsible for the abrasion resistance of the rod-like microstructure. While the localization of damage in stronger interfaces would lead to a higher resistance to penetration, it would also increase the probability of failure of the rods. In contrast, the weaker interfaces allow a higher probability of survival at the expense of more fragmentation and spread of damage in the interfaces. The computational models also addressed the influence of T_{max} and G_c, where the strength of the interfaces control the resistance to penetration of the microstructure. As observed in this study, understanding the competing mechanisms associated to these microstructures will aim to set design guidelines of new abrasion resistant materials. Future work is being directed towards the role of the fracture modes in the organic material.

CHAPTER 5. STRESS AND DAMAGE MITIGATION FROM ORIENTED NANOSTRUCTURES WITHIN THE RADULAR TEETH

The objective of this chapter is to explore the features of the ultrastructure (rod morphology and asperities) and site specific properties in different sections of the tooth. The modelling section of this chapter is oriented to answer questions about the optimal rod orientation in the tooth, and the influence of the rod diameter in the slope of the indentation data.

5.1 Core-shell architecture and rod-like microstructure

This analysis was necessary to understand the alignment of rods, the formation of the crystallites and morphology of the microstructure. The SEM images of this figure were taken in UC Riverside [67]. To assess the effects of nano- and microstructural features of both local and global properties of functional teeth, fractured specimens from fully mineralized teeth were prepared. Analysis of a longitudinally fractured surface within the interior of the middle cusp of the tooth reveals a core-shell structure (Figure 5-1A). A closer observation of the leading edge of the shell region uncovered ≈ 150 nm diameter nanorods which are aligned parallel to the long axis of the tooth (Figure 5-1B). In contrast, the core region does not appear to have any specific orientation (Figure 5-1C). Examination of the fracture at the apex of the middle cusp (Figure 5-1D) demonstrates that nanorods from the

leading edge of the tooth extend parallel to the surface of the tooth, effectively wrapping the entire shell structure. A latitudinal fracture close to the tip of the middle cusp of the tooth (Figure 5-1E, F) demonstrates that the nanorods follow the contour of the tooth, aligning parallel to its surface (highlighted with the yellow dashed lines in Figure 5-1A, D, and F). This alignment of nearly hexagonally close-packed nanorods can clearly be observed in a latitudinal section near the leading edge of the tooth (Figure 5-1G). In addition, the fractured surfaces of these rods (Figure 5-1G) appear conchoidal. This can be explained through examination of the tooth mineralization process. An SEM micrograph of a partially mineralized tooth (Figure 5-1H) shows the formation of large crystallites guided by organic fibers. The cores of these crystallites are single crystalline and multifaceted in nature [19]. Examination of fractured rods show features matching this morphology, with rods exhibiting smooth, and occasionally bipyramidal faceted fractures (circle in Figure 5-1G).

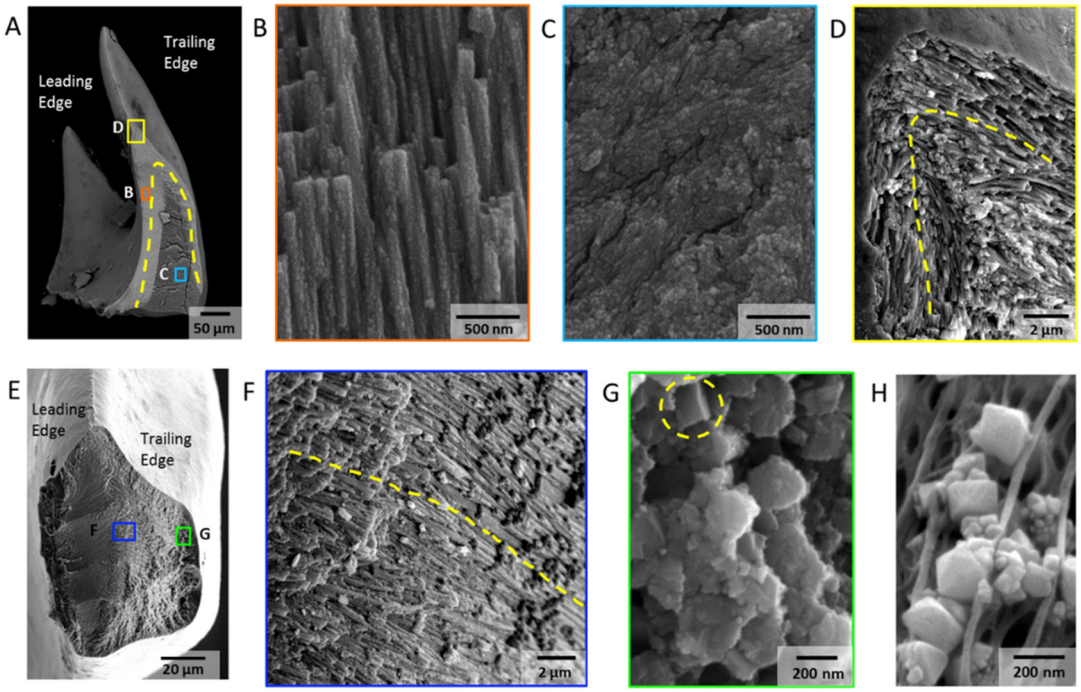

Figure 5-1 Core-shell architecture and local microstructural features of mineralized teeth. (A) BSE overview of a longitudinal fracture, highlighting a heavily mineralized outer shell and organic rich core; (B) Aligned and staggered nanorods in the leading edge of the shell; (C) Amorphous core region; (D) Apex of longitudinal fracture, revealing nanorod orientation and continuity around the shell of the tooth; (E) Latitudinal fracture near the tip of the tooth; (F) Center of the latitudinal fracture, demonstrating curvature of nanorods following the contour of the tooth; (G) Latitudinal fracture within the shell region, highlighting highly oriented nature of nanorods; (H) Micrograph of partially mineralized tooth showing mineral formation along alpha-chitin fibrils.

5.2 Micromechanical analysis

High-resolution nanoindentation was performed to ascertain the regional hardness and modulus of the chiton tooth. The information of the nanoindentation presented in this section was vital to characterize and compare the computational models. The nanoindentation tests reported in this section were made at UC Riverside [67].

Indents were performed on both latitudinal (Figure 5-2A, B, C) and longitudinal (Figure 5-2D, E, F) polished sections through the middle cusp of the tooth. The analysis plane was chosen such that the core of the tooth was exposed, to reveal the mechanical properties of the leading and trailing edges of the magnetite shell, as well as those of the iron phosphate core. Modulus (Figure 5-2B, E) and hardness (Figure 5-2C, F) maps of latitudinal and longitudinal sections of the tooth reveal that the stiffest and hardest portion of the tooth is at the mid-point of the leading edge. In this region, the highest reported values of modulus and hardness were obtained (E_r = 130.8 ± 7.3 GPa and H = 10.2 ± 1.3 GPa in the latitudinal section, and E_r = 128.5 ± 5.0 GPa and H = 10.4 ± 0.8 GPa in the longitudinal section). Average values for modulus and hardness on the trailing edge were E_r = 114.9 ± 8.2 GPa and H = 8.2 ± 1.0 GPa in the latitudinal section, and E_r = 97.6 ± 11.3 GPa and H = 7.5 ± 1.4 GPa in the longitudinal section. The core region shows a notable reduction in modulus and hardness (E_r = 28.6 ± 7.7 GPa and H = 1.5 ± 0.8 GPa in the latitudinal section, and E_r = 29.4 ± 9.1 GPa and H = 1.6 ± 0.5 GPa in the longitudinal section). In both latitudinal and longitudinal sections, there is a decrease in the modulus and hardness of the shell moving from the edges toward the core region.

On the leading edge of the longitudinal sample, a thin region with a reduced hardness and modulus is observed at the outermost edge. This reduction in mechanical properties is attributed to a crack through the tooth running parallel to the leading edge in the longitudinal section (Figure 5-2G). This crack traverses the entire leading edge, and is located 4.4 ± 2.0 μm into the tooth. Cracking was also observed between the hard shell of the tooth and the soft core (Figure 5-2H), with BSEM revealing that some of the magnetite shell remains attached to the core material following fracture.

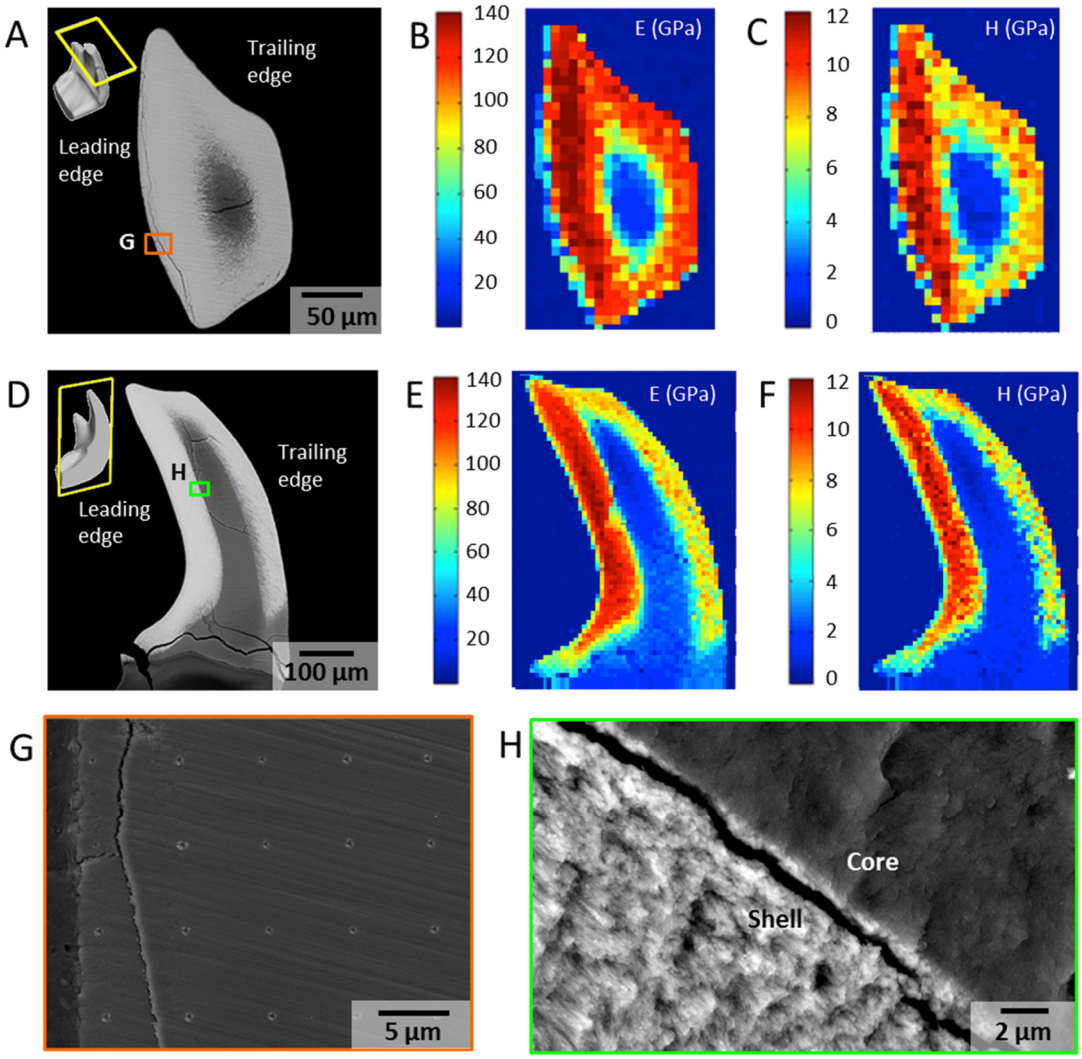

Figure 5-2 Nanomechanics of core and shell regions of a fully mineralized tooth in latitudinal and longitudinal sections. (A) BSE micrograph of a latitudinal polished section showing the core-shell structure of the tooth; (B) Modulus and (C) Hardness maps from nanoindentation of a latitudinal section; (D) BSE micrograph of a longitudinal polished section of the entire tooth, highlighting the thickness of leading and trailing edges as well as extent of core region throughout tooth; (E) Modulus and (F) Hardness maps from nanoindentation of the longitudinal section, demonstrating a clear interface between core and shell as well as a gradient from leading edge to trailing edge of the tooth; (G) SEM micrograph of the leading edge of the longitudinal section after indentation, highlighting a crack running parallel to the edge of the sample; (H) BSE micrograph revealing cracking at the core-shell interface of the tooth.

5.3 Surface analysis

A surface analysis was necessary to quantify the diameter of the rods at the leading and trailing edge of the tooth. The surface analysis presented in this section was performed in UC Riverside [67]. During rasping events, the surfaces of the radular teeth are placed in contact with rocky substrates. Thus, in order to interpret the role of microstructures within these surfaces, examination of longitudinally fractured fully mineralized teeth was performed. Upon close observation of the leading edge (Figure 5-3A), several interesting features are revealed. The outermost ≈ 2 μm of the tooth consists of a dense packing of sub-100 nm particles. This dense nanoparticulate region transitions to nanorods, which abruptly (within 1 μm) undergo a 90° rotation that aligns them with the long axis of the tooth. Examination of the trailing edge of the tooth (Figure 5-3B) reveals a thinner (approximately 1 μm) dense nanoparticulate layer that abruptly transitions to nanorods, which are oriented parallel to the tooth surface. Unlike the leading edge, no rotation of nanorods is observed on the trailing edge. The sizes of the rods at the leading and trailing edges were determined through image analysis of SEM micrographs. Rods at the leading edge measured 193 ± 23 nm in diameter (Figure 5-3C), while rods at the trailing edge measured 250 ± 27 nm (Figure 5-3D). It is also observed in Figure 5-3A and B, the difficulty to identify the length of the rods.

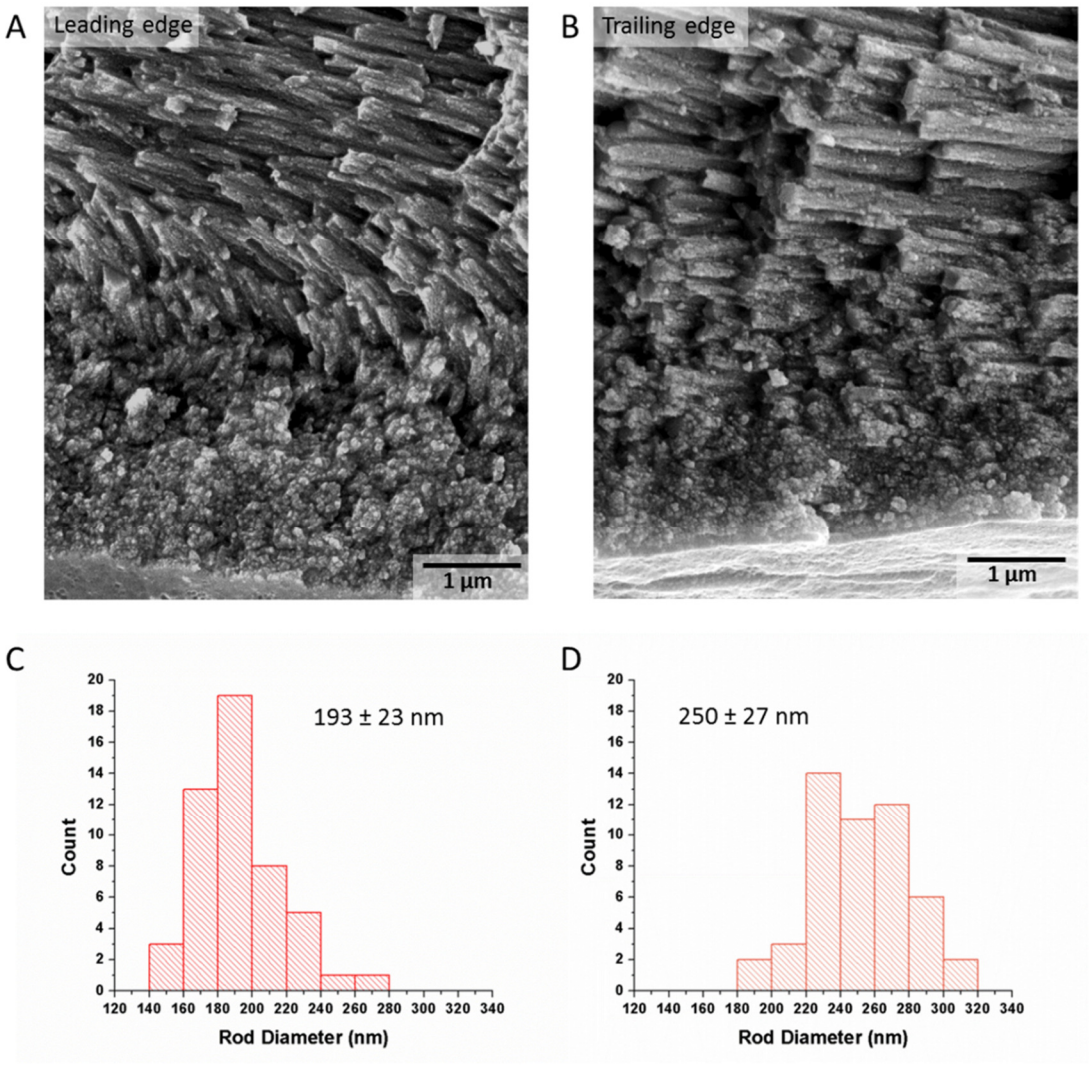

Figure 5-3 Surface analysis of the leading and trailing edges of the fully mineralized tooth. Longitudinal fracture surface of (A) the leading edge, highlighting a 2 µm thick dense nanoparticulate layer, transitioning to nanorods (observed perpendicular to the field of view), which rotate 90° over a region of ≈ 1 µm to orient parallel to the tooth surface; Longitudinal fracture surface of (B) the trailing edge, revealing a 1 µm thick dense nanoparticulate layer that abruptly transitions to nanorods oriented parallel to the tooth surface (no rod rotation observed); (C) Histogram of rod diameters on the leading edge; (D) Histogram of rod diameters on the trailing edge.

5.4 Modeling

Details of the geometry, ultrastructure and mechanical properties of the chiton tooth were employed to develop three-dimensional finite element models (FEM). A three-dimensional representation of the tooth was obtained using confocal fluorescence microscopy and subsequently digitized to obtain the CAD geometry (Figure 5-4A). The shape of the tooth was reconstructed by confocal microscopy at the Purdue University Multi-Scale Imaging Center of the Bindley Bioscience Center at Purdue University. A single tooth, connected to a small portion of the stalk, was removed manually from the anterior-most region of a radula following dehydration. The tooth was air dried and then immersed in the mixture of oil and fluorescent dye (DiI) between two thin glass slices. The prepared "sandwich" was examined from each side under confocal microscopy with a 10X objective lens and 5μm steps to obtain surface information. ImageJ, Amira5.3.0 and Catia v5 were used to combine the front and back surface data to generate the geometry of a full tooth. The model was divided into four isotropic mechanically distinct regions. Each region is modeled with a linear elastic model with different values of Young's modulus obtained directly from the nanoindentation experiments: (i) the tooth base (primarily consisting of alpha-chitin) (E = 7 GPa), (ii) an iron phosphate core region (E = 35 GPa), (iii) the leading edge (E = 130 GPa) and (iv) the trailing edge of the magnetite shell (E = 105 GPa). A 0.1 N point force was applied at the tip of the tooth to simulate the working condition of the rasping of radular teeth. The four parts and their associations are shown in Figure 5-4B. The mesh and boundary conditions for the model are presented in Figure 5-4C. The stress distribution in the tooth during a rasping event was revealed by the finite element model.

Figure 5-4D shows the distribution of the principal stresses inside the tooth. The maximum tensile stresses (Figure 5-4D, red) are mainly distributed along the leading edge of the tooth and are parallel to the surface of the leading edge. On the other hand, the maximum compressive stresses (Figure 5-4D, blue) are concentrated along the trailing edge and are parallel to the surface of the trailing edge. The lines connecting the principal directions form the tensile and compressive trajectories. These principal directions are not altered by the gradual wearing of the tooth (Figure 5-4D), proving the abrasion tolerance through the life of the tooth. At the transition zone between the leading and trailing edges, the direction of the stresses rotates gradually as shown by the dashed lines in Figure 5-4E. This rotation of stresses is aligned with the rotation of rods observed in the transition zone above the core region (Figure 5-1D). Strain maps are presented in Figure 5-5.

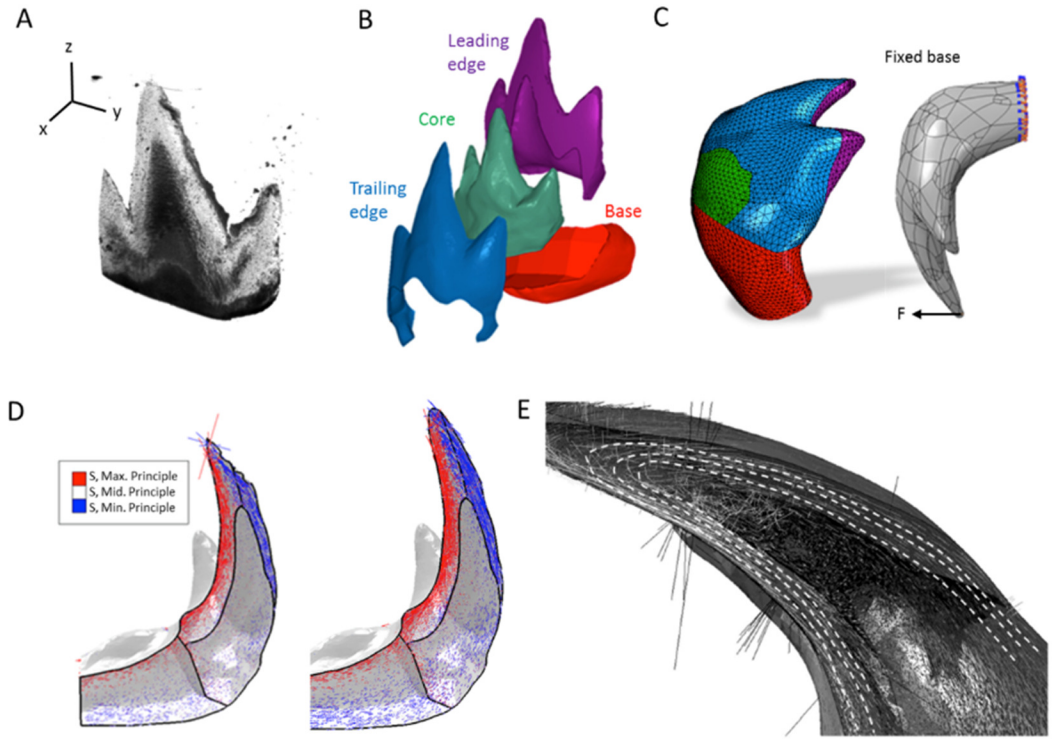

Figure 5-4 Finite element models of a fully mineralized tooth. (A) Digitization of tooth geometry; (B) The four individual components used to create the model and the association of each part into the full model; (C) Mesh and boundary conditions; (D) Direction of tensile (red) and compressive (blue) stresses in a worn (left) and fresh (right) tooth; (E) Rotation in the direction of stresses at the transition zone between the leading and trailing edges above the core.

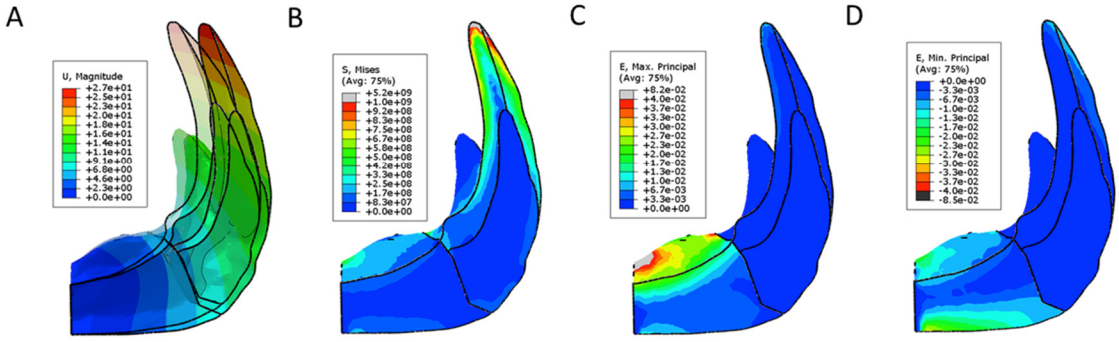

Figure 5-5 Displacement magnitude in micrometers showing initial and deformed position of the tooth at a load of 0.1N (A); contour of von Mises stress distribution in Pa (B); maximum and minimum principal strains showing regions with tensile deformations in the leading edge (C) and compressive strains in the trailing edge (D).

At the microscale, a micromechanical model of uniform hexagonal rods that incorporates an inelastic model for the individual rods and a cohesive model that mimics the organic material was developed under a continuum finite element framework. As a rod diameter distribution has been identified, hexagonal rods of 150 nm and 250 nm were modeled (Figure 5-6A, B) with the elastic-plastic properties of single crystal magnetite. The yield stress of single crystal magnetite (σ_{yield} = 3.5 GPa) was obtained with the contact formulation presented by Johnson [82] and the hardening parameter was obtained by comparing the load versus displacement curves of computational models with experimental nanoindentation data of monolithic magnetite performed by Chicot et al. [120]. Since it was also shown that the mechanical properties of the pure magnetite do not show any dependence on the crystallographic orientation, the FEM model considers homogenous and isotropic elastic-plastic properties in the rod-like microstructure of the tooth. The interface between the rods is modeled with a cohesive zone model with a bilinear traction-separation law. The interface between the rods is modeled with a cohesive zone model with a bilinear traction-separation law [53]. The traction takes into account a high initial strength (T_{max} = 1.5 GPa) to mimic the nanoscale features that prevent initial decohesion (e.g., mineral bridges and nanoasperities). The maximum displacement of the traction-separation law is defined as 200nm which is similar to those used for the organic material between nacre tablets[64]. As such the fracture energy or work of separation is defined as G_c = 150 J/m^2. A cube corner indenter geometry was modeled as a rigid frictionless surface. Indentation curves show that despite the difference observed in the experimental data, the FEM indicates that at a penetration of ≈ 160 nm the total energy volume dissipated at the interfaces of the smaller rods (E_{dis} = 0.1225 nJ) is greater than those with a larger rod cross

section (E_{dis} = 0.0062 nJ) (Figure 5-6C). High-load nanoindentation was used to produce cracks in a latitudinal polished section (Figure 5-6D). Following indentation, the sample was sonicated in acetone to remove debris along with a surface layer of organic, revealing the mineralized rod structure. SEM imaging of this sample highlights that cracks do not progress radially from the corner of the indent, as is observed in monolithic materials[121], but rather propagate around and between the mineralized rods in the organic-rich regions of the tooth (Figure 5-6E). The patterns of crack propagation are consistent with model results, where small radial cracks of the size of an element are observed in the edges and material removal is shown surrounding the planes of the sharp indenter (Figure 5-6F).

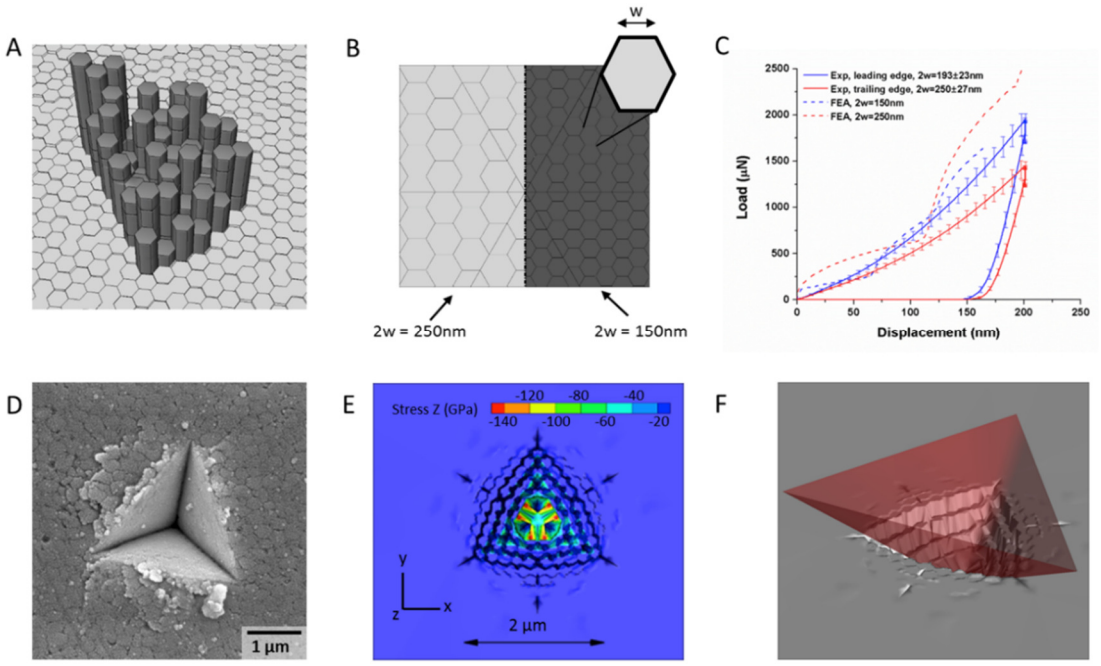

Figure 5-6 Pile up of staggered hexagonal rods idealized for illustration purposes to show the ultrastructure of the tooth; (B) Rod cross sections assumed in the FEM for the trailing edge (250 nm) and leading edge (150 nm); (C) Indentation data of experimental curves at the leading and trailing edge compared with the elastic-plastic FEM; (D) Indentation mark at the leading edge of the tooth with rods aligned orthogonal to the surface; (E) Comparison of stress contours in the same direction of indentation for an elastic model at maximum penetration (≈ 700 nm) showing material removal and crack propagation; (F) Cube corner indenter placed above the model showing material removal and small radial cracks.

5.5 Summary

Previous finite element simulations have shown that the curvature of the tooth leads to a redistribution of stresses to the base of the tooth, with the elimination of curvature resulting in stress concentrations at the tip of the tooth, where the structure is weak [69]. The hardness of the shell stems from mineralization by the hardest reported biomineral, magnetite [9]. This hard shell and soft core leads to crack deflection at the core-shell interface [9], [10]. When a crack approaches an interface, it is propagated through, deflected, or arrested, depending on the relative stiffness of the materials on either side of the interface [122]–[125]. With a large modulus mismatch between the shell and core of the chiton tooth, crack deflection occurs (Figure 5-2H). This toughening mechanism has been reported in other biological composites, where deflection of cracks at an interface prevent catastrophic failure of the structure during repetitive loading [123]. Following cracking, a portion of the magnetite shell remains attached to the core (Figure 5-2H). This is consistent with previous studies, which have shown that the core-shell interface is rough, with interlocking between the two phases [126]. This interconnected interface results in tortuous paths for crack propagation, leading to significant energy dissipation. The graded nature of the interface between the core and shell can be seen in modulus and hardness maps (Figure 5-2).

The magnetite shell of the chiton tooth consists of mineralized rods aligned parallel to the tooth surface. This architecture is reminiscent of a fiber reinforced composite, a design which is anisotropic, with high strength along the long axis of the fibers [127]. In the chiton tooth, as revealed by finite element simulations, the long axis of the mineralized

rods is oriented in the direction of principle stresses at all stages of wear, providing increased strength (see Figures 5.1A and 5.4E). Additionally, there are differences in the loading as well as the architectures of the rods between the leading and trailing edges of the tooth. The three-dimensional finite element analysis, which is in good agreement with previous works done in 2D [69] reveals a concentration of tensile stresses at the leading edge and compressive stresses at the trailing edge.

SEM analysis (Figure 5-3) reveals that rods on the leading edge have a smaller diameter than those on the trailing edge (193 ± 23 nm on the leading edge vs. 250 ± 27 nm on the trailing edge). While rod diameter varies with tooth size as well as location, the trend of smaller diameter rods on the leading edge is consistent with previous observations [19]. In fiber reinforced composites, smaller diameter fibers are preferred for tensile loading [127] as they have fewer flaws, making them less brittle and therefore stronger in tension [127], [128]. Thin fibers also have more flexibility, providing resistance to fracture during bending [127]. While unidirectional fibers perform well in tension, they are generally poor in compression. Composite longitudinal compressive strength, however, has been shown to correlate positively with fiber diameter [128], [129]. These factors indicate that the larger diameter rods observed on the trailing edge of the tooth are optimized to withstand the compressive loading concentrated in this region. Finally, finite element simulations reveal a rotation of principle stresses at the transition zone between the leading and the trailing edges. These stresses are again parallel to the long axis of the rods, as shown in the rotation of rods around the core of the tooth (Figure 5-4D).

In chiton teeth, the maximum stresses in the tooth are oriented parallel to the tooth surface. A crack initiating or propagating along the direction of principle stress would thus see the fibers at the edge of the tooth in a transverse orientation. Studies on fiber-reinforced composites have shown that initiation toughness increases by 26% when the crack propagation direction is transverse to the fibers (rather than parallel to them), and that fracture toughness increases with a rotation in fiber orientation angle [130]. As shown in Figure 5-2G, cracks are arrested at the outer region of the leading edge (≈ 4.4 μm into the tooth), where rod rotation occurs, and are prevented from propagating into the bulk of the tooth. Preceding rod rotation on the leading edge of the tooth is a layer of magnetite particles. These particles, also found at the trailing edge, provide a barrier to material loss in early stages of tooth use, and are reminiscent of cellular structures formed at the surface of bulk materials where accommodation of large sliding strains is required [131].

Nanoindentation maps (Figure 5-2) corroborate results from previous investigations,[9], [69] highlighting the difference in hardness between the leading and trailing edges of the tooth, a design which results in a self-sharpening condition [69]. In blunt contacts, a high ratio of hardness to modulus (H^3/E^2) is associated with an increase in abrasion resistance [9], [10], [132]. With its unique hardness to modulus ratio, the chiton tooth outperforms geologic magnetite in terms of abrasion resistance [9], [10]. Incorporation of the organic phase into the tooth also influences crack propagation. Through high-load nanoindentation, cracks were introduced into a latitudinal section of a chiton tooth (Figure 5-6D). Examination of the sample following indentation revealed that cracks propagate around the mineralized rods through the organic. This creates a tortuous crack pathway at the nanoscale, as corroborated in the micromechanical model, where the

intricate microstructural alignment impedes crack propagation in the bulk, localizing the damage in the area surrounding the sharp geometry of the cube corner tip. At early stages of tooth mineralization, large multifaceted magnetite crystals are observed forming along organic fibers (Figure 5-1H). A crack deviating from the organic phase into a mineralized rod will thus encounter another toughening mechanism, in the form of additional interfaces induced from crystal faceting (Figure 5-1G). A crack traveling along the boundary between two adjacent magnetite crystals will be redirected along the contours of the crystal surface, resulting in energy dissipation.

5.6 Conclusions

The design of abrasion resistant materials is a difficult task, as abrasion resistance is not an intrinsic material property, but dependent on a range of factors [133]–[135]. Rather than taking a trial and error approach to material design, however, engineers can draw inspiration from natural composites, which have evolved over millions of years. The chiton radular tooth is a complex hierarchically arranged composite, optimized to resist abrasive wear. Features of the tooth from the nano- to macroscale provide strength, abrasion resistance and toughness. The curvature of the tooth leads to a redistribution of stress concentrations away from the fragile tooth tip. A core-shell structure leads to crack deflection at the interface, preventing catastrophic failure. Rod orientation and diameter at various positions within the tooth provide strength optimized for specific loading conditions. Selective mineralization leads to a hardness gradient between the leading and trailing edges of the tooth, resulting in a self-sharpening condition, while incorporation of an organic phase results in a complex pattern of crack propagation. At the nanoscale, surface nanoasperities provide resistance to interfacial sliding between nanorods, and mineral bridges increase toughness.

CHAPTER 6. UNVEILING WITH BIOMIMETIC DESIGNS THE RESISTANCE TO PENETRATION OF THE RADULAR TEETH OF THE CRYPTOCHITON STELLERI

6.1 Introduction

After gaining insights of the geometrical features of the tooth in chapter 5, it was examined the influence of the aspect ratio and rod orientation, on the damage mechanisms observed during indentation of rod-like microstructures. Nanoindentation studies presented in chapter 5 of rods aligned parallel to the indenter tip [67] demonstrated that the highest Young's modulus (E_r) and hardness (H) occur in the leading edge of the tooth, the region that coincides with a smaller rod diameter (Figure 6-1). Figure 6-1 suggests that a decrease in the rod diameter between the leading and trailing edges of the teeth coincides with a 30% of increase in E_r and a 40% in H respectively. In chapter 5, it was demonstrated that even when more energy is dissipated at the interfaces of smaller rods, the mechanical response of the material to indentation is not significantly affected by the rod diameter [67]. While previous hierarchical models [93], [72] have addressed the influence of geometrical features in rod-like microstructures under tensile loads, questions remain regarding the effect of aspect ratio and rod alignment in the site-specific properties measured during indentation printing of bioinspired designs has gained considerable interest since its inception, primarily due the benefits of inexpensively building complex prototypes without

structural assembly. Some bioinspired applications include tissue engineering [136]–[138], drug delivery devices [139] and bone biocomposites and implants [140], [141]. Taking lessons learned from previous modeling and experimental work on the naturally-occurring nacre [64], [70], combinations of computational modeling and D printing were used to test some important hypotheses about the key morphological features of the microstructure of the nacre by conducting a rigorous parametric analysis to determine an optimal geometry and size scale of the microstructural building blocks that increase energy dissipation by more than 70 times [142], [143]. Mimicking the architectural designs of nanoscale aragonitic tablets surrounded by a much thinner organic layer, artificial nacre was created with brittle tablets of polymeric materials surrounded by a ductile interface [143]. Following experimental observations of nacre under uniaxial tensile stress [97], the 3D printed designs were able to provide insights into the effect of tablet waviness and interlocking in the energy dissipation mechanisms that act in the naturally occurring material.

The outline of this chapter is as follows: The biomimetic designs built for this study are first described in Section 6.2. The experimental methods and validation of procedures are discussed in Section 6.3. The experimental observations, property maps and material characterizations are discussed in Section 6.4. A FEM analysis of the experiments is presented in in Section 6.5 followed by a discussion of the relation between the aspect ratio of the rods and the damage mechanisms in Section 6.6. Finally, the conclusions are summarized in Section 6.7.

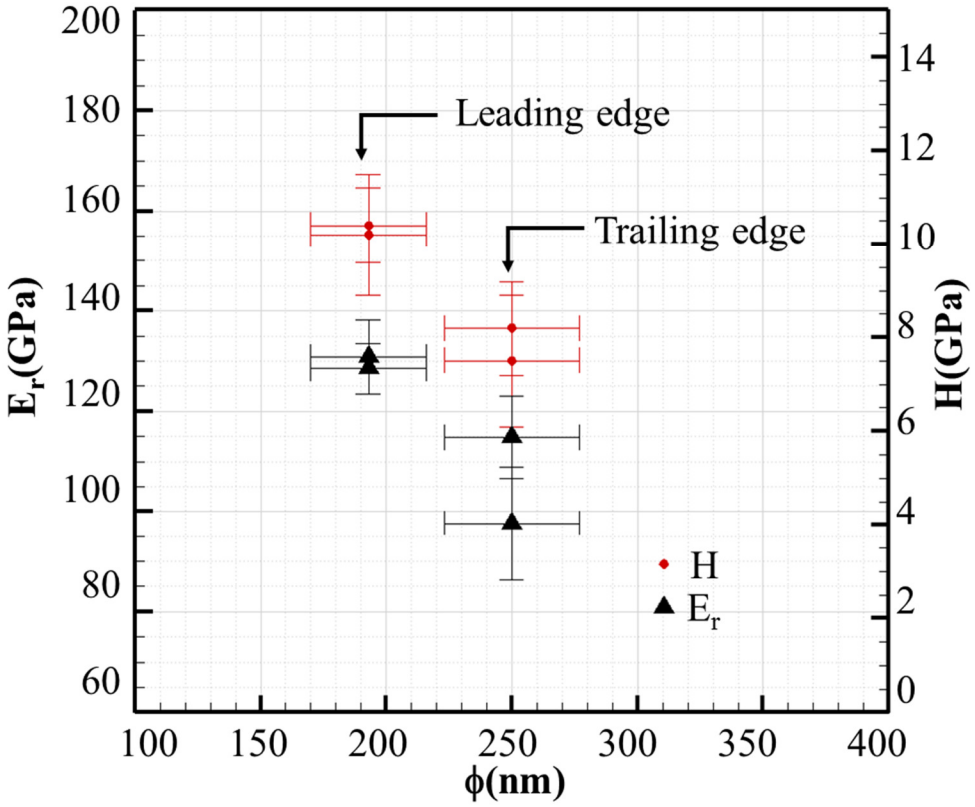

Figure 6-1 Experimental values of reduced modulus E_r and hardness, H, as a function of rod diameter (ϕ) measured from the leading and trailing edge of the mature tooth of the *Cryptochiton stelleri* [67].

6.2 Biomimetic composites

Using a biomimetic approach, an idealized rod-like microstructure was designed with a uniform pattern of hexagonal rods made of a stiff polymer surrounded by a soft and weak interfacial material. Such biomimetic composites are fabricated using a 3D printing technique and subsequently tested to study the effect of geometrical features (orientation, volume fraction and aspect ratio) on the overall mechanical response. Figure 6-2 shows the biomimetic composites in detail. I hypothesize that the particular geometry of the building

blocks and their arrangement contributes to the remarkable mechanical properties. It is worth mentioning that studying this idealized microstructure is the first step towards understanding the role of rods-like architectures in Nature.

The 3D printing process was carried out with an Object Eden 350V 3D printer, in which the primary material used for the rods is a rigid and semi-transparent polymer surrounded by a compliant elastomer. Details of the top and side of the 3D printed samples are shown in Figs.6.2B and C. The rods, which have a hexagonal cross section with sides *W* and a longitudinal length *L* are separated by a thin layer of thickness *t* of the interfacial material (shown in red in Fig. 6.2D).

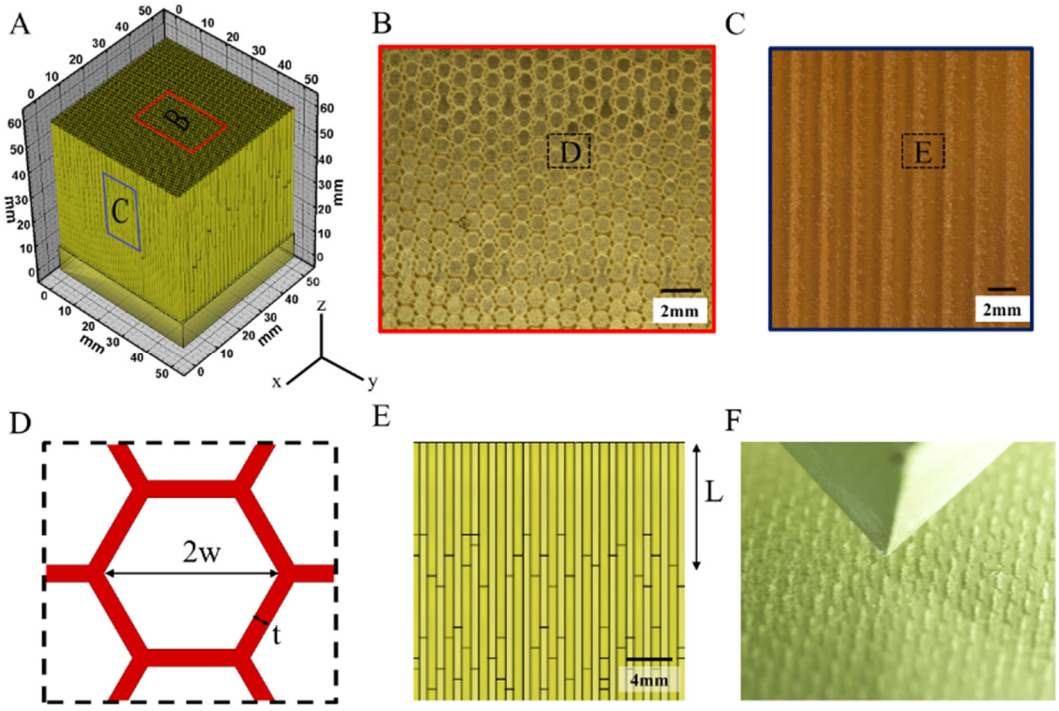

Figure 6-2 (A) Structural details of the idealized rod-like microstructure of the radular teeth. (B) Top and (C) side view with hexagonal cross sections and rods alignment. (D) Schematics and details of the design of the hexagonal rods with side length $W = 0.5$mm and interfacial material of thickness $t = 0.1$mm (E) side view showing staggered rods of variable length *L*. (E) Cube corner indenter placed above an intact sample (F).

Despite the advantages of the 3D printing technique, inaccuracies in resolution (e.g., approximately 20 to 85μm [144]) and material mixing can lead to material variability and distribution of defects (for example see [141]). In order to evaluate the printing resolution, biomimetic composites with different values of W and t were fabricated and analyzed at early stages of this study. These preliminary trials revealed that the hexagonal rods can be printed with W no less than 0.5 mm before the shape can no longer be accurately replicated by the printer. The same analysis yielded a minimum value of t = 0.1 mm before the rods begin to connect to each other. Given this values of W = 0.5mm and t = 0.1 for all our specimens, the value of L vary from 7 to 50 mm in the current study. As such, and assuming that $L >> t$ the volume fraction of interfacial material, V_{fs}, can be approximated as $V_{fs} = ((\sqrt{3}W + t)^2 - 3W^2)/(\sqrt{3}W + t)^2$.

While V_{fs} was kept constant at approximately 20%, the length, L, and therefore, the aspect ratios, $L/2W$, were varied. Following measurements done in similar biological materials (e.g., bone, nacre and enamel), the following range of aspect ratios $L/2W$ = 7, 10, 15, 25, 40, and 50)[145] are considered. As shown in Fig. 6.2E, the rods are staggered and the overlapping length is around 3mm. For comparison reasons, I also designed specimens with randomly oriented rods of 1mm of diameter ($L/2W$ = 15 and $V_{fs} \approx 20\%$).

6.3 Experimental setup and procedure

Once printed, these biomimetic composites are subsequently tested to study the effect of geometrical features (orientation, volume fraction and aspect ratio) on the overall mechanical response. Consistent with previous experimental data available from the literature on the chiton's tooth [9], [67], the mechanical response of our biomimetic composites under indentation was evaluated. Figure 6-2F shows the details of a rigid cube corner tip made of commercial aluminum with an indenter tip of 0.54 ± 0.19 mm and an effective angle of 35.3°. Cube corner indenters have the advantage of removing at least three times the amount of material for the same indentation depths as compared to other sharp indenters (e.g. Berkovich tips ≈ 65.3°) therefore enabling crack nucleation and propagation at lower loads [43], [94]. The indentation tests were performed at controlled environmental conditions in an electromechanical testing machine with a tension/compression load cell of 10 kN (MTS, Eden Prairie, MN, USA). Indentation tests were performed at a maximum penetration depth h_{max} = 6 mm in all the samples. An initial set of loading and unloading indentation experiments were performed at different loading rates. A final rate of 0.5 mm/min was found to be sufficiently slow to eliminate any time dependent effect from the viscoelastic behavior of the polymers and consider quasi-static conditions. The standard Oliver-Pharr method was used to obtain the effective E_r and H in this study (See Table 6-1) [28]. Prior to performing the indentation tests, the experimental procedure was validated with other materials of known modulus and good agreement was observed with literature values. To eliminate any aging effects observed in the polymers after a month, the mechanical tests were performed within 2 weeks of 3D printing. The

size of the specimens was also studied by varying the side of the cubic rod-like specimens from 16 to 50 mm. Our experimental results showed that convergent results of E_r and H were obtained for 33x33x33 mm or larger. As a results, all the tests reported in the present manuscript were obtained with 50x50x50 mm specimens. The maximum penetration followed the general rule of thumb that it should at least $1/10^{th}$ of the sample height [146].

Table 6-1 Experimental data obtained in indentation tests at a maximum depth of 6mm displaying volume fraction of interface material (Vf_s), orientation (OR), maximum load (P_{max}), reduced Young's modulus (E_r) and hardness (H).

L/2W	***Vf_s (%)***	***OR***	***P_{max}(N)***	***E_r (MPa)***	***H (MPa)***
7	21	∥	2565 ± 92	320.6 ± 15	31 ± 1
		⊥	2372 ± 74	296 ± 25	29 ± 1
10	21	∥	2648 ± 32	324 ± 27	33 ± 1
		⊥	2308 ± 111	307 ± 19	28 ± 1
15	21	∥	3030 ± 153	397 ± 25	37 ± 3
		⊥	2689 ± 40	386 ± 13	32 ± 1
25	21	∥	2737 ± 100	350 ± 23	34 ± 1
		⊥	2181 ± 95	309 ± 23	26 ± 1
40	21	∥	2618 ± 100	302 ± 13	33 ± 1
		⊥	2169 ± 90	280 ± 2	27 ± 1
50	21	∥	2465 ± 77	274 ± 29	32 ± 2
		⊥	1998 ± 57	258 ± 8	24 ± 1
Random 1	21	-	701 ± 200	132 ± 35	8 ± 3
Random 2	35	-	488 ± 143	116± 47	5± 2

6.4 Experimental results

6.4.1 Building blocks

Like many other naturally-occurring biomineralized materials, the rod-like architecture of the chiton tooth is comprised of stiff mineral building blocks (e.g. aragonite, hydroxyapatite and magnetite of $E \geq 85$GPa) and compliant organic constituents (e.g. collagen or α-chitin) [1], [2], [65]. Typically the elastic modulus and strength mismatch between these two components is several orders of magnitude, considering that the organic material is composed of both crystalline and amorphous components. To mimic this disparity in mechanical behavior, the rods are printed with a stiff polymer (RGD720), surrounded by a compliant and relatively weak elastomer (FullCure 705). To characterize the elastic modulus and hardness of these materials an independent set of indentation tests were carried out (See Table 6-2).

Table 6-2 Mechanical properties of the building blocks measured by independent set of tests.

	E_r **(MPa)**	H **(MPa)**
Rod (RGD720)	1954 ± 43	187 ± 7
Interface (FullCure 705)	0.97	0.37

To assess the interfacial fracture energy (G_c) of the interface material, I tested double cantilever specimens of the rod material, connected with a thin layer of interface material (Figure 6-3). The fracture toughness (G_c) of the interface material was quantified by 3D printing double cantilever beams of rod material with a thin interface layer between the beams. Also, the quantification of G_c is oriented to observe defects (e.g. rod-rod bridges) of the interface material generated during the 3D printing. These defects can generate strengthening of the G_c values or the propagation of fractures through the beams instead of the interfaces. The beams are 80 mm of length, 13 mm of width (b in equation 6.1), 3 mm of thickness (t in equation 6.1), with a pre-crack of 30mm and an interface of 0.1mm (Figure 6-3A). The tests were performed in a displacement control testing machine at controlled environmental conditions with a tension load cell of 100N and the same loading rate used in the indentation tests. The DCB tests shows a region of initial debonding, up to a displacement of 2 mm, and later interface degradation leading to failure at 11 mm. Following linear elastic fracture mechanics (*LEFM*), a comparison of the degradation region (between 2 mm and 11 mm) is made with respect equation 6.1 [33], showing values of G_c = 2-3.5J/m^2 (banded region in Figure 6-3B). In equation 6.1, E_r is the Young's modulus of the rods (table 6.2) and h is the opening displacement applied during the tests.

$$P \approx 0.44 \frac{\left(E_r b^4 {G_c}^3 t^3\right)^{\frac{1}{4}}}{h^{\frac{1}{2}}} \tag{6.1}$$

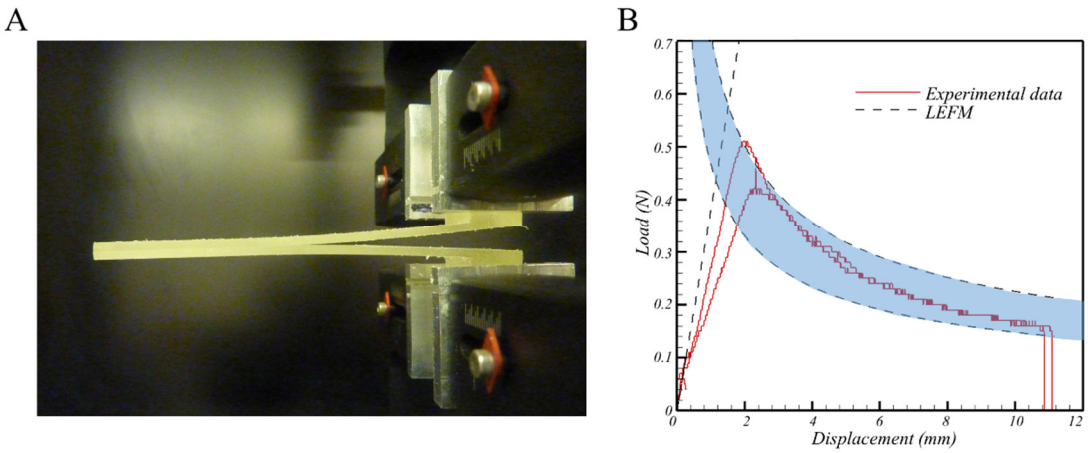

Figure 6-3 Double cantilever beams (DCB) manufactured to test the use of rapid prototypes in fracture mechanics problems, test were performed in an MTS machine of 0.1 kN-load cell. The total length of the beams was 80 mm, with a pre-crack of 30mm and an interface of 0.1 mm (same interface thickness used in our indentation studies). (A) Shows the DCB test in opening mode and (B) experimental and fitting curves under *LEFM* premises. Banded region in (B) is obtained from 6 for values of 2-3.5 J/m^2 of fracture energy.

6.4.2 Effect of spatial orientation

Similar to engineering composites (e.g., unidirectional fiber-reinforced composites) and biological materials (e.g. bones and wood), a geometrical alignment of the building blocks results in anisotropic mechanical behavior[1], [147]. To assess the anisotropy in our biomimetic composites, the specimens with the loading direction parallel and perpendicular to the longitudinal direction of the rods were indented. Figures 6.4A and B show the load versus displacement curves recorded during indentation of the different samples for the parallel and perpendicular configurations. Each line in these figures corresponds to the average of 4 independent tests done in similar samples, where the error bars denote the standard deviation. The results obtained revealed a maximum load, P_{max}

for most of the specimens tested in the parallel configuration (See inset in Fig. 6.4A). Figure 6-4C and D show the indentation mark for both set of experiments. Optical observations revealed that, in the parallel configuration (Fig. 6.4C), most of the energy is dissipated as median cracks in the interface material, while some crack propagation occurs parallel to the surface in the perpendicular configuration (Fig. 6.4D).

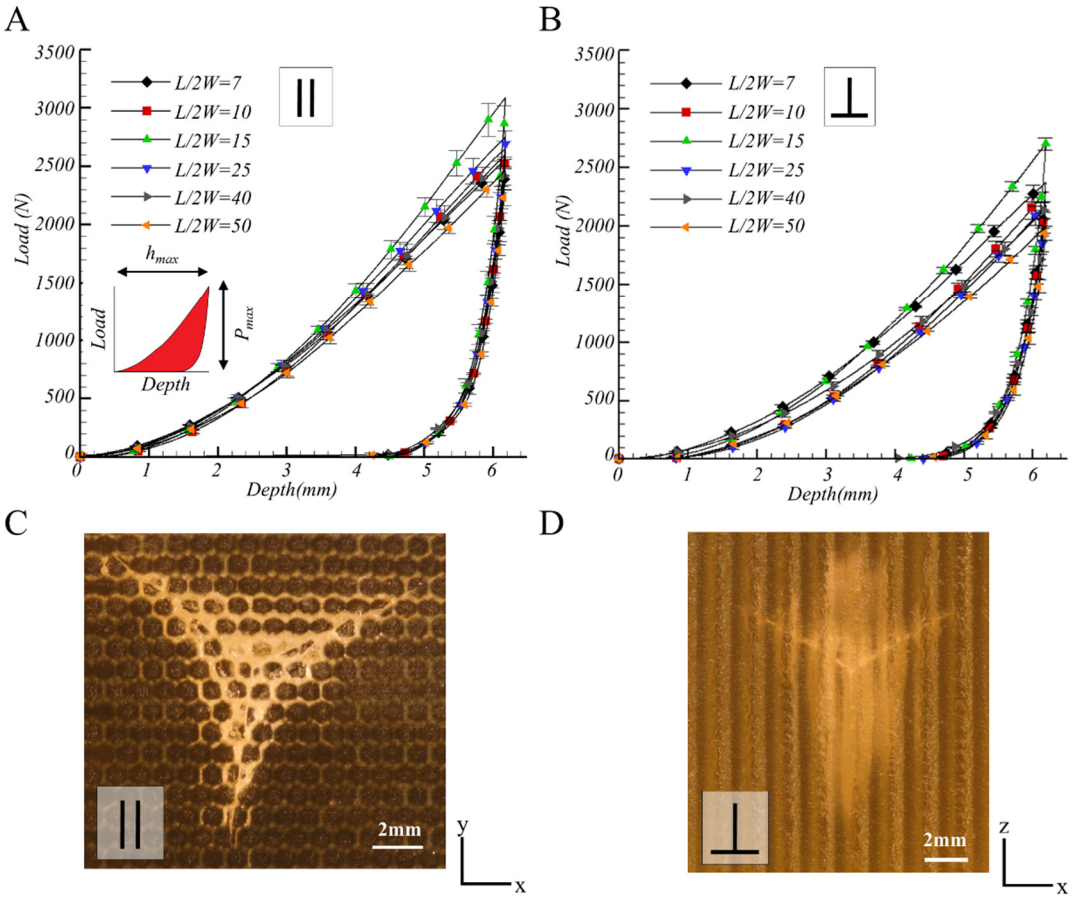

Figure 6-4 Load versus displacement curves for the parallel (A) and perpendicular (B) configurations, and different *L/2W* with error bars of one standard deviation. Inset in A indicating the value of P_{max} and h_{max} in an indentation test. Indentation marks with damage areas after indentation of rods (∥) parallel (C) and (⊥) perpendicular (D) to the indenter .

To characterize the fracture modes, I compare the tensile strength with the shear strength of the interface material. The experimental observations of the tensile strength were performed in the MTS machine of the civil engineering lab by Nobphadon Suksangpanya. The range of values obtained in this study were between T_{max}= 0.0534 - 0.1067 MPa. To investigate the shear strength of the compliant material, a set of lap joint shear strength tests were performed. Specimens were created by an Object Eden 350V 3D printer with the rigid material (RGD720). Figure 6-5A shows the dimension of the specimens to have a shear area of 12.5mm × 20mm. To minimize inertia effects, the tensile test was performed using a loading rate of 0.05mm/min. Figure 6-5B shows the results of the test to have an average maximum load at fracture P_{max} = 39.28 ± 6.32 N; and a maximum shear stress of τ_s = 0.16 ± 0.03 MPa. These results suggest a preferential crack propagation in tension mode.

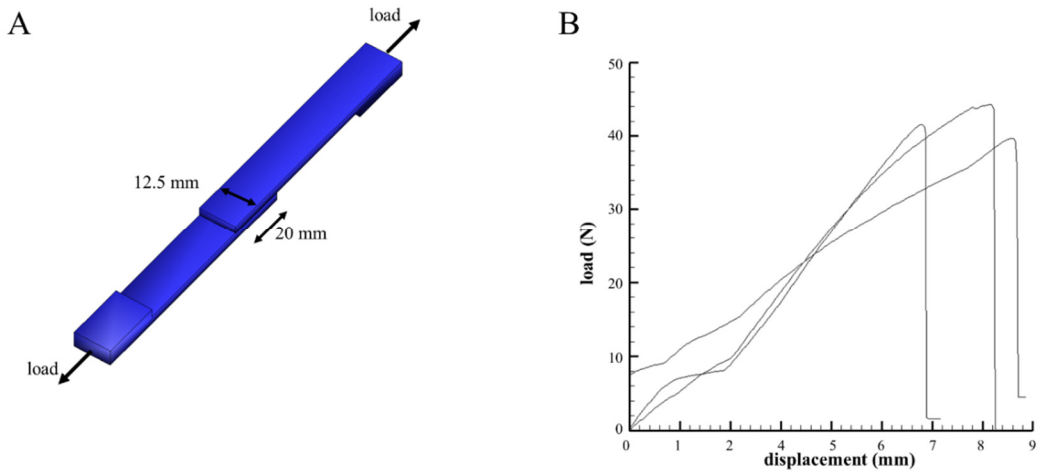

Figure 6-5 3D printed specimen used to quantify the shear strength in the interface material. The dimensions of the samples are shown in (A) and the loading curves obtained after the tests in (B).

6.4.3 Property maps

In order to observe the effects of aspect ratio, rod alignment and V_{fs} on the mechanical properties of the biomimetic composites. A comparison of the reduced modulus and hardness measured by indentation between different specimen configurations is shown in Figure 6-6A. For comparison, it is included an equivalent composite with randomly oriented rods (Fig. 6.6B) and rule of mixture values (e.g. Voigt and Reuss [148], [149]) with similar volume fractions of interface material (V_{fs} = 21%).This map indicates an average enhancement of the properties measured by indentation tests in the aligned rod-like microstructure as compared to the random materials of 50% and 73% in the values of E_r and H. A closer view of the randomly distributed composite (inset in Fig. 6.6B) reveals that some of rods are indeed connected, potentially strengthening the mechanical behavior. However, the site specific properties exhibit lower values as compared with the aligned rod-like microstructure. The randomly distributed rods also indicate that stronger materials are achieved by decreasing V_{fs} from 35% to 21%. The contribution of the rod alignment in the staggered configurations is also observed in Figure 6-6C and D, where the dashed lines denote the results for the parallel configuration and the solid lines the ones for the perpendicular configuration. In the parallel and perpendicular configurations, the lowest hardness and stiffness are shown for $L/2W$ = 50. Interestingly, this is the only aspect ratio of continuum rods that explicitly lack a staggered arrangement, as the rods connect through the structure to the solid bottom. On the other hand, the highest value of E_r and H is observed for $L/2W$ = 15. In the case of biological materials the mechanical anisotropy can be correlated to their hierarchical microstructure. An example can be seen in the

honeycomb-like microstructure of the American lobster, where an arrangement of protein fibers of nanoscale dimensions leads to a pronounced anisotropic macroscopic material [150]–[153]. The results obtained in this study could be used to quantify the mechanical anisotropy at different length scales. For example, at the bottom of the hierarchical structure of the American lobster [150]–[153] the bulk properties of the highly oriented 3D printed composites they could be considered as those of an arrangement of chitin-protein nano fibers.

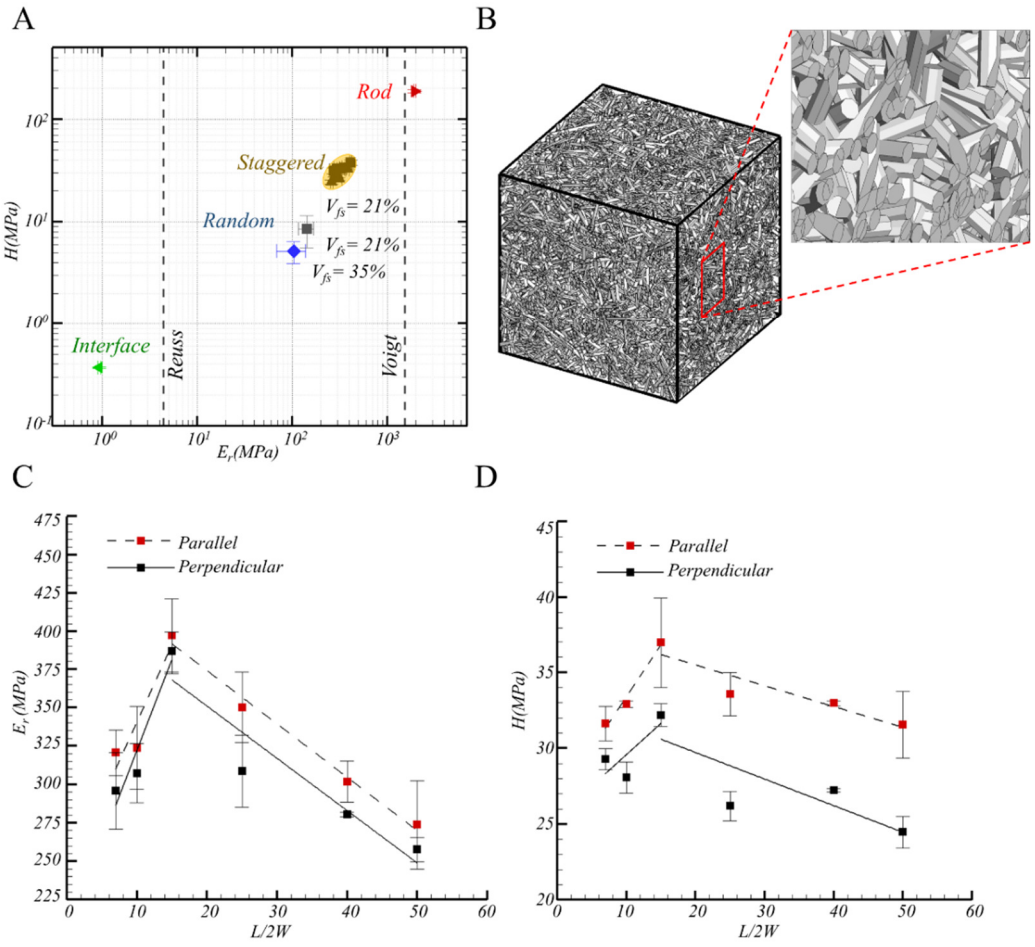

Figure 6-6 Effect of rod alignment in the site-specific properties (A). Despite having the same material composition, the staggered rods exhibit higher values of E_r and H than the randomly oriented composite. CAD of randomly distributed composite created with GeoDict [154] (B). (C) E_r vs. $L/2W$ and (D) H vs. $L/2W$. Errors bars indicate one standard deviation.

6.4.4 Abrasion resistance and fracture toughness

Since the early approaches of Palmqvist [37] to relate the length of radial cracks with fracture toughness (K_c), numerous models have explored the advantages of indentation tests [38], [40]. Fracture models applied to indentation tests can be classified by the type of fracture morphology (e.g. lateral, radial) and geometry of the indenter tip considered (e.g. Vickers, cube-corner). Although there are multiple techniques currently available to estimate K_c from experimental observations [40], Lawn et al. (*LEM*) developed an analytical solution of K_c with a half-penny shape configuration of radial/median orientation [30], [41], [42]. In this approach K_c is a function of the maximum load, P_{max}, defined before starting the test, the site-specific properties measured during indentation (E_r, H), a parameter (χ) that depends of the shape of the indenter (e.g., $\chi = 0.04$ for cube corner indenter[94]), and the length of the radial crack (c).

$$K_c = \chi \sqrt{\frac{E_r}{H}} \frac{P_{max}}{c^{3/2}} \tag{6.2}$$

After performing indentation tests in different samples at multiple h_{max} (varying from 2mm up to 6mm), it was noticed that at each h_{max} very small cracks approximately equal to the size of the indentation marks ($c \approx a$) were observed in the samples with rods oriented parallel to the penetration direction (Fig. 6.7A). Considering the onset of crack propagation ($c \approx a$), the following equation can be used to estimate K_c[27], [43], [155], [156], where the geometrical parameter $\alpha = 1.3$ for a cube corner indenter.

$$K_c \approx \alpha^{3/4} \chi (H {E_r}^2 P_c)^{1/4} \tag{6.3}$$

The plot in Fig. 6.7B displays the approximated values of K_c for the parallel configuration. Our biomimetic composites suggest an increase of 30% in the K_c values of $L/2W = 15$ with respect to $L/2W = 50$, where $L/2W = 15$ is the *optimum* aspect ratio to resist crack propagation. To understand the toughening associated with the composite and considering the fracture through the interfaces in mode I (Fig. 6.7A), I proceeded to compare the values of K_c from the composite and the interface. Estimating $K_c = (E_s G_c)^{1/2}$ in the interface material (Fig. 6.3B), an enhancement of two orders magnitude is measured in the rod-like microstructure.

Because of the lack of experimental evidence that radial crack propagation occurred in the samples of rods aligned orthogonally to the indenter, Equation 6.3 is only applied to analyze the parallel rod alignment. The center of an indentation mark is revealed in Figure 6-7C, where it is clear that plastic deformation has occurred in the rods during indentation. An inverse relationship between plastic deformation and toughness exists in most engineering materials, like ceramics, polymers and metals, and limits the use of those materials in damage tolerant applications[157]. Similar to engineering materials, biomimetic composites exhibit a trade-off between the fracture toughness (K_c) and critical load for plastic deformation (H^3/E_r^2). The term H^3/E_r^2 is a parameter used to quantify abrasion resistance, where materials with high values of H and low stiffness are preferred to resist larger inelastic deformations [10], [12], [47], [48], [158]. The abrasion resistance of a material (P_y) exposed to a spherical indenter of radius r is proportional to the modulus measured during indentation ($P_y = 0.78 r^2 H^3/E_r^2$)[45]. This proportionality has been correlated not only with spherical tips but also with pyramidal indenters [47], [48], [158].

The biomimetic designs reveal a trend-line to increase H^3/E_r^2 as the aspect ratio increases for the parallel configuration (Fig. 6.7D). It is also revealed that the optimum $L/2W$ = 50 to resist inelastic deformation is for the largest rods. Furthermore, an aspect ratio of $L/2W$ = 15 reveals a good resistance to crack propagation, while at the same time requiring a low load to initiate yielding (Fig. 6.7B and D).

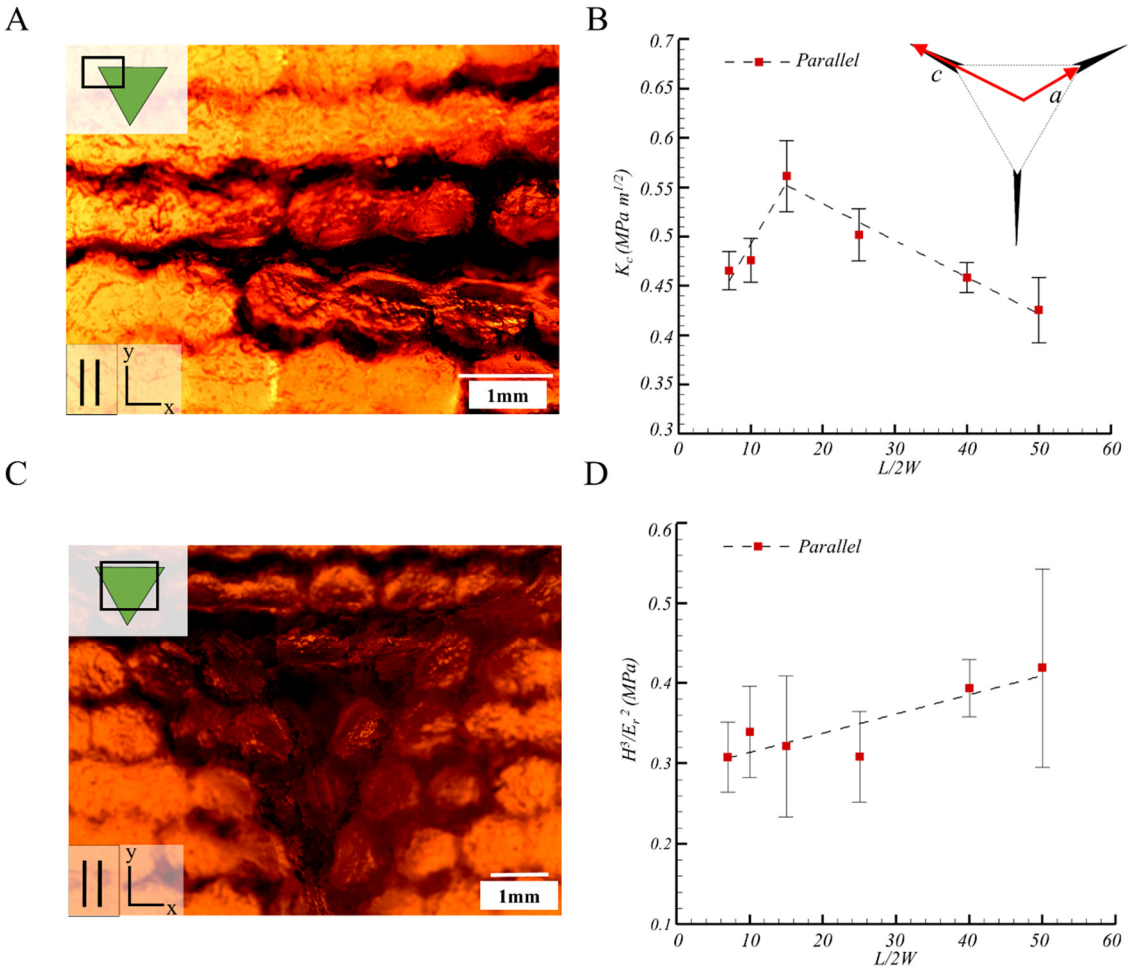

Figure 6-7 Higher magnification of the edge of an indentation mark exhibiting crack patterns in the interface material that surrounds the rods of parallel configuration (A). Values of K_c estimated with Equation 6.3 (B) as a function of $L/2W$. Parameters (c and a) from the *LEM* expression are shown in B. Inelastic deformation and damage at the center of the mark (C) and values of abrasion resistance (D) as a function of $L/2W$.

In the analysis of fracture toughness by indentation tests, a controversy exists regarding the estimation of the crack length [40], [44], [159]. Up to ±50% of discrepancy, it has been observed by comparing the values of K_c estimated with Equation 6.3 to those obtained with conventional mechanical tests[40], [44], [159]. To understand the limitations of Equation 6.3, indentation tests were performed in rods oriented parallel to the indenter with $L/2W = 15$ at different values of h_{max} (from 2mm to 6mm). The site-specific moduli were measured at each penetration and the K_c estimated with Equation 6.3. Despite the controversy that exist that to correctly estimate K_c from Equation 6.3 the values of $c/a \geq 2.5$ [40], [44], [159], our indentation analysis suggest that the K_c values estimated at the different h_{max} remained between those observed in Figure 6-7B. Respect to all values measured at the different penetrations, our analysis suggest up to a 17% of difference in the values of K_c estimated at h_{max} = 6mm (Figure 6-8).

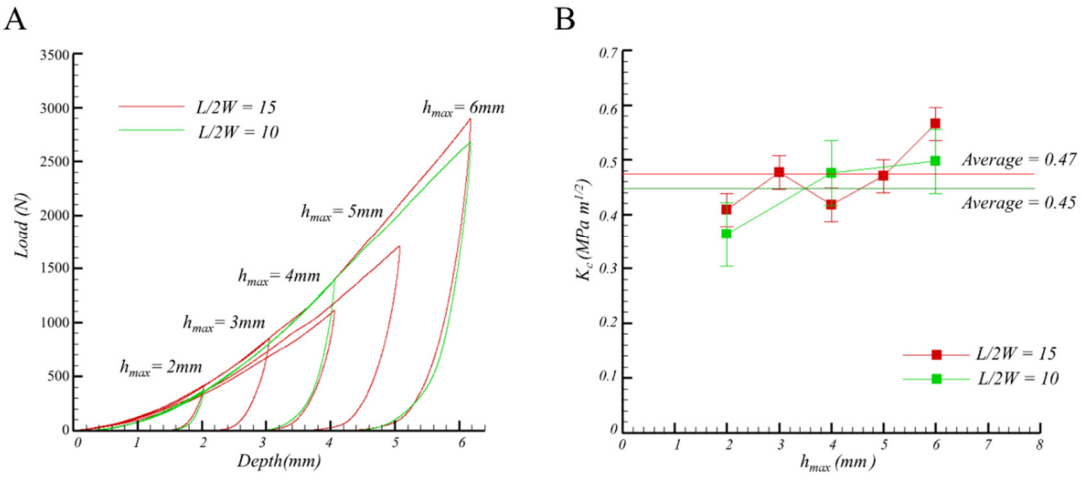

Figure 6-8 Load versus displacement curves at different maximum penetrations (A) and a comparison of the values of K_c obtained from $K_c \approx \alpha^{3/4}\chi(HE_r^{\ 2}P_c)^{1/4}$ [27], [43], [155], [156] with respect to h_{max} (B).

6.5 Computational models

A continuum model of indentation tests of low h_{max} (<1mm) is discussed in this section. The FEM is used to explain the onset of inelastic deformation in the rod-like microstructure, where the rods and interfaces deform plastically. A three dimensional model of a displacement controlled indentation test was implemented. The analysis considers a frictionless cube corner indenter (Fig. 6.9A) placed in contact with a matrix of rods and interface material (Fig. 6.9B). The rod-like microstructure includes a $1/6^{th}$ domain with the same rod dimensions and staggered configuration considered in the experimental section. In the discretization considered in the FEM both materials shown in Figure 7B share common nodes. The isotropic and homogenous rod and interface materials are considered independent. A von Misses yield criterion was assumed [160], where the linear isotropic strain-hardening parameters of the rods (σ_{yield} = 50MPa, H_{iso} = 5000MPa) and interface material (σ_{yield} = 0.7 MPa) are obtained by fitting the loading data of computational models with indentation data, values in agreement with contact mechanics [82]. The Young's modulus of the rods and interface were those obtained by indentation tests (See Table 6-2). As shown in the experimental results (section 6.4.4), H^3/E_r^2 tends to increase as $L/2W$ increases, therefore different $L/2W$ (10, 15, 25) were modeled in FEAP[20]. The non-linear computational model considers four node tetrahedral elements with symmetry planes in the sides of the body, a free end opposite to the indentation area, and rollers at the bottom of the geometry. The sensitivity of the mesh refinement was deemed to be sufficiently small to ensure convergence. A maximum penetration depth of

h_{max} = 1mm was modeled, satisfying the general rule of thumb that the maximum penetration should be less than $1/10^{th}$ of the sample height (25mm).

In order to quantify P_y, the 3D printed plastic composites are compared with an elastic model. As depicted in Figure 6-9C, the indentation curve of the elastic composite ($L/2W$ = 10) is a combination between the high stiffness of the rod material and the weak interfaces. Figure 6-9D shows a good agreement obtained between the experimental data and the FEM for $L/2W$ = 10. In particular, the red arrows in the loading curve indicate the contact between the indenter and a new set of rods. Following the experimental procedure, H and E_r were calculated for the different computation models [28].

Due to their macroscopic dimensions (e.g., nacre has a $2W \approx 8\mu m$ and a $\sigma_y \approx$ 2.5GPa[70], [161]), the material characterization of the rods is easier to perform as compared to the organic layer ($t \approx$ 20nm[161]). A sensitivity analysis was performed in order to quantify the effect of yield stress (σ_y) at the interface. By keeping the material properties in the rods constant (H_{iso} and σ_y) and increasing the yield stress (σ_y) of the interface material from 0.7 MPa to 0.8 MPa, the abrasion resistance (H^3/E_r^2) increases by 40% (see Table 6-3). This coincides with a separation from the linear-elastic composite (P_y) indicated by the arrows (Fig. 6.9D) [10]. The values of H^3/E_r^2 of the FEM (See Table 6-3) are of the same order of magnitude as those predicted by the experiments (H^3/E_r^2 =3.53 MPa) at h_{max} = 1mm.

Table 6-3 Effect in σ_{yield} of the interface material in the site specific properties measured after indentation in $L/2W = 10$

σ_{yield} (MPa)	E_r (MPa)	H (MPa)	H^3/E_r^2 (MPa)	$P_y(N)$
0.7	330	67	2.76	15.1
0.8	348	78	3.91	16.5

As compared with P_y, a value that can be measured from the separation between the composite and the linear elastic model, the value H^3/E_r^2 is not intuitive and requires analysis of the indentation data. The arrows in Figure 6-9E and F display the values of P_y for each $L/2W$. In this model, the value of H^3/E_r^2 can be correlated with the abrasion resistance measured in the cube corner indentation (P_y arrows in Fig. 6.9E and F) and that a large aspect ratio ($L/2W = 25$) exhibits a higher resistance to plastic deformation, which is in agreement with the experimental data (Fig. 6.7D).

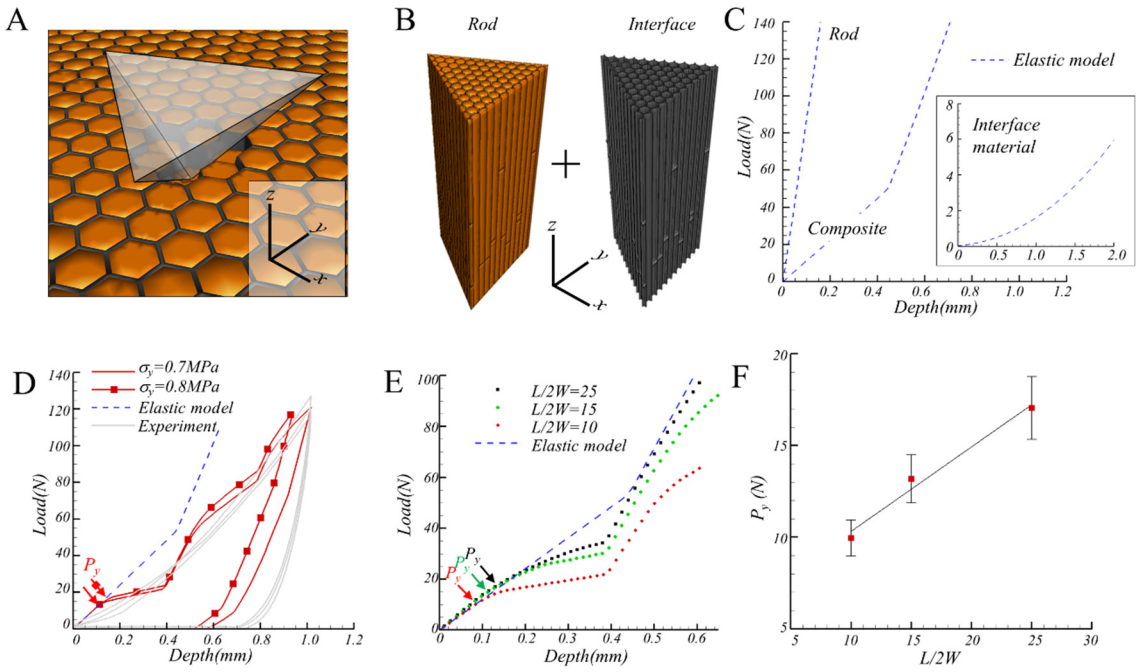

Figure 6-9 Cube corner indenter placed above a uniform rod-like microstructure of the same dimensions (*W,t*) that the 3D printing designs (A, B). FEM of indentation tests in an elastic microstructure (*L/2W* = 10), rod and support materials (C). Comparison between the elastic-plastic model of *L/2W* = 10, the experimental data and different values of *L/2W* (D). Effect of aspect ratio on P_y in the load displacement curve (E) P_y as a function of *L/2W* (F). Error bars in F account for the effect of mesh refinement in the load versus displacement curves (10%).

To further understand the deformation mechanisms acting in the biomimetic composites, maps of the effective strains in the interface material at different h_{max} and for *L/2W*=10, 15 and 25 were constructed and analyzed. The FEM shows an almost uniform effective strain at the interfaces of the smaller rods (*L/2W* = 10 and 15, Fig. 6.10A and B) as compared with a gradient at the tip of the larger rods (*L/2W* = 25, Fig. 6.10C) at an indentation depth of h_{max} = 0.15mm. As shown in Fig. 6.9E, the calculated indentation curves depart from ideal elastic response at penetration depths between 0.1 and 0.2 mm. At larger indentation depths (0.6mm), higher values of plastic strain field (above 35%) are

observed in several rods surrounding the indenter at smaller *L/2W* (Fig. 6.10D and E) as compared with larger *L/2W* (Fig. 6.10F), where higher values of plastic strain field seem to surround only the center rod. These results indicate that lower values of P_y coincide with a localization of effective strains in the smaller rods (*L/2W* = 10 and 15), and that larger rods, lacking a staggered alignment, are preferred for wear resistant applications.

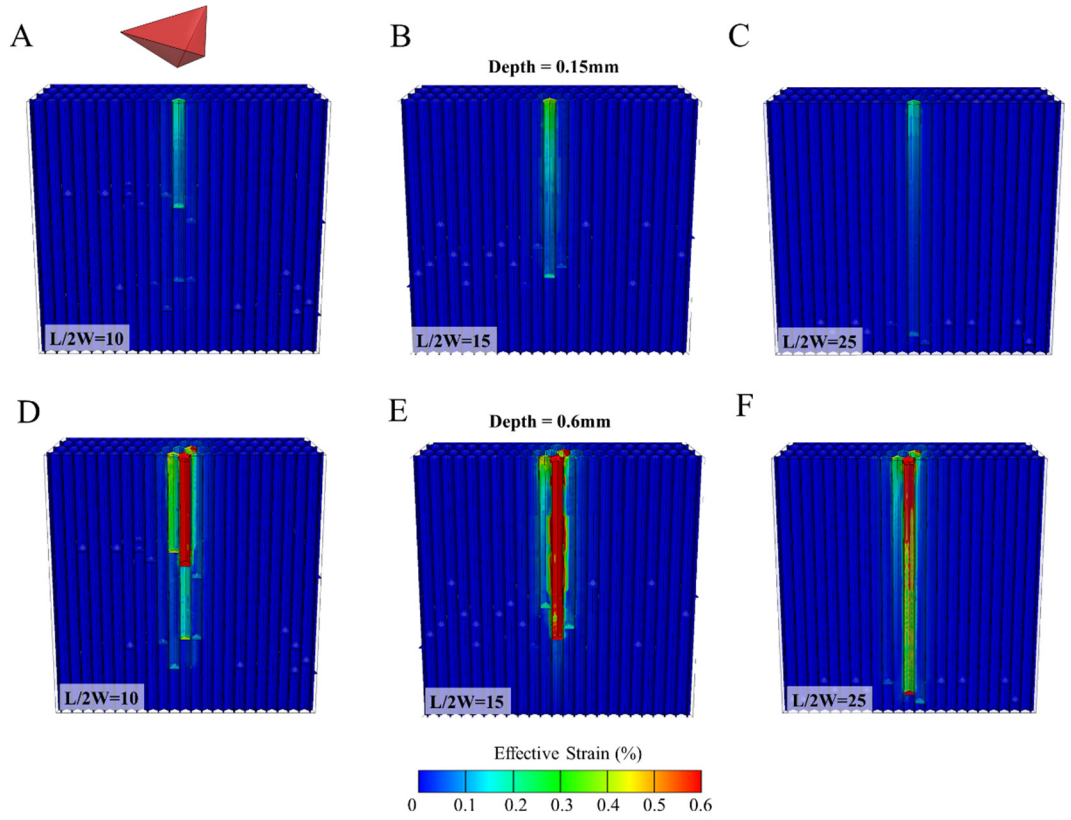

Figure 6-10 Values of effective strain in the interface material at different h_{max} = 0.15mm (A, B and C) and h_{max} = 0.6mm (D, E and F) for *L/2W* = 10, 15 and 25 obtained from our FEM simulations.

The high values of strain at the interfaces of the smaller rods (*L/2W* = 10) observed in Figure 6-10 can be explained by the analytical solution of Tsai et al. [162]. During indentation, large shear strains affects the interface material. The analytical solution of the

shear strain (γ) [162]accounts for elastic rods under compression (of length L), a force per unit length applied to the rods (T), the shear modulus at the interfaces and the rods (values calculated from the Lame's constant as G_i=1.5 MPa and G_r = 0.961 GPa respectively) and the thickness of the interface (t) (Fig. 6.11A).

$$\gamma = \frac{\beta T}{4G_i}\left[\frac{\sinh(-\beta x)}{3\cosh(\beta(L-\Delta x))} + \frac{\cosh(-\beta x)}{\sinh(\beta(L-\Delta x))}\right] \tag{6.4}$$

The parameter β is part of the closed form solution of equation 6.4, and is given by[162]:

$$\beta = \sqrt{\frac{6G_iG_r}{E_r 4W(tG_r+WG_i)}} \tag{6.5}$$

The analytical solution (equation 6.4) suggest an average enhancement of 100% in the shear strain (γ) measured at the interface between the two elastic beams for $L/2W$ = 10 as compared to $L/2W$ = 25 (Fig. 6.11B).

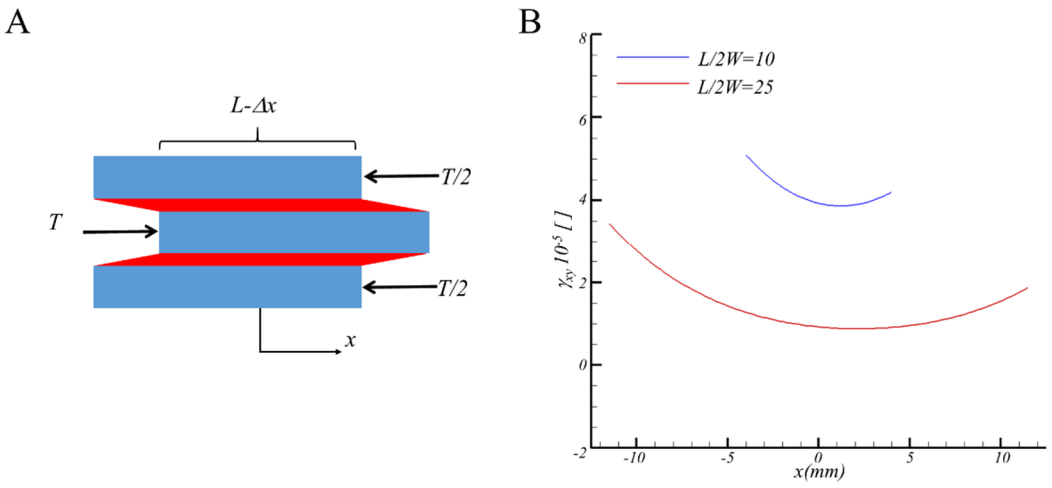

Figure 6-11 Comparison of the analytical model proposed by Tsai et al. [162] of rods surrounded by weak interfaces in shear mode. Configuration of rods exposed to a load per unit length (T = *1N/m*), where the shear strain (γ) in the interface material is expressed as a function of the shear modulus (G_i = 1.5 MPa and G_r = 0.961 GPa) and geometrical parameters of the rod-like microstructure (A). The overlap dimension considered is L-Δx, where Δx = *1mm.* Shear strains in the interface layer show higher values for the smaller $L/2W$ = 10 as compared with $L/2W$ = 25 (B), results that are in agreement with the FEM (Fig 6.10).

To understand the damage created in the perpendicular and parallel configurations, samples exposed to larger penetrations (h_{max} = 6mm) were carefully cut with a vertical band saw and the indented zones were examined by optical microscopy. Even with the difference in the hierarchical structure and composition, the biomimetic designs are able to replicate the energy dissipation mechanisms exhibited in parallel HAP crystallites of human enamel [163], [164]; where the interface material resembles the organic sheath (proteins and collagen) of the tooth that debonds surrounding the rods (See arrow a in Fig. 6.12A). The moderate pile-up observed in the area surrounding the indenter in the parallel and perpendicular configurations, might be an indication of ductile deformation [165]. Indentation marks of the rod-like microstructure of the chiton tooth has not been analyzed for pile-up formation, however ductile behavior has been recognized in the biomineralized microstructure of the fracture resistant conch shells [166].

As compared with the parallel configuration, examination of the perpendicular configuration reveals a preferential crack path through the solid (indicated with arrows b in Fig. 6.12B) and interface material (indicated with arrows c and d in Fig. 6.12B). These characteristic mixed-modes of energy dissipation, opening and in-plane shearing, affect the fracture toughness of biocomposites materials. Fracture tests performed in enamel in the longitudinal and transverse direction of the HAP crystals [164] have shown similar failure modes as those presented in Figures 6.12A and B. In fact, the measured K_c was higher when the crack is aligned parallel to the rods [164]. Although the profile views limit the complex crack tortuosity displayed (Fig. 6.12A and B), our experimental observations suggest that crack deflection within the weak interface layers is the preferential path for energy dissipation.

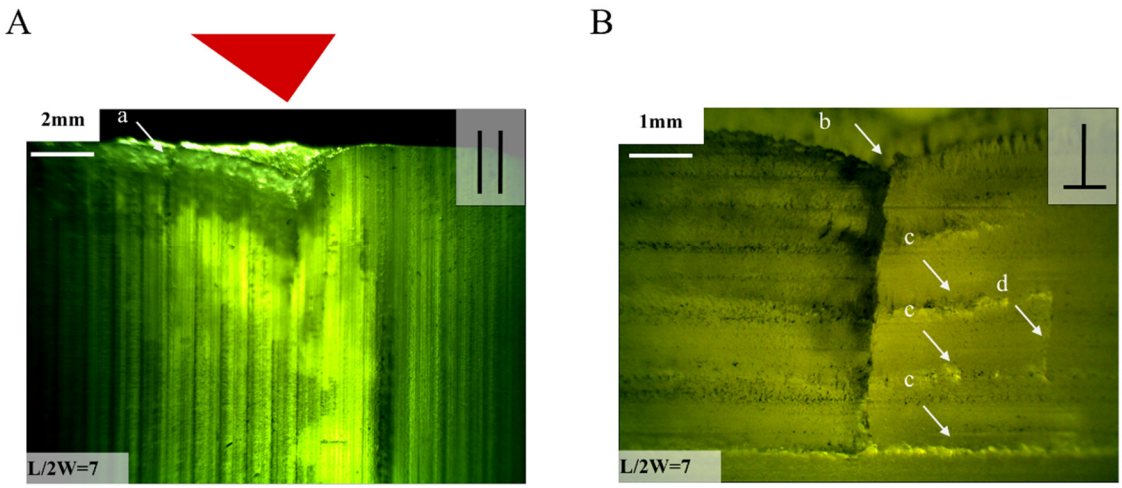

Figure 6-12 Sectioned samples of h_{max} = 6mm. (A) Parallel configuration: crack patterns propagate through the interface material (a arrow) but for the perpendicular configuration (B) Perpendicular configuration: the energy dissipates not only through the interface material (c and d arrows) but also though the rods (b arrow).

Figure 6-13A, D and G illustrates the displacement magnitude $|u_z|$ in the direction of penetration. The displacement magnitude indicates that the number of rods that are displaced by the indenter, increase with smaller *L/2W*. The displacement contours also confirm that a higher number of interface layers are activated with smaller rods, as observed in Figure 6-11. Similar to the classical theory of slender beams, load eccentricity produces large deformation of the rods in direct contact with the indenter [167]. A magnified image of the rod deformation at h_{max} = 0.6mm for *L/2W* = 10, 15 and 25, respectively, are observed in Fig. 6.13B, E and H. Lateral displacements reveal that the deflection mode of the rods is controlled by the aspect ratio, *L/2W,* during indentation. The radial displacement magnitude ($|u_r| = \sqrt{{u_{xx}}^2 + {u_{yy}}^2}$) was calculated in the rods and shown in Figures 6.13C, F and I to assess the effect of *L/2W* on the lateral deformation at the end of the rods in contact with the indenter. Figure 6-13I reveals that the highest radial

displacement magnitude is achieved for *L/2W* = 25. Also, the plots of Figure 6-13C, F and I confirm that at the free end, where the infinite half-space boundary conditions must be satisfied [146], the values $|u_r|$ are three orders of magnitude smaller than the maximum value achieved. The different deflection modes observed in Figures 6.13B, E and H indicate that larger rods show more lateral deformation. The lateral deformation also coincides with a higher P_y, suggesting that the deflection modes have a greater impact in the abrasion resistance of the rod-like microstructures. Deflection modes affect all kinds of structures [167] and is one of the principal mechanisms of failure.

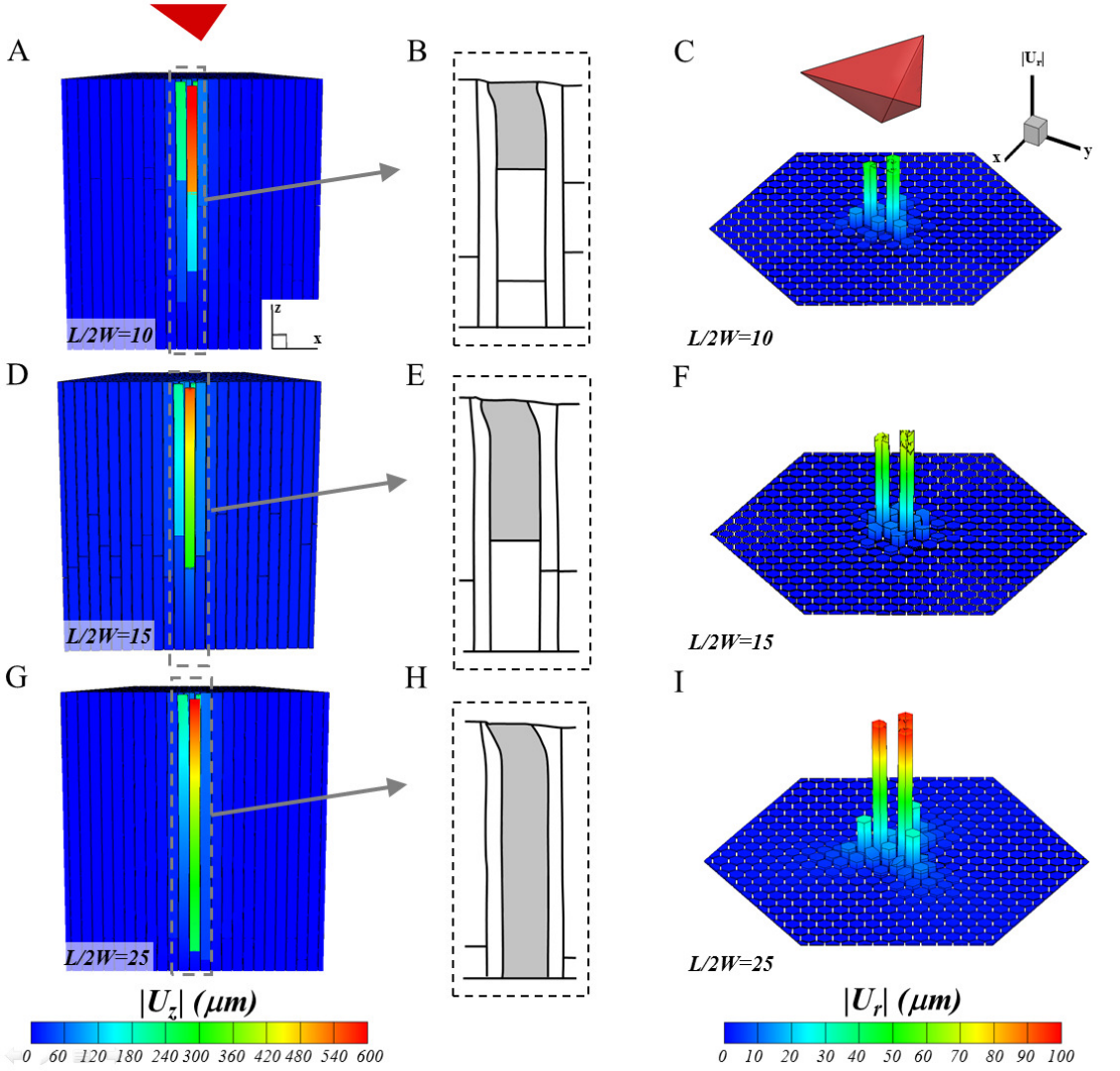

Figure 6-13 Comparison between the displacement magnitude in the direction of penetration ($|u_z|$), the magnified deformation and radial displacement ($|u_r|$) for *L/2W* = 10 (A, B and C), *L/2W* = 15 (D, E and F) and *L/2W* = 25 (G, H and I) respectively at 0.6mm of penetration. For displaying purposes, the deformation of the rods is magnified by 100 times in the X axis (B, E and H) and $|u_r|$ by 10 times in the vertical direction.

6.6 Discussion

In this work, a set of biomimetic designs has been used to quantify the effect of geometric features (*L/2W*, V_f) and rod alignment on the abrasion resistance and fracture toughness of a rod-like microstructure. Mechanical anisotropy of rods with parallel and perpendicular alignment (e.g. E_r, K_c) is common in many natural composite materials, like the enamel prisms of human teeth [164], [168], HAP crystals of the *P. Senegalus* [15], [22], and the twisted fibril pattern of the *Arapaima gigas* scales [23], [24]. In contrast to other biocomposites, the chiton has a preferential layout of rods oriented parallel to the concave axis of the tooth[9], [67]. In this study, the rods oriented parallel to the loading condition show an enhancement in H and E_r (average of 15% and 7% respectively for all *L/2W*) as compared with the perpendicular counterpart (Figs. 6.6C and D). The parallel alignment also shows higher indentation modulus than a random fibrous distribution (Fig. 6.6A), observations that confirm that rods oriented parallel to the penetration load are ideal for hard and stiff applications.

The lack of well-developed radial cracks and material removal (Fig. 6.14A) in post-indented marks is another feature of the rod-like microstructure of the chiton tooth [67]. The biomimetic composites tested in this study indicate that the dissipation of energy is by crack propagation in the interfaces surrounding the indentation mark (arrows Fig. 6.14B) and plastic deformation of the rods (Fig. 6.7C) in contact with the indenter. The onset of inelastic deformation is quantified in indentation tests by H^3/E_r^2, where larger rods (Fig. 6.7D) are optimum for the abrasion resistant biomimetic composites.

To explain the values of K_c obtained in Figure 6-7B, different deformation modes that influence the mechanical response of the rods were explored. The observations of K_c coincide with the P_{max} values (Fig. 6.14C) in which $L/2W = 15$ exhibits the highest value. In the computational models of the rods-like microstructure (Figs. 6.13B, E and H) at $h_{max} < 1$mm, was observed that the deformation modes are influenced by the $L/2W$. In this work, I propose that at a larger h_{max}, in the experimental section $h_{max} = 6$mm, the rods show both i) rotation and ii) side deflection. It is suggested that at low aspect ratios ($L/2W < 15$), the rods in direct contact with the indenter are undergoing rigid rotation, while those of higher aspect ratios ($L/2W > 15$) undergo lateral deformation with bending. This is depicted in the inset in Figure 6-14C.

To further analyze these competing mechanisms, I compared the critical loads required to initiate buckling in short and long rods of hexagonal cross section embedded in an elastic foundation considering both elastic bending and rigid rotation. In this particular study, the modulus of the elastic medium ($\beta = 2$MPa) was estimated from the limiting case of a concentrated force in an infinite elastic plane [169]. The critical compressive load required to trigger buckling in short rods, considering rigid rotation as the only buckling mechanism, shows a quadratic growth with respect to the aspect ratio of the bar [170]:

$$P_b = \frac{4}{3}\beta w^2 \left(\frac{L}{2W}\right)^2 \tag{6.6}$$

On the other hand, the critical load to trigger buckling (P_b) in an elastic long rod under axial compressive load shows a decay in Figure 6-14D with respect to $L/2W$ (where $L/2W$ is in the denominator of equation 6.7). Indeed, such load is a function of the elastic

modulus of the bar and a variable (ζ) that depends on β and the deflection modes of the rods [171].

$$P_b \approx 1.3 \frac{EW^2}{\left(\frac{L}{2W}\right)^2 \zeta^2} \tag{6.7}$$

Fig. 6.14D shows a comparison between the loads required to trigger buckling for rigid rotation and elastic bending as a function of *L/2W*. The instabilities arise as a consequence of the change in the number of sine waves illustrated [171] (Fig. 6.14D). Depending on the value of *L/2W*, it is possible to say that rigid rotation is dominated by rods with $L/2W < 6$, and elastic buckling dominates for rods with $L/2W > 6$. This leads to an optimum $L/2W \approx 6$. In structures, compressive *Euler* loads are used to derive critical loads to start buckling in elastic columns, which can lead to crushing. Despite a lack of experimental data regarding K_c values for the chiton tooth, equations 6.6 and 6.7 can be used to understand the role of the geometrical features of the rods (*L* and *2W*) to withstand damage. In natural ceramics, nanoscale features (e.g. interlocking and mineral bridges) are associated with an enhancement in K_c and strength [64], [96]. The chiton tooth is also characterized by nanoscale mineral bridges ($t \approx 25$nm), connecting adjacent rods, that can influence K_c[67]. In the biomimetic composites considered in this study, the rod to rod bridges were not directly taken into account. It is predicted that by improving the manufacturing process of the 3D printers, it will be possible to quantify the effect of mineral bridges in the mechanical properties.

The FEM observations presented in section 6.6.5 indicate a strain gradient in the larger rods (*L/2W = 25*) leading to an enhancement in P_y of 40% as compared to the

localization observed in $L/2W$ = 10 (Fig. 6.10D). In the studies of the chiton tooth, the length of the rods are difficult to estimate[9], [19], [67]. However, based on the results presented in this chapter I estimate that to endure the grinding forces the rod-like microstructure of the tooth is characterized with a large $L/2W$. The fact that material removal or chipping is not observed at $h_{max} \approx$ 2000nm in the chiton tooth (Fig. 6.14A) and h_{max} = 1mm in the biomimetic composites (Fig. 6.14B) also suggest that the rod-like microstructure is ideal for wear resistant materials. The benefits of these findings are envisioned in the fabrication of miniaturized materials that require tailor mechanical properties (e.g. coating and carbon nanotubes), in industrial tools of long working-life (e.g. drills) and in utensils of daily use (e.g. pencils and razors).

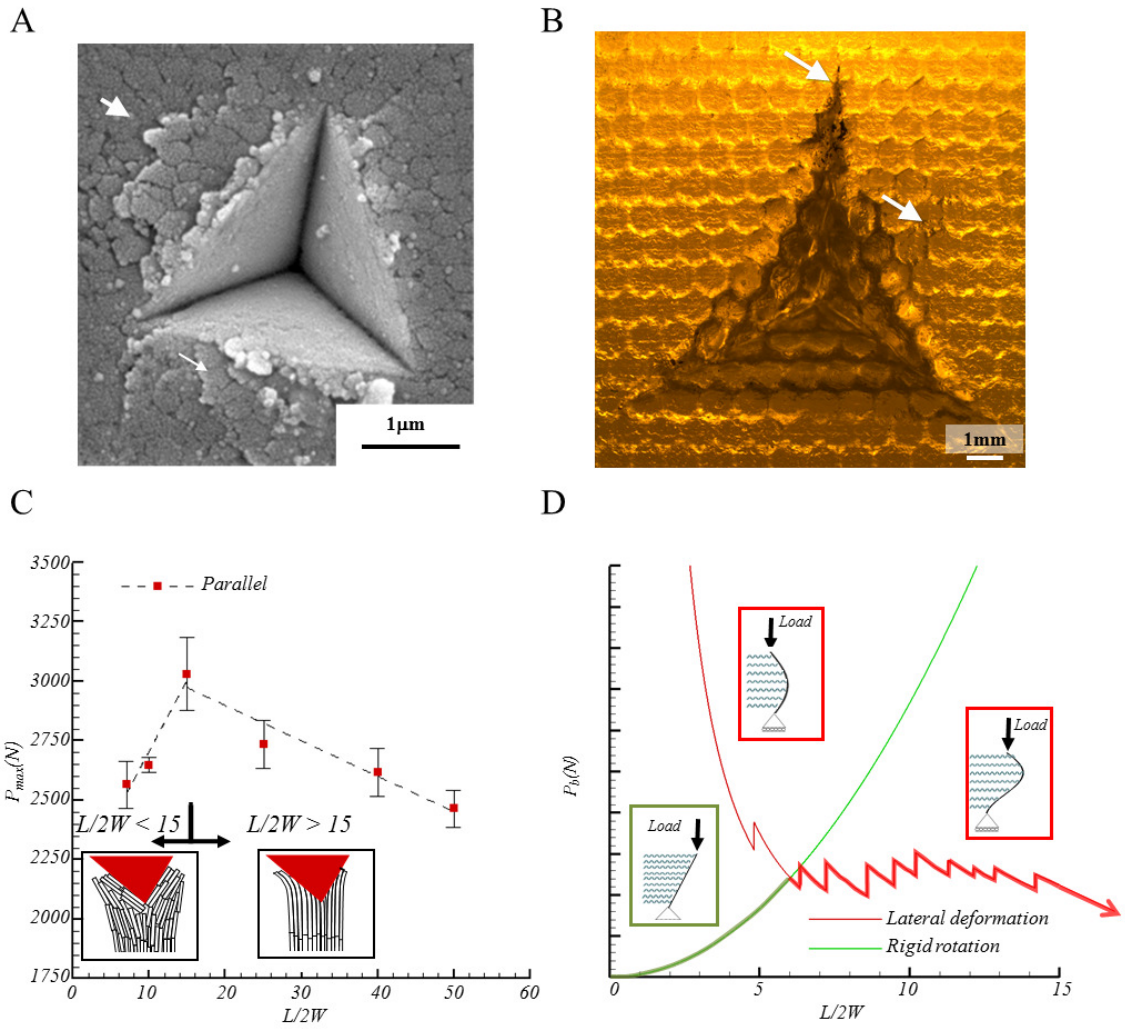

Figure 6-14 Comparison between a (A) post-sonication indentation mark at the leading edge of the tooth with rods oriented parallel to the indenter at maximum penetration of 2000nm[67] and (B) damage area surrounding biomimetic composites at maximum penetration of 6mm. Arrows in (A) and (B) pointing to regions with radial and circumferential cracks. Effect of *L/2W* in the P_{max} measured during the indentation tests (C), and comparison of critical loads P_b calculated with equations 6.6 and 6.7 with respect *L/2W* (D). The insets in (C) indicate rigid body rotation (*L/2W* < 15) and lateral bending (*L/2W* > 15). The insets in (D) show the rigid deformation of a rod (green) and bending (red) surrounded by an elastic matrix.

6.7 Conclusions

A set of 3D printed biomimetic composites has been exposed to cube corner indentation tests. The influence of geometrical features (*L/2W*) and rod orientation have been analyzed in the site specific properties measured during indentation. Up to a 50% increase in E_r, and 30% increase in H and K_c has been quantified by modifying *L/2W*. A tradeoff between toughness and inelastic deformation has been quantified in the biomimetic composites. The highest tolerance to fracture is exhibited in rods aligned parallel to the indenter at *L/2W*=15 while the highest abrasion resistance is observed in *L/2W* = 50. The optimum value of the fracture toughness is justified by the different deformation modes of the rods under large penetrations, where either rigid rotation or bending affects the rods. The FEM have been addresses to explain the abrasion resistance obtained from indentation tests (H^3/E_r^2). The parameter H^3/E_r^2 is correlated with P_y, a value that can be directly measured from the indentation tests. The FEM indicates large strains and localization of the damage in the smaller rods (*L/2W* = 10), reported to be in detrimental of the abrasion resistance. Despite the printing inconsistencies that might exist in the artificial microstructures created, the biomimetic designs mimic some of the fracture mechanisms observed after indentation of the chiton tooth (lack of well-developed radial/median cracks and material removal around the indenter). In this chapter, I limited our study to the hexagonal morphology idealized in the leading and trailing edges of the chiton tooth. Currently a new study is being implemented to study the effects of polygonal shapes in the mechanical properties measured by indentation.

CHAPTER 7. ROLE OF THE ROD-LIKE MICROSTRUCTURE UNDER TENSILE LOADING

7.1 Introduction

Natural materials are characterized by their ability to resist biting attacks and deteriorative effects due to environmental conditions. Natural materials are also known for their outstanding mechanical properties (e.g. toughness and strength), an example is the plate-like microstructure of nacre[64](Figure 7-1A).

A nanoscale infrastructure of polygonal plates, surrounded by an organic layer, defines the ultrastructure of nacre. Also known as the *brick wall*, the plate-like microstructure of nacre is composed of aragonitic tablets of 5-8 μm of diameter which are separated by an organic layer of 20 nm-30 nm of thickness [143], [161]. The nacre have been extensively studied for many years due its outstanding toughness (three orders of magnitude greater than the mineralized building block) and strength[172]. The toughening mechanisms of the tablets are attributed to geometrical features (e.g. waviness and staggered distribution) [64], size effects [108], aspect ratio [5], [72], enhancement of the tablets ductility by the presence of nano-grains[173] and hardening through the sliding of tablets [143]. Figure 7-1B displays stress-strain curves comparing a hydrated and dry nacre with respect the monolithic solid[64]. The highly mineralized shell of $V_{fm} = 95\%$ (V_{fm} refers to the volume fraction of the mineral) is composed of an stiff aragonite microstructure

(Young's modulus E= 90 GPa)[64], which, during erosive contact with particles or rocks is exposed to multiaxial stresses (Figure 7-1E and F) with respect the monolithic solid[64]. The highly mineralized shell of V_{fm} = 95% (V_{fm} refers to the volume fraction of the mineral) is composed of an stiff aragonite microstructure (Young's modulus E= 90 GPa)[64], which, during erosive contact with particles or rocks is exposed to multiaxial stresses (Figure 7-1E and F).

Similar to the plate-like microstructure of nacre, the mineralized shell of the chiton tooth is under large tensile and compressive stresses [67]. Figure 7-1C shows the bottom of a chiton of 15 mm of length with an arrow pointing towards the radular teeth. Seeking for algaes, the radular tooth of the *Cryptochiton Stelleri* abrades the bottom of the oceans in a repetitive cycle of mechanical loading [9]. FEM revealed that during rasping events (Figure 7-1G), the frontal section of the tooth is under tension (leading edge) while the back section (trailing edge) under compressive stresses [67], [69]. Studies performed in this thesis [67] suggest, that reducing the probabilities of flaws by the presence of smaller rods (≈ 193 nm) at the leading edge of the tooth aim in the resistance to tensile stresses.

Despite the advances in micromechanical testing, the nano-scale dimensions make the use of tensile stages in the ESEM to characterize the failure modes under tension more difficult. As previous studies proved the benefits of using biomimetics to unveil the failure modes of natural materials [141], [143], [174], a set of composites are proposed in this chapter to understand the mechanisms of energy dissipation in the rod-like microstructures under tensile loading. As the microstructure of nacre has been extensively studied before, the mechanisms to withstand damage of the rod-like microstructure are compared to a plate-like that resembles the brick wall. The complex mechanisms of crack propagation in

mineralized materials are represented by polymeric composites [141], [143], [174], which when compared with metals or hard ceramics, allow the fracture through the rods or interfaces. In this study, a strong polymer is used to mimic the plates/rods; it is surrounded by a weak interface that resembles the organic matrix. This chapter is divided in seven sections: The section 7.2 includes an analysis of the Tension Shear model proposed by Gao et al [93], [72]. Later in section 7.3, a parametric analysis of the geometrical features of the tooth are compared with respect to the nacre. The biomimetic designs included is this study are presented in section 7.4. The experimental observations are presented in section 7.5 and the discussion of the results in section 7.6. Finally, the conclusions are left for the end of this chapter.

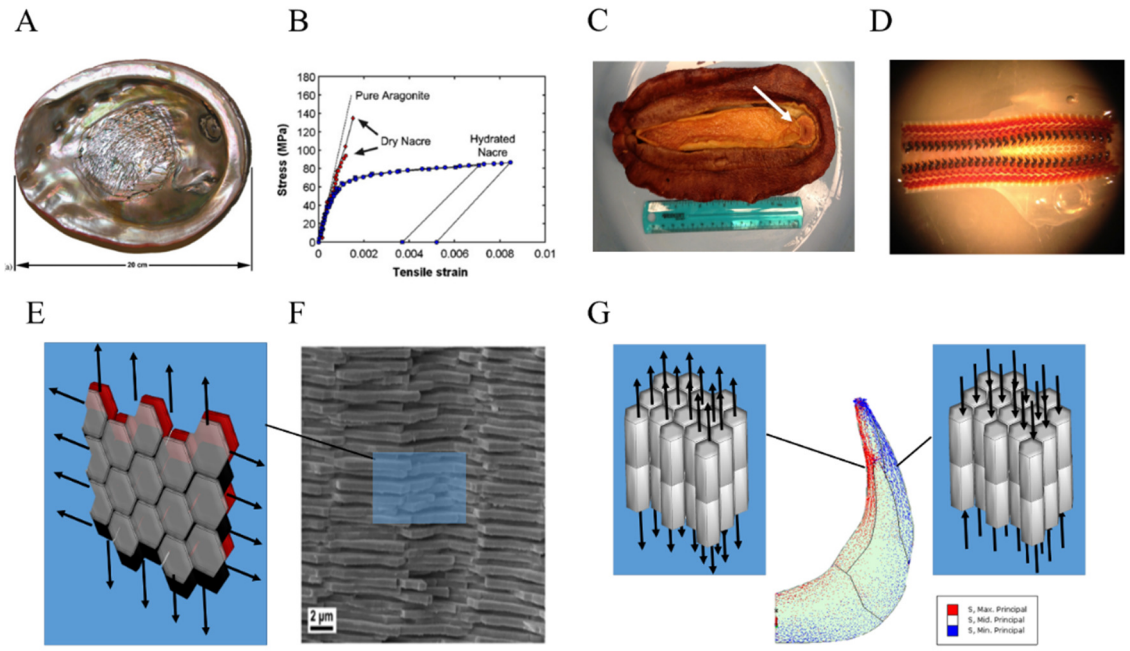

Figure 7-1 Overall comparison of the microstructure of the mother-of-pearl with respect to the chiton tooth. Inside view of the microstructure and strain-strain curves from Barthelat et al. [64] (A and B). Bottom view of the *Criptochiton stelleri* compared with a measuring stick of 15 cm of length (C) and rows of teeth located in the ribbon (D). Sheet arraignment of a plate-like microstructure displaying bi-axial forces (E) and close up of the plate-like microstructure (F)[64]. Rod-like microstructure working in tension in the leading edge and in compression in the trailing edge of the tooth (G)[67].

7.2 Theoretical background

Due to its simplicity, the tension shear model of biocomposites proposed by Gao et al. [93], [72] is widely referenced in the literature[175]–[178]. Inspired by the outstanding strength of bone and shell, the model accounts for staggered minerals of a defined aspect ratio (ρ), embedded in a matrix of organic material (Figure 7-2A). The model considers an average stress field ($\sigma_{ave\text{-}m} = \rho\tau/2$) along the mineral, where τ is the shear stress of the protein. To account for the strength of the biocomposite, the tension shear model proposes

that the mineral carries all the load and the strength is given by $\sigma_{bc} = V_{fm}\sigma_{ave\text{-}m}$ [93], [72]. As compared with the strength, the model considers the deformation of the organic matrix by shear and strain of the mineral ($\varepsilon = 2\varepsilon_p(1-V_{fm})/(V_{fm}\rho) + \Delta_m/l^*$). Where in the previous expression, ε_p is the shear strain of the protein, Δ_m is the deformation of the mineral in tension and l^* is the length of the building blocks (where $l^* = 2W$ for nacre or $l^* = L$ for the chiton) [93], [72]. Finally, by replacing the Young's modulus of the mineral (E_m) and the shear modulus of the protein (μ_p), the stiffness of the biological material is given by [93], [72]:

$$\frac{1}{E} = \frac{4(1-V_{fm})}{V_{fm}{}^2 \rho^2 \mu_p} + \frac{1}{V_{fm} E_m} \tag{7.1}$$

In this study, I use equation 7.1 to compare the influence of the material parameters (V_{fm} and aspect ratio of the rods) on the stiffness of the microstructures. A representation of the rod-like microstructure is shown in Figure 7-2B. The values of the material parameters that characterize the features of the chiton tooth and nacre are shown in Table 7-1. Notice, that the alignment of the rods/plates alignment defines the aspect ratio considered, where nacre has a $\rho = 2W/L$ and for the exterior shell of the tooth $\rho = L/2W$.

Table 7-1 Geometrical parameters of the chiton shell and Nacre microstructure [1], [2], [9], [10]

	chiton	*nacre*
W(nm)	100	4000
t(nm)	25	25
L(nm)	-	500

The first analysis of equation 7.1 suggest that the difference between the Young's modulus of the aragonite (E=100 GPa [64]) and magnetite (E=175 GPa [78]) leads to a higher stiffness in the rod-like microstructure of the chiton tooth (refer to Figure 7-2C). As mentioned before in this thesis, the estimations of the aspect ratio of the rods is a difficult task to perform due to the complexity of manipulating such small scales (diameter of rods ≈ 200nm). With values of $\rho < 10$, both microstructures indicate similar values of stiffness (Figure 7-2C). By increasing the aspect ratio, equation 7.1 predicts an enhancement of ≈ 43% in the stiffness values measured during tensile loading. Despite the fact, that the length of the chiton rods remains unknown, an estimation of the influence of the V_{fm} in the stiffness can be performed. Considering $\rho = 20$ for both microstructures, equation 7.1 estimates an enhancement in the natural response of the rod-like microstructure for a value of $V_{fm} > 60\%$ (Figure 7-2D). Based on estimations made from EDS[67] (chapter 4), the chiton has a $V_{fm} \approx 86\%$ in the trailing edge and $V_{fm} \approx 92\%$ in the leading edge of the tooth [67], values similar to the estimated $V_{fm} \approx 95\%$ of the nacre[161]. Despite the two dimensional assumptions made by the tension shear model [93], [72], it is suggested a global enhancement of the stiffness of the chiton tooth as compared with to the tough nacre.

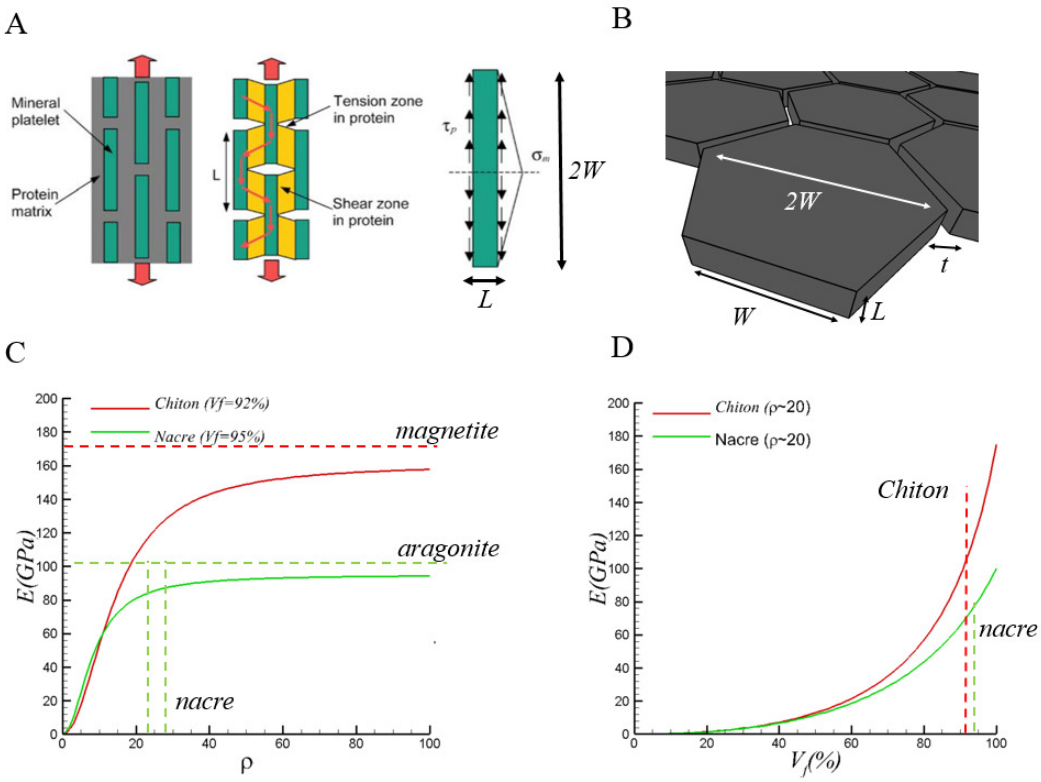

Figure 7-2 Tension shear model (A) adapted by Ji and Gao [4], [5]. Overview of the geometrical parameters of the microstructures (B). Predictions made by equation 7.1 of E for the nacre and chiton in tension, with constant V_{fm} (C) and $\rho = 20$ (D).

7.3 Parametrization

A parametrization is necessary to assess the influence of the geometrical features (*L, 2W* and *t*) of the different designs considered in this study. The representative volume element (RVE) of the chiton tooth and nacre is shown in Figure 7-3A. The difference in both microstructures is given by the direction of the tensile loads applied (Figure 7-3B): (i) biaxial loading conditions in the shell of the nacre or (ii) loading parallel to the rods in the rod-like microstructure of the tooth. The parameters of the RVE are indicated in Figure 7-3C and D. Based on this representation and knowing the dimensions of the microstructure in advance (table 7.1), it is possible to quantify the V_{fm} by:

$$V_{fm} = \frac{3w^2h}{\left(\sqrt{3}w+t\right)^2(h+t)} \tag{7.2}$$

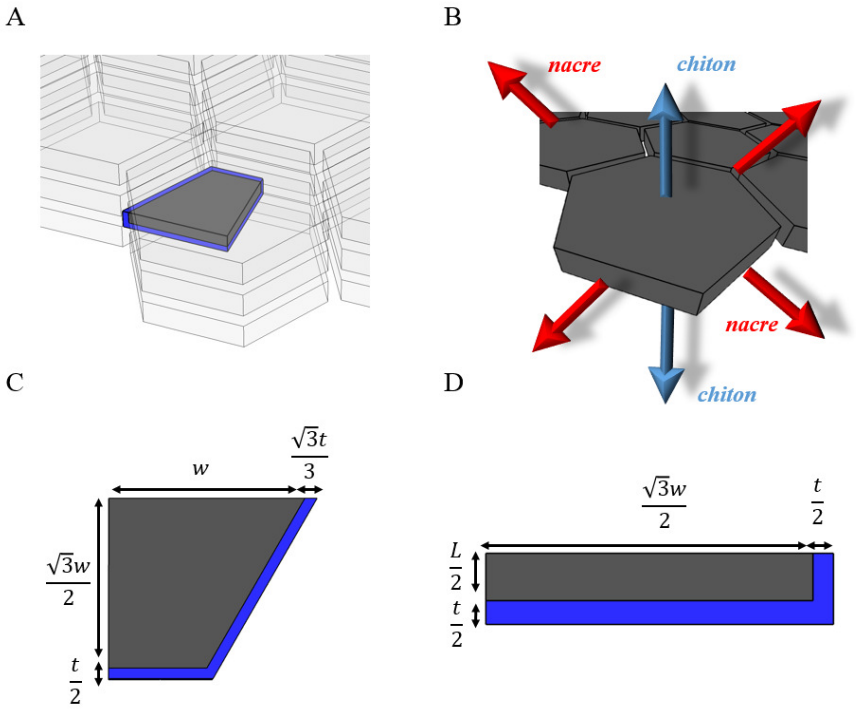

Figure 7-3 Representative volume element of the microstructures. RVE of a plate-like microstructure (A and B). Description of the RVE's in terms of *W, t* and *L* (C and D).

According to equation 7.2, the V_{fm} of the chiton tooth is 75% (table 7.2). The difference with respect to the values obtained by EDS[67] (of $V_{fm} \approx 86\%$ and 92%) can be explained by the thickness of the interface that was considered ($t \approx 25$ nm value estimated from SEM images of the rods in Chapter 4) and the fact that equation 7.2 is not taking the mineral bridges observed in the microstructure into account. The values of $V_{fm} \approx 95\%$ (table 7.2) of nacre predicted by equation 7.2 are in agreement with those estimated in the literature [97], [161].

In the study of nacre, hardening has been achieved by the sliding of the tablets[97]. It is then expected, that increasing the area of contact [127] between the mineral and protein layer would lead to an enhancement in the toughness of the biological composite by an improvement in the transfer of loads. This concept is similar to the interface area that has been estimated in fiber-reinforced composites [127], [179]–[181], sliding area which is inversely proportional to the diameter of the fibers. Based on the RVE of a rod- and plate-like microstructure (Figure 7-2A), it is proposed an expression to calculate the relation between the area in contact with the organic layer (A_{ol}) and the volume of the mineral (V_{mb}):

$$\frac{A_{ol}}{V_{mb}} = \frac{w\left(L+\frac{\sqrt{3}}{2}w\right)}{\frac{\sqrt{3}}{2}\left(w+\frac{\sqrt{3}}{3}t\right)^2(L+t)} \tag{7.3}$$

A comparison of the values obtained in the chiton and nacre microstructure (see Table 7-2), suggest that the relation between the area and volume (A_{ol}/V_{mb}) of the tooth is three times larger as compared to the nacre. These results predict an enhancement in the stiffness and strength obtained from the rod-like microstructure largely by increasing the potential regions with organic shear.

Table 7-2 Values of V_f (%) and A/V (1/nm) calculated in this study.

	chiton	*nacre*
V_{fm} (%) *(Eq. 7.2)*	75	95
A_{ol}/V_{mb} *(10^{-3} 1/nm) (Eq. 7.3)*	9.3	2.1

An isoparametric surface is shown in Figure 7-4, revealing the influence of W and L in equations 7.2 and 7.3. As expected, by increasing the cross section and length, the maximum V_{fm} (%) is obtained (Figure 7-A). Figure 7-4A also suggests that only a large reduction in W and L will lead to values of V_{fm} < 80%, where the chiton tooth and nacre display similar fractions of mineral. As compared with the V_{fm}, increasing the W and L would lead to a decay in the ratio of A_{ol}/V_{mb} (Figure 7-4B).

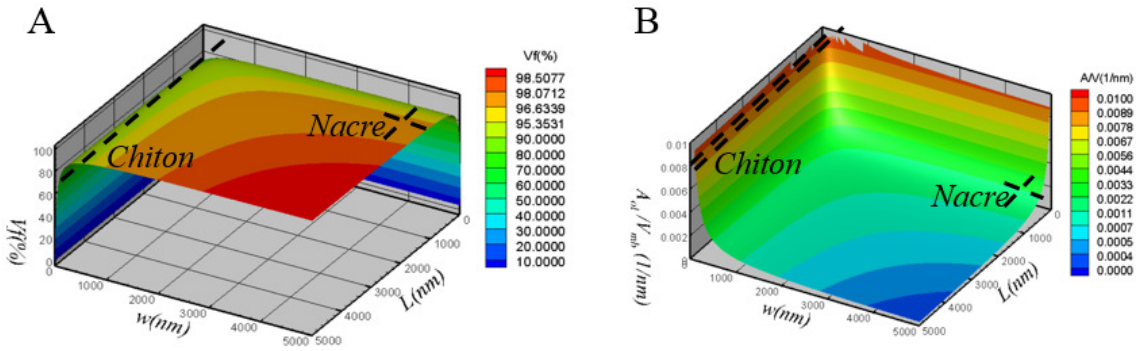

Figure 7-4 Isoparametric surfaces comparing the V_{fm} (A) and A_{ol}/V_{mb} (B) for the nacre and chiton tooth. Despite having the same order of V_{fm}, the rod-like microstructure of the chiton reveals a higher value of A_{ol}/V_{mb} as compared to the plate-like microstructure. The surfaces were generated with equations 7.2 and 7.3, with t = 25nm.

7.4 Biomimetic composites

To address the influence of the shape of the building blocks in the stiffness measured during tension, samples were 3D printed in dog bones of a rod-like and plate-like microstructure. A polyethylene-like material was considered for the planks (E = 1100-1700 MPa) [144] and a more compliant resin (E = 0.93GPa) to account for the weak interfaces. A displacement control tensile test (loading rate of 0.508 mm/sec) was performed in 3D printed dog bones of 140 mm x 40 mm x 10 mm (Figure 7-5A) in an electromechanical testing machine with a load cell of 300kN (MTS, Eden Prairie, MN, USA). The dogbones were manufactured in a Connex 350 3D printer machine [144] in the Microstructure Testing and Analysis Lab at Purdue University. As creep influences the mechanical attributes of the printed materials, the tensile tests were performed within the first 48 hours after the fabrication of the samples. The 3D printed composites included staggered rods of $2W$ = 1 mm and L = 20 mm and staggered plates of $2W$ = 10 mm and L = 0.5 mm, with an interface thickness (t) that varied between 0.1 mm and 0.4 mm (See Tables 7.3 and 7.4). The staggered distribution of the rods, followed the design guidelines mentioned in Chapter 5, with a separation of +/- 3 mm. The staggered alignment of the tablets followed the natural design of sheet nacre [172].

As observed in the design tables, both microstructures were 3D printed with the same V_f *(%)*, *A/V (1/mm)* and $\rho = 20$. To avoid inconsistencies while 3D printing the samples, the microstructures were printed with a layer of support material in the top and in the bottom section (Figure 7-5B) that was removed before the tests. The analysis of the displacement fields was carried out with two cameras (Figure 7-5C) following the

calibration procedures indicated by the Digital Image Correlation (DIC) [182]. The DIC also has the advantage that allows to estimate the deformation of the rods in the out of plane field. The preparation of the samples included a speckle pattern on the surface studied, which was painted with a spray primer for plastics (Figure 7-5D) and dried in environmental conditions.

Table 7-3 Parameters of the rod-like composites

	Rod-like		
W(mm)	0.5	0.5	0.5
t(mm)	0.1	0.3	0.4
L(mm)	20	20	20
ρ	20	20	20
$V_f()$	0.8	0.6	0.5
A/V (1/ mm)	1.8	1.3	1.1

Table 7-4 Parameters of the plate-like composites

	Plate-like		
W(mm)	5	5	5
t(mm)	0.1	0.3	0.4
L(mm)	0.5	0.5	0.5
ρ	20	20	20
$V_f()$	0.8	0.6	0.5
A/V (1/nm)	1.8	1.3	1.1

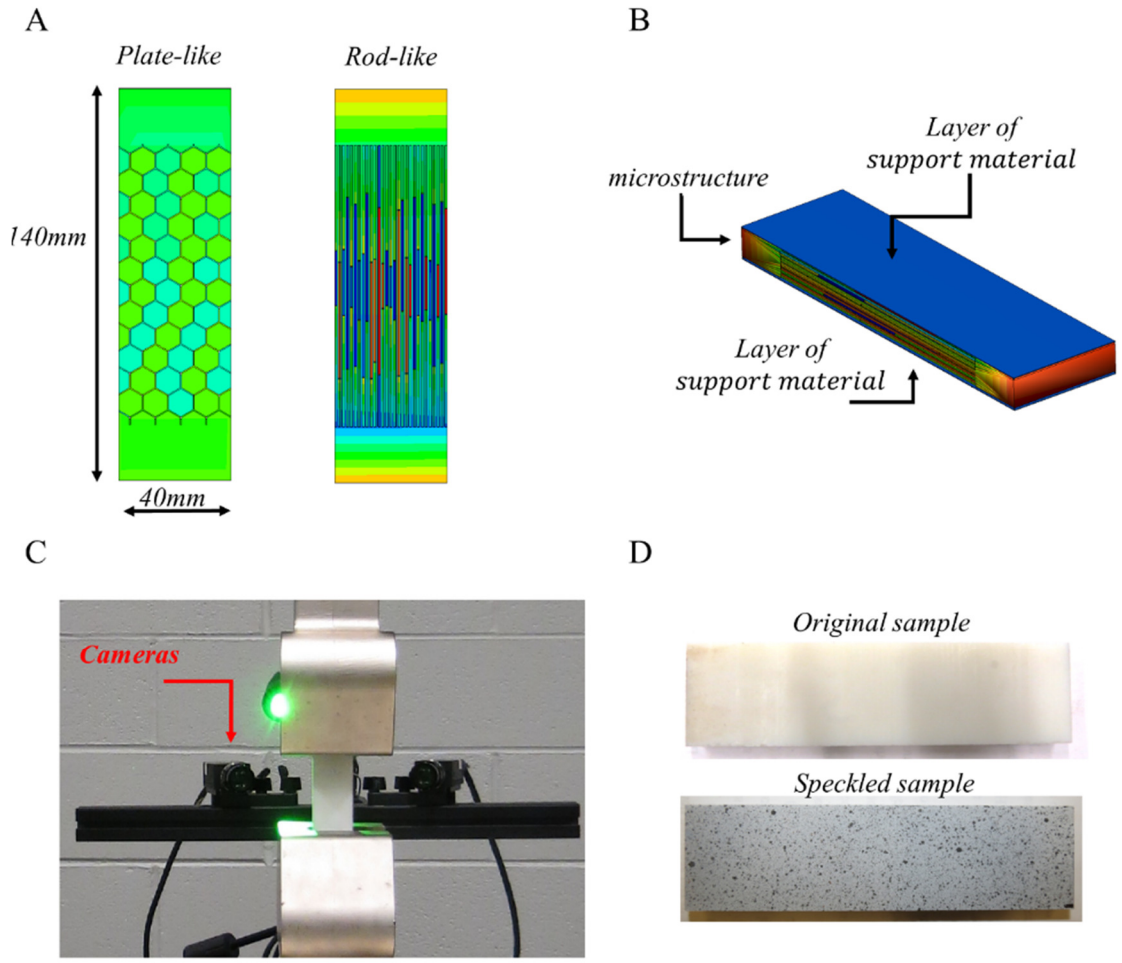

Figure 7-5 Experimental setup and biomimetic composites manufactured. Sketch of rapid prototypes used to test the effect of V_f and A/V (A). To avoid defects in the manufacturing process, the biomimetic designs were created with a layer of support material at the top and the bottom of the sample that was removed before the tests (B). Set of two cameras (C) and painted sample with a random distribution of speckles (D). C and D were required for the analysis made with the DIC.

7.5 Results

Figure 7-6 displays the loading versus displacement curves obtained in the tensile tests. The microstructures with the smallest layer of interface printed (t = 0.1 mm) coincide at a load of 150 N in an initial stiffness followed by a plateau (inset of Figure 7-6A). These regions of constant load can be explained by the presence of defects in the weak interface layer during the 3D printing of the dogbones in the Connex 350 machine[144]. Uniaxial tensile tests detected the presence of defects in the support layer for interface thickness with t < 0.3 mm[183]. These defects can be seen as rod to rod bridges or surface irregularities that strengthen the interfaces and toughness of the microstructures, where the plateau is due to an initial debonding of the defects. Figure 7-6A indicates that after the plateaus, hardening is observed followed by structural degradation that leads to lower reactions. An outstanding maximum peak in the load of ≈5050N is observed in the rod-like microstructure as compared with the load of ≈1200N achieved in the plate-like composite.

The plateau observed in the samples printed with the smallest interface thickness *(t* = 0.1 mm) is also observed in the response of the rod-like composite shown in Figure 7-6B with t = 0.3 mm. However, in the loading data of the plate-like composite the plateau in the response of the material is missing. By increasing the interface thickness, it is expected to decrease the presence of the interface defects. It is also observed in Figure 7-6B, that the maximum load of the rod-like microstructure is eight magnitudes greater than that of the plate-like microstructure. By increasing the interface thickness even more (t = 0.4 mm), Figure 7-6C indicates a greater peak in the reaction of the rod-like composite (≈ 220 N) as compared with the plate-like composite (≈ 73 N). Despite the presence of these

imperfections in the biomimetic composites, the natural response of the rod-like material is enhanced as compared to the plate-like material. SEM images were taking from the hexagonal rod cross sections with t = 0.1 mm, where surface irregularities are observed (Figures 7.6 D and E). The hexagonal microstructure is displayed in Figure 7-6F, where the surface defects are represented by bridges and asperities in the smaller interface thickness (t = 0.1 mm).

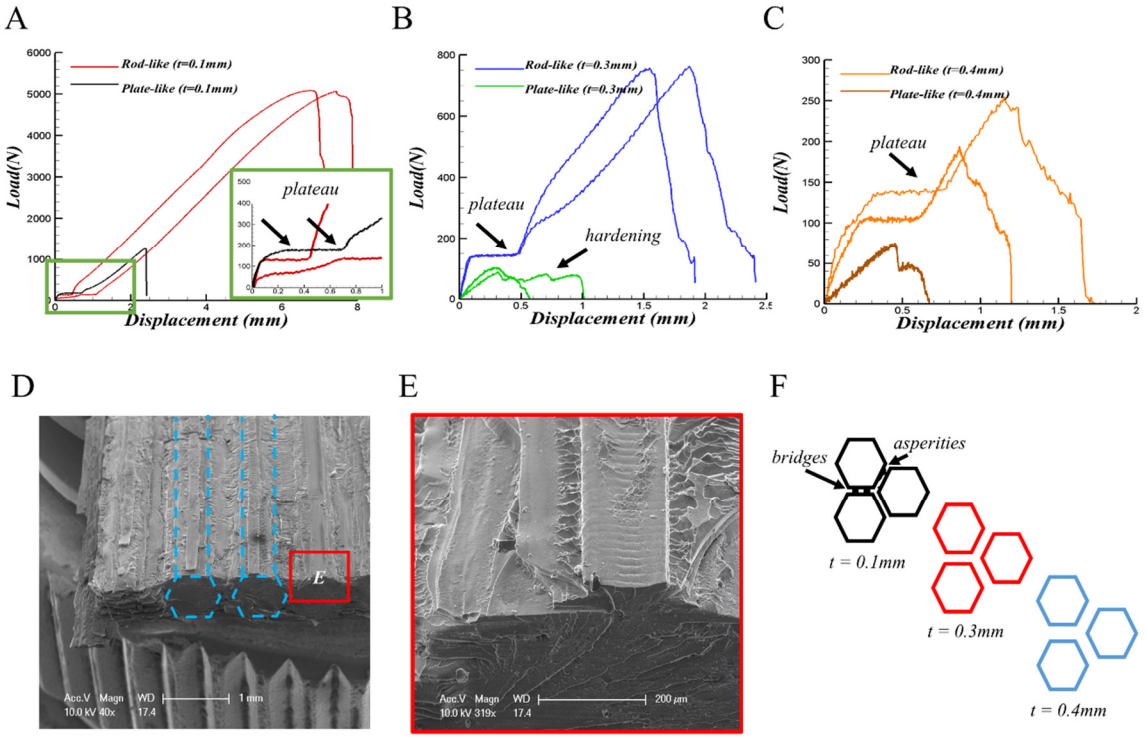

Figure 7-6 Load versus displacement curves obtained in the test at t = 0.1 mm (A), t = 0.3 mm (B) and t = 0.4 mm (C). SEM images displaying the rods of 1mm of cross section and t = 0.1 mm (D), where in the top of the rods surface irregularities are observed in (E) (SEM image courtesy of UC Riverside). Sketch magnifying the thickness of the binder, displaying the possible presence of defects at t = 0.1 mm of separation (F).

7.5.1 Strain contours

To address the interaction between the strong/weak materials in the biomimetic composites, the comparisons include the shear (e_{xy}) and tensile (e_{yy}) strain components. The response of the materials is analyzed at different stages of the tests, where the analysis is carried out with the DIC technique for the plate-like and rod-like composites.

7.5.1.1 Plate-like composites

The comparison of the shear and tensile strains for the plate-like composite with t = 0.1 mm is revealed in Figure 7-7. The results indicate an enhancement of the strains fields with the progression of the tensile test, where fracture of the interface is achieved at the bottom of the sample (Figure 7-7E). At early stages of the tests, the strain fields show a uniform pattern of deformation (Figure 7-7B and G). The plateau observed in Figure 7-7A coincides in low values of strain at the interfaces (Figure 7-7C), suggesting the debonding of the interface defects. As the mechanical tests progresses, the sliding of the tablets is noticed in the high values of e_{yy} (Figure 7-7D), where the non-symmetry of the strain contour can be explained by a small misalignment during the test. A comparison with respect to the e_{xy} indicates a lower shear deformation of $2x10^{-3}$ (Figure 7-7J) as compared with the maximum tensile strain of $5x10^{-3}$ observed at the end of the test (Figure 7-7E). The results also suggest that the sliding of the tablets is the main mechanism of hardening observed during the test.

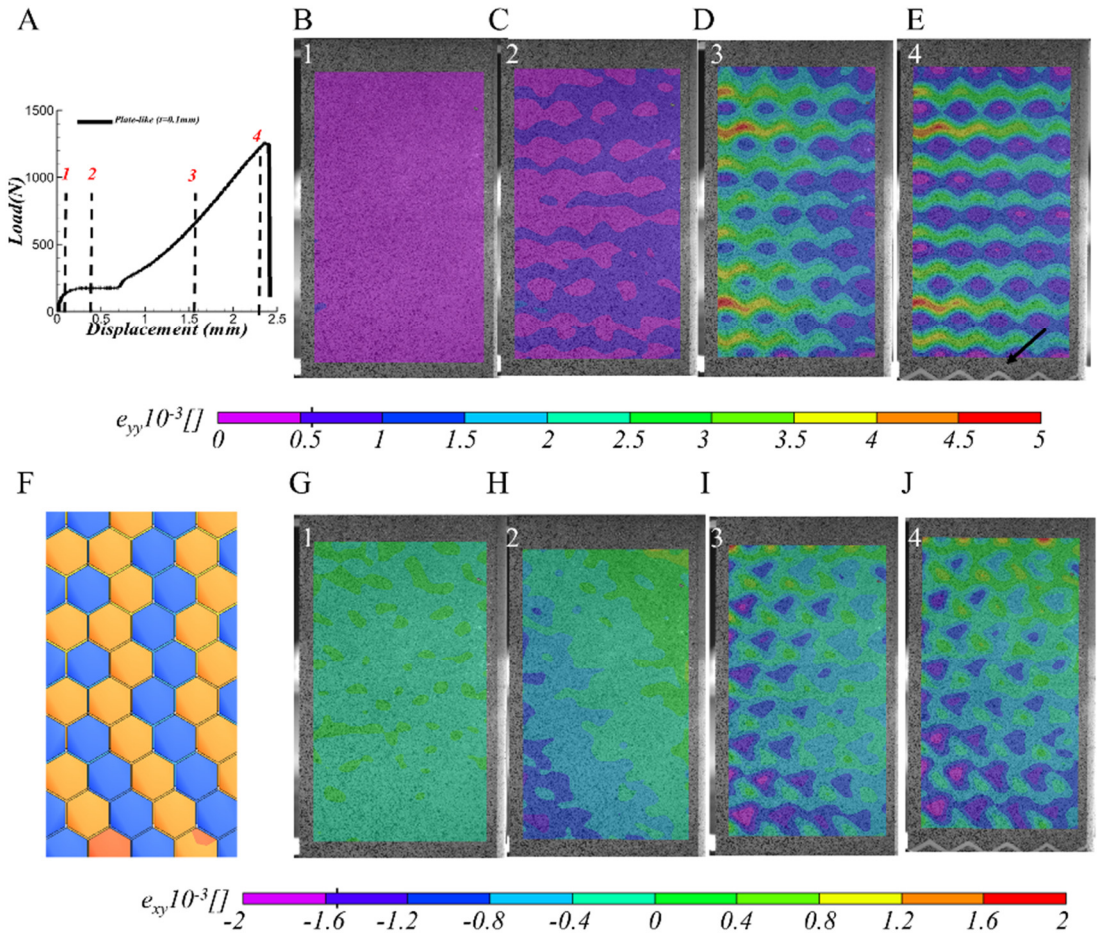

Figure 7-7 Analysis of strain contours in the plate-like microstructure at different penetrations. Experimental output obtained in A at t = 0.1 mm. Axial (ε_{yy}[]) and shear (ε_{xy}[]) strains at 0.05 mm (B,G), 0.6 mm (C,H), 2.1 mm (D,I) and 2.45 mm (E,J). The plate-like microstructure in F is shown at the same scale for comparison.

As compared to the previous loading data, the reactions measured during the tensile tests of the sample with t = 0.3 mm are lacking of a plateau region (Figure 7-8A). The sliding of the tablets is observed since early stages of the test (Figure 7-8B and G), where an initial fracture is revealed at 0.7 mm of displacement (arrow in Figure 7-8D). Despite the onset of fracture in the sample, the DIC data indicates that the sliding between the tablets is responsible for the hardening observed between 3 and 4 in the reactions measured

(Figure 7-8A). In Figure 7-8 it is possible to clearly identify the layers of support material between the tablets (Figure 7-8F), as they coincide with the maximum values of e_{yy} .The loading displacement curve of the plate-like composite resembles the response observed in hydrated nacre (Figure 7-1B) [97], with a region of large deformation and hardening, where increasing the shear contact between the interfaces since early stages improves the maximum deformation reached in the test (≈1 mm).

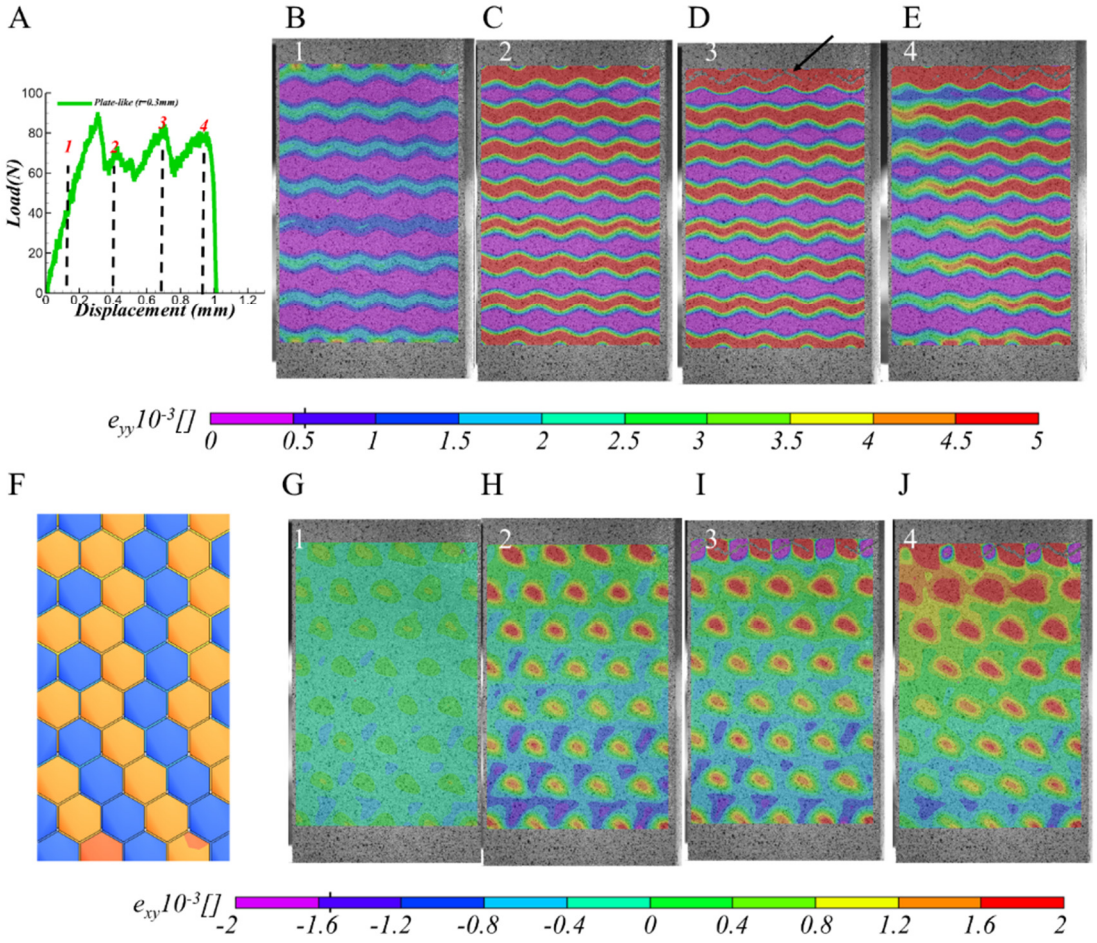

Figure 7-8 Analysis of strain contours in the plate-like microstructure at different penetrations. Experimental output obtained in A at t = 0.3 mm. Axial (ε_{yy}[]) and shear (ε_{xy}[]) strains at 0.09 mm (B,G), 0.42 mm (C,H), 0.76 mm (D,I) and 0.9 mm (E,J). The plate-like microstructure in F is shown at the same scale for comparison.

The analysis of the plate-like composite with interface thickness t = 0.4 mm is shown in Figure 7-9A. To address the effect of material defects in the building blocks, three tablets were removed from the sample surface. The loading curve indicates a maximum displacement of ≈ 0.6 mm, where sliding is observed since early stages of the test. The crack propagation is revealed at ≈ 0.4 mm (#2 in the loading data) of displacement, where the onset of fracture coincides with the region where the tablets are missing (Figure 7-9C and H). The results suggest that despite the damage localization and fracture indicated by the arrow in Figure 7-9D, the sliding in the tablets is observed in the lower section of the sample. These results confirm that even with the material removal and fracture propagation, the mechanical functionality of the microstructure to withstand loads remains active until failure [64], [142], [97].

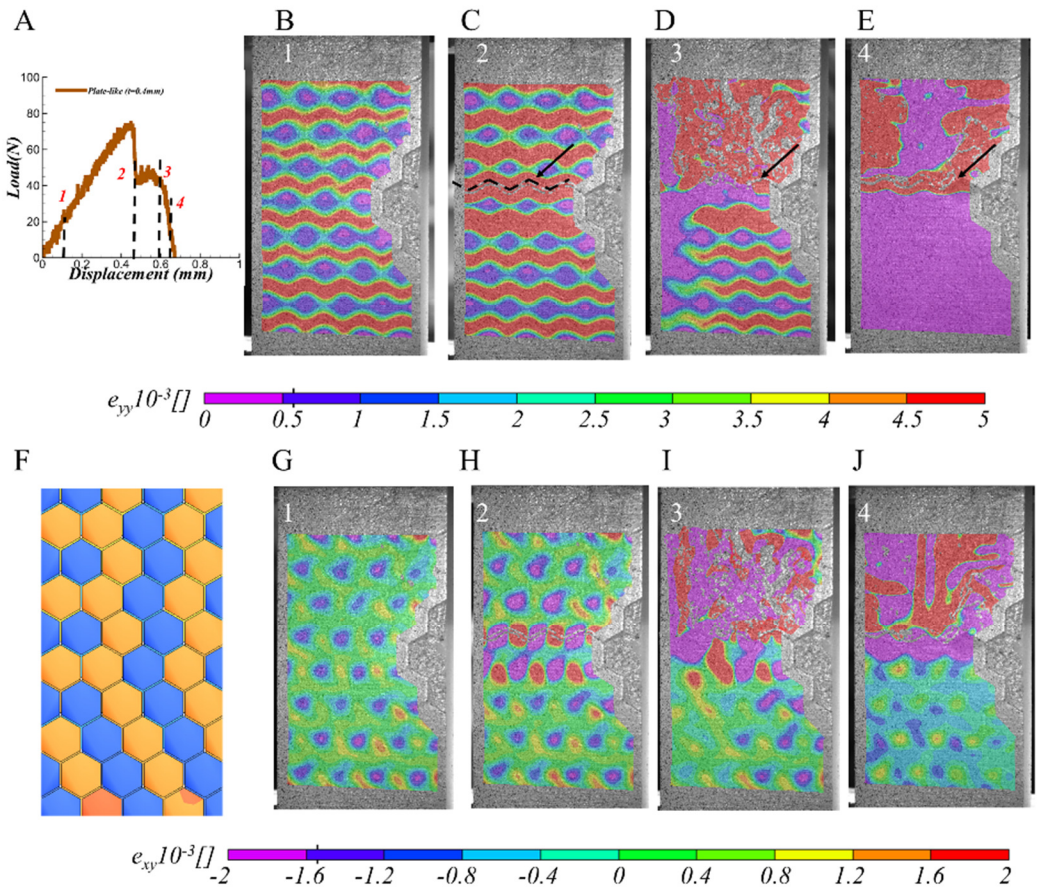

Figure 7-9 Analysis of strain contours in the plate-like microstructure at different penetrations. Experimental output obtained in A at t = 0.4 mm. Axial (ε_{yy}[]) and shear (ε_{xy}[]) strains at 0.17 mm (B,G), 0.38 mm (C,H), 0.47 mm (D,I) and 0.59 mm (E,J). The plate-like microstructure in F is shown at the same scale for comparison.

7.5.1.2 Rod-like composites

Similar to the plate-like composites, the rod-like materials were examined with the DIC to assess the effect of shear during tension. Figure 7-10 shows the results obtained with t = 0.1 mm. The analysis indicates that the plateau in the load observed in Figure 7-10A (2) coincides with the observations made in the plate-like composite (7.7C and H) of

an initial debonding of the rods at early stages of the test. As compared to the plate-like composite, the configuration of the rod-like material is not displaying large deformations in the interface layer. Localization of the fracture begins in the horizontal layer of the support material (arrow in Figure 7-7E) followed by a vertical crack (arrow in Figure 7-7J) which leads to sample failure.

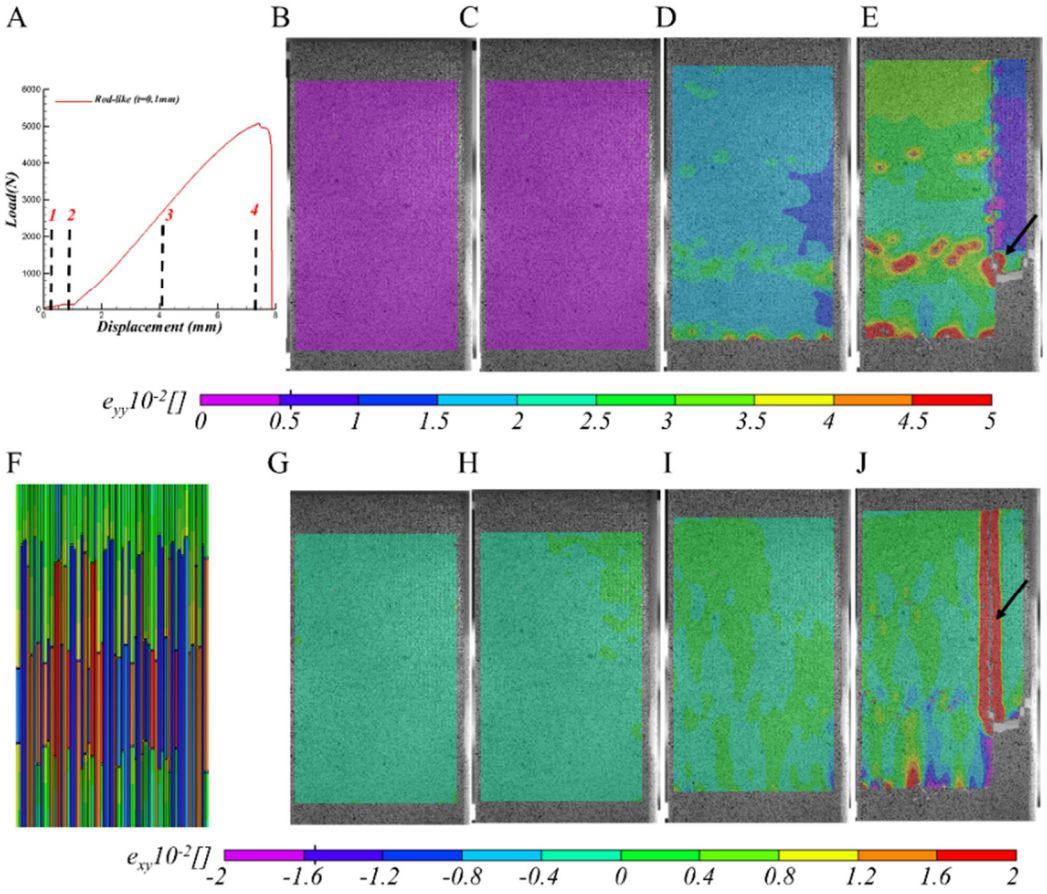

Figure 7-10 Analysis of strain contours in the rod-like microstructure at different penetrations. Experimental output obtained in A at t = 0.1 mm. Axial ($\varepsilon_{yy}[]$) and shear ($\varepsilon_{xy}[]$) strains at 0.21 mm (B,G), 0.19 mm (C,H), 4 mm (D,I) and 7.91 mm (E,J). The rod-like microstructure in F is shown at the same scale for comparison.

The deformation of the rods with an interface thickness t = 0.3mm is revealed in Figure 7-11. The rod-like composite displays large axial strains ($\approx 5x10^{-2}$) in the horizontal

staggered interfaces (Figure 7-11D), where the crack propagation in the interface layers is distributed across the entire sample (Figure 7-11E). As compared with the composite of separation t = 0.1 mm (Figure 7-10I), the shear strain contour reveals large values in the vertical direction that seem to coincide with the layers of support material between the rods (Figure 7-11I). Hardening is observed in the reactions measured in #3 (Figure 7-11A), explained by the enhancement of the shear strain in the interface layers (Figure 7-11I).

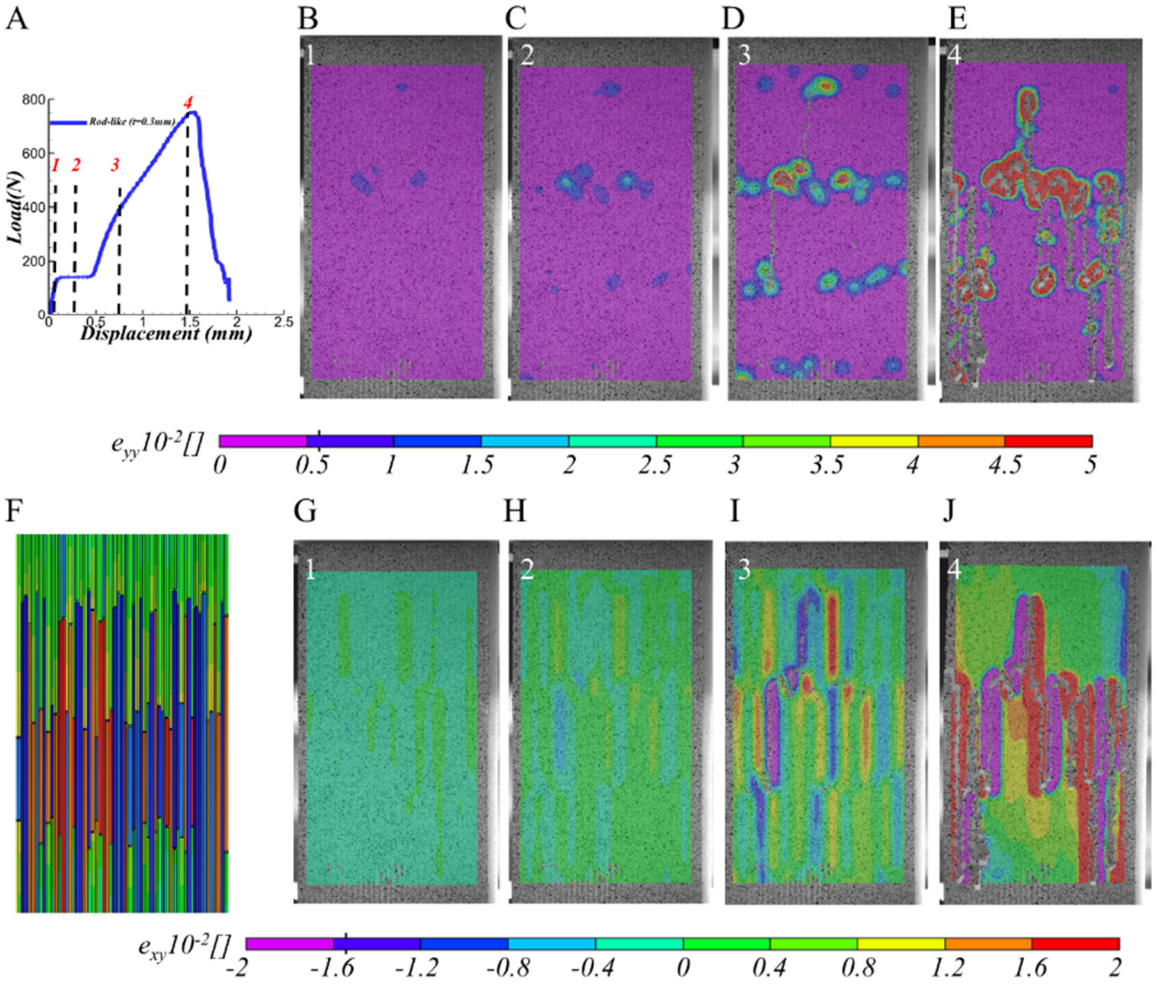

Figure 7-11 Analysis of strain contours in the rod-like microstructure at different penetrations. Experimental output obtained in A at t = 0.3 mm. Axial (ε_{yy}[]) and shear (ε_{xy}[]) strains at 0.18 mm (B,G), 0.6 mm (C,H), 1.25 mm (D,I) and 1.5 mm (E,J). The rod-like microstructure in F is shown at the same scale for comparison.

As compared to the previous rod-like composites, the microstructure with t = 0.4 mm shows the lowest peak load ≈ 220 N. Similarly to the previous cases, the plateau (2 in Figure 7-12A) concur with the beginning of interface debonding (Figure 7-12 C and H), which occurs at a displacement of ≈ 1mm (Figure 7-11A and 7.10A). The composite shows delamination at the last stages of the test, where the crack patterns have the maximum spread seen along the interface layers (Figure 7-12 E and J). Despite the spread of damage, hardening is observed in the tensile data in 3 (Figure 7-12 A), and is associated with the interaction between the rod and support material (Figure 7-12 D and I).

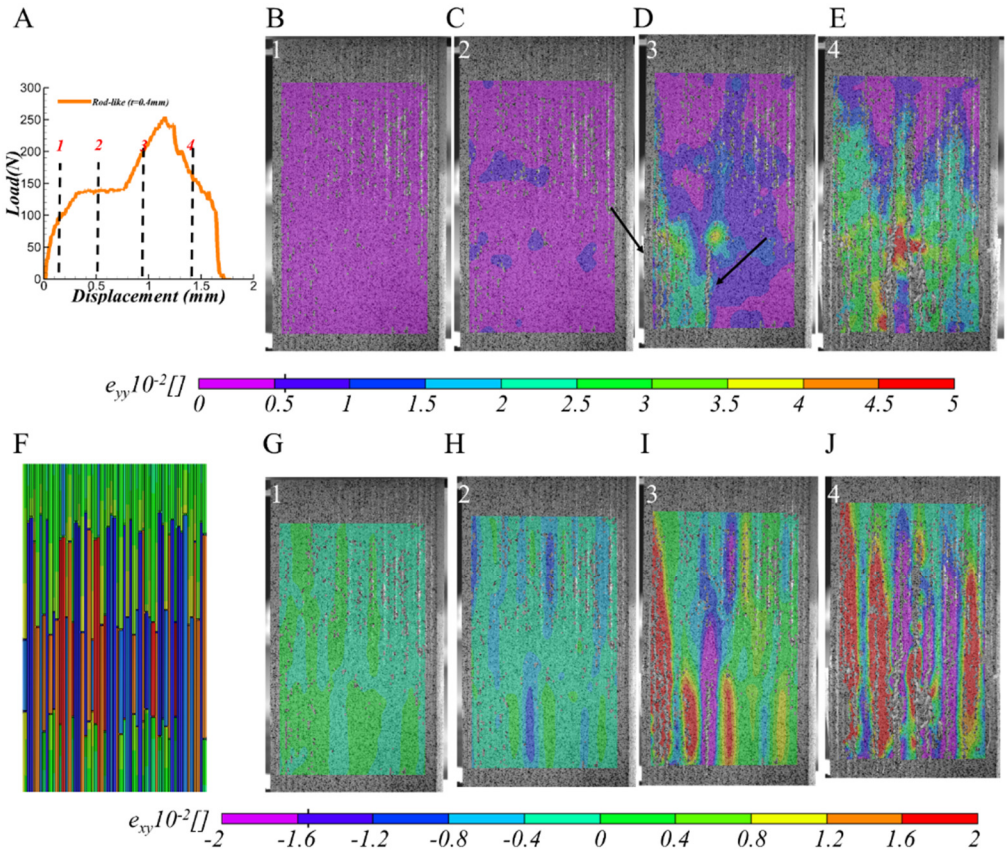

Figure 7-12 Analysis of strain contours in the rod-like microstructure at different penetrations. Experimental output obtained in A at t = 0.4 mm. Axial (ε_{yy}[]) and shear (ε_{xy}[]) strains at 0.15 mm (B,G), 0.5 mm (C,H), 0.99 mm (D,I) and 1.25 mm (E,J). The rod-like microstructure in F is shown at the same scale for comparison.

7.5.2 Stiffness calculation

The values of E were obtained from the plots of stress versus strain of the different composites and are compared with respect the values obtained from equation 7.1. Figure 7-13A shows an enhancement in E by increasing the V_f. At a value of $V_f() = 0.8$, the plate-like and rod-like composites have similar values of stiffness and a difference 47% with respect the value computed from equation 7.1. At a $V_f() = 0.56$, the value of E shows a larger difference of 69% between the rod and plate-like composite, as compared with the prediction made by equation 7.1 that shows a discrepancy of 9% with the plate-like composite. The larger difference with respect to equation 7.1 at a $V_f() = 0.8$ and 0.56 might be associated with the presence of surface irregularities (e.g. asperities) which could trigger an enhancement in the toughness of the rod-like composites that coincides in the presence of plateaus in the loading data. At a $V_f() = 0.48$, the differences in the values of E between the plate and the rod-like microstructure is 28% (inset in Figure 7-13A) and 4% with respect to the equation 7.1 The values of E are also enhanced by increasing the ratio of A/V (Figure 7-13B), where the correlation between V_f and the A/V is given by $A/V = (2h+ \sqrt{3}w) V_f/(\sqrt{3}wh)$.

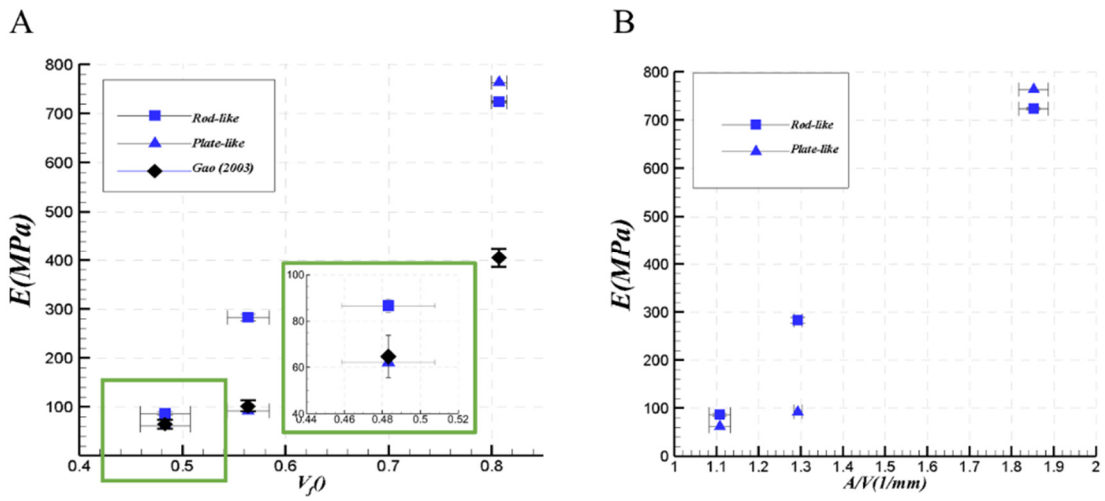

Figure 7-13 Summary of Young's modulus obtained in the tensile tests. Young's modulus versus the Vf() in (A) and versus A/V(1/mm) in (B).

7.6 Discussion

In this chapter, a set of biomimetic composites have been 3D printed and exposed to tensile loads. A parametrization has been addressed in section 7.3 to understand the role of the geometrical features (*W, L* and *t*) in V_{fm} and A_{ol}/V_{mb}. As depicted in this work, Gao et al. [93], [72] correlated the influence of the V_{fm} in the stiffness of the biocomposites, where it is predicted (Figure 7-2) an enhancement in the stiffness measured in the chiton as compared to the nacreous microstructure. To address the influence of the area between the organic layer and the mineral blocks, and following the learnings of composite materials [127] an expression to calculate A_{ol}/V_{mb} is given in equation 7.3. The isoparametric surfaces shown in Figure 7-4 suggest that while smaller rods are necessary to achieve higher values of A_{ol}/V_{mb}, which would lead to an improvement in the transfer of loads [127], higher values in the rod diameters and lengths are required to increase the V_{fm}. As compared to nacre, the

parametrization indicates that the chiton tooth has a similar amount of V_{fm}, but a ratio of A_{ol}/V_{mb} three orders of magnitude greater.

To address the influence of the shape and orientation of the building blocks, and to avoid inconsistencies in the analysis, the values of A_{ol}/V_{mb}, V_{fm} and ρ were kept constant between the pairs compared (Table 7.3 and 7.4). The results indicate an improvement in the maximum loads and displacement achieved in all the rod-like microstructures (Figure 7-6). The results suggest that decreasing the interface thickness from $t = 0.3$ mm to 0.1 mm correlates with the presence of plateaus in the loading data, which are associated with defects during the 3D printing process. The mechanical tests performed also indicate that sliding of the rods/tablets lead to hardening in the loading data, an interaction that remain active even with fractures (Figure 7-9 and 7.11). To understand the role of the rods/plates in the crack propagation, the DIC data was analyzed before reaching sample failure (Figure 7-14). The out of plane deformation shows the localization of the fractures in two sections of the rod-like composite with $t = 0.1$mm (Figure 7-14A). Increasing the interface thickness to $t = 0.3$mm the sample reveals spread of damage across the interfaces (Figure 7-14B). By increasing even more the interface thickness to $t = 0.4$mm, rod bending and material removal is observed (Figure 7-14C). While damage localization might lead to instabilities [64], the spread of damage could lead to an enhancement in the toughness of materials. As compared to the rod-like composite, the experimental results in the brick wall reveal a unique interface layer with fracture (Figure 7-14D) lacking of large out of plane deformation. These results suggest that through the spread of damage, the rod-like composites enhance the mechanical response of the material during tensile loading.

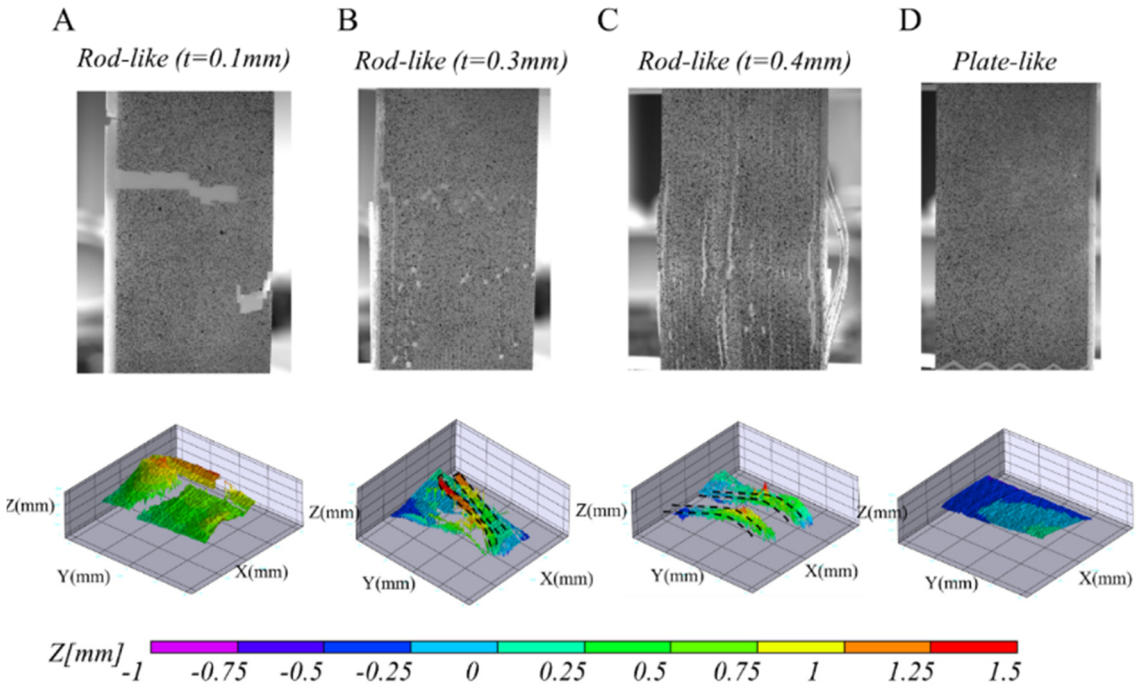

Figure 7-14 Failure modes observed in the rod-like and plate-like microstructures. While localized damage is observed at t = 0.1 mm (A), spread of damage and rod debonding is observed for t = 0.3 mm (B) and t = 0.4 mm(C). In contrast to the rod-like composites, the plate-like layout shows a row of plates with crack patterns (D). The contours below reveal the out of plane deformation of the samples.

7.7 Conclusions

A set of biomimetic composites have been 3D printed with a rod and plate-like microstructure, where the samples have been mechanically tested under tensile loads. The tension-shear model is used to analyze the influence of the geometrical parameters in the Young's modulus of the biological materials. Compared to nacre, the analysis of equation 7.1 predicts an enhancement of 43% in the stiffness of the rod-like microstructure of the chiton. To address the influence of the geometrical features, a parametrization of V_{fm} and A_{ol}/V_{mb} is presented in this study. The analysis suggest that despite the fraction of mineral

differs by a 10% in the chiton tooth and nacre, the ratio of A_{ol}/V_{mb} is three times larger in the tooth. Studies in composite materials suggest that increasing the A_{ol}/V_{mb} would lead to a better transfer of the loads and as consequence to an enhancement in the toughness of the microstructure. It is then proposed that the microstructure of the chiton tooth is optimized to withstand large tensile loads parallel to the main axis of the rods.

The analysis of the experiments has been carried out with the help of the DIC, where the shear and axial strain components are displayed. Plateaus in the loading data have been assessed by the presence of defects (e.g. rod to rod bridges and asperities) in the interfaces of the composites. Hardening in the experimental data is associated with the sliding of the rods/tablets. The damage in the biocomposites has been observed in the weak interfaces, where the shear between the rods enhances the spread of damage as compared to a more localized fracture in the tablets. Despite the defects that might exist in the 3D printed material, the rod-like composite suggest an overall enhancement in the maximum displacements and loads obtained during the tensile tests. In the experimental analysis I considered only one set of geometrical features: future extensions of this work must address the role of the geometrical parameters in the crack propagation, strength and using in situ ESEM mechanical tests in the biological materials. Possible applications of this work include the development of lightweight and tough resistant structures

CHAPTER 8. INVESTIGATING THE TOUGHENING MECHANISMS OF THE STROMBUS GIGAS

8.1 Introduction

The same principles considered in the study of the abrasion resistance of the chiton tooth (chapter 4, 5 and 6), can be considered to study other highly mineralized materials. An example of the application of this study can be seen in the Strombus gigas, also known as the "pink conch" [184], a gastropod that is commonly found in the Caribbean region [185]. The shell (Figure 8-1A) is composed of three distinct crossed lamellar layers (or 0^{th}), the inner middle and outer with differing 1^{st} order directions (Figure 8-1B). The crossed lamellar microstructure is a hierarchy composed at least of 4 different orders of features at length scales ranging from nanometers to millimeters [25], [186]. The 4^{th} order is comprised of individual aragonite crystallites of approximately 5 nm in size, which are twinned in the {110} direction (Figure 8-1C). Multiple 4^{th} order crystallites are combined together to form the 3^{rd} order lamellae in the shape of rectangular planks, approximately of 150 nm wide (*W*) by 100 nm thick (*T*) and several micrometers in length (Figure 8-1C). The 2^{nd} order lamellae are composed of tens of thousands of 3^{rd} order lamellae arranged into a rectangular beam that is 10-20 μm wide, 20-50 μm thick, and up to several hundred micrometers in length (Figure 8-1C). Within the 2^{nd} order lamella, the 3^{rd} order lamellas

are separated by a thin layer of organic material. The 1st order lamellae are composed of many parallel 2nd order beams arranged into a sheet (Figure 8-1C). The crossed lamellar system is composed of multiple parallel 1st order lamellastacked next to each other with perpendicular 2nd order directions between adjacent layers (Figure 8-1C).

The remarkable toughness of the crossed lamellar structure is due to a number of mechanisms. During bending the initiation of multiple cracks in the inner layer occurs due to a difference in toughness between the "weak" inner and "tough" middle layers [25], [186]. Each macro-layer has a "weak" direction that when load is applied causes delamination along 1st order lamella interfaces. However because the direction of 1st order lamellae is nearly perpendicular between adjacent layers, a crack that propagates through the weak direction in one layer is redirected at the interface of adjacent layer. Within a single 1st order lamella there are two principle directions in which a crack can grow; the weak direction which causes delamination along 2nd order interface, and the strong direction where the 3rd order lamellae are in tension. Fractures along the weak direction of 1st order lamella are bridged by adjacent 1st order lamellae that have their 2nd order lamellae in a perpendicular direction. The 1st order interfaces are rough to increase the friction between adjacent layers allowing for load to be transferred, the toughness of the 1st order interfaces were examined by 3pt bend[187]. Within the 3rd order lamella there is an increase in the formation of fractures compared to geological aragonite [25]. However the toughness of the 2nd order lamella is still unknown.

Nanoindentation can be utilized to determine the hardness and elastic modulus of different microstructural features by examination of the load-displacement curves using the methods outlined by Oliver and Pharr[86]. At higher indentation loads it is possible to

produce cracks radiating from the corners of the indentation probe. In homogenous materials the length of the resulting cracks is related to the fracture toughness of the material[41]. However this technique is not possible for materials with a fine microstructure, because multiple cracks will be imitated in the sample and not just at the corners of the probe. The purpose of this study is analyze the influence of the plastic dissipation and crack propagation in the natural response of the material.

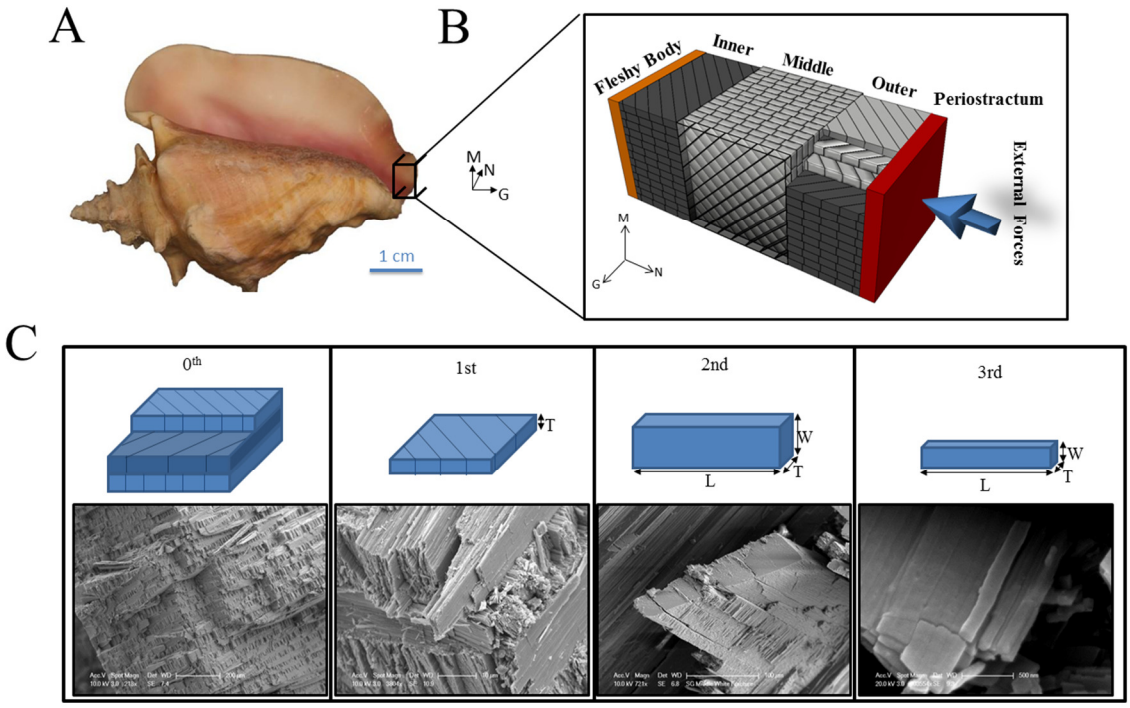

Figure 8-1 The Strombus Gigas in (A), a gastropod that can be found in the Caribbean region[185]. Its aragonite shell (B) is composed of different layers (Inner, Middle and Outer) with the dip directions aligned ± 45° from N (radial direction). An illustration of the fracture shell showing the different layers with alternating 1st order lamellae. Representation of the geometry of the 0th through 3rd order features of the cross lamellar structure, where the SEM images are shown at the bottom of (C). In (C), *T* is referred to the thickness and *W* to width of the blocks. Images on (C) are courtesy of UC Riverside.

8.2 Influence of the building block orientation in the surface damage

Nanoindentation was performed in UC Riverside by Chris Salinas, using Ti-950 nanoindenter (Hysitron usa) equipped with a low load, max 13mN transducers with cube corner probes. The indents were displacement controlled to a depth of 1μm. Indents were performed in the middle of the 1st order lamella in the ±45° orientation. In addition two orientations of indenter probe were examined, the first is with the triangular cube corner indent pointed towards the outer surface with one of the edges parallel to the 2nd order interface; in the second case the sample was rotated by 180° such that the point of the indent is towards the inner surface. In both planks orientations, the indentation data indicates a difference of 5% in the maximum load achieved (P_{max}) (Figure 8-2 A and B). Despite, the indentation data shows a similar response in both orientations, a difference is noticed in the damage associated to the surface of the microstructure. In rectangular planks oriented at -45°, the SEM images of the microstructure indicate material removal and spread of damage (Figure 8-2 C). In contrast, micro-cracks and localization are observed at +45 of plank orientation (Figure 8-2 D).

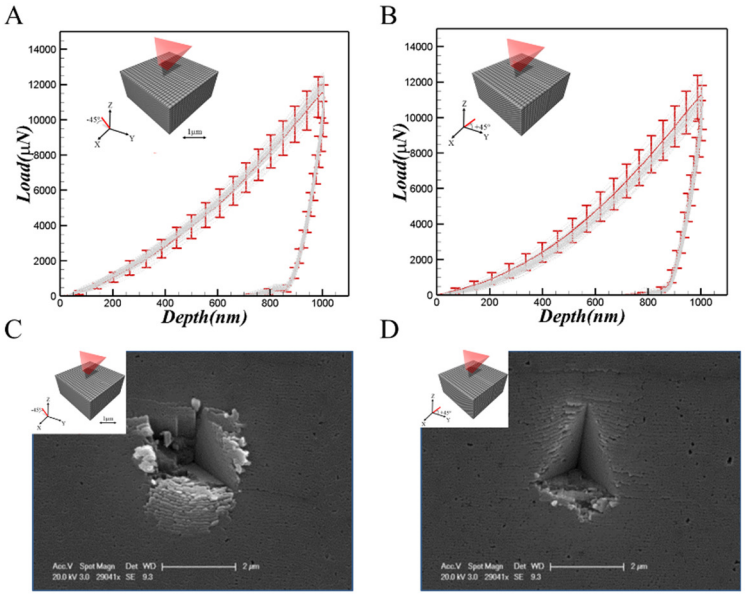

Figure 8-2 Indentation data obtained at ±45° of plank orientation (A and B). SEM images of the damage observed in the surface of the microstructure at -45° (C) and +45° (D) orientation.

8.3 Application of the micromechanical model

The micromechanical model have been addressed to study the correlation between the cracks patterns observed in Figure 8-2C and D, and the orientation of the third order lamellae. Noticing the characteristic rectangular shape of the 3rd order units (rectangular blocks of 150nm by 200nm of cross section and several micrometers of length), the model considers a bundle of oriented blocks under the penetration of a sharp cube corner indenter (internal angle ~35.3°). Due to the outstanding plastic behavior that have been observed in the aragonitic blocks with advanced microscopic techniques [116], a linear isotropic hardening model was considered (E = 90 GPa,ν=0.3 [64]). The contact formulation

presented by Johnson [82] is used to obtain the yield stress (σ_{yield} = 2.5GPa), which is in agreement with other previous works [70]. The linear isotropic strain-hardening parameter (H_{iso} = 40 GPa) of the von Mises yield function [79] was obtained by comparing the loading data of computational models with nano-indentation of monolithic aragonite [81]. Four different arrangements of uniformly distributed elongated blocks, oriented at -45°, +45° and 90° with respect to the Y axis (Z-Y plane), are modeled (Figure 8-3A, B and D). To observe the advantage with respect to the ±45°, the 90° of orientation have been studied.

A cohesive interface model is considered between the blocks to represent the behavior of 1 vol. % of chitin that wraps each unit volume. Previous studies have shown that micro-cracking and crack bridging are mechanisms of the Strombus Gigas microstructure to overcome catastrophic failure between the inner, middle and outer layer[25], [188], [189]. However, the role of the strength and cohesive energy of the organic material between the third order lamellae to withstand biting attacks has not yet been analyzed. The cohesive behavior of the organic material is modeled with a cohesive traction-separation law [53], in which the cohesive strength (T_{max}) and energy (G_c), peak traction and area under the traction-separation law shown in Figure 8-3C, respectively, mimic the nano-scale features that characterizes this type of microstructure (e.g. mineral bridges, asperities and molecular strength). The cube corner indenter was modeled as a rigid frictionless surface. To show that the indentation curves are independent of the microstructural alignment, an offset of 45° with respect to the X axis (X-Y plane) (Figure 8-3E) was purposely introduced in the -45° orientation (Figure 8-3A). A systematic and parametric analysis is carried out to study the role of T_{max} and G_c of the organic interface studied. As multiple data points have been obtained from the simulations, the loading

curves have been fitted with a power function ($P=c_1h^{\alpha}$) following references [28], [85], where c_1 is a parameter that depends on the microstructure, h is the depth, P the load and $\alpha = 1.5$ for a cube corner indenter. The indentation curves of the conch have a correlation coefficient with the power law of $R^2 = 0.98$, in which the material constant $c_1 = 0.368 \pm 0.024$ $\mu N/nm^{1.5}$. The loading results indicate that by increasing both T_{max} and G_c (laws I, II, III and IV in Figure 8-3C), the architectures increase their resistance to penetration, in which the traction-separation laws III and IV fit the experimental data. It is possible to predict that by increasing $T_{max} \rightarrow \infty$, the microstructures behave as a homogenous aragonitic material. The T_{max} value adapted in the traction-separation law of the organic interface of Figure 8-3F is of the same order of magnitude to those proposed for interfaces in similar biological systems [64], [190], [191]. In agreement with the observations made by nano-indentation experiments in the conch, the loading curves suggest that the different architectural designs modeled with the traction-separation law I do not show a significant difference in the load values.

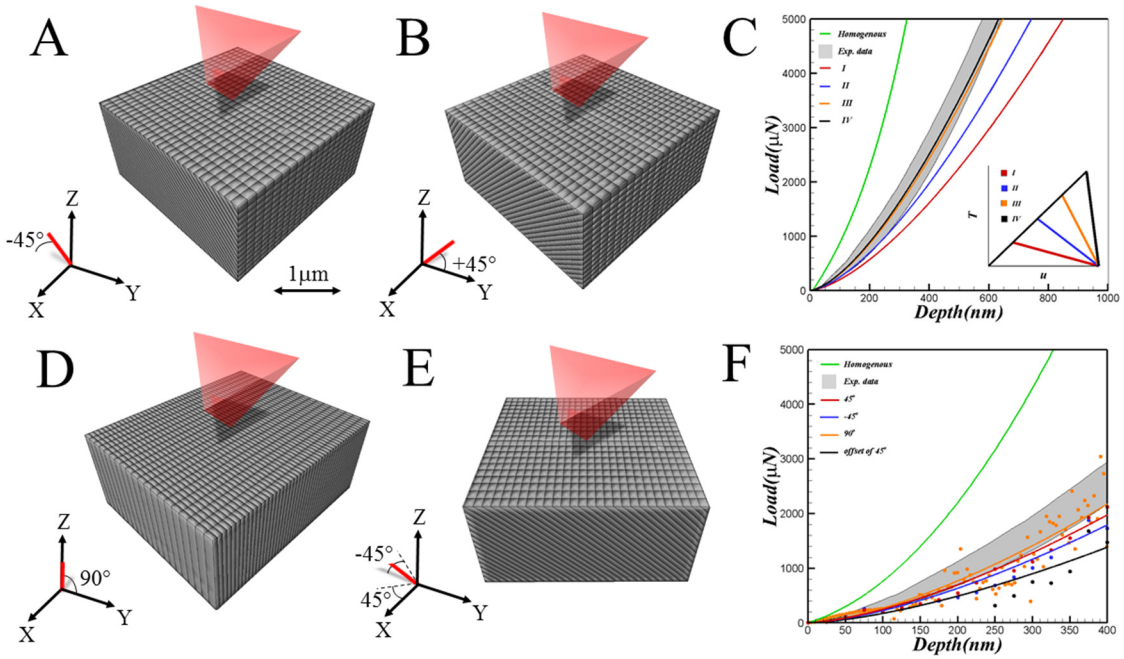

Figure 8-3 Diagram displaying the cube corner indenter alignment with respect a 2nd order lamellae (4 μm x 4 μm x 2 μm) embedded in a semi-infinite solid that for simplification is not shown above. Around 840 building blocks included in the model are exposed to the cube corner indenter with microstructural architecture of -45°, 45° and 90° with respect the Z-Y plane (A, B and D) and offset configuration of 45° with respect the X-Y plane (E). Comparison of an average experimental data shows that the continuum model predicts an increase in the loading response of -45° with respect the Z-Y plane, as T_{max} and G_c increase (C); an illustration plot of the different traction-separation laws is shown in C for I (T_{max}=12.5 MPa,G_c=0.625 J/m^2), II (T_{max}=25 MPa,G_c=1.25 J/m^2) ,III(T_{max}=200 MPa,G_c=10 J/m^2) and IV(T_{max}=800 MPa,G_c=40 J/m^2); FEM shows that microstructural alignment is not largely affecting the response of the material with a traction-separation law (I) (F). Values were fitted with the power function, $P=Ch^{\alpha}$, where C is a constant and α=1.5 for a cube corner indenter; data points are shown in F.

As the residual stress field beneath the indenter is only affecting a plastic zone of finite dimension, it is not always possible to estimate the mechanical anisotropy of bio-mineralized materials (Figure 8-4)[22]. The loading curves obtained with the -45°architecture (Figure 8-4A) show that the organic interfaces have an important contribution in the resistance to penetration and toughness of the conch. It is surmise a

competition between inelastic deformation and decohesion between them. As localized von Mises stresses are observed inside the blocks at the +45° orientation (Figure 8-4B), more pile-up and energy dissipation is shown in the -45° and offset alignment (Figure 8-4A and E). The damage observed is consistent to that of the conch at 500nm of maximum penetration (Figure 8-4C and D), in which large deformation is observed in the sides of the indenter planes and indentation marks are characterized by a lack of radial cracks. Our models predict that the blocks parallel to the loading direction Z (Figure 8-4A), dissipate more plastic deformation into other lamellas, suggesting that the 90° configuration will show less effective strength with respect the other configurations (Figure 8-3A, B and E) to withstand biting attacks, a trade-off for a higher resistance to crack propagation.

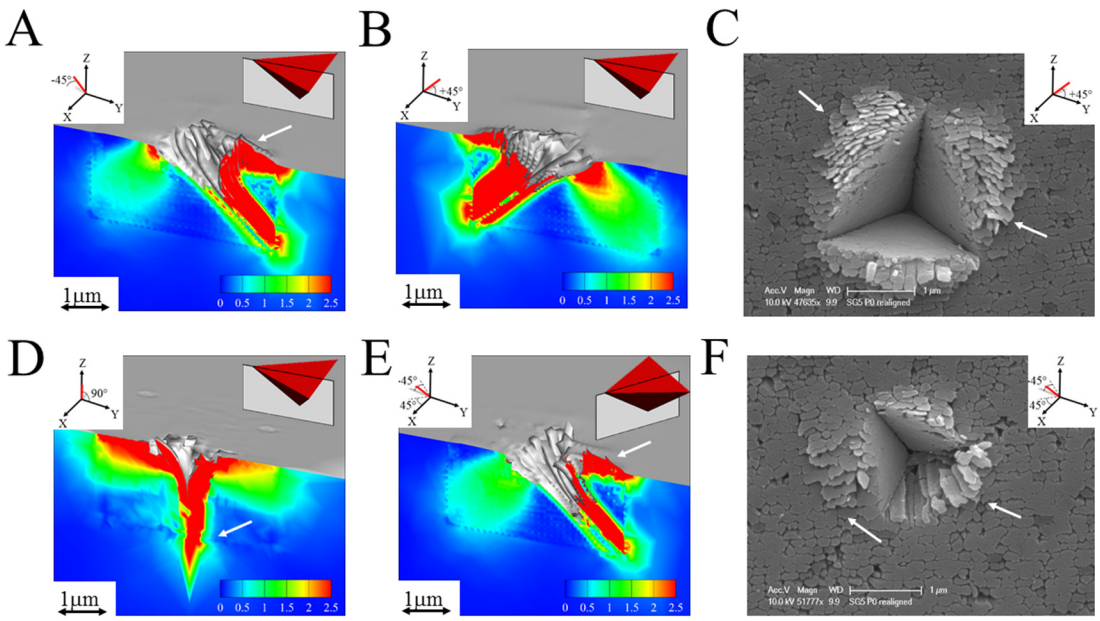

Figure 8-4 Sliced views of von Mises stress contours indicating regions with inelastic deformation in GPA at 400nm of penetration depth, the sliced views coincide with a symmetry plane of the indenter; despite obtaining similar loading indentation curves, cracks patterns and localized damage differ in the different configurations. While the orientation of 135° (A) and offset (E) alignments show similar crack patterns and deformation mechanisms to those analyzed by SEM (F), the 45° orientation shows an area with more localized damage (B) comparable with experimental observations made at a maximum displacement of 500nm of penetration (C); FEM of the 90° shows the disadvantage of 2nd order bricks perpendicular to the surface of the conch, where inelastic deformation is more evenly distributed affecting a larger number of aragonite blocks. Arrows indicate areas with pile up and crack patterns.

8.4 Biomimetic approach

To unveil the effect of plank orientation in the effective mechanical properties measured during indentation, biomimetic materials were fabricated with additive manufacturing following the 3rd order lamellae architecture. Samples were manufactured with 50mm x 50mm x 60mm of dimension, with rectangular building blocks (1mm x

0.5mm) surrounded by a thin weak layer (0.1mm), where the microstructures (90°,-45° and 45°) were exposed to an aluminum cube-corner indenter. A polyethylene-like material was considered for the planks (E = 1100-1700MPa) [144] and a more compliant resin (E = 0.93GPa)[63] in the weak interfaces. Displacement control indentation tests were performed in an electromechanical testing machine with a load cell of 10kN (MTS, Eden Prairie, MN, USA). As creep affects the mechanical attributes of the printed materials after two weeks of fabrication [63], indentation tests were performed within the first 24 hours of sample production. Subsequent to the indentation tests, the data was analyzed using the same experimental procedure followed in the conch. Figure 8-5A shows the results obtained for indentation tests at h_{max} = 3mm (90°) and h_{max} = 6mm (45° and -45°), where the difference in the maximum penetration is due to instabilities in the crack propagation for rods aligned with 90° of orientation. To test the critical load for catastrophic failure (P_{cri}), indentation tests were performed at different maximum penetrations (h_{max} varying from 1 mm to 6 mm). The P_{cri} measured in the samples, it refers to the maximum load obtained in the tests with stable crack propagation. The comparison in Figure 8-5A suggest that, despite the orientations of 45° and -45° show similar P_{cr} values, the critical loads are much greater than those obtained for 90°. In the case of the biomimetic designs, the energy dissipation and localized damage depends of the rod orientation, where superficial cracks follow the path of the weak interfaces at 45° and -45° (arrows in Figure 8-5B) and localized damage up to h_{max}=3mm at 90° (Figure 8-5C). An advantage of additive manufacturing is the possibility to control the ratio between the properties of the building blocks and the weak interfaces, where it is possible to replicate common nano-scale geometrical features (e.g. mineral bridges and asperities). Despite the presence of defects intrinsic of the

manufacturing process [141], leading to rod-rod bridging and surface asperities, the results suggest that energy dissipation occurs in the weakest interfaces. Similar to the micromechanical models, the biomimetic designs reveal that the rod orientation (with respect to the loading direction) influences the abrasion resistance of the samples of 90° of orientation when $h_{max} > 3$mm.

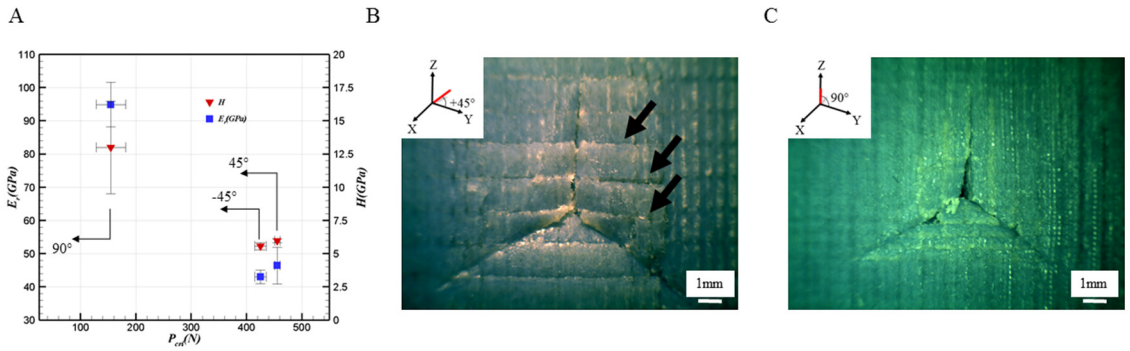

Figure 8-5 Overview of the indentation data and marks obtained in the biomimetic designs. (A) Indentation data obtained (E_r and H) versus P_{cri}, post intended marks showing energy dissipation at +45° (B) and 90° (C). Indentation marks in B were performed at h_{max}=6mm and in C at h_{max}=3mm.

8.5 Summary

A micromechanical analysis of the damage mechanisms to resist penetration of the 2nd order lamellae of the Strombus gigas has been presented. The computational model takes into account the plastic behavior of the aragonitic blocks and the fracture behavior of the interfaces. The constitutive model considered in the rods (σ_{yield} = 2.5GPa and H_{iso} = 40GPa), it was obtained by comparing the loading data of computational models with nano-indentation tests of the monolithic material. The analysis of the model included the

characterization by cube corner indentation tests of aragonitic rectangular planks oriented at ±45° and 90°. By comparing the computational models of +45° and -45°, it was shown that the microstructural alignment is not largely affecting the response of the material. However, the analysis of the stress fields revealed more localization in the +45° orientation and large deformation in the sides of the indentation marks of the -45°. As compared to the ±45°configurations, the rods oriented parallel to the indenter showed large spread of damage towards the other lamellae. To analyze even further the advantages of the different architectures, a set of biomimetic designs were 3D printed with the same alignments analyzed in the computational models. Indentation tests in the samples coincided in a large localization of damage at 90° of orientation with the FEM. The analysis of the results obtained in the ±45° orientations, also indicated higher loads to achieve critical failure as compared to the 90° layout. These results suggest the advantages of the natural ±45° layout of the aragonite layer to resist biting attacks. Compared to the standard experimental tests where site-specific moduli are the only parameters obtained from the indentation curves, the computational models demonstrated the benefits of visualizing the stress fields under the indenter. Similar to the shell of the Strombus gigas, other mineralized microstructures can be analyzed with these methods.

CHAPTER 9. CONCLUSIONS

A set of experimental tests as well as computational and analytical models have been addressed to understand the mechanical behavior of the highly mineralized rod-like microstructure of the *Cryptochiton stelleri*.

A material characterization was carried out in the exterior shell and core of the tooth. Nanoindentation tests revealed a gradient of site specific moduli. A higher reduced Young's modulus (E_r) and hardness (H) was observed in the leading edge of the tooth, a region that coincides with a smaller rod diameter and which is dominantly loaded in tension. To understand the influence of the geometrical and nano-scale features, a three dimensional continuum micromechanical model of indentation tests has been applied.

The damage criterion has been applied to study the crack propagation in an isotropic material of a given input value of fracture toughness (K_c) and Young's modulus (E). The visualization of the crack patterns suggests the evolution of radial cracks into a half-penny crack morphology, where the values of K_c measured with the LEM model revealed a 10% of accuracy with respect to the input value. The validation of the model also included the comparison of the values of E_r predicted at different penetrations with the Oliver and Pharr formulation that was used to characterize the mollusk.

The results obtained from the analytical model, showed a 3% error with respect to the input value of E. This particular approach has the advantage that it allows to quantify the value K_c of a solid, independentlyof the length of the cracks considered in the LEM model.

After studying the energy dissipation in isotropic material, simulations were carried out with a continuum micromechanical model that takes into account homogenous and isotropic rods surrounded by interfaces allowed to break. In the rods, a plasticity model of the monolithic magnetite (σ_y = 3.5 GPa, H_{iso} = 40 GPa) was considered. The values were obtained by fitting the numerical models to the indentation data of the mineral. To avoid inconsistencies while comparing the indentation data of several microstructures, the FEM was compared with the slope of the indentation data (c_1). The dimensional analysis suggests that the maximum strength (T_{max}) and yield stress (σ_y) has a greater influence on the resistance to penetration, as compared to G_c and H_{iso}, respectively. To account for the nanoscale features which prevent decohesion of the interfaces, different values of interface strength (T_{max}) were considered. The comprehensive study indicates a correlation between energy dissipation mechanisms and the slope of the indentation data of the tooth. The FEM suggests that through the energy dissipation in the interfaces, the rod-like microstructure avoids high stresses that could lead to the failure of the rods. By tracking the energy dissipation and plotting the three dimensional maps, a competing mechanism between energy dissipation in the rods and interfaces has been revealed. While the localization of damage in stronger and tough interfaces would lead to a higher resistance to penetration, it would increase the probability of failure in the rods. In

contrast, it is observed a higher probability of survival of the rod material at the expense of more fragmentation and spread of damage in the interfaces.

To address the influence of the geometrical features during indentation tests, a set of 3D printed materials were indented with a cube corner tip. Compared to the rods of random and perpendicular orientation, the property maps showed an enhancement in the site-specific modulus of the rods parallel to the indenter. The influence of the aspect ratio ($L/2W$) on the toughness (K_c) and the abrasion resistance (H^3/E_r^2) has been quantified. To justify the enhancements in the values of K_c and P_{max} in $L/2W$ = 15, the critical compressive loads required to trigger side deflection and rigid rotation was considered. These results indicate that lower values of P_y coincide with a localization of effective strains in the smaller rods ($L/2W$ = 10). However, larger rods lacking of staggered alignment are preferred for wear resistant applications.

Mimicking the alignment of the rods at the leading edge of the tooth, the 3D printed composites were exposed to tensile loads. Since the microstructure of nacre has been extensively studied before, the mechanisms to withstand damage of the rod-like microstructure are compared to a plate-like composite that resembles the brick wall. With the use of the DIC, the analysis of the experimental results suggest an enhancement through the spread of damage in the rods as compared to a more localized fracture in the tablets. Compared to the nacre, the area in contact with the organic material and the volume of the mineral (A_{ol}/V_{mb}) is three times larger in the chiton tooth. As the ratio of A_{ol}/V_{mb} increases, an improvement in the transfer of loads is expected. The comparison with respect to the tough nacre suggests a superiority in the mechanical behavior of the chiton.

Finally, a comprehensive study of the influence of the building blocks alignment in the damage observed after indentation was discussed. Similar to the highly mineralized rod-like microstructure of the chiton, the Strombus gigas is composed of hierarchical levels from nanometers to millimeters of scale. Through the combination of the computational and biomimetic studies, the advantages in the localization of damage and lower critical load for failure of the ±45° orientation were demonstrated. These results suggest the advantages of the natural ±45° layout of the aragonite layer to resist biting attacks.

As a result of the analysis presented in this Ph.D. thesis, it was possible to quantify the influence of geometrical (aspect ratio, diameter of the rods and alignment of the microstructure) and damage mitigation mechanisms in rod-like microstructures. The novel micromechanical model was developed during the last years of this work. Future improvements of this research could be addressed to gain a better understanding of the mechanical behavior of the α-chitin in the rod-like microstructure. It is expected that with the advances in miniature tensile stages, it would be possible to directly obtain the values of T_{max} and G_c, as well as the shape of the fracture law considered. Also, it would be possible to test micro scale composites made out of the leading edge of the tooth. In this study, uniform rods that behave as the monolithic magnetite were considered. As nano-grains might influence the ductility of the solid material, a better knowledge of the mechanical behavior of the nanoscale rods is necessary. The findings of this research are applicable to study other biomineralized materials, and to gain insights in the development of wear and tough resistant composites. Also, the computational models

presented in this study could be applied to improve some of the empirical coefficients considered in the analysis of nanoindentation tests.

LIST OF REFERENCES

LIST OF REFERENCES

[1] M. Ashby and L. Gibson, “The mechanical properties of natural materials. I. Material property charts,” *Proc. Math. Phys. Sci.*, vol. 450, no. 1938, pp. 123–140, 1995.

[2] P. Chen, J. McKittrick, and M. Meyers, “Biological materials: functional adaptations and bioinspired designs,” *Prog. Mater. Sci.*, vol. 57, no. 8, pp. 1492–1704, Nov. 2012.

[3] M. Meyers, P. Chen, A. Lin, and Y. Seki, “Biological materials: structure and mechanical properties,” *Prog. Mater. Sci.*, vol. 53, no. 1, pp. 1–206, Jan. 2008.

[4] H. Gao, B. Ji, and I. Jäger, “Materials become insensitive to flaws at nanoscale: lessons from nature,” *Proc. …*, vol. 100, no. 10, pp. 5597–5600, 2003.

[5] B. Ji and H. Gao, “Mechanical properties of nanostructure of biological materials,” *J. Mech. Phys. Solids*, vol. 52, no. 9, pp. 1963–1990, Sep. 2004.

[6] J. Rho, “Mechanical properties and the hierarchical structure of bone,” vol. 20, pp. 92–102, 1998.

[7] H. D. Espinosa, J. E. Rim, F. Barthelat, and M. J. Buehler, “Merger of structure and material in nacre and bone – Perspectives on de novo biomimetic materials,” *Prog. Mater. Sci.*, vol. 54, no. 8, pp. 1059–1100, Nov. 2009.

[8] P. Fratzl, H. S. Gupta, E. P. Paschalis, and P. Roschger, “Structure and mechanical quality of the collagen?mineral nano-composite in bone,” *J. Mater. Chem.*, vol. 14, no. 14, p. 2115, 2004.

[9] J. C. Weaver, Q. Wang, A. Miserez, A. Tantuccio, R. Stromberg, K. N. Bozhilov, P. Maxwell, R. Nay, S. T. Heier, E. DiMasi, and D. Kisailus, “Analysis of an ultra hard magnetic biomineral in chiton radular teeth,” *Mater. Today*, vol. 13, no. 1–2, pp. 42–52, Jan. 2010.

[10] S. Amini and A. Miserez, “Acta Biomaterialia Wear and abrasion resistance selection maps of biological materials,” *Acta Biomater.*, vol. 9, no. 8, pp. 7895–7907, 2013.

[11] D. Tabor, “Indentation hardness: Fifty years on a personal view,” *Philos. Mag. A*, vol. 74, no. 5, pp. 1207–1212, Nov. 1996.

[12] F. W. Zok and a Miserez, “Property maps for abrasion resistance of materials.,” *Acta Mater.*, vol. 55, no. 18, pp. 6365–6371, Oct. 2007.

[13] B. Bar-On and H. D. Wagner, “Structural motifs and elastic properties of hierarchical biological tissues - A review.,” *J. Struct. Biol.*, vol. 183, no. 2, pp. 149–64, Aug. 2013.

[14] S. Nikolov, M. Petrov, and L. Lymperakis, “Revealing the Design Principles of High-Performance Biological Composites Using Ab initio and Multiscale Simulations: The Example of Lobster Cuticle,” *Adv. Mater.*, vol. 22, no. 4, pp. 519–526, 2010.

[15] L. Wang, J. Song, C. Ortiz, and M. C. Boyce, “Anisotropic design of a multilayered biological exoskeleton,” *J. Mater. Res.*, vol. 24, no. 12, pp. 3477–3494, Jan. 2011.

[16] J. Y. Rho, M. E. Roy, T. Y. Tsui, and G. M. Pharr, “Elastic properties of microstructural components of human bone tissue as measured by nanoindentation.,” *J. Biomed. Mater. Res.*, vol. 45, no. 1, pp. 48–54, Apr. 1999.

[17] C. A. Grant, D. J. Brockwell, S. E. Radford, and N. H. Thomson, “Effects of hydration on the mechanical response of individual collagen fibrils Effects of hydration on the mechanical response of individual collagen fibrils,” *Appl. Phys. Lett.*, vol. 92, no. 23, pp. 126–129, 2008.

[18] A. Zamiri and S. De, “Mechanical properties of hydroxyapatite single crystals from nanoindentation data.,” *J. Mech. Behav. Biomed. Mater.*, vol. 4, no. 2, pp. 146–52, Feb. 2011.

[19] Q. Wang, M. Nemoto, D. Li, J. C. Weaver, B. Weden, J. Stegemeier, K. N. Bozhilov, L. R. Wood, G. W. Milliron, C. S. Kim, E. DiMasi, and D. Kisailus, “Phase Transformations and Structural Developments in the Radular Teeth of Cryptochiton Stelleri,” *Adv. Funct. Mater.*, vol. 23, pp. 2908–2917, Jan. 2013.

[20] O. Zienkiewicz and R. Taylor, *The finite element method*, no. May. 1977.

[21] B. Bruet, J. Song, M. Boyce, and C. Ortiz, “Materials design principles of ancient fish armour,” *Nat. Mater.*, vol. 7, no. 9, pp. 748–56, Sep. 2008.

[22] L. Han, L. Wang, J. Song, M. C. Boyce, and C. Ortiz, “Direct quantification of the mechanical anisotropy and fracture of an individual exoskeleton layer via uniaxial compression of micropillars.,” *Nano Lett.*, vol. 11, no. 9, pp. 3868–74, Sep. 2011.

[23] E. a Zimmermann, B. Gludovatz, E. Schaible, N. K. N. Dave, W. Yang, M. a Meyers, and R. O. Ritchie, “Mechanical adaptability of the Bouligand-type structure in natural dermal armour.,” *Nat. Commun.*, vol. 4, no. May, p. 2634, Oct. 2013.

[24] W. Yang, I. H. Chen, B. Gludovatz, E. a Zimmermann, R. O. Ritchie, and M. a Meyers, “Natural flexible dermal armor.,” *Adv. Mater.*, vol. 25, no. 1, pp. 31–48, Jan. 2013.

[25] S. Kamat, X. Su, R. Ballarini, and a H. Heuer, “Structural basis for the fracture toughness of the shell of the conch Strombus gigas.,” *Nature*, vol. 405, no. 6790, pp. 1036–40, Jun. 2000.

[26] C. Salinas and D. Kisailus, “Fracture Mitigation Strategies in Gastropod Shells,” *J. Mater.*, vol. 65, no. 4, pp. 473–480, Feb. 2013.

[27] A. Miserez and J. Weaver, “Effects of laminate architecture on fracture resistance of sponge biosilica: lessons from nature,” *Adv. Funct. …*, vol. 18, no. 8, pp. 1241–1248, Apr. 2008.

[28] W. C. O. and G.M.Pharr, “An improved technique for determining hardness and elastic modulus using load and displacement sensing indentation experiments,” *J. Mater. Res.*, vol. 7, no. 6, pp. 1564–1583, 1992.

[29] T. U. Manual, “TI 950 TriboIndenter User Manual,” pp. 1–262.

[30] B. R. Lawn, A. Evans, and D. B. Marshall, “Elastic/plastic indentation damage in Ceramics: the lateral crack system,” *J. Am. Ceram. Soc.*, vol. 65, no. 11, pp. 561–566, 1980.

[31] I. Sneddon, “The relation between load and penetration in the axisymmetric Boussinesq problem for a punch of arbitrary profile,” *Int. J. Eng. Sci.*, vol. 3, no. 638, pp. 47–57, 1965.

[32] C.-T. Sun and Z.-H. Jin, *Fracture Mechanics*, vol. 10. Academic Press, 2012.

[33] T. L. Anderson, *Fracture Mechanics: Fundamentals and Applications*. CRC Press, 1995.

[34] E. Rocha-rangel, “Fracture Toughness Determinations by Means of Indentation Fracture,” no. c, 2003.

[35] H. Tada, P. P. C. Paris, and G. R. Irwin, *The Stress Analysis of Cracks Handbook*. American Society of Mechanical Engineers, 2000.

[36] G. Bao and Z. Suo, "Remarks on crack-bridging concepts," *Appl. Mech. Rev.*, 1992.

[37] S. Palmqvist, "Occurrence of crackformation during Vickers indentation as a measure of toughness of hard materials," *Arch. fuer das Eisenhuettenwes.*, vol. 33, pp. 333–629, 1962.

[38] C. . Ponton and R. D. Rawlings, "Vickers indentation fracture toughness test Part1 Review of literature and formulation of standardised indentation toughness equations," *Mater. Sci. Technol.*, vol. 5, no. September, pp. 865–872, 1989.

[39] D. Morris and R. Cook, "In Situ Cube-Corner Indentation of Soda–Lime Glass and Fused Silica," *J. Am. Ceram. Soc.*, 2004.

[40] J. J. Kruzic, D. K. Kim, K. J. Koester, and R. O. Ritchie, "Indentation techniques for evaluating the fracture toughness of biomaterials and hard tissues.," *J. Mech. Behav. Biomed. Mater.*, vol. 2, no. 4, pp. 384–95, Aug. 2009.

[41] B. R. Lawn, A. Evans, and D. B. Marshall, "Elastic / Plastic Indentation Damage in Ceramics : The MediadRadial Crack System I '," *J. Am. Ceram. Soc.*, vol. 63, no. 9–10, pp. 574–581, 1980.

[42] D. Marshall and B. Lawn, "Residual stress effects in sharp contact cracking," *J. Mater. Sci.*, vol. 14, no. 1979, 1979.

[43] J. Jang and G. M. Pharr, "Influence of indenter angle on cracking in Si and Ge during nanoindentation," *Acta Mater.*, vol. 56, no. 16, pp. 4458–4469, Sep. 2008.

[44] P. Chantikul and G. Anstis, "A critical evaluation of indentation techniques for measuring fracture toughness: II, strength method," *J. …*, vol. 64, no. 9, pp. 539–543, 1981.

[45] K. L. Johnson, *Contact Mechanics*. Cambridge University Press, 1987.

[46] Z. Xie and M. Hoffman, "Deformation of a hard coating on ductile substrate system during nanoindentation: Role of the coating microstructure," *J. Mater. …*, vol. 21, no. 2, pp. 437–447, 2006.

[47] T. Y. Tsui, G. M. Pharr, W. C. Oliver, C. S. Bhatia, R. L. White, S. Andres, A. Anders, and I. G. Brown, "Nanoindentation and nanoscratching of hard carbon coatings for magnetic disks," vol. 383, pp. 447–452, 1995.

[48] J. Musil, F. Kunc, H. Zeman, and H. Polakova, “Relationships between hardness , Young ’ s modulus and elastic recovery in hard nanocomposite coatings,” vol. 154, pp. 304–313, 2002.

[49] A. Muchtar, L. C. Lim, and K. H. Lee, “Finite element analysis of vickers indentation cracking processes in brittle solids using elements exhibiting cohesive post-failure behaviour,” *J. Mater. Sci.*, vol. 38, no. 2, pp. 235–243, Jan. 2003.

[50] J. H. Lee, Y. F. Gao, K. E. Johanns, and G. M. Pharr, “Cohesive interface simulations of indentation cracking as a fracture toughness measurement method for brittle materials,” *Acta Mater.*, vol. 60, no. 15, pp. 5448–5467, Sep. 2012.

[51] K. Johanns and G. Lee, JH, Gao, YF, Pharr, “An evaluation of the advantages and limitations in simulating indentation cracking with cohesive zone finite elements,” *Model. Simul. …*, vol. 015011, 2014.

[52] H. C. Hyun, J. H. Lee, H. Lee, D. H. Kim, and J. H. Hahn, “Analysis of Cracking Characteristics with Indenter Geometry Using Cohesive Zone Model,” *Trans. Korean Soc. Mech. Eng. A*, vol. 37, no. 12, pp. 1453–1463, Dec. 2013.

[53] H. D. Espinosa and P. D. Zavattieri, “A grain level model for the study of failure initiation and evolution in polycrystalline brittle materials. Part II: Numerical examples,” *Mech. Mater.*, vol. 35, no. 3–6, pp. 365–394, Mar. 2003.

[54] M. Ortiz and A. Pandolfi, “Finite-deformation irreversible cohesive elements for three-dimensional crack-propagation analysis,” *Int. J. Numer. Methods …*, vol. 1282, no. May 1998, pp. 1267–1282, 1999.

[55] M. Ortiz and A. Pandolfi, “Finite-deformation irreversible cohesive elements for three-dimensional crack-propagation analysis,” *Int. J. Numer. Methods …*, vol. 1282, no. May 1998, pp. 1267–1282, 1999.

[56] H. D. Espinosa and P. D. Zavattieri, “A grain level model for the study of failure initiation and evolution in polycrystalline brittle materials. Part I: Theory and numerical implementation,” *Mech. Mater.*, vol. 35, no. 3–6, pp. 333–364, Mar. 2003.

[57] J. Hay, A. Bolshakov, and G. Pharr, “A critical examination of the fundamental relations used in the analysis of nanoindentation data,” *J. Mater. Res.*, vol. 14, no. 6, 1999.

[58] A. G. Atkins and D. Tabor, “Plastic indentation in metals with cones,” vol. 13, no. 1954, 1965.

[59] R. F. Cook and G. M. Pharr, “Direct Observation and Analysis of Indentation Cracking in Glasses and Ceramics,” *J. Am. Ceram. Soc.*, vol. 73, no. 4, pp. 787–817, Apr. 1990.

[60] C. Cattano, T. Nikou, and L. Klotz, “Teaching Systems Thinking and Biomimicry to Civil Engineering Students,” *J. Prof. Issues Eng. Educ. Pract.*, vol. 137, no. October, pp. 176–182, 2011.

[61] Z. Qin, N. M. Pugno, and M. J. Buehler, “Mechanics of fragmentation of crocodile skin and other thin films.,” *Sci. Rep.*, vol. 4, p. 4966, 2014.

[62] F. E. Fish, P. W. Weber, M. M. Murray, and L. E. Howle, “The tubercles on humpback whales’ flippers: application of bio-inspired technology.,” *Integr. Comp. Biol.*, vol. 51, no. 1, pp. 203–13, Jul. 2011.

[63] E. Escobar de Obaldia, C. Jeong, L. K. Grunenfelder, D. Kisailus, and P. Zavattieri, “Analysis of the mechanical response of biomimetic materials with highly oriented microstructures through 3D printing, mechanical testing and modeling,” *J. Mech. Behav. Biomed. Mater.*, no. http://dx.doi.org/10.1016/j.jmbbm.2015.03.026, 2015.

[64] F. Barthelat, H. Tang, P. Zavattieri, C. Li, and H. Espinosa, “On the mechanics of mother-of-pearl: A key feature in the material hierarchical structure,” *J. Mech. Phys. Solids*, vol. 55, no. 2, pp. 306–337, Feb. 2007.

[65] S. Nikolov, M. Petrov, L. Lymperakis, M. Friák, C. Sachs, H.-O. Fabritius, D. Raabe, and J. Neugebauer, “Revealing the design principles of high-performance biological composites using ab initio and multiscale simulations: the example of lobster cuticle.,” *Adv. Mater.*, vol. 22, no. 4, pp. 519–26, Jan. 2010.

[66] L. HC, B. H, and W. JH, *Heavy metals in the jaws of invertebrates*, vol. 4. Wiley & Sons, 2008.

[67] L. K. Grunenfelder, E. Escobar de Obaldia, Q. Wang, D. Li, B. Weden, C. Salinas, R. Wuhrer, P. Zavattieri, and D. Kisailus, “Stress and Damage Mitigation from Oriented Nanostructures within the Radular Teeth of Cryptochiton stelleri,” *Adv. Funct. Mater.*, vol. 24, no. 39, pp. 6093–6104, Oct. 2014.

[68] H. A. LOWENSTAM, “Magnetite in Denticle Capping in Recent Chitons (Polyplacophora),” *Geol. Soc. Am. Bull.* , vol. 73 , no. 4 , pp. 435–438, Apr. 1962.

[69] P. van der Wal, H. J. Giesen, and J. J. Videler, “Radular teeth as models for the improvement of industrial cutting devices,” *Mater. Sci. Eng. C*, vol. 7, no. 2, pp. 129–142, Feb. 2000.

[70] F. Barthelat and C. Li, “Mechanical properties of nacre constituents and their impact on mechanical performance,” *J. Mater. Res.*, vol. 3111, no. July 2005, pp. 1977–1986, 2006.

[71] X.-W. Su, D.-M. Zhang, and a. H. Heuer, “Tissue Regeneration in the Shell of the Giant Queen Conch, Strombus gigas,” *Chem. Mater.*, vol. 16, no. 4, pp. 581–593, Feb. 2004.

[72] E. Arzt, P. Fratzl, H. Gao, B. Ji, and I. L. Ja, “Materials become insensitive to flaws at nanoscale :,” vol. 100, no. 10, pp. 5597–5600, 2003.

[73] S. Kamat, H. Kessler, R. Ballarini, M. Nassirou, and A. H. Heuer, “Fracture mechanisms of the Strombus gigas conch shell: II-micromechanics analyses of multiple cracking and large-scale crack bridging,” *Acta Mater.*, vol. 52, no. 8, pp. 2395–2406, May 2004.

[74] “http://www.montereybayaquarium.org/.” .

[75] E. Rabinowicz, *Friction and wear of materials*. 1995.

[76] M. Q. Chandler, P. G. Allison, R. I. Rodriguez, R. D. Moser, and A. J. Kennedy, “Finite element modeling of multilayered structures of fish scales.,” *J. Mech. Behav. Biomed. Mater.*, vol. 40, pp. 375–89, Dec. 2014.

[77] W. Weibull, “A statistical distribution function of wide applicability,” no. 18, pp. 293–297, Jan. 1951.

[78] D. Chicot, F. Roudet, V. Lepingle, and G. Louis, “Strain gradient plasticity to study hardness behavior of magnetite (Fe3O4) under multicyclic indentation,” *J. Mater. Res.*, vol. 23, no. 3, pp. 749–759, 2009.

[79] F. Auricchio and R. L. Taylor, “Two material models for cyclic plasticity: Nonlinear kinematic hardening and generalized plasticity,” *Int. J. Plast.*, vol. 11, no. 1, pp. 65–98, Jan. 1995.

[80] C. S. Desai, S. Somasundaram, and G. Frantziskonis, “A Hierarchical Approach for Constitutive Modeling of Geologic Materials,” *Int. J. Numer. Anal. Methods Geomech.*, vol. 10, no. 3, pp. 225–257, 1986.

[81] C. Kearney, Z. Zhao, B. J. F. Bruet, R. Radovitzky, M. C. Boyce, and C. Ortiz, “Nanoscale anisotropic plastic deformation in single crystal aragonite.,” *Phys. Rev. Lett.*, vol. 96, no. 25, p. 255505, Jun. 2006.

[82] K. Johnson, “The correlation of indentation experiments,” *J. Mech. Phys. Solids*, vol. 18, no. 1, 1970.

[83] W. Oliver and G. Pharr, “An improved technique for determining hardness and elastic modulus using load and displacement sensing indentation experiments,” *J. Mater. Res.*, 1992.

[84] A. Giannakopoulos and S. Suresh, “Determination of elastoplastic properties by instrumented sharp indentation,” *Scr. Mater.*, vol. 40, no. 10, pp. 1191–1198, 1999.

[85] Y.-T. Cheng and C.-M. Cheng, “Scaling, dimensional analysis, and indentation measurements,” *Mater. Sci. Eng. R Reports*, vol. 44, no. 4–5, pp. 91–149, Aug. 2004.

[86] W. C. Oliver and G. M. Pharr, “An improved technique for determining hardness and elastic modulus using load and displacement sensing indentation experiments,” *J. Mater. Res.*, vol. 7, no. 06, pp. 1564–1583, Jan. 2011.

[87] D. Tromans and J. . Meech, “Fracture toughness and surface energies of minerals: theoretical estimates for oxides, sulphides, silicates and halides,” *Miner. Eng.*, vol. 15, no. 12, pp. 1027–1041, Dec. 2002.

[88] D. Chicot, J. Mendoza, A. Zaoui, G. Louis, V. Lepingle, F. Roudet, and J. Lesage, “Mechanical properties of magnetite (Fe3O4), hematite (α-Fe2O3) and goethite (α-FeO·OH) by instrumented indentation and molecular dynamics analysis,” *Mater. Chem. Phys.*, vol. 129, no. 3, pp. 862–870, Oct. 2011.

[89] M. Q. Chandler, P. G. Allison, R. I. Rodriguez, R. D. Moser, and A. J. Kennedy, “Finite element modeling of multilayered structures of fish scales.,” *J. Mech. Behav. Biomed. Mater.*, vol. 40, pp. 375–89, Dec. 2014.

[90] C. B. Ponton and R. D. Rawlings, “Vickers indentation fracture toughness test Part 2 Application and critical evaluation of standardised indentation toughness equations,” *Materials Science and Technology*, vol. 5, no. 10. pp. 961–976, 1989.

[91] W. Li and T. Siegmund, “An analysis of the indentation test to determine the interface toughness in a weakly bonded thin film coating – substrate system,” *Acta Mater.*, vol. 52, no. 10, pp. 2989–2999, Jun. 2004.

[92] H. C. Hyun, F. Rickhey, J. H. Lee, J. H. Hahn, and H. Lee, “Characteristics of Indentation Cracking Using Cohesive Zone Finite Element Techniques for Pyramidal Indenters,” *Int. J. Solids Struct.*, Sep. 2014.

[93] B. Ji and H. Gao, “Mechanical properties of nanostructure of biological materials,” *J. Mech. Phys. Solids*, vol. 52, no. 9, pp. 1963–1990, Sep. 2004.

[94] G. M. Pharr, “Measurement of mechanical properties by ultra-low load indentation,” *Mater. Sci. Eng. A*, vol. 253, no. 1–2, pp. 151–159, Sep. 1998.

[95] A. Bolshakov and G. M. Pharr, “Influences of pileup on the measurement of mechanical properties by load and depth sensing indentation techniques,” *J. Mater. Res.*, vol. 13, no. 04, pp. 1049–1058, Jan. 1998.

[96] S. Fan and B. Yilong, “Mineral bridges of nacre and its effects,” *Acta Mech. Sin.*, vol. 17, no. 3, pp. 251–257, Aug. 2001.

[97] F. Barthelat and H. D. Espinosa, “An Experimental Investigation of Deformation and Fracture of Nacre–Mother of Pearl,” *Exp. Mech.*, vol. 47, no. 3, pp. 311–324, Mar. 2007.

[98] S. Bargmann, I. Scheider, T. Xiao, E. Yilmaz, G. a. Schneider, and N. Huber, “Towards bio-inspired engineering materials: Modeling and simulation of the mechanical behavior of hierarchical bovine dental structure,” *Comput. Mater. Sci.*, vol. 79, pp. 390–401, Nov. 2013.

[99] G. Camacho and M. Ortiz, “Computational modelling of impact damage in brittle materials,” *Int. J. Solids Struct.*, vol. 33, no. 2, pp. 2899–2938, 1996.

[100] P. D. Zavattieri, “Modeling of Crack Propagation in Thin-Walled Structures Using a Cohesive Model for Shell Elements,” *J. Appl. Mech.*, vol. 73, no. 6, p. 948, 2006.

[101] P. G. Allison, R. D. Moser, J. P. Schirer, R. . Martens, J. B. Jordon, and M. Q. Chandler, “In-situ nanomechanical studies of deformation and damage mechanisms in nanocomposites monitored using scanning electron microscopy,” *Mater. Lett.*, vol. 131, pp. 313–316, Sep. 2014.

[102] A. Khayer Dastjerdi, R. Rabiei, and F. Barthelat, “The weak interfaces within tough natural composites: experiments on three types of nacre.,” *J. Mech. Behav. Biomed. Mater.*, vol. 19, pp. 50–60, Mar. 2013.

[103] A. G. Atkins and D. Tabor, “Plastic indentation in metals with cones,” *J. Mech. Phys. Solids*, vol. 13, no. 3, pp. 149–164, 1965.

[104] Y.-T. Cheng and C.-M. Cheng, “What is indentation hardness?,” *Surf. Coatings Technol.*, vol. 133–134, pp. 417–424, Nov. 2000.

[105] A. Khayer Dastjerdi, R. Rabiei, and F. Barthelat, “The weak interfaces within tough natural composites: Experiments on three types of nacre,” *J. Mech. Behav. Biomed. Mater.*, 2013.

[106] T. F. Page and S. V. Hainsworth, “Using nanoindentation techniques for the characterization of coated systems: a critique,” *Surf. Coatings Technol.*, vol. 61, no. 1–3, pp. 201–208, 1993.

[107] S. K. Lawrence, D. P. Adams, D. F. Bahr, and N. R. Moody, “Deformation and fracture of a mudflat-cracked laser-fabricated oxide on Ti,” *J. Mater. Sci.*, vol. 48, no. 11, pp. 4050–4058, Feb. 2013.

[108] Y. Shao, H.-P. Zhao, and X.-Q. Feng, “Optimal characteristic nanosizes of mineral bridges in mollusk nacre,” *RSC Adv.*, vol. 4, no. 61, p. 32451, Jun. 2014.

[109] R. D. Cook, D. S. Malkus, M. E. Plesha, and R. J. Witt, *Concepts and Applications of Finite Element Analysis, 4th Edition*. Wiley, 2001.

[110] B. Lawn and M. Swain, “Microfracture beneath point indentations in brittle solids,” *J. Mater. Sci.*, vol. 10, 1975.

[111] A. Crouch, “High-Temperature Deformation of Polycrystalline Fe2O3,” *J. Am. Ceram. Soc.*, no. July 1970, pp. 558–563, 1972.

[112] H. Siemes, B. Klingenberg, E. Rybacki, M. Naumann, W. Schäfer, E. Jansen, and K. Kunze, “Glide systems of hematite single crystals in deformation experiments,” *Ore Geol. Rev.*, vol. 33, no. 3–4, pp. 255–279, Jun. 2008.

[113] A. Matthews, “Magnetite formation by the reduction of hematite with iron under hydrothermal conditions,” *Am. Mineral.*, vol. 6, pp. 927–932, 1976.

[114] a Jaytilaka and K. Trustrum, “Statistical approach to brittle fracture,” *J. Mater. Sci.*, vol. 12, pp. 1426–1430, 1977.

[115] Z. P. Bazant and J. Planas, *Fracture and Size Effect in Concrete and Other Quasibrittle Materials*. CRC Press, 1997.

[116] H. Li, Y. Yue, X. Han, and X. Li, “Plastic Deformation Enabled Energy Dissipation in a Bionanowire Structured Armor.,” *Nano Lett.*, Apr. 2014.

[117] J.-Y. Kim and J. R. Greer, “Tensile and compressive behavior of gold and molybdenum single crystals at the nano-scale,” *Acta Mater.*, vol. 57, no. 17, pp. 5245–5253, Oct. 2009.

[118] F. Zhou and J. F. Molinari, “Dynamic crack propagation with cohesive elements: a methodology to address mesh dependency,” *Int. J. Numer. Methods Eng.*, vol. 59, no. 1, pp. 1–24, Jan. 2004.

[119] L. HA and W. S, “On Biomineralization,” *Oxford Oxford Univ.*, 1989.

[120] D. Chicot, F. Roudet, a. Zaoui, G. Louis, and V. Lepingle, “Influence of visco-elasto-plastic properties of magnetite on the elastic modulus: Multicyclic indentation and theoretical studies,” *Mater. Chem. Phys.*, vol. 119, no. 1–2, pp. 75–81, Jan. 2010.

[121] D. S. Harding, W. C. Oliver, and G. M. Pharr, “Cracking During Nanoindentation and its Use in the Measurement of Fracture Toughness,” *MRS Proc.*, vol. 356, p. 663, Feb. 2011.

[122] H. Ming-Yuan and J. W. Hutchinson, “Crack Deflection at an Interface Between Dissimilar Elastic Materials,” *Int. J.Solids Struct.*, vol. 25, no. 9, pp. 1053–1067, 1989.

[123] J. C. Weaver, G. W. Milliron, A. Miserez, K. Evans-Lutterodt, S. Herrera, I. Gallana, W. J. Mershon, B. Swanson, P. Zavattieri, E. DiMasi, and D. Kisailus, “The stomatopod dactyl club: a formidable damage-tolerant biological hammer.,” *Science*, vol. 336, no. 6086, pp. 1275–80, Jun. 2012.

[124] P. Fratzl, H. S. Gupta, F. D. Fischer, and O. Kolednik, “Hindered Crack Propagation in Materials with Periodically Varying Young’s Modulus—Lessons from Biological Materials,” *Adv. Mater.*, vol. 19, no. 18, pp. 2657–2661, Sep. 2007.

[125] P. Murali, T. K. Bhandakkar, W. L. Cheah, M. H. Jhon, H. Gao, and R. Ahluwalia, “Role of modulus mismatch on crack propagation and toughness enhancement in bioinspired composites,” *Phys. Rev. E*, vol. 84, no. 1, p. 015102, Jul. 2011.

[126] M. Saunders, C. Kong, J. A. Shaw, and P. L. Clode, “Matrix-mediated biomineralization in marine mollusks: a combined transmission electron microscopy and focused ion beam approach.,” *Microsc. Microanal.*, vol. 17, no. 2, pp. 220–5, Apr. 2011.

[127] A. K. Kaw, *Mechanics of Composite Materials*. CRC Press, 1997.

[128] S. L. Bazhenov, a. M. Kuperman, E. S. Zelenskii, and a. a. Berlin, “Compression failure of unidirectional glass-fibre-reinforced plastics,” *Compos. Sci. Technol.*, vol. 45, no. 3, pp. 201–208, Jan. 1992.

[129] Y. Xu and K. Reifsnider, “Micromechanical modeling of composite compressive strength,” *J. Compos. Mater.*, 1993.

[130] J. Andersons and M. König, “Dependence of fracture toughness of composite laminates on interface ply orientations and delamination growth direction,” *Compos. Sci. Technol.*, vol. 64, no. 13–14, pp. 2139–2152, Oct. 2004.

[131] D. A. Rigney and W. A. Glaeser, “The Significance of Near Surface Microstructure in the Wear Process,” *Wear*, vol. 46, pp. 241–250, 1978.

[132] H. C. Lichtenegger, H. Birkedal, and J. H. Waite, “Heavy Metals in the Jaws of Invertebrates, in Biomineralization: From Nature to Application,” vol. 4, pp. 295–325, 2008.

[133] I. M. Hutchings, “Wear-resistant materials: into the next century,” *Mater. Sci. Eng. A*, vol. 184, no. 2, pp. 185–195, Aug. 1994.

[134] D. . Li, “Development of novel wear-resistant materials: TiNi-based pseudoelastic tribomaterials,” *Mater. Des.*, vol. 21, no. 6, pp. 551–555, Dec. 2000.

[135] K. H. Zum Gahr, *Microstructure and Wear of Materials*, vol. 10. Elsevier, 1987.

[136] C. Norotte, F. S. Marga, L. E. Niklason, and G. Forgacs, “Scaffold-free vascular tissue engineering using bioprinting.,” *Biomaterials*, vol. 30, no. 30, pp. 5910–7, Oct. 2009.

[137] F. P. W. Melchels, M. a. N. Domingos, T. J. Klein, J. Malda, P. J. Bartolo, and D. W. Hutmacher, “Additive manufacturing of tissues and organs,” *Prog. Polym. Sci.*, vol. 37, no. 8, pp. 1079–1104, Aug. 2012.

[138] M. Lee, J. C. Y. Dunn, and B. M. Wu, “Scaffold fabrication by indirect three-dimensional printing.,” *Biomaterials*, vol. 26, no. 20, pp. 4281–9, Jul. 2005.

[139] M. Cima, E. Sachs, and L. Cima, “Computer-derived microstructures by 3D printing: bio-and structural materials,” *Solid Free. Fabr.*, pp. 181–190, 1994.

[140] C. Bergmann, M. Lindner, W. Zhang, K. Koczur, A. Kirsten, R. Telle, and H. Fischer, “3D printing of bone substitute implants using calcium phosphate and bioactive glasses,” *J. Eur. Ceram. Soc.*, vol. 30, no. 12, pp. 2563–2567, Sep. 2010.

[141] L. S. Dimas, G. H. Bratzel, I. Eylon, and M. J. Buehler, “Tough Composites Inspired by Mineralized Natural Materials: Computation, 3D printing, and Testing,” *Adv. Funct. Mater.*, vol. 23, no. 36, pp. 4629–4638, Jun. 2013.

[142] H. D. Espinosa, A. L. Juster, F. J. Latourte, O. Y. Loh, D. Gregoire, and P. D. Zavattieri, “Tablet-level origin of toughening in abalone shells and translation to synthetic composite materials.,” *Nat. Commun.*, vol. 2, no. 2, p. 173, Jan. 2011.

[143] J. E. Rim, P. Zavattieri, A. Juster, and H. D. Espinosa, “Dimensional analysis and parametric studies for designing artificial nacre.,” *J. Mech. Behav. Biomed. Mater.*, vol. 4, no. 2, pp. 190–211, Feb. 2011.

[144] “http://www.stratasys.com.” .

[145] S. Bechtle, S. F. Ang, and G. a Schneider, “On the mechanical properties of hierarchically structured biological materials.,” *Biomaterials*, vol. 31, no. 25, pp. 6378–85, Sep. 2010.

[146] B. Poon, D. Rittel, and G. Ravichandran, “An analysis of nanoindentation in linearly elastic solids,” *Int. J. Solids Struct.*, vol. 45, no. 24, pp. 6018–6033, Dec. 2008.

[147] R. Weinkamer and P. Fratzl, “Mechanical adaptation of biological materials — The examples of bone and wood,” *Mater. Sci. Eng. C*, vol. 31, no. 6, pp. 1164–1173, Aug. 2011.

[148] W. Voigt, “Uber die Beziehung zwischen den beiden Elastizitatskonstanten isotroper Korper,” *Philos. Trans.*, vol. 38, pp. 573–587, 1889.

[149] A. Reuss and Z. Angew, “Berechnung der Flie grenze von Mischkristallen auf Grund der Plastizit tsbedingung für Einkristalle,” *ZAMM- J. Appl. Math. Mech.*, vol. 9, pp. 49–58, 1929.

[150] C. Sachs, H. Fabritius, and D. Raabe, “Influence of microstructure on deformation anisotropy of mineralized cuticle from the lobster Homarus americanus,” *J. Struct. Biol.*, vol. 161, pp. 120–132, 2008.

[151] H. O. Fabritius, C. Sachs, P. R. Triguero, and D. Raabe, “Influence of structural principles on the mechanics of a biological fiber-based composite material with hierarchical organization: The exoskeleton of the lobster homarus americanus,” *Adv. Mater.*, vol. 21, pp. 391–400, 2009.

[152] D. Raabe, P. Romano, C. Sachs, H. Fabritius, a. Al-Sawalmih, S. B. Yi, G. Servos, and H. G. Hartwig, “Microstructure and crystallographic texture of the chitin-protein network in the biological composite material of the exoskeleton of the lobster Homarus americanus,” *Mater. Sci. Eng. A*, vol. 421, pp. 143–153, 2006.

[153] S. Nikolov, H. Fabritius, M. Petrov, M. Friák, L. Lymperakis, C. Sachs, D. Raabe, and J. Neugebauer, “Robustness and optimal use of design principles of arthropod exoskeletons studied by ab initio-based multiscale simulations.,” *J. Mech. Behav. Biomed. Mater.*, vol. 4, no. 2, pp. 129–45, Feb. 2011.

[154] “http://www.geodict.de/.” .

[155] X. Yang, X. Liu, Z. Huang, X. Yao, and G. Liu, “Vickers indentation crack analysis of solid-phase-sintered silicon carbide ceramics,” *Ceram. Int.*, vol. 39, no. 1, pp. 841–845, Jan. 2013.

[156] J. Lankford and D. Davidson, “The crack-initiation threshold in ceramic materials subject to elastic/plastic indentation,” *J. Mater. Sci.*, vol. 14, 1979.

[157] R. O. Ritchie, “The conflicts between strength and toughness.,” *Nat. Mater.*, vol. 10, no. 11, pp. 817–22, Nov. 2011.

[158] D. . Shtansky, S. . Kulinich, E. . Levashov, a. . Sheveiko, F. . Kiriuhancev, and J. . Moore, “Localized deformation of multicomponent thin films,” *Thin Solid Films*, vol. 420–421, pp. 330–337, Dec. 2002.

[159] K. Niihara, R. Morena, and D. Hasselman, “Evaluation of KIc of brittle solids by the indentation method with low crack-to-indent ratios,” *J. Mater. Sci. …*, vol. 1, pp. 13–16, 1982.

[160] J. Lubliner, R. Taylor, and F. Auricchio, “A new model of generalized plasticity and its numerical implementation,” *Int. J. Solids …*, vol. 30, no. 22, pp. 3171–3184, 1993.

[161] R. Z. Wang, Z. Suo, A. G. Evans, N. Yao, and I. A. Aksay, “Deformation mechanisms in nacre,” *J. Mater. Res.*, vol. 16, no. 09, pp. 2485–2493, Jan. 2011.

[162] M. Tsai, D. Oplinger, and J. Morton, “Improved theoretical solutions for adhesive lap joints,” *Int. J. Solids Struct.*, vol. 35, no. 12, pp. 1163–1185, 1998.

[163] L. H. He and M. V Swain, “Understanding the mechanical behaviour of human enamel from its structural and compositional characteristics.,” *J. Mech. Behav. Biomed. Mater.*, vol. 1, no. 1, pp. 18–29, Jan. 2008.

[164] M. Yahyazadehfar, D. Bajaj, and D. D. Arola, “Hidden contributions of the enamel rods on the fracture resistance of human teeth.,” *Acta Biomater.*, vol. 9, no. 1, pp. 4806–14, Jan. 2013.

[165] J. Chen and S. J. Bull, “Multi-cycling nanoindentation study on thin optical coatings on glass,” *J. Phys. D. Appl. Phys.*, vol. 41, no. 7, p. 074009, Apr. 2008.

[166] H. Li, Z.-H. Xu, and X. Li, “Multiscale hierarchical assembly strategy and mechanical prowess in conch shells (Busycon carica).,” *J. Struct. Biol.*, vol. 184, no. 3, pp. 409–16, Dec. 2013.

[167] Z. Baiant and L. Cedolin, “Stability of structures,” 1991.

[168] S. N. White, W. Luo, M. L. Paine, H. Fong, M. Sarikaya, and M. L. Snead, “Biological Organization of Hydroxyapatite Crystallites into a Fibrous Continuum Toughens and Controls Anisotropy in Human Enamel,” *J. Dent. Res.*, vol. 80, no. 1, pp. 321–326, Jan. 2001.

[169] C.-T. Doyle, J.F. and Sun, "Theory of Elasticity," *A&AE 553 Cl. Notes, Purdue Univ.*, 1999.

[170] K. Hjelmstad, *Fundamentals of structural mechanics*. 2005.

[171] S. P. Timoshenko and J. M. Gere, *Theory of Elastic Stability. 2.ed*. McGraw-Hill, 1961.

[172] J. Currey, "Mechanical properties of mother of pearl in tension," *Proc. R. Soc. …*, vol. 196, no. 1125, pp. 443–463, 1977.

[173] X. Li, Z.-H. Xu, and R. Wang, "In situ observation of nanograin rotation and deformation in nacre.," *Nano Lett.*, vol. 6, no. 10, pp. 2301–4, Oct. 2006.

[174] E. Lin, Y. Li, J. C. Weaver, C. Ortiz, and M. C. Boyce, "Tunability and enhancement of mechanical behavior with additively manufactured bio-inspired hierarchical suture interfaces," *J. Mater. Res.*, vol. 29, no. 17, pp. 1867–1875, Jul. 2014.

[175] S. Bechtle, H. Özcoban, E. T. Lilleodden, N. Huber, A. Schreyer, M. V Swain, and G. a Schneider, "Hierarchical flexural strength of enamel: transition from brittle to damage-tolerant behaviour.," *J. R. Soc. Interface*, vol. 9, no. 71, pp. 1265–74, Jun. 2012.

[176] M. A. Meyers, J. McKittrick, and P.-Y. Chen, "Structural biological materials: critical mechanics-materials connections.," *Science*, vol. 339, no. 6121, pp. 773–9, Feb. 2013.

[177] Z.-H. Xie, M. V Swain, G. Swadener, P. Munroe, and M. Hoffman, "Effect of microstructure upon elastic behaviour of human tooth enamel.," *J. Biomech.*, vol. 42, no. 8, pp. 1075–80, May 2009.

[178] L. H. He and M. V. Swain, "Contact induced deformation of enamel," *Appl. Phys. Lett.*, vol. 90, no. 17, p. 171916, 2007.

[179] C. Chamis, "Mechanics of Load Transfer at the Fiber/Matrix Interface.," 1972.

[180] C. C. Chamis, "Mechanics of Load Transfer at the Fiber/Matrix Interface.," Feb. 1972.

[181] A. S. for Testing, *Interfaces in Composites*. ASTM International.

[182] H. A. Bruck, S. R. McNeill, M. A. Sutton, and W. H. Peters, "Digital image correlation using Newton-Raphson method of partial differential correction," *Exp. Mech.*, vol. 29, no. 3, pp. 261–267, Sep. 1989.

[183] N. Suksangpanya and P. D. Zavattieri, “Fracture Analysis on the Bouligand Structure in Stomatopod Dactyl Club under Uniaxial Loading,” no. to be submitted, 2015.

[184] J. Randall, “Contributions to the biology of the queen conch, Strombus gigas,” *Bull. Mar. Sci.*, no. 541, 1964.

[185] M. Ray and A. Stoner, “Growth, survivorship, and habitat choice in a newly settled seagrass gastropod, Strombus gigas,” *Mar. Ecol. Prog. Ser. Oldend.*, 1995.

[186] R. Ballarini, R. Kayacan, F.-J. Ulm, T. Belytschko, and a. H. Heuer, “Biological Structures Mitigate Catastrophic Fracture Through Various Strategies,” *Int. J. Fract.*, vol. 135, no. 1–4, pp. 187–197, Sep. 2005.

[187] L. Chen and R. Ballarini, “Bioinspired micro-composite structure,” *J. Mater. …*, 2007.

[188] S. Kamat, H. Kessler, R. Ballarini, M. Nassirou, and A. H. Heuer, “Fracture mechanisms of the Strombus gigas conch shell: II-micromechanics analyses of multiple cracking and large-scale crack bridging,” *Acta Mater.*, vol. 52, no. 8, pp. 2395–2406, May 2004.

[189] H. Li, Z.-H. Xu, and X. Li, “Multiscale hierarchical assembly strategy and mechanical prowess in conch shells (Busycon carica).,” *J. Struct. Biol.*, vol. 184, no. 3, pp. 409–16, Dec. 2013.

[190] a K. Dastjerdi, M. Pagano, M. T. Kaartinen, M. D. McKee, and F. Barthelat, “Cohesive behavior of soft biological adhesives: experiments and modeling.,” *Acta Biomater.*, vol. 8, no. 9, pp. 3349–59, Sep. 2012.

[191] A. Khayer Dastjerdi, E. Tan, and F. Barthelat, “Direct Measurement of the Cohesive Law of Adhesives Using a Rigid Double Cantilever Beam Technique,” *Exp. Mech.*, vol. 53, no. 9, pp. 1763–1772, May 2013.

VITA

VITA

In November of 2004, Enrique Escobar de Obaldia obtained a bachelor degree in mechanical engineering at the Universidad Simon Bolivar in Venezuela. He continued his education enrolling in a Master of Science in mechanical engineering at Mississippi State University, where he obtained a research assistantship at the Center for Advanced Vehicular Systems and graduated in 2007. His thesis in the Master of Science focused in the development of hydrogen porosity models for aluminum alloys, obtaining a best chapter award by the American Foundry Society in 2008. After working as an intern at the research and development center in Volkswagen AG and as a project engineer specialized in foundry technology in Germany and USA, he joined the Ph.D. program of Purdue University. In 2011, he started to work with Professor Pablo Zavattieri in mechanics of materials. Enrique Escobar de Obaldia also holds the prestigious Roberto Rocca Fellowship granted between 2010 and 2011 and the Nellie Munson Teaching Assistant Award in 2013. His research interests focus in the development of continuum models for multi-physic applications.